

Epitaxial growth and characterization of dilute nitride based “W”-quantum well heterostructures for laser applications

Dissertation

zur

Erlangung des Doktorgrades

der Naturwissenschaften

(Dr. rer. nat.)

dem

Fachbereich Physik

der Philipps-Universität Marburg

vorgelegt von

Jannik Lehr

Aus

Weilburg

Marburg (Lahn), 2022

Vom Fachbereich Physik
der Philipps-Universität Marburg
als Dissertation angenommen am: 11.03.2022
Erstgutachter: Prof. Dr. Wolfgang Stolz
Zweitgutachter: Prof. Dr. Wolfram Heimbrod
Tag der mündlichen Prüfung: 21.03.2022
Hochschulkennziffer: 1180

Zusammenfassung

Das Internet und seine Anwendungen wachsen seit ihrer Erfindung stetig und sind aus der modernen Welt nicht mehr wegzudenken. Durch Anwendungen wie Videostreaming, Videokonferenzen und Cloud Computing werden die Anforderungen an die Bandbreite immer größer. Diese können schon seit dem Aufkommen des Internets nicht mehr allein durch elektrische Signalübertragung gewährleistet werden. Stattdessen sorgen optische Übertragungswege für eine schnelle und zuverlässige Übermittlung. Diese optischen Übertragungswege basieren auf optischen Glasfasern, die ein großes, die gesamte Welt umspannendes Netz bilden. In diese Glasfaserkabel wird Licht eingespeist, an das einige Anforderungen gestellt werden. Zum einen muss es möglich sein, die Lichtquelle schnell elektrisch modulieren zu können, um die entsprechende Bandbreite realisieren zu können. Außerdem soll das Signal möglichst weit ungestört übertragen werden können, weshalb das Absorptionsspektrum von Glasfaserkabeln betrachtet werden muss. Dieses hat ein Absorptionsminimum bei einer Wellenlänge von $1.55\text{ }\mu\text{m}$, also im infraroten Bereich. Nicht nur die Absorption ist wichtig, sondern auch die Dispersion, die möglichst gering sein sollte, damit einzelne Lasermode wiederum eine möglichst geringe Phasendifferenz untereinander erfahren. Dies ist bei einer Wellenlänge von $1.3\text{ }\mu\text{m}$ möglich. All diese Anforderungen werden ideal durch Halbleiterlaserdioden mit Emissionswellenlängen in der Nähe von $1.3\text{ }\mu\text{m}$ oder $1.55\text{ }\mu\text{m}$ erfüllt, weshalb diese für Anwendungen der optischen Signalübertragung zum Einsatz kommen.^{1,2}

Typische Materialien für solche Laser basieren auf InP-Substraten und beinhalten (In,Ga)(As,P)-, (Al,Ga,In)As- oder (Ga,In)As-Quantenfilme. Alle diese Materialien haben das Problem, dass sie große Auger- und andere Verluste aufweisen und damit die Struktur erhitzen.³⁻⁵ Gleichzeitig sind diese aber auch temperatursensitiv, weshalb externe Kühler verwendet werden müssen, die wiederum die Gesamteffizienz der Systeme absenken.^{6,7}

Eine weitere Problematik InP-basierter Materialsysteme ist das Substrat selbst, weshalb andere Substrate bevorzugt werden würden. So hat GaAs den Vorteil, dass alle Prozesse zur Verarbeitung etabliert sind und günstige, große Wafer für hohen Produktionsdurchsatz verfügbar sind. Außerdem existiert mit (Al,Ga)As ein fast gitterangepasstes Material, mit dem Bragg-Spiegel hoher Qualität hergestellt werden können. Leider wurde bis heute kein Materialsystem gefunden, das auf GaAs mittels metallorganischer Gasphasenepitaxie (MOVPE) gewachsen werden kann und gleichzeitig unter Raumtemperaturbedingungen bei $1.55\text{ }\mu\text{m}$ Laseremission aufweist, da alle typischen GaAs-basierten Materialien vorher durch zu starke Verspannung limitiert werden.

Um die oben genannten Auger-Verluste zu umgehen^{8,9} und gleichzeitig die Emissionswellenlänge weiter in Richtung von 1.55 μm zu verschieben, wurden Typ-II Strukturen vorgeschlagen, welche auf mehreren Quantenfilmen basieren, die eine Typ-II Bandanordnung ausbilden. Dabei bilden sich Quantisierungs-niveaus für Elektronen und Löcher in unterschiedlichen Materialien aus, was eine separate und präzisere Modifikation der elektrischen Eigenschaften für Elektronen und Löcher erlaubt. In der Vergangenheit wurden verschiedene GaAs-basierte Typ-II Heterostrukturen untersucht, wie z.B. $(\text{Ga,In})\text{As}/\text{Ga}(\text{As,Sb})/(\text{Ga,In})\text{As}$ Typ-II „W“ Heterostrukturen, für die sogar effiziente Laser realisiert werden konnten¹⁰. Als „W“ Strukturen werden Heterostrukturen bezeichnet, die nicht nur einen Elektronenquantenfilm enthalten, sondern zwei, die durch einen Lochquantenfilm getrennt werden. Eine solche Bandanordnung weist einen höheren Wellenfunktionsüberlapp der Loch- und Elektronenzustände auf, wodurch ein höherer Materialgewinn zu erwarten ist. Dieses Material ist ebenfalls durch Verspannung auf Emissionswellenlängen unter 1.3 μm limitiert, da beide Materialsysteme kompressiv verspannt sind.

Um dieses Problem zu umgehen, wurden verdünnt stickstoffhaltige Quantenfilme für Elektronen $\text{Ga}(\text{N,As})$ oder $(\text{Ga,In})(\text{N,As})$ vorgeschlagen. Damit konnte gezeigt werden, dass Emissionswellenlängen von bis zu 3 μm theoretisch möglich sind. Aufgrund von fehlenden Optimierungen konnte jedoch für entsprechende Laserstrukturen bis jetzt nie bei Raumtemperatur die Laserschwelle überschritten werden.^{11–14}

In dieser Arbeit wurde das epitaktische Wachstum mittels MOVPE und die Eigenschaften von verdünnt stickstoffhaltigen Typ-II Laserstrukturen untersucht, um Laseremission bei Raumtemperatur zu erzielen. Dabei wurden die drei folgenden Heterostrukturen als Typ-II „W“ Strukturen eingesetzt: $\text{Ga}(\text{N,As})/\text{Ga}(\text{As,Sb})/\text{Ga}(\text{N,As})$, $\text{Ga}(\text{N,As})/(\text{Ga,In})\text{As}/\text{Ga}(\text{N,As})$ und $(\text{Ga,In})(\text{N,As})/\text{Ga}(\text{As,Sb})/(\text{Ga,In})(\text{N,As})$.

Das epitaktische Wachstum erwies sich als Herausforderung, da Antimon und Indium als große Elemente dazu neigen, zum Teil an der Wachstumsoberfläche zu segregieren und damit auch einen Einfluss auf die Abscheidung der folgenden Schichten nehmen. Für alle Materialsysteme wurden deshalb Wachstumsstudien ausgeführt, um die Qualität der Struktur zu optimieren. Dabei wird ein besonderer Fokus auf den Einfluss von Antimon auf den Stickstoffeinbau der folgenden $\text{Ga}(\text{N,As})$ Schicht gelegt. Die Untersuchungen wurden in Gasphasen- und Oberflächeneffekte eingeteilt. Gasphaseneffekte wurden mittels eines in-situ Massenspektrometers analysiert, während Wachstumsexperimente an dicken $\text{Ga}(\text{N,As})$ Schichten für die Charakterisierung von Oberflächeneffekten verwendet wurden. Dabei wird ersichtlich, dass der typischerweise verwendete Präkursor für Stickstoff 1,1-Dimethylhydrazin (UDMHy) seine Dekompositionstemperatur zu höheren Temperaturen verschiebt, wenn Antimonatome die Oberfläche belegen. Im Vergleich dazu kann

dieser Effekt bei Verwendung der neuartigen Stickstoffquelle di-*tert*-butyl-amino-arsan (DTBAA) nicht beobachtet werden. In gleicher Weise wird ein stark reduzierter Stickstoffeinbau in Ga(N,As) Schichten beobachtet, wenn kleine Mengen der Antimonpräkursors angeboten werden und UDMHy als Stickstoffquelle verwendet wird. Im Kontrast dazu bleibt der Stickstoffeinbau unter Verwendung von DTBAA vollkommen unverändert, trotz hoher Oberflächenbelegung mit Antimonatomen.

Die oben beschriebenen Erkenntnisse bestätigten sich bei der Untersuchung von doppelten Quantenfilmstrukturen auf Basis von Ga(As,Sb)/Ga(N,As) Heterostrukturen, bei denen zunächst ein Ga(As,Sb) Quantenfilm und anschließend ein Ga(N,As) Quantenfilm gewachsen wurden. Der Stickstoffeinbau in die Ga(N,As) Schicht reduziert sich in diesem Fall um ungefähr 60% im Vergleich zum Wachstum auf GaAs Oberflächen. Im Folgenden wurde analysiert, wie diese reduzierten Einbauten kompensiert werden können. Es stellte sich heraus, dass der UDMHy Anteil an der Gasphase während des Wachstums der Ga(N,As) Schicht erhöht werden kann, um höhere Einbauten zu erzielen. Auf diese Weise kann in den vollständigen „W“ Strukturen ein gleicher Stickstoffeinbau in beide Ga(N,As) Quantenfilme erzielt werden.

Zusätzlich werden die inneren Grenzflächen der „W“ Struktur optimiert, indem an der ersten Grenzfläche eine kurze Vorbelegung mit Antimonatomen eingeführt wurde, während an der Grenzfläche nach dem Ga(As,Sb) Quantenfilm eine TBAs stabilisierte Wachstumsunterbrechung zur Desorption von oberflächensegregierten Antimonatomen genutzt wurde. Beides führt zu einem abrupteren Antimon-Einbauprofil. Es stellte sich heraus, dass die Dauer dieser Wachstumsunterbrechung entscheidend für die Optimierung der inneren Grenzfläche ist. Zu lang andauernde Wachstumsunterbrechungen führen nicht nur zur Desorption der Oberflächenatome, sondern auch zur Desorption von Antimon aus dem bereits gewachsenen Kristall, was dazu führt, dass Löcher in der Wachstumsoberfläche entstehen. Bevor dieser Effekt einsetzt, wurde jedoch eine Verbesserung der Oberflächenqualität beobachtet. Als ideale Längen der Wachstumsunterbrechungen wurde in Abhängigkeit von der Wachstumstemperatur 20 s für 550°C und 30 s für 525°C bestimmt. Bei diesen Dauern ist davon auszugehen, dass noch oberflächensegregiertes Antimon vorhanden ist, jedoch ist die Anzahl dieser Atome bereits drastisch reduziert und die Oberflächenqualität optimiert.

Eine ähnliche Problematik tritt beim epitaktischen Wachstum von Ga(N,As)/(Ga,In)As/Ga(N,As) auf. Dort wird der Stickstoffeinbau durch oberflächensegregierte Indiumatome in die zweite Ga(N,As) Schicht um 40% reduziert. Im Gegensatz zu Antimonatomen sind Indiumatome weitaus weniger flüchtig, was dazu führt, dass es in diesem Fall unpraktikabel ist, diese zu desorbieren. Nach 120 s TBAs stabiler Wachstumsunterbrechung zeigte sich zwar eine Optimierung der optischen Qualität, jedoch noch keine Änderung des Stickstoffeinbaus.

Noch kritischer ist ein ausreichender Stickstoffeinbau, wenn sowohl Indium- als auch Antimonatome gleichzeitig vorhanden sind, wie es bei $(\text{Ga,In})(\text{N,As})/\text{Ga}(\text{As,Sb})/(\text{Ga,In})(\text{N,As})$ Heterostrukturen der Fall ist. Daher wurde für dieses Materialsystem erfolgreich die neuartige Stickstoffquelle DTBAA eingesetzt, die in diesen Fällen einen unbeeinflussten Stickstoffeinbau aufweist.

Basierend auf diesen Wachstumsexperimenten wurden vollständige Laserstrukturen hergestellt und ausführlich charakterisiert. Alle untersuchten Materialsysteme haben die Eigenart, dass als wichtigstes Element kleine Mengen an Stickstoff dazu benutzt werden, die Leitungsbandkante erheblich zu reduzieren. Daher wurde zunächst der Einfluss des Stickstoffgehalts auf die optischen Eigenschaften der Strukturen untersucht. Dabei wurde für alle Materialsysteme ein Einfluss festgestellt, der bei $(\text{Ga,In})(\text{N,As})/\text{Ga}(\text{As,Sb})/(\text{Ga,In})(\text{N,As})$ Heterostrukturen nur minimal ist, jedoch bei beiden anderen Materialsystemen die optische Effizienz bei steigendem Stickstoffgehalt exponentiell verringern lässt. Dies ist damit zu erklären, dass Stickstoff zu spezifischen Defekten führt, die als nichtstrahlende Rekombinationszentren die optische Ausgangsleistung stark verringern. Damit erwiesen sich $\text{Ga}(\text{N,As})/(\text{Ga,In})\text{As}/\text{Ga}(\text{N,As})$ Heterostrukturen als das am wenigsten geeignete aktive Lasermaterial, da diese in weiterer Analyse zeigten, dass bis zu 4% Stickstoff notwendig sind, um eine Emissionswellenlänge von $1.3\ \mu\text{m}$ zu erreichen. Dagegen zeigte sich, dass $\text{Ga}(\text{N,As})/\text{Ga}(\text{As,Sb})/\text{Ga}(\text{N,As})$ Heterostrukturen nur einen Stickstoffeinbau von ungefähr 2% benötigen und $(\text{Ga,In})(\text{N,As})/\text{Ga}(\text{As,Sb})/(\text{Ga,In})(\text{N,As})$ „W“ Strukturen sogar nur von 1%. Mit letzterem konnte sogar mit vergleichsweise wenig Stickstoff eine Emissionswellenlänge von $1.55\ \mu\text{m}$ erzielt werden.

Bei der Analyse der optischen Ausgangsleistungen in Abhängigkeit von der Anregungsdichte zeigte sich, dass $\text{Ga}(\text{N,As})/\text{Ga}(\text{As,Sb})/\text{Ga}(\text{N,As})$ Strukturen mit weniger als 3% Stickstoff eine Sättigung der optischen Ausgangsleistungen aufweisen. Bevor ausreichend große Ladungsträgerdichten in den Kavitäten erreicht werden können, ermöglicht eine Besetzung von höheren quantisierten Zuständen eine Leckage von Elektronen in Barrierenzustände. Im Fall von Stickstoffeinbauten über 3% sind die nichtstrahlenden Rekombinationsprozesse an durch Stickstoff bedingten Defekten der limitierende Faktor. Beide Verlustprozesse führten dazu, dass die Laserschwelle für die untersuchten Laserstrukturen noch nicht erreicht wurde. Auch an den alternativen „M“ Strukturen $\text{Ga}(\text{As,Sb})/\text{Ga}(\text{N,As})/\text{Ga}(\text{As,Sb})$ wurden diese beiden Verlustprozesse festgestellt. Die optischen Eigenschaften der „M“ Strukturen erwiesen sich durch die verringerte Kopplung der $\text{Ga}(\text{As,Sb})$ Lochquantenfilme als schlechter als die von „W“ Strukturen. Diese ergibt sich durch die hohe effektive Masse der Lochzustände.

Indem $\text{Ga}(\text{N,As})$ in diesen Strukturen durch $(\text{Ga,In})(\text{N,As})$ ersetzt wurde, konnten diese Probleme teilweise umgangen werden, da zum einen der notwendige Stickstoffeinbau niedriger ist, aber

gleichzeitig durch den zusätzlichen Indiumeinbau eine ausreichend hohe Barriere im Leistungsband verfügbar ist. Mit diesen Strukturen konnte so das große Ziel eines bei Raumtemperatur funktionierenden Typ-II Lasers auf Basis von verdünnt stickstoffhaltigen Materialien erreicht werden. Dieser wies bei einem Stickstoffinhalt von 1.1% eine Schwellstromdichte von 9.5 kA/cm^2 , eine differenzielle Effizienz von 1% und eine optische Effizienz von 4.6 mW/A auf. Eine pumpstromlimitierte maximale Ausgangsleistung von $27.5 \text{ }\mu\text{W}$ wurde gemessen. Die spektrale Analyse führte zur Emissionswellenlänge von $1.28 \text{ }\mu\text{m}$.

Laserstrukturen basierend auf $\text{Ga(N,As)/(Ga,In)As/Ga(N,As)}$ wiesen zu geringe Höhen der Barrieren insbesondere im Valenzband auf, wodurch sich Zustände ausbilden, die die gesamte „W“ Heterostruktur umfassen. Dadurch wurde auch für dieses Materialsystem kein Laserbetrieb beobachtet.

Wenn alle möglichen verdünnt stickstoffhaltigen Materialsysteme auf GaAs Substrat auf ihre Nutzbarkeit als aktives Lasermaterial untersucht werden, fällt auf, dass bis jetzt nur sehr spezifische Materialien als aktives Material für Laser benutzt werden konnten. Dazu zählen $(\text{Ga,In})(\text{N,As})$ ⁵⁹, $(\text{Ga,In})(\text{N,As,Sb})$ ⁷¹ und $(\text{Ga,In})(\text{N,As})/\text{Ga(As,Sb)}/(\text{Ga,In})(\text{N,As})$ Typ-II „W“ Strukturen. Im Gegensatz dazu konnte mit Ga(N,As,Sb) oder Ga(N,As) nie ein funktionierender Laser bei Raumtemperatur gezeigt werden. Auffällig ist, dass die geeigneten Materialien immer Indium enthalten. Da Stickstoff im Allgemeinen zu einer erhöhten Defektdichte führt, muss thermisches Annealing („ausheilen“) angewandt werden, durch das die mikroskopische Anordnung der Stickstoffatome so verändert wird, dass die Defektdichte reduziert wird. In indiumhaltigen Schichten geschieht dies durch Platzwechsel der Stickstoffatome in indiumreichen Umgebungen. In einer Publikation zeigten Volz et al., dass so bei $(\text{Ga,In})(\text{N,As})$ Quantenfilmen eine Verbesserung der Homogenität der Stickstoffverteilung erzielt werden kann, während die Homogenität bei Ga(N,As) Quantenfilmen wahrscheinlich durch fehlendes Indium verringert wurde¹⁵. Dadurch könnten sich in Ga(N,As) Schichten eventuell weitere Ansammlungen von Stickstoffatomen bilden, die die optische Qualität verringern. Dies könnte ein Hinweis darauf sein, warum Indium für die Verwendung als aktives Lasermaterial bisher eine Notwendigkeit darstellte.

Im weiteren Verlauf wurden optimale Annealingbedingungen sowohl für in-situ Reaktorannealing als auch für zusätzliches Rapid Thermal Annealing (RTA) analysiert. Dabei wurden verschiedene Temperaturen und verschiedene Zusammensetzungen der umgebenden Gasphase untersucht. Es zeigte sich, dass alle Strukturen durch diese Prozesse in ihren Eigenschaften deutlich verschlechtert werden, was auf ein zu langes oder zu intensives Annealing zurückgeführt wurde, da der notwendige Überwachsprozess mit dem p-Kontakt bereits einen Annealingschritt darstellt.

Zusammenfassend wurde bewiesen, dass die Entwicklung eines Lasers auf Basis von verdünnt stickstoffhaltigen Typ-II Materialien möglich ist, indem zum ersten Mal Laserbetrieb bei Raumtemperatur für ein solches Materialsystem gezeigt wurde. Aufbauend auf diesen guten Ergebnissen werden in Zukunft einige Optimierungen an den oben diskutierten Laserstrukturen ausgeführt. Dazu zählt eine weitere Aufreinigung der Stickstoffquelle DTBAA, um eine deutlich verbesserte Materialqualität zu erreichen. Gleichzeitig werden Studien zum epitaktischen Wachstum von $(\text{Ga,In})(\text{N,As})/\text{Ga}(\text{As,Sb})/(\text{Ga,In})(\text{N,As})$ Typ-II „W“ Strukturen mit dem etablierten Präkursor UDMHy realisiert. Da passendes Annealing trotz der diskutierten Ergebnisse wahrscheinlich zu verbesserten optischen Eigenschaften führen wird, werden in Zukunft neue Strukturen weiter dazu benutzt, um optimierte Annealingbedingungen zu finden. Um mikroskopische Prozesse während des Annealings zu verstehen, müssen dabei zusätzliche Messungen mit dem Transmissionselektronenmikroskop durchgeführt werden. Eine Optimierung der chemischen Zusammensetzungen der einzelnen Schichten und der entsprechenden Schichtdicken werden weiter die Eigenschaften der Laserstrukturen wie die differenzielle Effizienz oder die Schwellstromdichte verbessern. Gleichzeitig wird eine solche Verbesserung auch die Emissionswellenlänge weiter in Richtung $1.55 \mu\text{m}$ verschieben. Zusätzliche Analysen und Optimierungen der inneren Grenzflächen können auch zu weiteren Verbesserungen der Effizienz der Typ-II Rekombinationen führen. Des Weiteren könnte die Reflektivität mindestens einer Laserfacette durch Beschichtung erhöht werden, um die optischen Verluste der Struktur zu verringern, wodurch die Schwellstromdichte sinken wird.

Die GaAs Barrieren, in die $\text{Ga}(\text{N,As})/\text{Ga}(\text{As,Sb})/\text{Ga}(\text{N,As})$ „W“ Heterostrukturen abgeschieden werden, sollten in weiteren Experimenten durch andere Materialien wie $\text{Ga}(\text{As,P})$ oder $(\text{Al,Ga})\text{As}$ ersetzt werden, um so die Barriere im Leitungsband zu erhöhen. Dadurch könnte die Ladungsträgerleckage verringert werden und eventuell die Laserschwelle erreicht werden. Zusätzliche Beschichtung der Facetten würde die Photonendichte in den Kavitäten deutlich verbessern.

Nicht nur weitere Experimente in Bezug auf Typ-II Strukturen sind denkbar, sondern auch zu verdünnt stickstoffhaltigen Materialien im Allgemeinen. Für $(\text{Ga,In})(\text{N,As,Sb})$ Quantenfilme wurden in der Vergangenheit bereits Laserdioden gezeigt, die bei Raumtemperatur betrieben werden können. Aufgrund der Komplexität des Wachstums konnten diese jedoch nur mit Molekularstrahlenepitaxie realisiert werden. Mit Hilfe des neuen Präkursors DTBAA könnte jetzt auch ein epitaktisches Wachstum mittels MOVPE möglich sein.

Außerdem können weitere Grundlagenexperimente durchgeführt werden, die den Effekt des reduzierten Stickstoffeinbaus aufklären, wenn UDMHy als Stickstoffquelle zusammen mit Indium- oder Antimon-Oberflächenbelegung eingesetzt wird. Dazu sollten detaillierte Zerlegungsexperimente mit Hilfe des in-situ Massenspektrometers mit ergänzender Analyse der Oberflächenstruktur mit

Reflexionsanisotropiespektroskopie durchgeführt werden. Dabei müssen vor allen Dingen die unterschiedlichen Zerlegungspfade in Abhängigkeit der Oberfläche untersucht werden.

Publications

Parts of this thesis were already published:

J. Lehr, L. Hellweg, C. Fuchs, S. Firoozabadi, P. Kükelhan, A. Beyer, K. Volz, W. Stolz. Effect of growth interruption on Ga(N,As)/Ga(As,Sb)/Ga(N,As) type-II-“W” quantum well heterostructures. *Journal of Crystal Growth* **582**, 126501 (2022) doi: <https://doi.org/10.1016/j.jcrysgro.2021.126501>

J. Lehr, C. Ritter, S. Reinhard, A. Ruiz Perez, C. von Hänisch, W. Stolz. Room temperature laser emission of (Ga,In)(N,As)/Ga(As,Sb)/(Ga,In)(N,As) type-II ‘W’ quantum well heterostructures. *Electronics Letters* (2022) doi: <https://doi.org/10.1049/ell2.12427>

Further publications:

T. Hepp, J. Lehr, R. Güntel, O. Maßmeyer, J. Glowatzki, A. Ruiz Perez, S. Reinhard, W. Stolz, K. Volz. Room-temperature laser operation of a (Ga,In)As/Ga(As,Bi)/(Ga,In)As W-type laser diode. *Electronics Letters* **58**, 70-72 (2022) doi: <https://doi.org/10.1049/ell2.12353>

L. Rost, J. Lehr, M. Maradiya, L. Hellweg, F. Fillsack, W. Stolz, W. Heimbrod. The influence of growth interruption on the luminescence properties of Ga(As,Sb)-based type-II heterostructures. *Journal of Luminescence* **231**, 117817 (2021) doi: <https://doi.org/10.1016/j.jlumin.2020.117817>

D. Duffy, I. Marko, C. Fuchs, T. Eales, J. Lehr, W. Stolz, S. Sweeney. Performance characteristics of low threshold current 1.25 μm type-II GaInAs/GaAsSb ‘W’-lasers for optical communications. *Journal of Physics D: Applied Physics* **54**, 365104 (2021) doi: <https://doi.org/10.1088/1361-6463/ac0b72>

J. Ornik, J. Lehr, M. Reuter, D. Jahn, F. Beltran-Mejia, J. Balzer, T. Kleine-Ostmann, M. Koch. Repeatability of material parameter extraction of liquids from transmission terahertz time-domain measurements. *Optics Express* **28**, 28178 (2020) doi: <https://doi.org/10.1364/OE.403159>

D. Jahn, M. Weidenbach, J. Lehr, L. Becker, F. Beltran-Mejia, S. Busch, J. Balzer, M. Koch. 3D Printed Terahertz Focusing Grating Couplers. *Journal of Infrared, Millimeter, and Teahertz Waves* **38**, 708-716 (2017) doi: <https://doi.org/10.1007/s10762-017-0370-5>

Contents

CHAPTER 1	INTRODUCTION	17
CHAPTER 2	PHYSICAL BACKGROUND.....	21
2.1	Semiconductors	21
2.1.1	Structural properties	21
2.1.2	Band structure and electronic properties	24
2.1.3	Semiconductor random alloys	30
2.2	Epitaxial growth of semiconductors.....	33
2.2.1	Strain.....	35
2.2.2	Alloys	37
2.3	Heterostructures	39
2.3.1	Band alignments	39
2.3.2	Quantum wells.....	40
2.3.3	Influence of strain on band structure	42
2.3.4	pn-junction	43
2.4	Dilute nitrides	44
2.4.1	Annealing.....	48
2.5	Semiconductor Lasers	49
2.5.1	Active region and pump source.....	50
2.5.2	Cavity	53
2.5.3	Mathematical description	55
2.5.4	Nonradiative transitions and loss channels	58
2.6	Type-II heterostructures for device applications.....	62
CHAPTER 3	EXPERIMENTAL METHODS.....	65
3.1	Metalorganic Vapor-Phase Epitaxy	65
3.1.1	Precursor molecules	65
3.1.2	Technical implementation	67
3.1.3	Experimental details	70

3.2	High Resolution X-ray diffraction	71
3.3	Photoluminescence Spectroscopy	73
3.4	Electroluminescence Spectroscopy	77
3.5	Atomic force microscopy	81
3.6	Rapid thermal annealing.....	82
3.7	Simulation of laser devices	82
CHAPTER 4 EPITAXIAL GROWTH OF SINGLE QUANTUM WELLS		85
4.1	Gallium indium arsenide (Ga,In)As	86
4.2	Dilute incorporation of nitrogen into GaAs: gallium nitride arsenide Ga(N,As)	88
4.2.1	Dimethylhydrazine (UDMHy) as nitrogen source	89
4.2.2	Di-tert-butyl-amino-arsane as nitrogen and arsenic source.....	91
4.2.3	Nitrogen profiles in thin quantum wells	92
4.3	Gallium arsenide antimonide Ga(As,Sb)	94
4.4	Quaternary material: gallium indium nitride arsenide (Ga,In)(N,As).....	97
4.5	Influence of antimony on nitrogen incorporation into Ga(N,As)	100
4.5.1	Gas phase effects.....	100
4.5.2	Influence of antimony surface coverage on nitrogen incorporation.....	104
4.5.3	Compensation of reduced incorporation efficiency	108
4.5.4	Discussion	109
CHAPTER 5 Ga(N,As)/Ga(As,Sb)/Ga(N,As) “W” TYPE-II HETEROSTRUCTURES.....		111
5.1	Band alignments and challenges.....	111
5.2	Epitaxial growth of consecutive Ga(As,Sb)/Ga(N,As) quantum well layers	113
5.2.1	Growth with UDMHy as nitrogen source	113
5.2.2	Growth with DTBAA as nitrogen and arsenic source for Ga(N,As) growth	115
5.2.3	Growth parameters of single quantum well layers	116
5.3	Preparation of internal interfaces.....	120
5.3.1	Interface 1.....	121
5.3.2	Interface 2.....	121

5.4	Nitrogen incorporation symmetry optimization using growth interruptions	124
5.5	Symmetry optimization of “W”-quantum well heterostructures	127
5.6	Investigation of Laser structures	131
5.6.1	Double quantum well heterostructure laser device	132
5.6.2	Dependence of device properties on nitrogen content	134
5.6.3	Number of “W” quantum well heterostructures	143
5.6.4	Nitrogen precursor comparison: DTBAA and UDMHy	147
5.6.5	Comparison of WQWH and “M” quantum well heterostructures	151
5.6.6	RTA annealing	155
5.7	Summary and discussion	157
CHAPTER 6 GA(N,AS)/(GA,IN)AS/GA(N,AS) “W” TYPE-II HETEROSTRUCTURES		159
6.1	Introduction and band structure	159
6.2	Epitaxial growth of consecutive (Ga,In)As/Ga(N,As) quantum wells	160
6.3	Optical properties	161
6.4	Preparation of internal interface	164
6.5	Laser structures	165
6.6	Conclusion and discussion	167
CHAPTER 7 (GA,IN)(N,AS)/GA(AS,SB)/(GA,IN)(N,AS) “W” TYPE-II HETEROSTRUCTURES		169
7.1	Introduction and electronic properties	169
7.2	Epitaxial growth	171
7.3	Laser structures	171
7.3.1	Nitrogen content	172
7.3.2	Lasing characteristics	174
7.3.3	Cavity length	177
7.3.4	Temperature dependency	178
7.3.5	Influence of annealing	179
7.4	Conclusion and discussion	185

CHAPTER 8	CONCLUSION AND OUTLOOK.....	189
CHAPTER 9	BIBLIOGRAPHY.....	195
APPENDIX I	SAMPLE INDEX.....	209

Chapter 1 Introduction

The internet and its applications are of outstanding importance for the modern world and have shown an ever-increasing growth since its development due to applications like video streaming, video conferences, cloud computing, and many more. All these applications increase the demand for high bandwidths that cannot be achieved with conventional electric signal transmission. Instead, optical glass fibers are used to carry optical signals, especially over longer distances. This places several requirements regarding the used light sources. A quick electrical modulation must be possible. Glass fibers exhibit an absorption minimum at 1550 nm and a dispersion minimum at 1300 nm. Consequently, light sources used for optical communication must utilize emission wavelengths in close vicinity to one of these minima to be able to transmit data over a maximum possible length. Diode lasers can fulfill all of these demands.^{1,2}

Suitable semiconductor materials for such diode lasers make use of InP substrates and include (In,Ga)(As,P), (Al,Ga,In)As and (Ga,In)As. Their weak point is that they suffer from large amounts of Auger losses responsible for 50 to 80% of their threshold current. A wide variety of other loss channels were also reported.^{3–5} Additionally, a high-temperature sensitivity compared to other materials yields the necessity for temperature stabilization, causing the wall-plug efficiency to drop significantly.^{6,7}

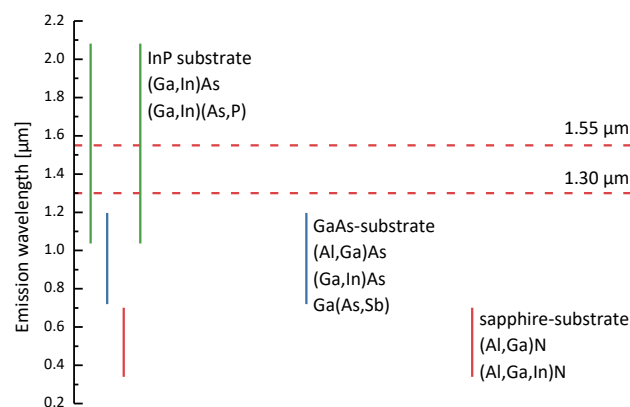


Figure 1.1 Reachable wavelengths of semiconductor compounds on different substrates are illustrated. For short wavelength applications GaN-based materials are employed. For visible light applications GaAs substrates are well suited, while for long wavelength emission InP substrates can be utilized. Adapted from¹⁶.

Compared to InP, the GaAs platform profits from well-established manufacturing techniques and larger wafer diameters, enabling a higher production yield while offering lower wafer prices. Additionally, high quality lattice matched (Al)GaAs-AlAs DBR stacks provide high refractive index contrasts rendering the possibility for high quality vertical-cavity surface-emitting laser (VCSEL) and

vertical-external-cavity surface-emitting laser (VECSEL) devices¹⁷. Thus, a lot of research effort has been made to develop laser devices based on GaAs substrate emitting at 1.3 μm or 1.55 μm . Several approaches were investigated, including quantum well lasers based on (Ga,In)As^{18–26} or Ga(As,Sb)^{27–40} quantum wells. While (Ga,In)As provides good carrier confinement in the conduction band as well as the valence band, Ga(As,Sb) quantum wells combined with GaAs barriers are assumed to even form a type-II band alignment due to the conduction band offset³⁸. Hence, electrons are only weakly confined, if at all. Possible emission wavelengths of both materials are limited by strain with a maximum value of about 1.28 μm . To overcome these strain limits, metamorphic buffer layers were employed consisting of thick relaxed layers of for example (Ga,In)As deposited on GaAs on which (Ga,In)As active layers can be grown with a higher indium content than what would be possible on GaAs substrates, shifting the emission wavelength further towards essential regions.^{41–43} Besides that, diluted incorporation of relatively large or small elements like bismuth or nitrogen cause the band gap to be reduced significantly⁴⁴. However, only Ga(As,Bi) lasers were presented^{45–48} while Ga(N,As) lasers could never be realized most probably because the effect of band gap reduction takes place only in the conduction band and no hole confinement is possible. Nevertheless, dilute nitrides played an essential role in further developments of quaternary compounds. Ga(N,As,Sb) quantum wells promise good electron and hole confinement but showed no room temperature lasing^{49–52}. In contrast, the investigation of (Ga,In)(N,As) quantum wells resulted in the development of laser devices emitting near 1.3 μm and even 1.55 μm while exhibiting a strong nitrogen penalty.^{53–67} Going one step further, even (Ga,In)(N,As,Sb) showed room temperature laser emission of up to 1.55 μm but due to significant challenges of growing such complex materials with metal organic vapor phase epitaxy, only molecular beam epitaxy can be used for realizing these structures.^{68–73} Another approach to overcome strain issues is using quantum dots based on In(Ga)As.^{74–76} With this, emission wavelengths of 1.3 μm can be easily reached but the extension to 1.5 μm is complex.^{77–79} Most recently, “W” type-II quantum well heterostructures based on (Ga,In)As/Ga(As,Sb)/(Ga,In)As exhibiting laser emission at room temperature emitting at 1.3 μm were presented.¹⁰ These materials enable more degrees of freedom when band structure engineering is considered, promising for example a reduction of Auger recombinations^{8,9} and an improvement of charge carrier confinement. However, this material is limited by strain because (Ga,In)As as well as Ga(As,Sb) are both compressively strained when grown on GaAs substrates. Therefore, Ga(N,As) or (Ga,In)(N,As) were investigated as a replacement for (Ga,In)As electron quantum wells in order to shift the emission to longer wavelengths. However, no room temperature lasing was achieved so far^{11–14}.

In this thesis, an in-depth discussion of the epitaxial growth and resulting devices of these dilute nitride-based type-II “W” quantum well heterostructures will be carried out with the ultimate goal of room temperature laser emission. Further description of type-II band alignments and devices will be

presented together with an overview of the physical background in Chapter 2. All applied experimental methods will be discussed in Chapter 3, followed by a combined experimental and literature review of single quantum wells in Chapter 4 that will be employed as parts of the following type-II heterostructures. The next three chapters are dedicated to “W” type-II heterostructures considering the epitaxial growth using metal organic vapor phase epitaxy and in-depth discussions of laser structure characteristics. As first heterostructures $\text{Ga(N,As)/Ga(As,Sb)/Ga(N,As)}$ quantum wells will be presented in Chapter 5, in which Ga(N,As) is used as electron confining material and Ga(As,Sb) for hole confinement. Similarly, $\text{Ga(N,As)/(Ga,In)As/Ga(N,As)}$ heterostructures are discussed in Chapter 6, in which holes are confined in a $(\text{Ga,In})\text{As}$ quantum well. $(\text{Ga,In})(\text{N,As})/\text{Ga(As,Sb)}/(\text{Ga,In})(\text{N,As})$ heterostructures resemble the last material system investigated in this thesis in Chapter 7. All obtained results are concluded in Chapter 8, yielding possibilities for future studies.

Chapter 2 Physical Background

2.1 Semiconductors

This section covers the basic principles of semiconductor physics. First, the structural properties will be regarded, and afterward the electronic properties with particular emphasis on the band structure will be discussed. Next, the modification of these electronic properties by alloying will be introduced. An excellent overview of most topics can be found in Kittel's book⁸⁰, and an in-depth discussion of many of these topics can be found in Ashcroft's book⁸¹.

2.1.1 Structural properties

All materials investigated in this thesis are based on inorganic III/V semiconductors which means that they consist of crystallized main group III (boron, aluminum, gallium, indium) and group V (nitrogen, phosphorus, arsenic, antimony) atoms. Besides that, other common semiconductor compounds include II/VI and IV/IV materials. Semiconductors are a material class that is situated between metals and insulators in terms of conductivity, meaning that they are not conductive at very low temperatures while they show conductivity at room temperature to some extent. A more precise definition will follow in this chapter. In the upcoming part, the structural properties of crystalline solids will be summarized.

The mathematical description of crystals is based on the periodical repetition of atomic groups called basis. In the simplest case this basis consists of only one atom but in general can comprise an arbitrary number of atoms. At each lattice points whose positions can be described with a vector \mathbf{T} a basis is placed:

$$\mathbf{T} = n_1 \mathbf{a}_1 + n_2 \mathbf{a}_2 + n_3 \mathbf{a}_3 \quad (2.1)$$

In this equation the numbers n_1, n_2, n_3 are integer numbers and $\mathbf{a}_1, \mathbf{a}_2, \mathbf{a}_3$ translation vectors defined in a way that every lattice point can be translated to every other lattice point using a linear combination of these translation vectors. The volume that they frame is called unit cell. Since the choice of the translation vectors is not definite, the unit cell can be chosen in various ways for one single crystal lattice. However, a primitive unit cell can be defined that represents the unit cell with the smallest volume containing only one lattice point. It can be constructed as a Wigner-Seitz cell

around one lattice point. A Wigner-Seitz cell includes all points to which this lattice point is the closest possible lattice point.

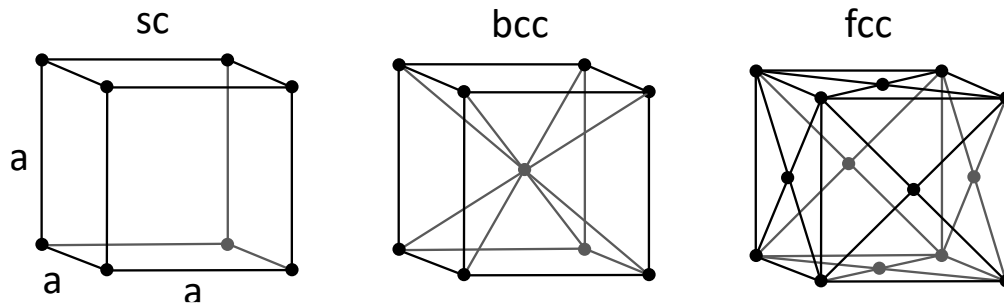


Figure 2.1 Unit cells of the simple cubic (sc), body-centered cubic (bcc) and face-centered (fcc) cubic lattices. The edge lengths of these unit cells are called lattice constant a . In a bcc lattice one additional lattice point is located in the center of the cube, while for fcc lattices lattice points are added in the center of all faces.

For all crystal lattices lattice constants can be defined corresponding to the length of the respective translation vectors. Crystal lattices cannot only be symmetric with translation but also a variety of symmetry operations such as rotation and mirroring can be applied to them, allowing to classify them by their possible symmetry operations. The most accessible and fortunately most important class is the cubic structure based on a cubic unit cell exhibiting only one lattice constant a . It subdivides into several subclasses: simple cubic (sc), body-centered cubic (bcc), and face-centered cubic (fcc) of which the most common unit cells are depicted in Figure 2.1. The sc structure is the simplest of them because it only has lattice points at the corners of the cube. If one additional lattice point is added into the center of the cube, the lattice becomes a bcc lattice. If instead lattice points are added into the face centers of the cube, the lattice becomes a fcc lattice.

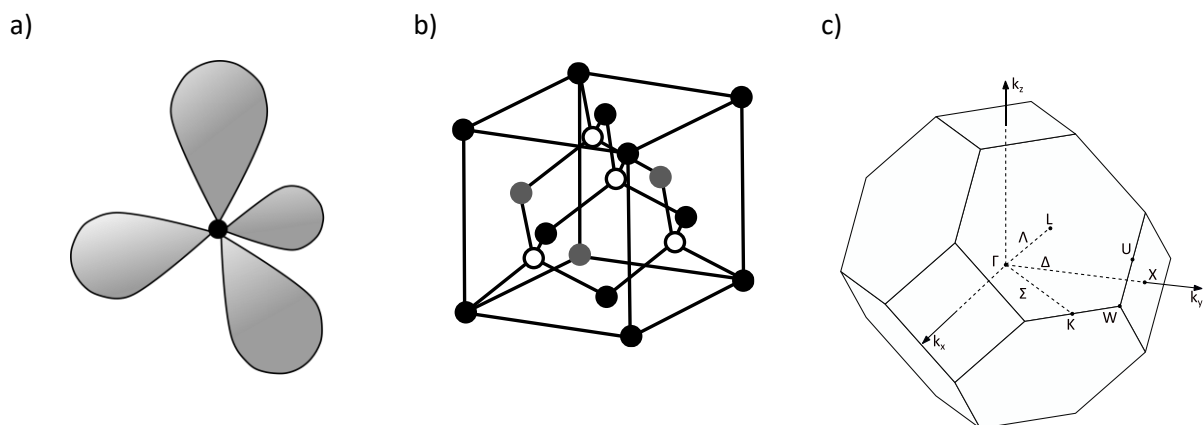


Figure 2.2 a) Shows the tetragonal arrangement of the sp^3 hybridization orbitals. The angle between the orbitals is 109.5° . In b) the Zincblende structure is schematically drawn. The bonds between the group III and V atoms are tetragonally arranged. c) First Brillouin zone of a fcc lattice. Multiple symmetry points are inscribed. Image adapted from⁸².

Interatomic bonding plays a crucial role in understanding why different material systems can exhibit different crystal structures. Group III and V atoms form covalent bonds in conjunction with other

group III and V atoms resulting from overlapping orbitals and the accompanying interaction between the electrons in these orbitals. In this particular case, the orbitals involved are sp^3 hybridization orbitals, which form by one s-orbital merging with three p-orbitals and as a result four new orbitals that are tetrahedrally arranged around the atomic core are created. In Figure 2.2 a) the shape of these sp^3 orbitals around the ion core is schematically illustrated, exhibiting angles of 109.5° . This formation of new orbitals is energetically favorable for bonding and is thus found in III/V semiconductor crystal structures. Most III/V semiconductors crystallize in Zincblende crystal structure, whose unit cell is shown in Figure 2.2 b). A fcc lattice can describe the Zincblende structure with a two atomic basis, including a group III and a group V atom. These atoms are spatially translated by $\frac{1}{4}$ of the space diagonal with respect to each other. One exception from this rule is the material class of nitrides (GaN, InN, ...), which crystallizes in a hexagonal wurtzite crystal structure.

In nature, these crystal atoms are not static and may vibrate due to temperature. These lattice vibrations can be treated as quasi particles which are called phonons. They are involved in a variety of processes by transferring their momentum to other particles to ensure momentum conservation.

For the description of the electric properties as well as the structural analysis it is functional to introduce the reciprocal lattice. Generally speaking, it is the quasi-Fourier transformed lattice of the real space lattice introduced before. Like for the real space lattice it can be described by a set of vectors:

$$\mathbf{G} = n_1 \mathbf{b}_1 + n_2 \mathbf{b}_2 + n_3 \mathbf{b}_3 \quad (2.2)$$

The lattice vectors of the reciprocal lattice can be calculated with the lattice vectors of the real space lattice and the volume of the unit cell V_a by the following equations:

$$\mathbf{b}_1 = \frac{2\pi}{V_a} (\mathbf{a}_2 \times \mathbf{a}_3), \mathbf{b}_2 = \frac{2\pi}{V_a} (\mathbf{a}_3 \times \mathbf{a}_1), \mathbf{b}_3 = \frac{2\pi}{V_a} (\mathbf{a}_1 \times \mathbf{a}_2) \quad (2.3)$$

From this can be shown directly, that a fcc lattice in real space is a bcc lattice in reciprocal space and vice versa. Similar to the real space lattice a Wigner-Seitz cell can be defined in the reciprocal space, the so-called Brillouin zone which is of special importance for characterizing the band structure of the material. Figure 2.2 c) shows the first Brillouin zone of a fcc lattice. In this Brillouin zone specific symmetry points and lines are defined. The highly relevant center point is for instance called Γ point.

The reciprocal lattice can also be used to describe lattice planes, which are typically named by the Miller indices. For cubic crystal structures this set contains three integers h, k, l with the notation (hkl) . It defines a set of parallel lattice planes that can alternatively be described by a point in the reciprocal lattice in which Miller indices are the factors in front of the reciprocal lattice vectors. The

corresponding set of lattice planes are perpendicular to the reciprocal vector. In a cubic crystal the distance between lattice planes d_{hkl} can be calculated using the following equation, if a is the lattice constant:

$$d_{hkl} = \frac{a}{\sqrt{h^2 + k^2 + l^2}} \quad (2.4)$$

Lattice planes will be used to name substrate orientations defining the growth direction and in high-resolution X-Ray diffraction measurements.

2.1.2 Band structure and electronic properties

The electronic energy states of atoms are well known to be discrete. They can be calculated by finding the Eigenvalues of the Schrödinger equation with the ion core potential of the atom. Wavefunctions which are the solutions of the Schrödinger equations describe the probability of finding electrons and are known to resemble orbitals. If atoms are forming a periodical arrangement like in a crystal structure, the orbitals overlap. Hence, the electrons occupying the orbitals also interact with each other and new states are formed. With an increased number of atoms, the number of formed states increases until the states can practically not be distinguished anymore. In real crystals these states subsequently form quasi continuous bands of allowed energetic states.

A simple explanation is given by Bloch's theorem in the one electron approximation. A periodic potential $U(\mathbf{r})$ of the crystal ion cores is assumed as a starting point.

$$U(\mathbf{r}) = U(\mathbf{r} + \mathbf{T}) \quad (2.5)$$

The vector \mathbf{T} represents all lattice points in the direct lattice. The potential is typically a superposition of the ion core potentials with the potential of all electrons. To find out all possible energetic states of this quantum mechanical problem, the Schrödinger equation must be considered:

$$\frac{\hbar^2}{2m} \Delta \psi(\mathbf{r}) + (E - V(\mathbf{r}))\psi(\mathbf{r}) = 0 \quad (2.6)$$

If the Schrödinger equation is solved with this potential, the solutions of the wavefunctions are Bloch functions:

$$\psi_{\mathbf{k}}(\mathbf{r}) = u_{\mathbf{k}}(\mathbf{r}) \exp(i\mathbf{k} \cdot \mathbf{r}) \quad (2.7)$$

These solutions are composed of two functions. One is a periodic function, and the second exponential function equates to a planar wave. Where $u_{\mathbf{k}}(\mathbf{r}) = u_{\mathbf{k}}(\mathbf{r} + \mathbf{T})$ has the same periodicity as the periodic potential $U(\mathbf{r})$. With the right choice of the periodic function the solution is a freely

moving wave, meaning that electrons can move freely through the crystal if they occupy certain energy states. Thus, they may get diffracted at the potentials of the ion cores and for some states if the Bragg reflection condition is fulfilled destructive interference annihilates the wavefunction completely, resulting in forbidden energy bands whose energy levels cannot be occupied by charge carriers. This is the illustrative reason for so called band gaps. These band gaps determine the characteristic of the material. The band gap energy allows an alternative classification of metals, semiconductors, and insulators. An electron can only move through the crystal if there are free states in its respective energy band. If a partly filled band exists at 0 K, the material gets therefore classified as metal because conductivity can be observed even without further excitation. If the highest occupied band is fully occupied at 0 K, the material is a semiconductor because no conductivity will be measurable until thermal excitation lifts charge carriers into the next free band. If room temperature is not sufficient to excite charge carriers, meaning that the band gap is too wide, the material is classified as insulator.

The minimum distance between the conduction band and the valence band is called band gap E_g . Its temperature dependence, caused by lattice expansion and increased electron-phonon coupling is given empirically by Varshni's equation⁸³ using the band gap at 0 K and two empirical parameters α and β :

$$E_g(T) = E_g(0) - \frac{\alpha T^2}{T + \beta} \quad (2.8)$$

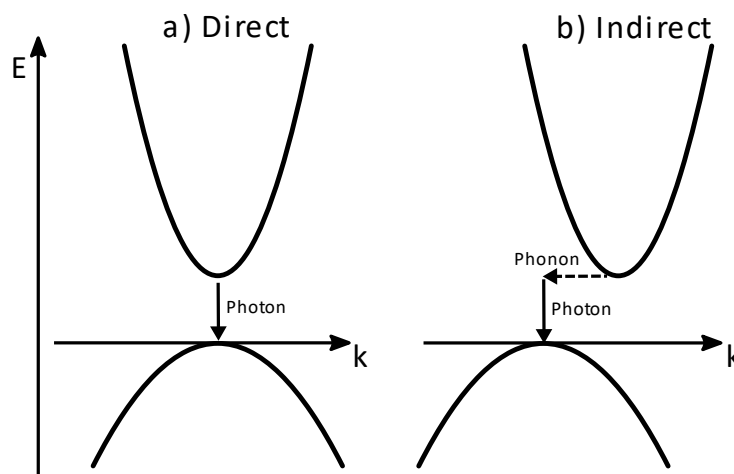


Figure 2.3 a) Band structure of a direct semiconductor. The conduction band minimum is at the same position in k-space as the valence band maximum. b) In contrast, an indirect semiconductor is characterized by conduction band minimum and valence band maximum being at different positions in k-space. In contrast to transitions in direct semiconductors, phonons must be involved in transitions of indirect semiconductors.

For semiconductors band diagrams are illustrated by plotting the electron energy as a function of its wavevector k . Alternatively, band edge diagrams are a common way to describe the electric

properties of semiconductors. In these diagrams, only the band edges, meaning the maximum of the valence band and the minimum of the conduction band are indicated for a spatial coordinate in the crystal. The wavevector is proportional to the momentum of the electron, which can be expressed by $\hbar\mathbf{k}$ while moving through the crystal. Two example band diagrams are schematically drawn in Figure 2.3. The first unoccupied band is called the conduction band, and occupied bands are called valence bands. In atoms radiative and non-radiative transitions can occur between the discrete states. The same is true for semiconductor materials, but in this case the transition occurs between states included in the energy bands. Unoccupied states in mostly occupied bands are called holes and can be treated as quasi particles. All considerations regarding electron behavior can also be applied to holes. Electrons and holes make up the group of charge carriers inside a semiconductor. On the left side of Figure 2.3, this transition from the lower band to a higher band can be done without violating the energy and momentum conservation laws because no momentum must be transferred. This is the case for direct semiconductors, in which the conduction band minimum and the valence band maximum are at the same position in k -space. If these points are at different positions in k -space, the material is called indirect semiconductor. Then, a phonon must be included in the absorption process to ensure momentum conservation. Therefore, radiative transitions are much less likely in indirect semiconductors, making them unfavorable for optical applications. In the vicinity of extrema, the bands can be approximated for III/V semiconductors with a parabolic shape:

$$E(\mathbf{k}) = E_g + \frac{\hbar^2 \mathbf{k}^2}{2m^*} \quad (2.9)$$

This dispersion relation looks similar to the dispersion relation of an electron in free space with a different effective mass m^* . It is important to note that the effective mass is higher if the energy band is flatter. Since the band structure is generally three dimensional, the effective mass is a tensor with multiple components. Typical band diagrams are described in a single particle picture. Normally, the description of the entire semiconductor would be a many-body problem since the interaction between the electrons is also playing an important role. Solving this problem is very difficult and is far beyond the scope of this work.

The movement of charge carriers as a reaction to an external electric field is determined by the influence of the periodic potentials and must be treated as wave packets that propagate through the crystal. This influence is a descriptive explanation for the different effective mass compared to movement in free space. From equation (2.9) it gets clear that the effective mass m^* is anti-proportional to the second derivative of the dispersion relation, i.e. of the corresponding band to \mathbf{k} :

$$m^* = \hbar^2 \left[\frac{d^2 E}{dk^2} \right]^{-1} \quad (2.10)$$

The distribution of charge carriers to the available states can be expressed with Fermi-Dirac statistics, owing to the fermion character of electrons and holes. It describes the macroscopic behavior of Fermions in thermodynamic equilibrium. Statistics for Fermions include that Fermions are invariant against exchange and each state can only be occupied by one Fermion according to Pauli's principle. The probability of occupation at a given energy level E can be calculated by the Fermi distribution function $f(E)$, which is given by the following equation:

$$f(E) = \frac{1}{\exp\left(\frac{E - \mu}{k_B T}\right) + 1} \quad (2.11)$$

In which T is the temperature of the carrier system and μ the chemical potential. At 0 K the chemical potential is defined to be the Fermi energy E_F .

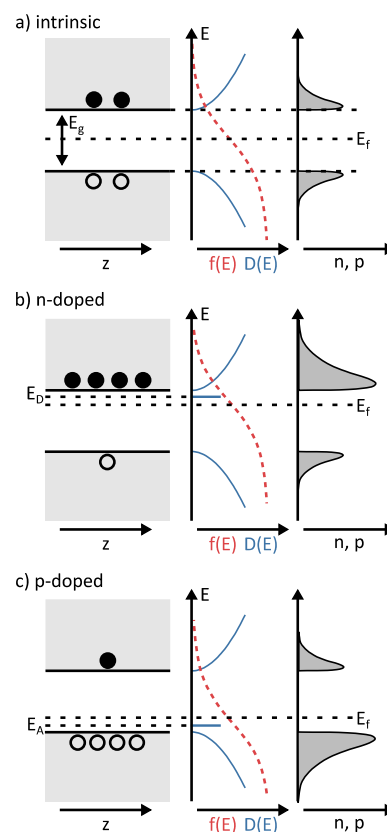


Figure 2.4 On the left side the band edge diagrams of a) intrinsic, b) n-doped and c) p-doped semiconductors are schematically depicted. In this diagram, the acceptor and donor levels E_A and E_D are drawn in vicinity to the band edges. In the center image, the density of states for equal conduction and valence bands are given. A peak at the donor and acceptor levels appears in b) and c). Due to the doping and the additional charge carriers, the Fermi functions depicted in red, are shifted towards the conduction band edge in b) and towards the valence band edge in c). The resulting charge carrier densities are drawn on the right side of the image. For n-doped semiconductors, the electron density is much larger than the hole density. For p-doped semiconductors, this is vice-versa. Adapted from⁸⁴.

In the center image of Figure 2.4 a), the Fermi distribution function is plotted in red for a temperature above 0 K. The shape of these function at 0 K is a step function with the step at the Fermi energy. Every energy state below the Fermi energy is fully occupied, while every state above the Fermi energy is not occupied. For higher temperatures, this function is smeared out.

Further above it was already said that the states in the energy bands are quasi continuously distributed. Therefore, it is purposeful to introduce a density of states which describes the number of states per energy interval. It can be shown that the density of states $D_{CB}(E)$ of the conduction band and $D_{VB}(E)$ of the valence band depend on the effective masses and can be calculated by the following equations if a three dimensional carrier system is considered:

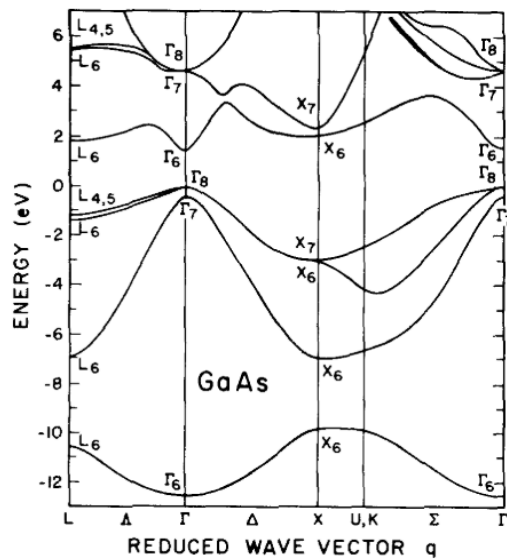
$$D_{CB}(E) = \frac{(2m_e^*)^{3/2}}{2\pi^2\hbar^3} \sqrt{E - E_C}, \quad D_{VB}(E) = \frac{(2m_h^*)^{3/2}}{2\pi^2\hbar^3} \sqrt{E_V - E} \quad (2.12)$$

Where E_C and E_V are the conduction band minimum and the valence band maximum, respectively. To calculate the density of charge carriers the density of states must be multiplied with the Fermi distribution function. In the center image of Figure 2.4 a) an example density of state function is depicted in blue for the valence and the conduction band. The result of the multiplication with an example Fermi function given in the same plot is then depicted on the right side of the figure, in which the charge carrier density is shown.

The charge carrier density and thus to some extent the conductivity of intrinsic semiconductors can be modified by doping. Doping is the deliberate introduction of point defects or impurities into the crystal. These impurities can be elements from neighboring main groups and usually have either one electron less or one electron more available. They can be thought of like a hydrogen atom consisting of a positively charged core with valence electrons. This means that the additional electron is localized, i.e. bound to the impurity, due to further quantized states in close vicinity to the band edges. When a specific thermal energy is applied, the impurity can be ionized by lifting the excess electron to the conduction band, making it no longer localized and contributing to the conductivity in the crystal. This process requires significantly less energy than lifting electrons from the valence to the conduction band. The same is valid for impurities close to the valence band with one electron less, lifting a valence band electron into the impurity state. This is typically the case at room temperature. Impurities that provide at least one electron are called donor resulting in a n-doped semiconductor and impurities with at least one electron less are called acceptors resulting in a p-doped semiconductor. Introducing these impurities will also modify the density of states and the Fermi level. Both are given in Figure 2.4 b) and c). At the impurity level a peak in the density of states is formed. Due to the additional charge carriers the Fermi level also shifts. For n-doped semiconductors the Fermi energy is shifted towards the conduction band and hence the electron

density in the conduction band increases. Electrons are then called majority carriers and holes minority carriers. If the doping level reaches a particular value, the interaction between the impurities plays an important role. Then, an impurity band will form that possibly overlaps with the conduction or valence band.

a)



b)

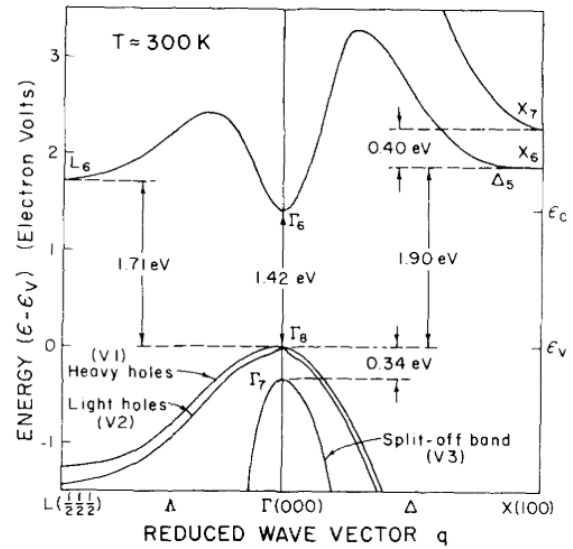


Figure 2.5 In a) the entire calculated band structure of GaAs is plotted with essential symmetry points of the first Brillouin zone. The center of this zone is marked with Γ . At this point the shortest distance between the upper valence and the lowest conduction band can be found, making it the most interesting point in the k -space. Therefore, a zoomed picture is depicted in b). The band gap for GaAs is 1.42 eV at the Γ point. Close to the upper valence band, two additional bands can be seen. The two upmost bands are called heavy hole and light hole band, according to their electron mass. The third band is the spin-orbit split-off band. Both images are taken from⁸⁵.

As an example band structure, the calculated band structure of GaAs is shown in Figure 2.5 a). In this figure the valence band maximum is set as 0 eV. The symmetry points already defined in Figure 2.2 c) are used to describe the band structure. Both, the highest valence band and the lowest conduction band have their extrema at the Γ point. Thus, GaAs is a direct semiconductor. Figure 2.5 b) shows a zoomed detail of the GaAs band structure in the vicinity of the Γ point. At the Γ point, three different valence bands are in close proximity to each other, while only a single conduction band is available. All four bands can be approximated by parabolic functions in this region. The two upper valence bands are called heavy hole and light hole band because of their different effective masses. The third valence band is called spin-orbit split-off band. The smallest energetic distance between the valence and the conduction band is 1.42 eV.

2.1.3 Semiconductor random alloys

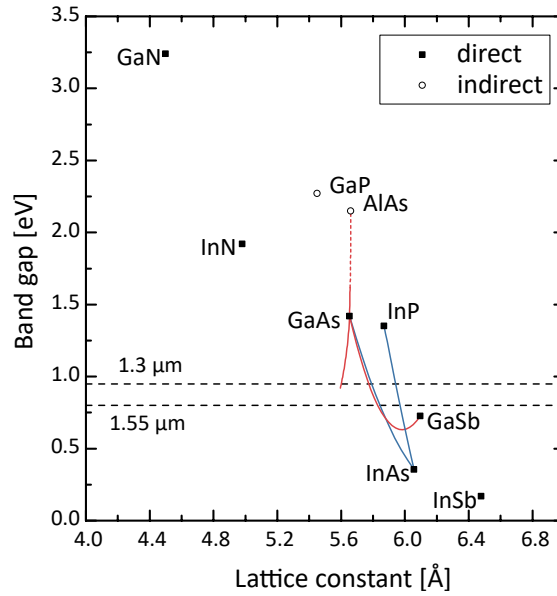


Figure 2.6 Band gap as a function of the lattice constant for important binary III/V semiconductors. Selected band gap vs. lattice constant curves of ternary alloys are plotted according to the bowing parameters given below. The horizontal dashed lines indicate the telecommunication wavelengths. The dashed part of the (Al,Ga)As curve specifies an indirect semiconductor. The data is based on^{86,87}.

III/V semiconductors have significantly different electrical and structural properties, depending on the elements they are composed of. An overview of the band gap and the lattice constant for typical binary III/V semiconductors can be seen in Figure 2.6. Technological applications are not limited to these properties, as they can be heavily tuned by alloying. This means that the group III or group V lattice points can be occupied by different atoms of the respective main group. In random alloys the distribution of these atoms is considered to be completely random and the probability of finding them at a particular lattice point is given by the molar fraction. The notation for alloys is $(A_x B_{1-x})C$ or $A(B_x C_{1-x})$, depending on which sublattice the alloying takes place. The lattice constant can be calculated using Vegard's law as a weighted linear combination of the lattice constant of the binary materials. For a ternary compound semiconductor $(A_x B_{1-x})C$ it can be written as⁸⁸:

$$a_{ABC} = x_A \cdot a_{AC} + (1 - x_A) \cdot a_{BC} \quad (2.13)$$

Where a_{AC} and a_{BC} are the lattice constants of the two binary semiconductors and x_A the fraction of atom A in the alloy. This simple equation cannot be applied for band gaps and other material parameters such as effective masses. However, a bowing parameter b can be introduced to find approximated parameters P_{ABC} for most alloys based on the values of the binary materials P_{AC} and P_{BC} .

$$P_{ABC} = x \cdot P_{AC} + (1 - x) \cdot P_{BC} - x(1 - x)b \quad (2.14)$$

In Figure 2.6 the band gap bowing of some important alloys is included. Notably, (Al,Ga)As is almost lattice matched on GaAs, which enables the growth of thick defect free layers on GaAs substrates. Therefore, it is often used for distributed Bragg reflectors and cladding layers in particular devices. The wavelength reduction of Ga(As,Sb) and (Ga,In)As is very similar and in theory, band gaps in vicinity of the crucial wavelengths 1.3 μm and 1.55 μm can be achieved. However, the band gaps that can be reached with these alloys on GaAs substrates are limited by strain. The bowing curve of Ga(N,As) is illustrated partly with a red line. Contrary to the expectations, the band gap decreases with nitrogen incorporation, despite GaN having a larger band gap than GaAs. This effect is due to extraordinary material properties of dilute nitrides that will be discussed in section 2.4. A summary of essential band parameters based on the review articles by Vurgaftman et al.^{86,87} is given in Table 2.1. The bowing parameters for some properties for selected ternary compounds are summarized in Table 2.2.

Modern telecom lasers are typically grown on InP substrates with (In,Ga)(As,P)⁸⁹ active regions. They can easily reach emission wavelengths of 1.3 μm and 1.55 μm , as indicated with the blue bowing curves in Figure 2.6.

In reality, random alloying is challenging to achieve for many materials because they tend to form clusters or exhibit disorder. Chain like ordering of Nitrogen in (Ga,In)(N,As) is an actual example for this clustering effect⁹⁰.

Table 2.1 Band parameters for important binary III/V semiconductors, taken from⁸⁶.

Parameter	GaAs	AlAs	InAs	GaSb	GaN (zinc blende)	InP
a [Å] at 300 K	5.65325	5.6611	6.0583	6.0959	4.50	5.8697
E_g^r [eV] at 0 K	1.519	3.099	0.417	0.812	3.299	1.4236
$\alpha(\Gamma)$ [meV/K]	0.460	0.885	0.276	0.417	0.593	0.363
$\beta(\Gamma)$ [K]	204	530	93	140	600	162
Δ_{SO} [eV]	0.341	0.28	0.39	0.76	0.017	0.108
m_e^* [m_0]	0.067	0.15	0.026	0.039	0.15	0.0795
m_{hh}^* [m_0] in [001]	0.35	0.47	0.33	0.25	0.85	0.53
m_{lh}^* [m_0] in [001]	0.09	0.185	0.027	0.044	0.24	0.12
m_{so}^* [m_0]	0.172	0.28	0.14	0.12	0.29	0.21
VBO [eV]	-0.80	-1.33	-0.59	-0.03	-2.64	-0.94

Table 2.2 Bowing parameters for major band parameters for ternary III/V compounds, taken from⁸⁶.

Parameter	(Ga,In)As	Ga(As,Sb)	(Al,Ga)As	In(As,P)
E_g^r [eV]	0.477	1.43	-0.127+1.31x	0.10
Δ_{SO} [eV]	0.15	0.6	-	0.16
m_e^*	0.0091	-	-	-
m_{hh}^*	-0.145	-	-	-
m_{lh}^*	0.0202	-	-	-
VBO [eV]	-0.38	-1.06	-	-

2.2 Epitaxial growth of semiconductors

Modern semiconductor materials and devices consist of multiple thin layers in the nanometer scale of different semiconductor alloys. These require a non-equilibrium growth technique with nanometer accuracy ensuring high material quality. Today there are mainly two established growth techniques for producing these semiconductor materials, namely metalorganic vapor-phase epitaxy (MOVPE) and molecular beam epitaxy (MBE).

Epitaxy in general is the growth in crystalline form on crystalline substrates. MOVPE is based on metalorganic molecules (precursors) that contain atoms to be deposited on a substrate. A gas flow leads these molecules into a reactor where the gas phase is enriched with these molecules.

During the MOVPE process multiple complex physical and chemical processes take place. Although many approaches have been tried to more or less successfully model MOVPE processes^{91–94}, the processes are still too complex to be fully described theoretically. Some are schematically drawn in Figure 2.7. The metalorganic source molecules are transported by the carrier gas H_2 into the hot reactor and diffuse into the boundary layer. In the gas phase of this boundary layer, these molecules may decompose due to thermal energy. Additionally, gas phase reactions can occur between the different metalorganic molecules and their decomposition products. Therefore, it is clear that the complexity of the gas phase reactions can be very high when multiple precursors are used for growth.

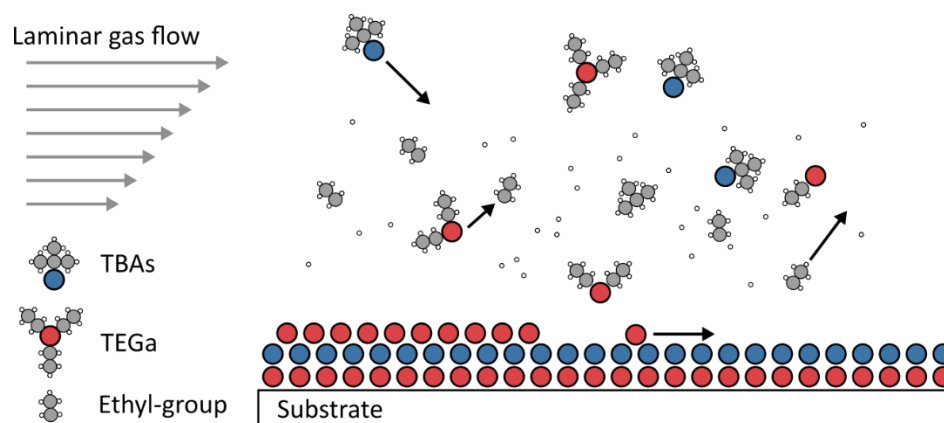


Figure 2.7 Schematic representation of the MOVPE process of GaAs deposition. Gallium atoms are represented in red and arsenic atoms in blue. The respective precursors diffuse in the layer near the substrate, where they decompose due to the temperature. The remaining molecules adsorb on the growth surface or get carried out of the reactor into the exhaust system. On the surface they can diffuse until they get chemisorbed at a lattice site.

The partly decomposed molecules can diffuse to the vicinity of the substrate surface where they can be adsorbed. This takes place first by physisorption caused by van der Waals forces until it may find a free lattice site to be chemisorbed⁹⁵. The adsorbed molecules may contain organic groups that can

then be decomposed at the surface or in the worst case incorporated into the crystal. All adsorbates diffuse on the surface until they incorporate into the solid crystal or desorb from the surface. Also, inside the bulk crystal diffusion can occur because of the growth temperature that must be applied during the entire process. These bulk diffusions are most probably weak inside the buried bulk layers but can be more pronounced in the layers that are near the growth surface. All atoms and molecules that are not incorporated into the crystal are then transported into the exhaust system. The desorption depends on the vapor pressure/the volatility of the adsorbed particles. Group III atoms have typically a lower vapor pressure than group V atoms, so the supply in the gas phase of group V atoms must be generally higher than that of group III atoms. Hence, the growth rate depends almost entirely on the amount of group III source molecules supplied to the reactor, if the growth rate is limited by the mass transport. If the temperature is low, the growth rate is limited by the not occurring decomposition of the source molecules while at high temperatures the growth rate is limited by strongly increased desorption from the growth surface, as can be seen in Figure 2.8. In between these temperature regimes the growth rate is only limited by the mass transport. The adsorption depends strongly on the surface reconstruction and competing species of the same main group.

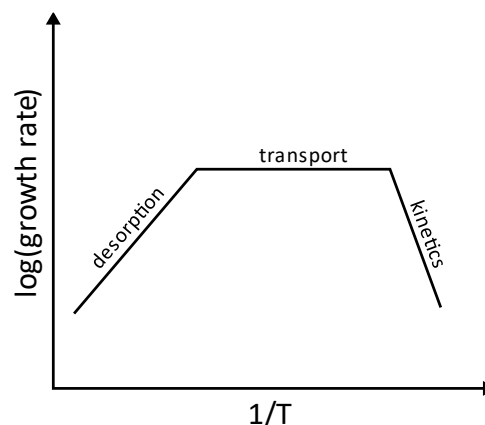


Figure 2.8 The growth rate is logarithmically illustrated as a function of the inverse temperature. Three main regimes can be observed: At low temperatures the growth rate is limited by reaction kinetics due to not occurring decomposition reactions. At high temperatures a highly increased desorption. At intermediate temperatures the supply of precursor molecules determines the growth rate.

Thermodynamics plays a significant role in the crystallization process since it is the driving force behind the formation of the crystal structure. The reactor maintains constant pressure and constant temperature. In the most straightforward consideration, two phases are present: first, the solid phase of the crystal and second the gas phase with the precursor molecules. In this case, a chemical potential μ_i can be defined as state function for each of these phases i . It describes the amount of energy that is required to move a number of moles n_i to the respective phase.

$$\mu_i = \left(\frac{\partial G}{\partial n_i} \right) \quad (2.15)$$

Where G is the Gibbs free energy. The Gibbs free energy is a thermodynamic potential and is defined as the capacity of a thermodynamical system to do non mechanical work. It can be expressed by the sum over all chemical potentials of all phases:

$$G = \sum_i \mu_i n_i \quad (2.16)$$

It is especially useful as a thermodynamic state function for processes with constant pressure and temperature, which applies well to the MOVPE process. In equilibrium the sum of chemical potentials of all phases in a system is zero or in other words, the Gibbs free energy has a minimum. In this case the chemical potentials of the solid and the vapor phase must be equal. If a gradient of chemical potential exists between two phases or the Gibbs energy would be reduced, phase transitions can happen. In other words, the chemical potential of the solid and the vapor phase must not be equal in order to allow the phase transition from vapor phase to the solid phase to happen. Some metastable alloys require the chemical potential difference to be high, the growth conditions must be far from equilibrium.

2.2.1 Strain

In all epitaxial growth processes, a crystalline substrate is required on which additional layers are epitaxially grown. If layers consisting of the same semiconductor material as the substrate are grown, the process is called homo epitaxy. If different materials compared to the substrate are grown, the process is called hetero epitaxy. Since modern devices require multiple layers of different materials, hetero epitaxy is the most common case. As demonstrated in section 2.1.3 these materials can exhibit a wide range of lattice constants, due to the variety of atomic sizes and electronegativities. This difference in lattice constants cause the unit cells to distort tetragonally depending on the substrate's thicknesses and on the epitaxially grown layer. The thickness of the substrate is typically thick enough so this strain causes no change of the lattice constants of the substrate. This is not the case for the epitaxially grown layers (epilayers). They are tetragonally distorted depending on the lattice constant of the substrate and of the epilayer. The epilayer will adopt the substrate's lattice constant perpendicular to the growth direction, while the lattice constant parallel to the growth direction will be stretched or compressed according to the Poisson effect. This effect is illustrated in Figure 2.9 for a) tensile and b) compressive strain. If the lattice constant of the epilayer a_L is smaller than the substrate's lattice constant a_S , the unit cell of the epilayer is compressed perpendicular to the growth direction (tensile strain). If it is the other way around, the epilayer is elongated

(compressive strain). The lattice mismatch ε^\perp can be calculated with the lattice constant of the epilayer parallel to the growth direction a^\perp and the following equation:

$$\varepsilon^\perp = \frac{a^\perp - a_S}{a_S} \quad (2.17)$$

It is related to the relaxed lattice mismatch ε with the elastic constants C_{11} and C_{12} .

$$\varepsilon = \frac{a_L - a_S}{a_S} = \frac{C_{11}}{C_{11} + 2C_{12}} \varepsilon^\perp = \nu \varepsilon^\perp \quad (2.18)$$

With ν being the Poisson's ratio.

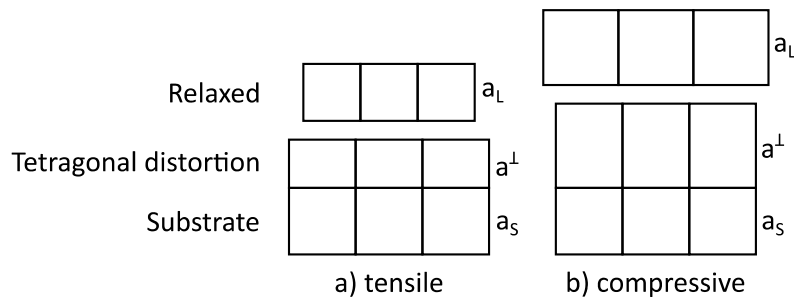


Figure 2.9 On top of a substrate with lattice constant a_S , a different material with a relaxed lattice constant a_L is grown. If this relaxed lattice constant is smaller than the substrate's lattice constant (a), the tetragonal distortion causes the lattice constant of the epilayer to be compressed and the strain is called tensile strain. If the unit cell is elongated because the relaxed lattice constant is larger than the substrate's lattice constant (b), the strain is called compressive.

Obviously, the distortion comes with mechanical strain energy according to Hook's law. With each strained atomic layer, the strain energy of the full structure sums up, until the strain energy reaches the energy required for dislocation formation. At a critical layer thickness, the strain energy exceeds this value and dislocations are formed, resulting in relaxation of the epilayer⁹⁶. Below the critical layer thickness, the growth occurs without dislocation formation and is therefore pseudo-morphic. Multiple repetitions of a strained quantum well can be employed in laser devices. For each quantum well, the strain energy builds up and quantum wells at the top of the quantum well stack could eventually relax. To increase the number of possible pseudo-morphic quantum wells, the strain can be compensated by additional layers that are oppositely strained (see Figure 2.10).

Strain can also influence the growth process: If a strained material is grown the strain state of the crystal can change the incorporation behavior. This process is called lattice pulling or lattice latching effect, if the composition is increased or decreased, respectively.

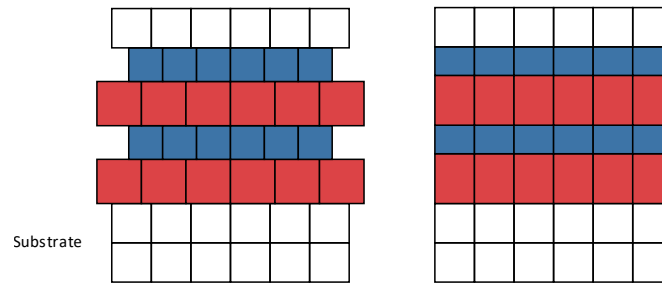


Figure 2.10 If a material causes compressive strain (red), this strain can be compensated by layers with tensile strain (blue). In total, net strain of the overall layer stack can be reduced or even zero.

2.2.2 Alloys

In section 2.1.3 semiconductor random alloys were introduced. In this subsection the thermodynamics of mixed crystals and alloys are briefly introduced.

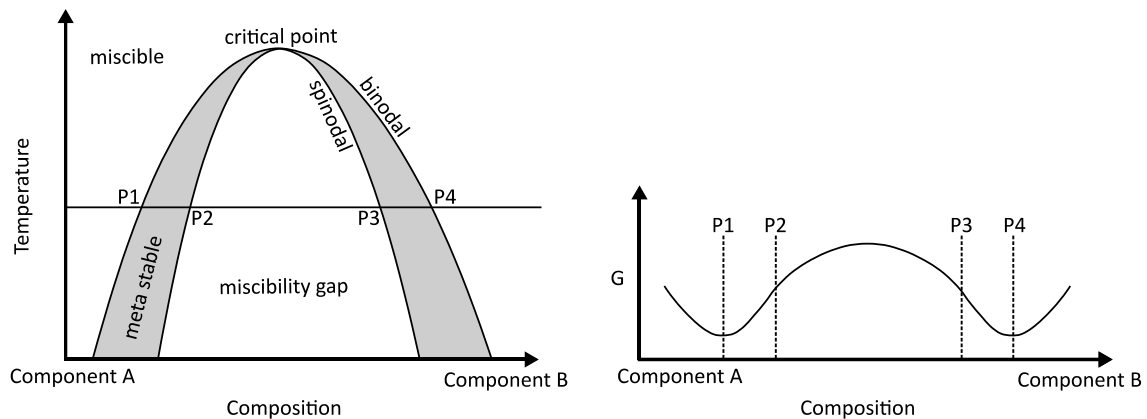


Figure 2.11 On the left side the phase diagram of a binary mixture is schematically illustrated. Above the binodal line the mixture is stable. Below the spinodal line no stable phase can be achieved. Between these lines, metastable phases exist. On the right side, the Gibbs free energy is drawn for a particular temperature indicated with the solid line in the left plot. Adapted from⁸².

In Figure 2.11 the phase diagram of a semiconductor alloy is presented as a function of the composition and for different temperatures. Two curves are important in this diagram. In this phase diagram above the binodal line, every point is stable and can therefore be grown. The second significant curve is the spinodal, under which all points are unstable. In between there is a metastable region where solid solutions can also be deposited. The maximum of the binodal line is called upper critical solution temperature, above which an alloy of all compositions could be theoretically deposited. The unstable area is called miscibility gap. To understand this behavior, the shape of the Gibbs energy must be considered. As outlined before, a chemical reaction like crystallization can only happen, if the process reduces the Gibbs energy. The Gibbs energy of this example has two minima at which the solid is stable. Between the points P2 and P3, the system contains enough energy for a spontaneous phase transition into element A rich or element B rich

phases, meaning a formation of clusters or other microscopic structures. The ranges between P1 and P2 or P3 and P4 are metastable regions, since the stored energy is not high enough for starting the spontaneous phase transition.

These simple thermodynamic considerations do not account for strain effects. Lattice pulling effects can change phase diagrams. Especially in materials with atoms that have a high difference in size and electronegativity, these miscibility gaps are found, and the growth must be carried out in the metastable growth regime⁹⁷. The properties of real alloys that are, of course, not perfectly ordered differ drastically from the properties of ideal random alloys. Stringfellow writes in his famous book: “specification of the composition of an alloy does not completely determine the properties. The microscopic arrangement of the atoms must also be considered” (Stringfellow⁹⁵ p.45). This sentence is of extreme importance for all metastable material systems like Ga(N,As) and (Ga,In)(N,As) because clustering of nitrogen atoms could have a major influence⁹⁸.

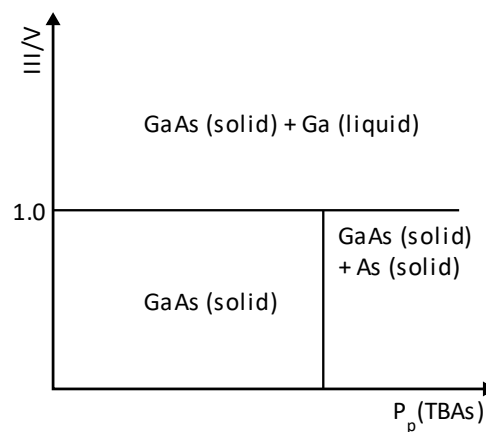


Figure 2.12 Phase diagram of GaAs growth. If the III/V ratio is below 1.0, the amount of arsenic precursor TBAs exceeds the amount of the gallium precursor. Only then a well-defined GaAs solid phase can be formed. If the TBAs partial pressure exceeds a critical limit, which is typically not achievable in MOVPE reactors, an additional arsenic solid phase can form. For III/V ratios above 1.0 liquid gallium is forming on the surface and metallic gallium cluster formation is unavoidable. Reproduced from⁹⁵.

A phase diagram that can be used for MOVPE processes can be seen in Figure 2.12. There, the temperature was constant, and the III/V ratio of the precursors used was plotted on the y-axis and the partial pressure of the arsenic precursor on the x-axis. The III/V ratio is defined by the sum of all group III precursor partial pressures divided by the sum of all group V precursor partial pressures. Three important phase regimes are depicted: For III/V ratios above 1.0 the growth gets gallium rich, and a liquid gallium phase will form besides the GaAs crystal resulting in gallium droplets. III/V ratios below 1.0 can yield in a GaAs solid phase and in GaAs solid combined with a solid arsenic phase. However, a solid arsenic phase cannot be observed under realistic reaction conditions and arsenic precursor partial pressures.

2.3 Heterostructures

A heterostructure describes at least two semiconductor materials with different constituents that are grown in sequence resulting in interesting electronic effects. This subchapter is dedicated to the properties of these heterostructures.

2.3.1 Band alignments

If two semiconductor materials are combined, the band structure can align in three different possibilities, which are illustrated in Figure 2.13. The first possibility is called type-I band alignment or straddled band line-up. In this case the conduction band minimum and the conduction band maximum can be found in one material. The second type is the type-II band alignment or staggered band line-up in which the conduction band minimum and valence band maximum are in different materials with the restriction that the conduction band minima of both materials are energetically above both valence band edges. If this condition is fulfilled a type-III alignment or broken gap is observed. The important parameters are the hetero-offsets for the valence band and the conduction band which were marked in Figure 2.13 as ΔE_V and ΔE_C , respectively.

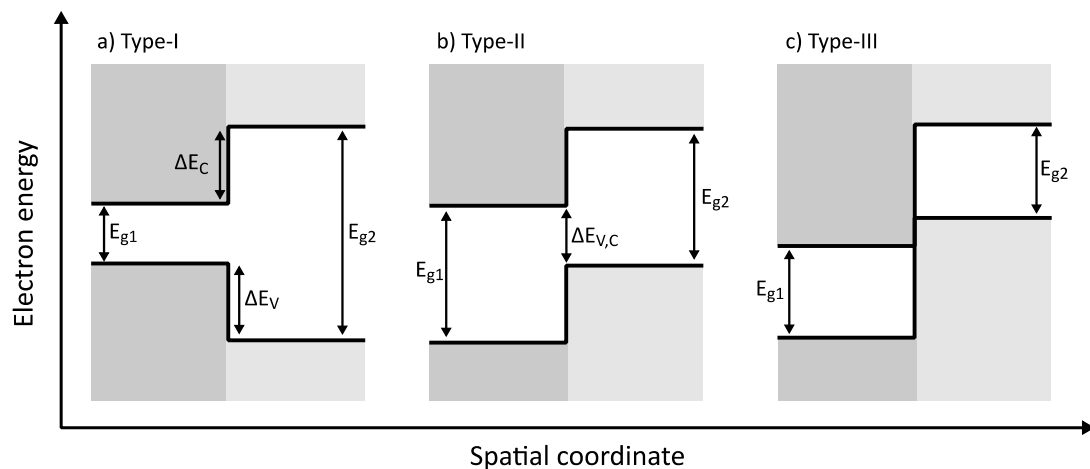


Figure 2.13 Three possible band alignments between two different semiconductor materials. a) Type-I alignment or straddled band line-up. b) Type-II alignment or staggered band line-up c) Type-III alignment or broken gap. Adapted from⁸².

What kind of band alignment two materials form depends on the deposited materials and cannot be easily predicted, despite a few models were proposed in the past that work for very limited cases but fail in general^{99,100}. However, sophisticated theoretical modelling can lead to much more precise predictions^{101,102} as well as experimental approaches using for example X-ray photoelectron spectroscopy¹⁰³. Examples for band alignments and hetero offsets can be seen in Figure 2.14 in which important semiconductors are shown. It can be clearly derived that GaAs/(Ga,In)As will form a type-I

band alignment while (Ga,In)As/Ga(As,Sb) can form a type-II band alignment, depending on the compositions.

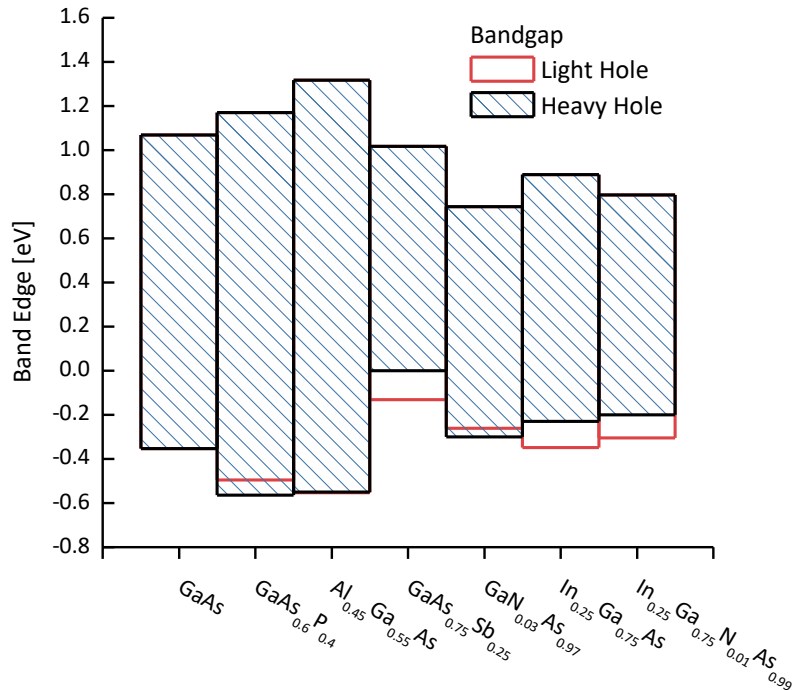


Figure 2.14 Simplified band edge diagrams for different materials grown on GaAs substrates. The black boxes illustrate the band gap boundaries of the conduction band edge to the heavy hole edge and the red lines indicate the light hole band edges. All values are provided by Dr. Ada Bäumer.

2.3.2 Quantum wells

A potential well for electrons and holes can be created by growing a material with a narrower band gap into barriers with a wider band gap while forming a type-I band alignment (see Figure 2.15). If the middle layer thickness is in the order of the De Broglie wavelength, quantum mechanical effects come into play and the charge carriers are confined. Hence, a so-called quantum well is formed, in which charge carriers have discrete energy levels plotted in Figure 2.15 a), due to the confinement. Similar carrier confinement can occur in materials with a type-II band alignment, but holes and electrons are separated in two materials, as shown in Figure 2.15 b). Thinner layers cause the quantization to become stronger and the discrete energy levels to become energetically higher. For the approximation of infinite potential wells the energy levels are proportional to $1/L^2$ where L is the quantum well thickness. For finite barrier height, the wavefunction of the quantized states penetrates the barrier and shows an exponential decay that depends on the energy barrier height. Additionally, the wavefunctions depend on the effective masses of the respective bands. A heavier effective mass results a reduced penetration depth into the energy barrier. The radiative

recombination processes, which will be discussed later in detail, can only occur between two quantized states with the same quantization number, as marked as arrows in Figure 2.15. The distance between the states of different quantization numbers depends on the width of the potential well. If the width is large, the distance between the states is reduced.

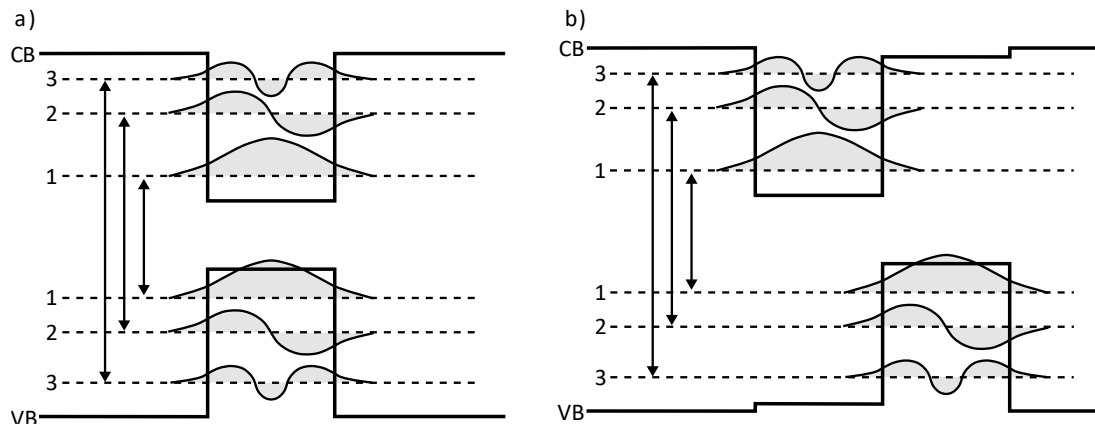


Figure 2.15 Simplified band edge diagrams of a type-I quantum well a) and of a type-II quantum well b). Quantum wells confine charge carriers in the respective quantum well materials. Hence, new discrete states are forming. Transitions are only allowed between two states of equal quantum numbers. The wavefunctions are also schematically drawn into the quantum wells and the overlap of two states of the same quantum number determines the probability of recombination. Accordingly, the recombination probability is higher for type-I quantum wells. Adapted from¹⁰⁴.

A quantum well also changes the density of states because the charge carriers are confined in one direction and the symmetry of the carrier system is reduced to two dimensions. Instead of the \sqrt{E} dependency showed in section 2.1.2, the density of states $D(E)$ changes to a step function with steps at the quantized energy levels, as illustrated in blue in Figure 2.16. Nevertheless, the density of states still depends on the effective mass and is in this case proportional to it. In Figure 2.16, the band edge diagram of a quantum well is shown on the left side with the simplification of only one valence band and two quantized states. The structure is grown in z -direction. In each band, quantized states are formed. In the middle, the respective k -space diagram is shown, in which the dispersion in k_x - and k_y -direction is depicted. The electron dispersion is in these spatial directions similar to the bulk material with the band edges at the energetic positions of the quantized states. If multiple valence bands are present, like in III/V semiconductors, quantized states will form for every valence band. These would eventually overlap, but since band mixing is not possible, the quantized valence bands will change their shape to avoid a crossing or mixing of two bands. On the right side of Figure 2.16, the density of states is shown combined with an example Fermi function $f(E)$ and the resulting carrier concentrations n and p . In contrast to bulk semiconductors, the density of states is already high at the band edge. Hence, the charge carrier concentrations are also the highest at the band edges and decrease with higher energies in the shape of the Fermi function. This is of particular importance for laser devices.

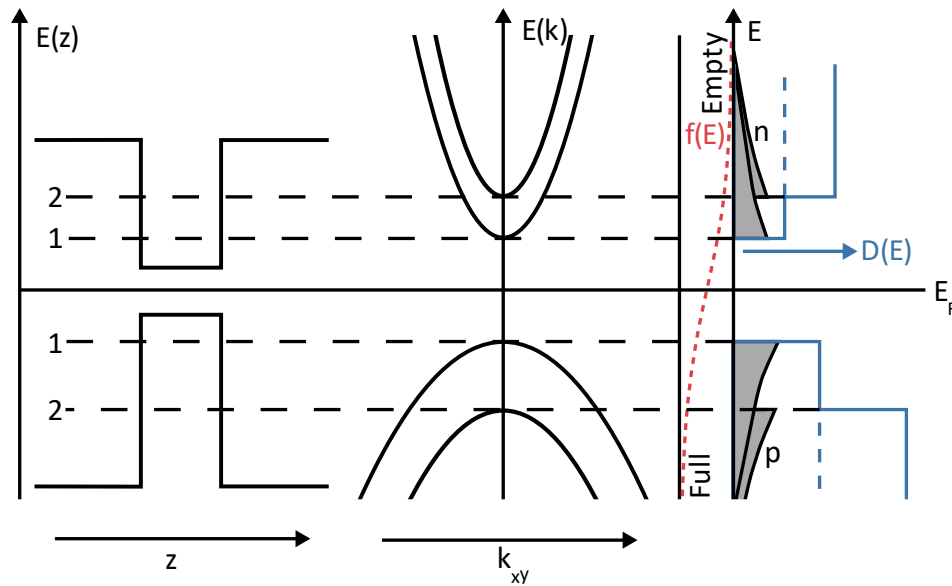


Figure 2.16 Left: Band edge diagram in growth direction (z). A material with a narrower band gap is sandwiched between a material with a broader band gap resulting in a type-I band alignment. Thus, a quantum well is formed in the valence and conduction band, in each of which two quantized states are established. At these quantized states, the electron dispersion emerges, as it is shown in the middle. The density of states is depicted in blue in the right part together with an example Fermi function in red. Contrary to the bulk case, a stepped shape is observed with steps at the quantized energy levels. In the graph of the density of states, the resulting carrier densities are shown in grey. Adapted from¹⁰⁴.

2.3.3 Influence of strain on band structure

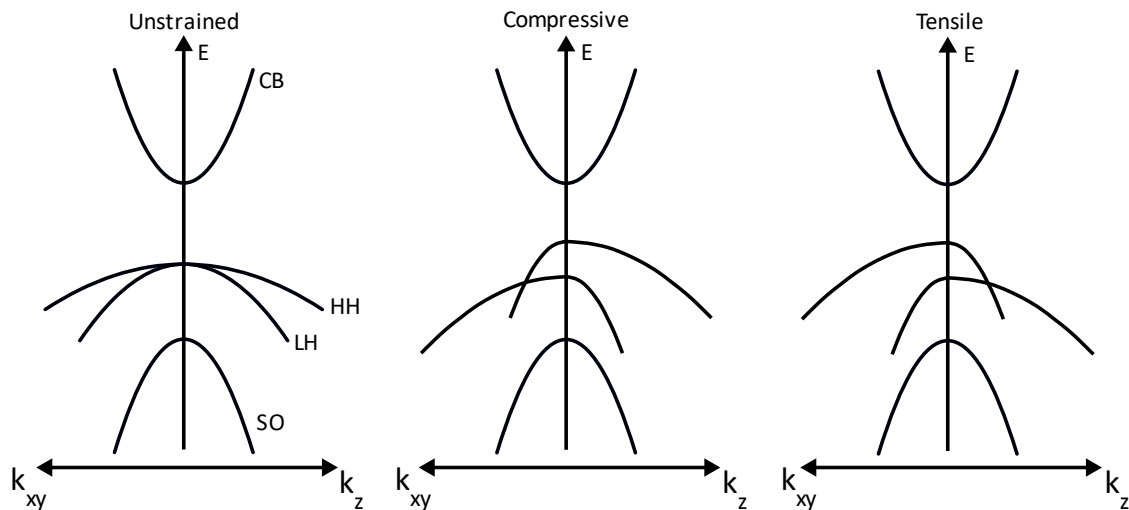


Figure 2.17 Band structures of bulk semiconductor material for different strain states. The growth direction is the z -direction. On the left side the unstrained band structure is shown. For both strain states the valence band structure changes. In the middle, the effect of compressive strain is represented. In plane, the light hole band is shifted to higher energies, while the highest valence band in growth direction becomes heavy. For tensile strain the opposite effect can be observed. Based on⁹⁶.

Strain shows major influence on the band structure as is illustrated in Figure 2.17^{96,105–107}. On the left, the unstrained band structure of GaAs is illustrated around the Γ point. Strain removes the degeneracy of the heavy-hole and the light-hole valence band maximums at the Γ point. When strain is introduced to the layer, the band gap gets reduced for tensile strain and increased for compressive

strain¹⁰⁷. A splitting of the degeneracy at the Γ point of about 80 meV is observed at 1% strain¹⁰⁸. Compressive strain affects the upper valence band so that the holes get light in in-plane directions and heavy in growth direction. For a tensile strain, the effect on the valence band is vice-versa.

Only the in-plane dispersion is relevant in strained quantum well layers since the charge carriers are confined in the growth direction¹⁰⁸. Because the effective masses are changing due to strain, the density of states of the quantum well states is also changing. This is especially beneficial for lasers^{96,105}, which is why all modern quantum well lasers rely on strained layers.

2.3.4 pn-junction

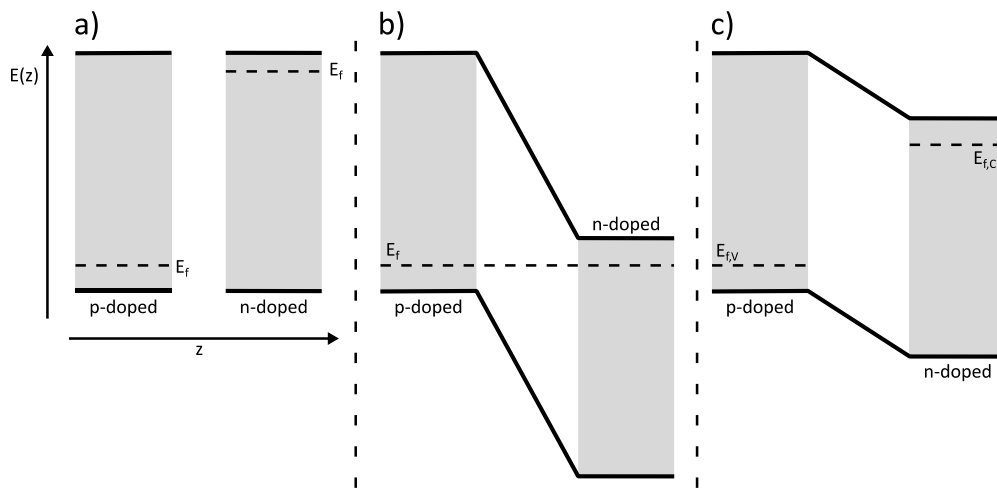


Figure 2.18 Band edge diagrams of a pn junction in different states. In a) pn junction that is separated. Due to the doping, the Fermi levels of both p- and n-doped regions are at different energy levels. If both layers are brought into contact, charge carriers diffuse over the interface and form a depletion region. The Fermi levels of both layers are now on one position and the bands are bent. In c) an external voltage is applied in a way that electrons are resupplied into the n-doped region and holes into the p-doped region (forward bias). The band bending decreases and a current flow can be observed because carriers recombine in the region near the interface.

A pn-junction is formed when two differently doped semiconductor materials are grown in sequence. As already outlined in section 2.1.2, the Fermi level is close to the valence band edge in the p-doped layer while in the n-doped layer it is close to the conduction band (Figure 2.18 a)). Due to the difference of Fermi energy in both layers, charge carriers diffuse into the other material, holes diffuse to the n-doped layer and electrons into the p-doped layer. Because of the excess electrons in the p-doped layer next to the interface and the missing holes, the p-doped region in vicinity of the interface is negatively charged. Due to the same effect, the respective n-doped region is positively charged. Hence, these regions are depleted of charge carriers which is why they are named depletion regions. Their widths in n-direction x_n and in p-direction x_p can be calculated by solving the Poisson's equation considering the number of donors N_d and the number of acceptors N_a .

$$x_n = \sqrt{\frac{2\varepsilon V_0}{q} \frac{N_a}{N_d(N_a + N_d)}}, \quad x_p = \sqrt{\frac{2\varepsilon V_0}{q} \frac{N_a}{N_d(N_a + N_d)}} \quad (2.19)$$

In the band structure this means that the Fermi levels are aligned to one level and the bands are bent as shown in Figure 2.18 b). The band bending can be interpreted as follows exemplary for the conduction band: Due to the diffusion of electrons into the p-doped side, the electrostatic potential acts on them. Hence, a potential barrier is formed. If an external voltage source is applied to the structure so that electrons get supplied into the n-doped side and holes into the p-doped side (forward bias), this potential decreases, and electrons and holes recombine radiatively or non-radiatively in the center region of the junction. Due to the constant pumping of new charge carriers, the n- and p-doped sides are enriched with additional electrons and holes. Because the inter band recombination of charge carriers is occurring on a larger timescale than the intra band relaxation, the Fermi levels in the p- and n-doped sides are then on different energetic levels and are therefore called quasi Fermi levels. The concept of quasi Fermi levels applies to systems in which carriers are excited with an external pump source and is also applicable for optically pumped systems. If the voltage applied to the pn-junction is applied in the opposite direction (reverse bias), the barrier for charge carriers across the pn-junction gets increased, and only a low saturation current can flow until the voltage reaches a critical value causing a junction break down and thus a high current flow.

2.4 Dilute nitrides

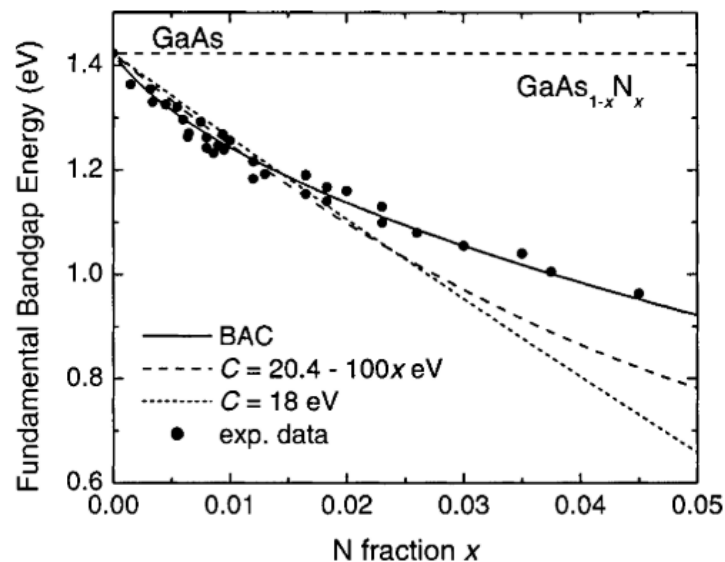


Figure 2.19 Band gap energy as a function of the nitrogen fraction in Ga(N,As). The band gap gets drastically reduced by the incorporation of tiny amounts of nitrogen, which a bowing factor cannot explain. Image taken from⁸⁷.

Dilute nitride material systems comprise all V/III semiconductor materials, accommodating diluted amounts of nitrogen on group V lattice sites. Due to the vast difference in electronegativity and

atomic size compared to arsenic and other group V atoms, the impact on the electronic structure is tremendous, and the band gap change cannot be grasped with the standard bowing parameter model but instead the bowing is composition depended and paramount for small nitrogen fractions.¹⁰⁹ At low nitrogen fractions, the bowing can be as high as 0.1 eV/nitrogen.¹¹⁰ For comparison, some atomic size and electronegativity values are presented in Table 2.3. The bond length in the crystal gets reduced by 20% if a nitrogen atom is replacing an arsenic atom,¹¹¹ disturbing the lattice severely.

Table 2.3 Important properties of nitrogen in comparison to antimony and arsenic. The covalent radius of the nitrogen atom is significantly smaller. The electro-negativity is larger. Thus, it behaves differently when alloyed into a GaAs based compound. Table source⁹⁷.

Element	Covalent radius [pm]	Lattice constant Ga-compound [nm]	Electronegativity
N	75	0.452	3.04
As	119	0.565325	2.18
Sb	138	0.609593	2.05

Owing to this difference, in a simple picture, nitrogen atoms form localized states near the conduction band edge of many III/V semiconductors. When incorporated into GaP nitrogen related defect states do arise below the conduction band inside the band gap^{112,113}. Contrary, the usage of GaSb and InSb as well as GaAs as host matrix results in localized states slightly above the conduction band edge. For this reason, the conduction band edge shifts drastically with small fractions of nitrogen incorporated. This effect was observed in experiments with photoluminescence spectroscopy and absorption spectroscopy¹¹⁰ and extensively studied by theory groups¹¹⁴ and can even result in a semi metallic band structure in In(N,Sb)¹¹⁵.

A simple model for explaining this band gap change is given by the band anticrossing model (BAC) that supposes randomly distributed nitrogen atoms in the crystal lattice and for each nitrogen atom a resonant defect level state slightly above the conduction band edge with energy E_N is formed¹¹³. This defect level perturbs the conduction band of the host material and the conduction band is split into two sub bands named E_+ and E_- , which was experimentally confirmed under large hydrostatic pressure for (Ga,In)(N,As) bulk layers^{116,117}. It was found that the transition from nitrogen acting as an isoelectric impurity to splitting of the conduction band takes already place at a low nitrogen content of 0.2%¹¹⁷. The dispersion based on the BAC for both conduction bands is given by the following equation⁸⁷:

$$E_{\pm}(k) = \frac{1}{2} \left([E_c(k) + E_N] \pm \sqrt{[E_c(k) - E_N]^2 + 4V_{Nc}^2 x} \right) \quad (2.20)$$

In which V_{Nc} describes the matrix element which resembles the interaction between the localized nitrogen state and the conduction band and $E_c(k)$ is the dispersion of the conduction band. The complete conduction band structure obtained by BAC is schematically shown in Figure 2.20 and the parameters used for BAC calculations for Ga(N,As) and (Ga,In)(N,As) are summarized in Table 2.4.

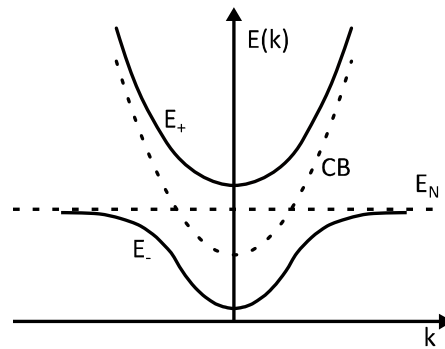


Figure 2.20 Conduction band (CB) structure of dilute nitride Ga(N,As) according to the band anticrossing model. The localized resonant state E_N of the nitrogen atom is indicated with the horizontal dashed line. The dashed CB is split into two sub bands E_+ and E_- . As a result, the band gap is reduced irregularly strong.

Table 2.4 BAC parameters for Ga(N,As) and (Ga,In)(N,As) according to⁸⁷.

Alloy	E_N with respect to valence band maximum	V_{Nc}
Ga(N,As)	1.65	2.7
Ga _{1-x} In _x NAs	$1.65(1-x) + 1.44x - 0.38x(1-x)$	$2.7(1-x) + 2.0x - 3.5x(1-x)$

With this BAC-model, theory groups also tried to explain the band gap change of bismuth containing alloys and predicted that local states in the valence band are formed if alloyed in GaAs. Similar band splitting is then predicted for the valence bands causing a substantial reduction of the band gap as well.¹¹⁸

For dilute nitride materials, the BAC-model indicates that nitrogen incorporation does not change the valence band structure at all. Several experimental studies tried to gain insights into the valence band offset. Some found a type-II band alignment when Ga(N,As) is sandwiched into GaAs barriers^{119,120}, but the error bars of the experimental determination of the valence band offset were quite large. Contrary to that result, other studies found a type-I band alignment^{121–123}. However,

Vurgaftman et al. recommend in their review article a valence band offset of 0 and interprets the other values found in literature as a result of strain⁸⁷.

The BAC-model provides an accessible model for explaining the band gap change if diluted amounts of nitrogen are incorporated in many III/V alloys. However, it reveals some drawbacks if a closer look at the atomic ordering and other parameters besides the band gap is taken. For example the effective mass calculated in this theoretical framework was determined to be $0.1 m_e$ at 2% nitrogen content^{124,125} while the experimental determination¹²⁶ obtained $0.19 m_e$. The BAC-model only considers single nitrogen atoms surrounded by other elements and parameters like the effective mass of conduction band states, and other parameters cannot be derived from this BAC. It was found that nitrogen forms next nearest neighbor clusters that change the electronic properties significantly. The short-range order of nitrogen atoms has a severe impact on the electronic structure of the semiconductor.¹²⁷ The most straightforward nitrogen cluster that can be found is the double nitrogen complex N-Ga-N. It was shown experimentally⁹⁸ and theoretically^{128,129} that the electronic structure of this complex causes the localized state to move to the inside of the band gap resulting in an electron trap level. More extended clusters can be distinguished between gallium centered clusters and chain like ordering. Gallium centered nitrogen clusters are formed of a gallium atom surrounded by nitrogen atoms. They are also known for creating electronic states inside the band gap below the conduction band edge. Deeper defect levels are formed by “nitrogen chains”, consisting of chain-like nitrogen ordering, separated by group III atoms (N-III-N-III-...), which was shown theoretically for varied numbers of nitrogen atoms¹²⁸. This study also revealed that the energy of the defect level gets decreased with increasing number of nitrogen atoms involved. When the nitrogen composition is raised, the band gap shifts to lower energies, but the energetic positions of the localized cluster states do not change¹¹⁷. These cluster levels can act as deep level traps and are accordingly a cause for non-radiative recombinations, as will be discussed in section 2.5.4. Nitrogen chains were found to form in growth direction with a distance similar to the determined minority carrier diffusion length of electrons in p-doped (Ga,In)(N,As)^{130,131}. This highlights the ability of these chains to act as trap states for electrons. These cluster effects can also explain the rapidly increasing effective mass of the conduction band electrons, which is much higher compared to for example in (Ga,In)As or GaAs^{113,126,132–135}.

However, dilute nitrides gained much attention due to the strong band gap reduction and the possibility of reaching photon energies of radiative recombination that correspond to a wavelength of $1.55 \mu\text{m}$. The further reduction of the lattice constant introduced by alloying with nitrogen in most compounds opened the possibility to reduce the strain and grow band gap tailored lattice matched materials. This resulted for example in (Ga,In)(N,As)^{54,59,61,67}, (Ga,In)(N,As,Sb)⁷⁰ or other laser devices¹³⁶ and further device concepts such as solar cells^{137,138}.

An extensive discussion of the growth parameters of Ga(N,As) and (Ga,In)(N,As) will be presented in Chapter 4.

2.4.1 Annealing

The epitaxial growth of dilute nitride alloys implies incorporating nitrogen-related defects into the crystal, as described above. Thus, the optical properties are overall worse than for other III/V compounds, originating from the non-radiative recombination centers introduced by these defects. However, thermal annealing can enhance the optical performance of dilute nitrides significantly. For optimum annealing conditions, the photoluminescence peak intensity was for example shown to enhance by up to 10 times¹³⁹. Thermal annealing is understood as heating the sample to a specific temperature. The amount of thermal energy applied to the sample determines the strength of the annealing and can only be changed by the temperature and duration at/for which the annealing takes place. Typically, annealing durations are in the range between several seconds to one hour.

For (Ga,In)(N,As) thermal annealing results in a great improvement of the photoluminescence peak intensity until the optimum annealing temperature is reached. However, the optical quality deteriorates rapidly at a critical temperature due to phase separation of the included elements¹³⁰. The annealing efficiency peaks at temperatures that are specific for the given nitrogen and indium contents. Besides that, the linewidth gets narrower. The band gap transition energy of (Ga,In)(N,As) was proven by absorption spectroscopy to shift blue with thermal annealing without changing the composition¹⁴⁰. This blueshift was observed by multiple groups and found to be highest for ample nitrogen and indium contents^{130,140,141}.

The chain-like ordering of nitrogen atoms in (Ga,In)(N,As) can be dissolved if thermal energy is supplied to initiate diffusion processes¹⁴². If nitrogen atoms can diffuse to other lattice sites, they tend to move to indium rich environments. This way the total strain energy can be reduced because indium-nitrogen bonds reduce the strain compared to Ga-N bonds, when grown in GaAs substrates^{90,142,143}. This is favorable even though the gallium-nitrogen bond is stronger than the indium-nitrogen bond¹⁵. As a result, the nitrogen distribution takes the same random alloy distribution as the indium distribution^{15,144}. To enable diffusion, arsenic vacancies are necessary. Hence, the effect of annealing on the PL intensity is much more severe and sets in at lower temperatures if it is conducted under H₂ ambient compared to TBAs enriched ambient¹³⁰. The optimized annealing conditions for (Ga,In)(N,As) should be roughly between 650°C and 725°C for typical nitrogen and indium compositions. This diffusion effect causes the blueshift, due to the change of microscopic nitrogen ordering¹⁴¹ and removes nitrogen clusters and chains as non-

radiative recombination centers. However, if excessive annealing temperatures or times are chosen, the indium diffuses out of the quantum well^{145,146} or nitrogen can accumulate at the interfaces¹⁴⁷.

For other dilute nitride materials like Ga(N,As), the situation is not as straightforward as for (Ga,In)(N,As). Some groups report on a blueshift with increasing annealing temperature, while others report on a redshift^{139,148}, especially for weak annealing conditions. Nevertheless, all these studies report a great improvement of the photoluminescence intensity, with an optimum annealing temperature that depends on the nitrogen content.

The blueshift was attributed to a diffusion of nitrogen atoms out of the quantum well and a reduction of the average nitrogen content¹⁴⁹. Also gallium vacancies that play a more prominent role for large nitrogen fractions¹⁵⁰ were proposed to heal out with thermal annealing¹³⁹. The change of microscopic nitrogen ordering plays an additional role.

Contrary, a redshift can be attributed to the removal of N-H interstitial defects due to the out diffusion of hydrogen off the quantum well layers. Two interstitial hydrogen defects are possible: N-Ga-H antibonding ordering or N-H-Ga bond centered ordering. These interstitials are also expected to occur in (Ga,In)(N,As) as well. If a hydrogen atom binds to a nitrogen atom at a lattice site, the nitrogen atom gets passivated and cannot contribute to the band gap reduction. Hence, the removal of hydrogen atoms results in a reduction of the band gap.^{150–152}

Additionally, the exchange of nitrogen atoms from interstitial sites to substitutional sites is also responsible for a redshift.¹⁵³

One primary result regarding Ga(N,As) annealing was achieved by Volz et al. when the microscopic nitrogen ordering of Ga(N,As) was compared with (Ga,In)(N,As) before and after annealing utilizing transmission electron microscopy. The authors found that in contrast to (Ga,In)(N,As), Ga(N,As) tends to accumulate nitrogen in the center of the quantum well layers due to phase separation, activated by thermal annealing. Hence, significant clustering effects and substantial amounts of non-radiative recombination centers can be expected in annealed Ga(N,As) layers.¹⁵

All in all, annealing is a critical process for dilute nitride materials. Its effectiveness depends severely on the actual annealing conditions such as temperature, duration, and ambient. They must be carefully adjusted for each structure.

2.5 Semiconductor Lasers

Laser devices are decisive for a wide variety of applications. Many achievements of the modern world would have been impossible without them. These include the entire field of

telecommunications¹, data storage on Blu-ray and CDs¹⁵⁴, medical¹⁵⁵ or industrial¹⁵⁶ applications, and the automation of self-driving cars and robots¹⁵⁷. In science, they play a prominent role in spectroscopy. A variety of different laser types have been developed in the past. Among them solid state lasers, gas lasers, diode lasers and some others¹⁶. In this work, diode lasers are the subject of investigation, and therefore, this chapter highlights the basics behind diode lasers. However, many important concepts apply to all kinds of lasers since the structure of lasers is always similar.

Laser is an acronym for light amplification by stimulated emission of radiation. An active region is required embedded in a resonator or cavity, and which is responsible for the stimulated emission leading to lasing. Additionally, a way to pump charge carriers into the active region is required. The cavity consists of at least two mirrors, of which one must be partly reflective. Between these mirrors, photons are reflected back and forth and are thus confined in one direction. This chapter will address the basics of these three components, focusing on laser diodes. An in-depth discussion of lasers and laser diodes can be found in the literature^{16,84,104}.

2.5.1 Active region and pump source

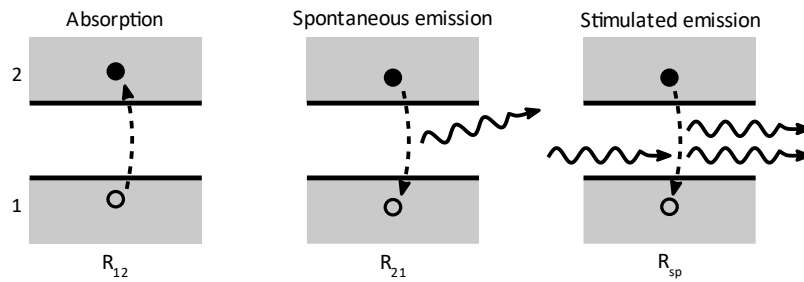


Figure 2.21 Radiative recombination processes in semiconductor material. The left process depicts an absorption process in which an incident photon is absorbed by excitation of an electron. The spontaneous emission of photons describes a spontaneous recombination of an electron to a state in the conduction band. The released energy gets emitted as a photon. The third process is the stimulated emission that involves an incident photon that stimulates the recombination of an electron to a state in the valence band. The energy is emitted with a photon that has the same phase, direction and wavelength as the incident photon, which is therefore doubled. Adapted from¹⁰⁴.

The active region is the most crucial component of a semiconductor laser. A wide variety of active materials are conceivable, for example bulk materials or lower dimensional materials like quantum wells^{158,159}, quantum wires¹⁶⁰, and quantum dots^{75,161}. The most important type is the quantum well material which is considered in this section. In the active region, the radiative recombinations take place that enable the entire structure to work as a laser. Radiative transition processes are classified into three processes shown in Figure 2.21: The simplest is the spontaneous recombination, where an electron of the conduction band is recombining spontaneously with a hole in the valence band with the emission of a photon. In the case of a quantum well laser, the recombination processes take place in between quantized states. A recombination can only happen if momentum and energy conservation are maintained. The energetic distance between these states determines the energy of

the emitted photon. The second process is absorption, where a photon is fully absorbed by exciting an electron from a valence band state to a conduction band state. The third process is the stimulated emission, in which an incident photon interacts with an electron in a conduction band state and stimulates it to recombine with a free state in the valence band. The energy gets emitted as a photon with the same energy as the incident photon. In addition, the emitted photon exhibits the same phase and movement direction (coherence). This process is the basis for lasing. The rate at which these processes occur depend on a recombination constant which is named R_r for absorption and stimulated emission and $R_{r,sp}$ for spontaneous emission. The respective real recombination rates can be derived by also taking the probability of occupation f_1 and f_2 of the two states into account:

$$R_{12} = R_r f_1 (1 - f_2), \quad R_{21} = R_r f_2 (1 - f_1), \quad R_{sp} = R_{r,sp} (1 - f_1) \quad (2.21)$$

The recombination constants defined above can be calculated for the single particle approximation using Fermi's golden rule, where $|H_{21}|^2$ is the transition matrix element that defines the strength of the interaction and the density of final states $\rho_f(E_{21})$:

$$R_r = \frac{2\pi}{\hbar} |H_{21}|^2 \rho_f(E_{21}) \Big|_{E_{21}=\hbar\omega} \quad (2.22)$$

It is important to note that the transition matrix element depends on the overlap of the wavefunctions of the starting and ending state of the transition. For quantum wells these wavefunctions were already shown in Figure 2.15. The recombination rate is higher for type-I quantum wells since the transition matrix element increases if the wavefunction overlap increases. For quantized states, it is only non-zero if the states have equal quantum numbers.

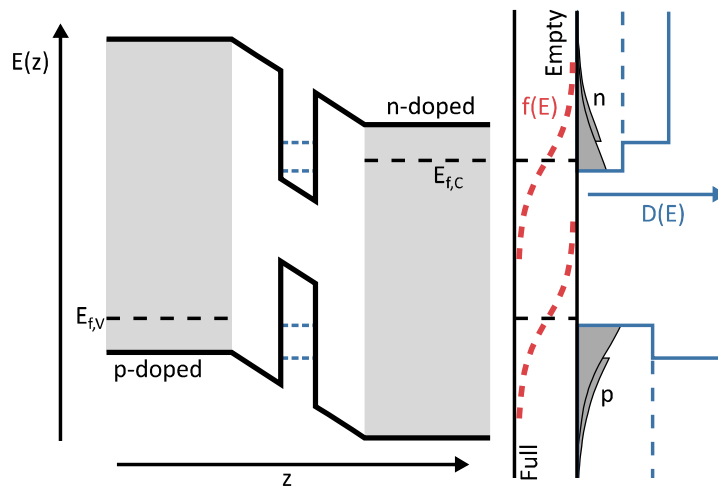


Figure 2.22 The band edge diagram of a quantum well in a pn-junction with an external voltage applied is illustrated on the left. The quantized states are indicated with blue dashed lines. Due to the pumping, the quasi Fermi level that are plotted in red are separated with respect to each other. The charge carriers shown in grey on the right side occupy the states of the quantum well according to the quasi Fermi levels and the density of states given in blue.

As the probability of occupation plays a vital role in the equations given above, the pump source must be discussed before further considerations are taken. A previous section dealt with the possibility of pumping charge carriers into a semiconductor material by using a pn-junction with an externally applied voltage. Such structures can be utilized to pump quantum wells that are used as active material, which is sketched in Figure 2.22. The voltage causes a current flow of both carrier types into the active quantum well material. Due to the potential that is present for the carriers in both bands, the charge carriers relax into the quantum well states and may recombine. The Fermi functions give the probability of occupation with the quasi Fermi levels depicted in red in Figure 2.22. If the Fermi functions are inserted in the equations for the transition rates, it can be shown that the fraction of the absorption and the stimulated emission is given by:

$$\frac{R_{21}}{R_{12}} = e^{(\Delta E_f - E_{21})/(k_B T)} \quad (2.23)$$

Where E_{21} resembles the energy difference of the two states involved in the transition and $\Delta E_f = E_{f,C} - E_{f,V}$ is the energy difference of the quasi Fermi levels. This equation is of outstanding importance for semiconductor lasers since this fraction must be larger than one for the stimulated emission to exceed the absorption, which is the case if the availability of states for the stimulated emission exceeds the availability of states for absorption, which is called population inversion. From the equation it can be directly derived that the difference in quasi Fermi levels must be greater than the difference of the two states E_{21} .

$$\Delta E_f > E_{21} \quad (2.24)$$

In the case of quantum well lasers, E_{21} is the energy difference between the first quantized states of the valence and conduction band, and for bulk semiconductor lasers the band gap E_g . In Figure 2.22 the quasi Fermi levels are depicted in a way that this inequation is fulfilled. It should be noted that the quasi Fermi levels do not necessarily need to exceed both respective states for this equation to become true. Moreover, the shift of the quasi Fermi level of the valence band states is typically shifted weaker with increasing forward voltage because the density of states is larger due to the heavier hole effective masses. Thus, the advantage of strained quantum well lasers is becoming evident since compressively strained quantum wells reduce the in-plane effective mass of the valence band and as a result the density of states, as already discussed in section 2.3.3. The hole quasi Fermi level then shifts stronger with increasing pump current density, and the population inversion can already be reached for smaller pump current densities.

If a photon density N_p travels through a short distance Δz of active region, it gets modified by the light-matter interaction. The change in photon density ΔN_p can be written as:

$$\Delta N_p = N_p e^{g\Delta z} - N_p \quad (2.25)$$

With this equation the material gain g is defined. If the material gain is positive, the photon density increases exponentially by moving through the material. If it is negative, losses exceed the gain process and the photon density gets exponentially decreased by absorption. It is important to note, that the photon density and the material gain in the above equation depend on the wavelength of the considered photons. The material gain is a gain spectrum depending on the electric properties of the active region. Alternatively, if g is negative, its symbol gets replaced by the losses $\alpha = \alpha_i + \alpha_m$. Losses can be classified into two categories: α_i represents all internal photon losses like scattering and absorption and α_m the mirror losses which will be defined in the next section.

2.5.2 Cavity

Besides the active region and the pump source, a laser consists of at least two mirrors that reflect the light back and forth. The distance that one photon travels to reach the starting point is called round trip. Such mirror arrangements form a Fabry-Perot resonator in which only specific light modes can be retained that fulfill the resonance condition $\lambda = \frac{2n_0L}{k}$ with k being an integer, λ the wavelength of the light, n_0 the refractive index of the material in the cavity and L the cavity length. Apart from the material gain defined in the previous section, this resonance condition is of major importance for the emission spectra of lasers. Only modes that fulfill the resonance condition contribute to the lasing output. In the case of simple edge emitting devices that are used in this work, the cavity consists of two mirrors, each created by the refractive index difference of the GaAs to air transition. The raw laser material is cleaved on both sides in a way that the (110) plane is forming these mirrors. This lattice plane is favorable since it provides the minimum surface energy, and smooth surfaces can be cleaved¹⁶². The refractive index n_0 of GaAs is approximately 3.3⁸⁵. Using the following Fresnel equation for normal incidence^{163,164}, the reflectivity $R \approx 0.3$ of such mirrors can be calculated:

$$R = \frac{(n_0 - 1)^2}{(n_0 + 1)^2} \quad (2.26)$$

This reflectivity value is sufficient for laser applications, but 70% of the light stored in the cavity gets transmitted out of the laser. Hence, for the lasing process itself the outcoupling of photons out of the cavity acts as loss channel. Thus, an additional mirror loss term α_m is introduced that must be added to the loss given in the previous section.

$$\alpha_m = \frac{1}{L} \ln \left(\frac{1}{R} \right) \quad (2.27)$$

The mirror loss depends on the length of the cavity and the reflectivity of the mirrors. For smaller cavity lengths the mirror losses are much more severe. In some applications these mirrors must be improved, which is achieved by coating the facets of an edge emitter for example^{165,166}. In VCSEL and VECSEL devices, distributed Bragg reflectors are used for one side of the cavity, showing a significantly increased reflectivity value.

The edge emitting devices presented in this work additionally feature separate confinement heterostructures (SCH) and gold stripes to form the cavity in the remaining directions. The SCHs encase the active region, and due to the difference in refractive indices between the SCH layers and the surrounding cladding layers an optical waveguide is formed. Therefore, the overall thickness of the SCH layers and the active region must be in the order of the emission wavelength, taking the refractive index into account. The spatial intensities of the optical mode can be simulated. The overlap of the optical mode and the active region is an important parameter since the crucial gain process for photons takes place in the active region. Mathematically this overlap can be expressed by the optical confinement factor Γ . It can be calculated by integrating the quadratic electrical field E of the optical mode spatially over the active region and relating this integral to the integration over the complete wave guide structure using equation (2.28).

$$\Gamma = \frac{\int_{active} E^2 dx}{\int_{waveguide} E^2 dx} \quad (2.28)$$

With this the modal gain g_{modal} can be defined: $g_{modal} = \Gamma \cdot g$.

In the remaining spatial direction, the optical mode is confined by gain guiding^{167,168}. This means that the pump current is only applied to a narrow contact on the laser device. Every part outside of the pumped region suffers from losses while the material gain amplifies the part of the optical mode that is in pumped areas. As a result, the optical mode is confined to the pumped volume of the material. The cavity is responsible for fulfilling the second laser condition: During one round trip the number of photons in the cavity must increase. This means that the modal gain must exceed the optical losses induced by the material α and by outcoupling out of the cavity α_m .

$$g_{modal} > \alpha + \alpha_m \quad (2.29)$$

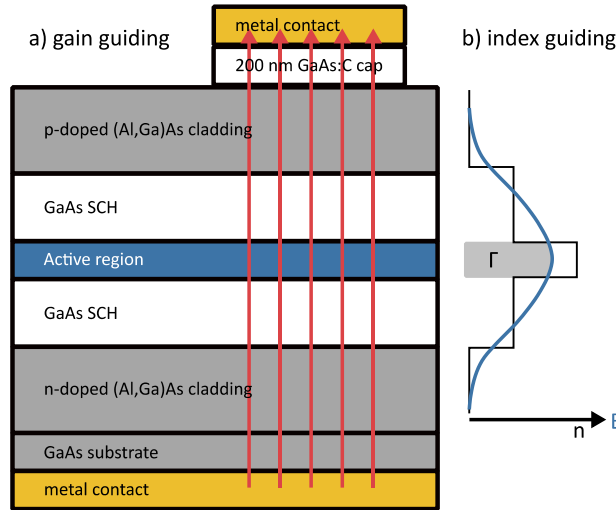


Figure 2.23 The optical mode inside the laser structure is confined in all directions. Besides the cleaved facets, the optical mode in the other in-plane direction is confined by a) gain guiding. In growth direction the mode is confined by b) index guiding.

2.5.3 Mathematical description

The following section is primarily based on Coldren and Corzine's book¹⁰⁴. Starting point of the mathematical treatment of semiconductor laser properties are the densities of carriers N and the density of photons N_p but first only the density of carriers is considered. This density is changed by recombination processes of holes and electrons and by pumping carriers into the active region. In this treatment the pumping process is called generation of carriers even though they are not really generated but injected. All possible recombination processes are cumulated in the recombination rate R_{rec} .

$$R_{rec} = R_{sp} + R_{nr} + R_l + R_{st} \quad (2.30)$$

Possible recombination paths are spontaneous recombination, non-radiative recombination, carrier leakage, and stimulated recombination represented by R_{sp} , R_{nr} , R_l and R_{st} , respectively. All these rates are given per volume of the active region V and per time. The carrier generation rate is represented by G_{gen} , for which applies the following relation in which I is the injected current and q the charge of each carrier.

$$G_{gen} = \frac{\eta_i I}{qV} \quad (2.31)$$

Since in real devices the current applied to the structure is not fully flowing through the active region, but parasitic current paths are also present, the total current flow reaching the active region

is reduced. To account for that the internal quantum efficiency η_i is introduced which corresponds to the fraction of the current that contributes to carrier generation inside the active region.

The total change of the carrier density can be expressed by:

$$\frac{dN}{dt} = G_{gen} - R_{rec} = \frac{\eta_i I}{qV} - R_{sp} - R_{nr} - R_l - R_{st} \quad (2.32)$$

One must keep in mind that the recombination rates in real systems also depend on the carrier density. In the following the optical output power of laser diodes is derived from this point for the LED and the laser regime.

2.5.3.1 Spontaneous emission and LED regime

The operating conditions of a laser below threshold correspond to the operating conditions of LEDs. In both cases the stimulated emission is zero, which means that R_{st} vanishes in equation 2.30. If the steady state condition is considered in which $\frac{dN}{dt} = 0$ the rate equation 2.30 becomes:

$$\frac{\eta_i I}{qV} = R_{sp} + R_{nr} + R_l \quad (2.33)$$

The most interesting recombination process is spontaneous recombination since it is the only radiative recombination in this case. To quantify the fraction of radiative recombination of all recombination paths, the radiative efficiency η_r is defined.

$$\eta_r = \frac{R_{sp}}{R_{sp} + R_{nr} + R_l} \quad (2.34)$$

Additionally, the net collection efficiency η_c is important. It accounts for the fact that spontaneous emission is not directional but emits photons in all directions and gives the fraction of emitted photons emitted into the measured angular range.

The optical output power of a LED or a laser device below threshold can be derived with all given equations. To obtain a power, the spontaneous emission rate must be multiplied by the Volume of the active region V and the photon energy $h\nu$.

$$P_{LED}(I) = \eta_c h\nu V R_{sp} = \eta_c \eta_i \eta_r \frac{h\nu}{q} I = \eta_{ex} \frac{h\nu}{q} I = \eta_\lambda I \quad (2.35)$$

All the different efficiency factors are summarized by the external quantum efficiency η_{ex} . For convenience, an optical efficiency η_λ is introduced, which accounts for all factors besides I in the equation above. The linear dependency between the optical output power and the pump current is

the main result of this derivation. If the optical output power is measured with respect to the pump current the external quantum efficiency and the optical efficiency can be easily determined.

2.5.3.2 Stimulated emission and Laser regime

A laser diode that operates above lasing threshold must be described differently since the stimulated recombination is the major recombination process. This includes that the photon density N_p inside the laser cavity plays an important role because the stimulated recombination rate depends on the photon density. Thus, also a rate equation for the change in photon density must be considered:

$$\frac{dN_p}{dt} = \Gamma R_{st} + \Gamma \beta_{sp} R_{sp} - \frac{N_p}{\tau_p} \quad (2.36)$$

This equation accounts for the optical losses like absorption of photons and mirror losses with the term $\frac{N_p}{\tau_p}$ with τ_p is equal to the average photon lifetime. The generation of photons can occur by stimulated emission and spontaneous emission. These rates are the same as for the carrier density rate equation, but it must be considered that the overlap of the active region with the optical mode plays an important role. Hence, the optical confinement factor Γ is included. The spontaneous emission factor β_{sp} must be additionally used since it describes how much of the spontaneous emission gets emitted into the optical mode of the resonator. Before writing the rate equation of the carrier density again, it must be noted that the spontaneous emission rate can also be expressed by the group velocity v_g , the photon density and the gain g : $R_{st} = v_g g N_p$. For the carrier density rate equation follows:

$$\frac{dN}{dt} = \frac{\eta_i I}{qV} - R_{sp} - R_{nr} - R_l - v_g g N_p \quad (2.37)$$

Special attention should be paid to the fact that both rate equations are coupled. This highlights the important interplay between the carrier density and the photon density in a laser diode. Prior to the derivation of the optical output power of a laser above threshold, it must be noted that the gain as well as the carrier density clamp to their values at lasing threshold because all excess carriers will raise the stimulated emission rate for a short time reducing the carrier density automatically.

The recombination rates in equation 2.35 are dependent on the charge carrier density, which is why they clamp at their value at threshold. Together with equation 2.31 a new rate equation can be written above threshold current I_{th} :

$$\frac{dN}{dt} = \frac{\eta_i (I - I_{th})}{qV} - v_g g N_p \quad (2.38)$$

And for the photon density at steady state condition:

$$N_p = \frac{\eta_i(I - I_{th})}{v_g g q V} \quad (2.39)$$

From that, the energy density in the cavity can be easily determined which is then used as starting point for the determination of the optical output power by considering the mirror losses per round trip. As result the final equation for the output power of a laser diode above threshold is obtained:

$$P_o(I) = \eta_d \frac{h\nu}{q} (I - I_{th}) = \eta_\lambda (I - I_{th}) \quad (2.40)$$

In this equation the differential quantum efficiency η_d is introduced which accounts for the fraction of charge carriers injected into the active region and contributing to the stimulated emission process. As for the equation below lasing threshold, a linear dependency on the pump current is found. Analogous to this, an optical efficiency η_λ is defined as proportionality factor between $I - I_{th}$ and the optical output power P_o .

2.5.4 Nonradiative transitions and loss channels

Besides the stimulated and spontaneous emission of a photon, multiple non-radiative recombination processes and other loss channels can reduce the number of charge carriers inside the active region. To maintain momentum and energy conservation, these processes come primarily with the emission of a phonon, but some loss channels include the emission of photons. However, these photons do not contribute to the lasing mode and are therefore also a loss channel. The energy is transferred to the lattice in the case of phonon emission, so the temperature increases. Since the optical properties of laser devices depend heavily on the operation temperature, they must be cooled down, for example by using a Peltier element with a temperature controller. This consumes energy, and this cooling process drastically lowers the wall-plug efficiency for laser diodes with high amounts of non-radiative losses.

2.5.4.1 Shockley-Read-Hall and interface recombination

The effect of oxygen that is incorporated into a III/V semiconductor lattice is devastating because an energy state is formed inside the band gap. Such states are localized, which means that electrons trapped in these states cannot move freely through the crystal. Therefore, these states are called trap states. A recombination can occur from the conduction band to the trap state, and from there a further recombination to the valence band can happen. The energy can be either emitted by the emission of a phonon, which results in heating of the lattice, or by emission of a photon. These recombination processes are called Shockley-Read-Hall recombinations^{169,170}.

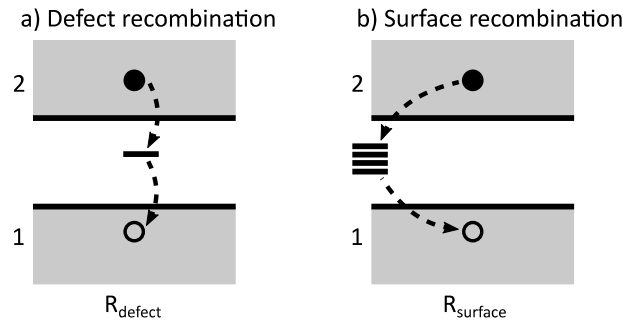


Figure 2.24 a) Shockley-Read-Hall recombination over a localized state inside the band gap. The excess energy will be transferred to the lattice as phonons or emitted as photons. b) Similar recombination process over surface or interface states.

The rate of recombination depends on the energy level and is maximized if the trap state is near the center of the band gap. Such states are called deep-level traps. The abovementioned oxygen would be an example for deep-level traps¹⁷¹. The recombination rate can be written in the high carrier density case as¹⁰⁴:

$$R_{\text{defect}} = nA_d \quad (2.41)$$

With A_d being the proportionality factor which depends on the trap state density N_t . If N_t has a larger value, the recombination rate increases.

Besides impurity atoms, also crystal defects like vacancies, interstitial defects and antisites will act as deep-level traps. Since the number of traps is limited and the average carrier lifetime in these trap states is finite, this kind of recombination can be saturated. Hence, it dominates at low carrier densities and for laser devices the effect is primarily on threshold current. While most laser materials can be grown very purely, dilute nitride-based laser materials have been found to exhibit a significant amount of deep-level traps and therefore Shockley-Read-Hall recombinations. Also Ga(As,Sb) lasers suffer from non-radiative recombinations because of trap states, that could come from antimony cluster formation⁴⁰.

Similar trap states can be observed at interfaces and surfaces, which result from broken bonds at the interface. Especially for laser materials based on type-II transitions, the internal interface plays a predominant role.

2.5.4.2 Auger recombination

In the Auger recombination process an electron of the conduction band recombines with a hole of a valence band. The energy gets transferred to a third charge carrier which is then emitted as a phonon and causing the lattice to heat up. Additionally, a phonon is involved in phonon assisted Auger

recombination to conserve the momentum. The different possibilities for Auger processes are shown in Figure 2.25 and named depending on the energy bands involved. The conduction band is denoted by the letter C, the heavy-hole band by H, the light-hole band by L, and the spin-orbit split-off band by S. This results in the following designations: CHCC for processes in which a transition occurs from the conduction band to the heavy-hole band and energy is delivered to an electron in the conduction band, which is then lifted to a higher state in the conduction band. Analogously, CHSH and CHLH processes are also possible.

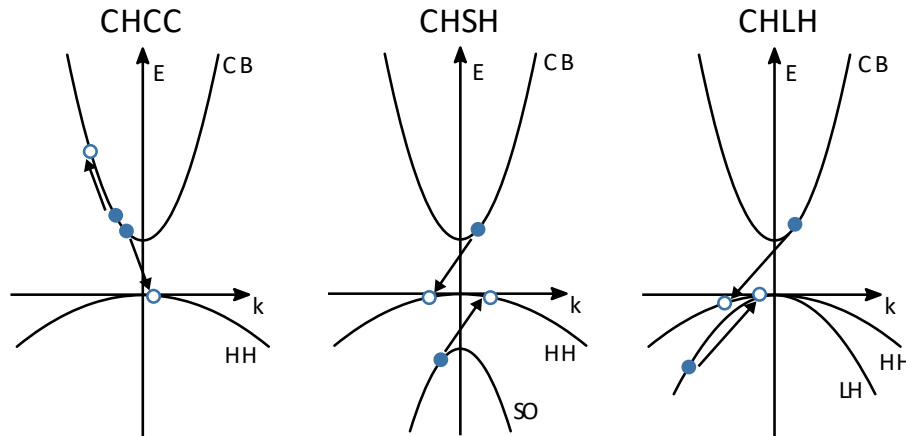


Figure 2.25 Variety of Auger processes. The CHCC process involves recombination from the conduction band to the heavy hole band. The excess energy is transferred to an electron in the conduction band which is excited to a free conduction band state. In the CHSH process the energy is instead transferred to an electron in the spin-orbit split-off band which is then excited to the heavy hole band. In the CHLH process the excited electron stems from the light hole band. Based on¹⁰⁴.

Depending on the charge carrier type to which the energy gets transferred, the recombination rate is proportional to n^2p if it is an electron or np^2 if a hole is involved. The full formula which is for example derived in Coldren's book¹⁰⁴ is given by:

$$R_{Auger} = (C_n n + C_p p)(np - n_0 p_0) \quad (2.42)$$

In this equation C_n and C_p are the Auger coefficients that can be experimentally determined. It can be also shown that the Auger recombination rate increases exponentially with temperature. In addition, the band gap influences the probability of Auger recombination because all states that are involved in these processes must be unoccupied. The occupation probability decreases with the energetic distance between the state and the band extremum. Since a higher band gap means more transferred energy, the probability of occupation of all involved states is lower for higher band gaps. Phonon assisted Auger recombinations constitute a significant effect if the band gap is relatively large, for example GaAs at room temperature. In materials with lower band gaps, for example (In,Ga)(As,P) normal Auger recombinations dominate at room temperature, however, at low temperatures phonon assisted recombinations take over.

Since three charge carriers are involved, the process dominates at high charge carrier densities. Auger recombination is a major loss process especially in lasers emitting in the telecommunication wavelength range.

2.5.4.3 Carrier leakage

Heterostructures like quantum wells have finite potential barriers. Electrical pumping of the active region raises the quasi Fermi level with increasing pump current density. Consequently, a part of the Fermi function protrudes beyond the barrier and, depending on further parameters such as the density of states and effective mass, charge carriers in these states can be excited to barrier states. The band edge diagram explaining this effect is presented in Figure 2.26. In this example a conduction band arrangement is shown, however, this effect can also occur in the valence band. Besides the electrical pumping also the thermal smearing of the Fermi functions must be considered. As a good approximation the thermal contribution to the energy can be estimated by $k_B T$, where k_B is Boltzmann's constant and T the temperature. For 300 K the thermal contribution to the charge carrier energy is 25 meV. The band offset should be a multiple of this value to ensure a sufficiently high energy barrier.

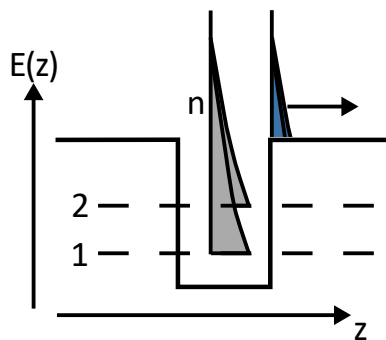


Figure 2.26 Conduction band of quantum well heterostructure. In grey the electron density is shown. The fraction of the electron density highlighted in blue exceeds the barrier height and can therefore drift into the barrier materials. These electrons are lost for the laser process.

If a laser material is affected by carrier leakage before the laser threshold is exceeded, then more and more carriers are lost into the barriers when a higher pump current density is applied and lasing can no longer be achieved since the carrier density inside the quantum well can only be raised slowly because the quasi Fermi level is only very slowly increasing. As countermeasures, alternative barrier materials with enhanced potential height can be used or electron blocking layers can be employed^{43,172}.

2.6 Type-II heterostructures for device applications

Type-II structures gained attention for several of their properties that can be beneficial for a variety of applications and devices. However, in section 2.5.1 the dependence of the recombination rates on the wave function overlap was stated due to the transition matrix element used in Fermi's Golden rule in equation 2.21. Hence, a major disadvantage of type-II heterostructures for optical applications is the small wave function overlap. To overcome this issue, the wave function overlap can be enlarged if a second electron quantum well is added to the structure¹⁷³. The hole quantum well is then sandwiched by two electron quantum wells that form new energetic states and thus, new wave functions are formed that increase the overlap to the hole wavefunction. These heterostructures are called "W" type-II quantum well heterostructures (WQWH) and were investigated for multiple different materials. A wide variety of type-II heterostructures were investigated on GaAs substrates for long wavelength emission with the ultimate goal to reach 1.55 μm emission wavelength with a laser device at room temperature. But also other substrates facilitate the possibility to grow type-II heterostructures, for example (In,Ga)N/Ga(N,As) dilute arsenic heterostructures based on GaN emitting in the blue wavelength region¹⁷⁴. Furthermore (Ga,In)As/Ga(As,Sb) type-II heterostructures can be grown on InP substrates and room temperature lasing was recently shown at 2.56 μm ^{172,175}.

On GaAs substrates, due to the availability of high quality structures, spectroscopic^{176–178} and theory¹⁷⁹ work was conducted for the (Ga,In)As/Ga(As,Sb)/(Ga,In)As WQWH material system. In spectroscopic studies combined with investigations of the internal interface between the (Ga,In)As to Ga(As,Sb) layers and vice versa, the strong influence of the optical properties on the internal interface quality was demonstrated^{177,178}. Interfaces with a high number of broken atomic bonds may lead to non-radiative recombination centers and an increased threshold current. Devices containing this material system as active regions were presented with low threshold currents for edge emitting laser diodes¹⁸⁰ and high output power VECSELs^{17,181}. Recent results promise the implementation of efficient THz emitters based on type-II heterostructures as a further field of application¹⁸². Wavelength extension with this material is limited by strain because both materials are compressively strained. Additionally, the growth of Ga(As,Sb) is difficult, because segregation effects and Sb clustering lead to non-ideal compositional profiles¹⁸³.

It is favorable in terms of wavelength and strain if (Ga,In)As is replaced by Ga(N,As) in the WQWH material discussed above, due to its tensile strain and the unique reduction of the conduction band edge, as highlighted in section 2.4. Combined with Ga(As,Sb), which acts mostly in the valence band, emission wavelengths up to 3 μm were theoretically predicted for nitrogen contents of up to 5%¹⁸⁴. A further important feature of Ga(N,As)/Ga(As,Sb) type-II structures is the possibility to compensate

the net strain of WQWH since Ga(N,As) is tensilely strained and contrary, Ga(As,Sb) is compressively strained¹⁴. So far, no laser devices operating at room temperature were shown for Ga(N,As)/Ga(As,Sb) type-II heterostructures.^{11,13,14,184,185} Lately, efforts to grow solar cells based on Ga(N,As)/Ga(As,Sb) were taken^{186–189}. Similar wavelength with less nitrogen content can be achieved for (Ga,In)(N,As)/Ga(As,Sb) type-II heterostructures while maintaining a high conduction band confinement^{11,12}. The reduction of the nitrogen content should be particularly favorable since nitrogen induced defects are known for limiting the device efficiencies. In comparison to Ga(N,As), (Ga,In)(N,As) is compressively strained, and no strain compensation can be achieved. The combination of Ga(N,As) and (Ga,In)As can also lead to a type-II band alignment if the nitrogen content is larger than 1%, but no further studies were carried out to investigate the usefulness of these heterostructures for device applications^{190–192}.

The bismuth containing type-II heterostructures are still under investigation, and despite serious growth peculiarities of Ga(As,Bi) most recently a laser device based on Ga(As,Bi)/(Ga,In)As was demonstrated¹⁹³. However, due to strain limitations and limitations of the achievable compositions, the emission wavelength reached only 1037 nm. To shift the emission wavelength to longer wavelengths, Ga(N,As) can be deployed. Then the epitaxial growth gets complicated and the interaction between Ga(N,As) and Ga(As,Bi) layers is not yet fully understood¹⁹⁴. Therefore, no lasing could be shown so far.

In the following, the advantages, disadvantages, and general properties of type-II heterostructures and WQWH will be discussed thoroughly.

An obstacle of many type-I heterostructures are the insufficiently high quantum well barriers of at least one charge carrier type causing carrier leakage. The confinement of electrons and holes in different materials allows the hetero offset for both charge carrier types to be tailored individually and thus counteracting charge carrier leakage. Furthermore, the achievable wavelength of type-I heterostructure based laser devices are limited by the composition which is limited by strain. To achieve longer wavelengths type-II heterostructures are a promising path if the hetero offsets of certain compounds are exploited in a suitable way. This was proven for instance for (Ga,In)As/Ga(As,Sb) type-II heterostructures, which demonstrate photoluminescence emission at 1.3 μm instead of shorter wavelengths presented for (Ga,In)As and Ga(As,Sb) type-I heterostructures¹⁹⁵.

Standard InP based laser diodes for longer wavelengths at 1.3 μm or 1.55 μm suffer from severe Auger losses that can make up to 80% of the threshold current density resulting in an intense heating of the devices, which requires energy for temperature stabilization⁴. A study conducted on InAs/(Ga,In)Sb type-II and WQWH structures grown on GaSb substrate, presents the experimentally

determined Auger coefficients of these samples as a function of the band gap. The investigated type-II structures showed band gaps corresponding to wavelengths between 3 and 5 μm . Similar type-I heterostructures based on InAs, In(As,Sb) and several others were compared. The Auger coefficients of the type-I heterostructures showed a clear dependence on the band gap.¹⁹⁶ The astonishing result revealed by comparing the type-II with the type-I samples uncovered that the Auger coefficients of the type-II samples were one order of magnitude lower than that of the type-I samples promising more efficient laser devices based on type-II heterostructures, which was also predicted by theory studies^{8,9}.

A unique feature of type-II heterostructures is the dependence of the emission wavelength on the charge carrier density in the quantum wells^{197,198}. In a type-II heterostructure holes and electrons are confined in different layers. Due to Coulomb interaction the bands will bend as a result of band filling and charge carrier density. This band bending effect results in a blueshift of the emission wavelength and the gain peak, which counteracts the endeavor of reaching a longer wavelength in the vicinity of 1.3 μm or 1.55 μm wavelengths. However, the band bending effect can be also advantageous because the wavefunction overlap increases with this band bending and hence, the transition matrix element increases¹⁹⁷, which causes higher gain values similar to that of type-I heterostructures.

Additionally, the blueshift can be facilitated to reduce the temperature dependence of the emission wavelength of laser diodes. Due to thermal effects on the band gap, emission from laser diodes tends to shift red with higher temperatures. If the properties of a type-II heterostructure are tailored appropriately, the blueshift induced by charge carrier separation can compensate the redshift or even blueshifts can be observed.¹⁰

The interface quality between the quantum wells is of major importance. Charge carriers are recombining over these interfaces and can be trapped by interface defect states. Additionally, rough interfaces can change the hetero offsets in an unfavorable way^{199,200}.

A vital design property of type-II WQWH is the thickness of the individual quantum well layers. With thicker layers the wavefunction overlap is reduced. It was found that the charge separation and accordingly the blueshift is more pronounced if the layers are thicker. Due to the weaker quantization effect, the energetic separation of the $n=1$ and $n=2$ quantized states is less and for thick layers the $e2h2$ transition could play a more prominent role.

Chapter 3 Experimental Methods

3.1 Metalorganic Vapor-Phase Epitaxy

In section 2.2 the theoretical background of epitaxial layer growth with MOVPE was discussed. In this section, the technical implementation and challenges are discussed. First, demands regarding precursor molecules suitable for MOVPE processes will be defined and essential precursors used in experiments conducted for this thesis will be reviewed. Second, technical details of the MOVPE machine and processes will be examined. In the end, details regarding the actual experiments will be given.

3.1.1 Precursor molecules

The choice of precursor molecules is of major importance for the MOVPE process. Therefore, they are subject to various special requirements. Precursors must fulfill the requirement to be stored stably at room temperature. Their vapor pressure must be sufficiently high to achieve significant growth rates, while being able to decompose at the lowest possible temperatures, which is contrary since higher vapor pressures typically go with higher decomposition temperatures²⁰¹. Preferred vapor pressures begin in the range between 1 and 10 mbar at temperatures between 0 and 20°C, to avoid the need for further measures such as heated lines²⁰². It is also advantageous for laboratory safety if they are non-flammable and non-toxic. In addition, safety and ease of handling are increased if the chemicals are present as a liquid at room temperature, but nevertheless, some common precursors are also gases and solids at room temperature (for example trimethylindium is a solid at room temperature and arsine a gas). In order to grow materials that raise special requirements in terms of purity, as it is the case with optical materials, very high demands are also placed on the achievable purity of the precursor. Particularly the oxygen content should be low because oxygen forms deep level traps in III/V semiconductors. From an economic perspective, it is useful especially in terms of industrial application, when production costs are low, and the growth efficiency is excellent.

Precursor molecules that are commonly used are a variety of metal alkyls with different alkyl groups. Common precursors feature three methyl- or ethyl groups, for example trimethylgallium (TMGa) and triethylgallium (TEGa). The decomposition temperatures of these precursors depend on the size of the metal atom included and the alkyl groups attached to it. In this work, the triethyl- precursors are preferably chosen, since they offer larger ethyl groups, which brings several advantages. First, the ethyl-based precursors decompose typically with β -hydride elimination reactions, which is beneficial

because this process can occur at lower temperatures. Second, the resulting ethyl radicals bind comparatively weak to the surface which causes faster desorption and hence less carbon incorporation into the crystal, compared to methyl-based precursors²⁰³. The methyl-based precursors tend to form CH_2 radicals suspected of incorporating carbon into the crystal²⁰⁴. However, TMIn is chosen as indium precursor because of its relatively high vapor pressure compared to other indium sources and the fact that TEIn decomposes already in the bubbler during storage⁹⁵. In this work, ethyl-based precursors are used for antimony and gallium: triethylgallium (TEGa) and triethylantimony (TESb).

The reduction of carbon incorporation from alkyl groups is reduced if a sufficiently high amount of atomic hydrogen is supplied as a decomposition product. This can be ensured by the most common group V precursors such as arsine. With atomic hydrogen present alkyl radicals may saturate with hydrogen to form alkanes that cannot bind to the growth surface. If group V precursors like TESb are used, which do not form atomic hydrogen as decomposition product, higher carbon incorporation is expected.²⁰⁵

However, due to safety precautions, arsine is not used in any experiment carried out for this work. As alternative, tertiarybutylarsine (TBAs) is used in all experiments as arsenic precursor. It was shown that the carbon incorporation with this precursor could be even less than for arsine²⁰⁶, because also atomic hydrogen is produced during the decomposition process²⁰⁷. However, arsenic-hydrogen bonds can lead to hydrogen incorporation into the crystal.

The choice of nitrogen precursor is a challenging task. Ammonia is the simplest precursor, which is only suitable for high temperature growth and is therefore only used for III/nitride epitaxy. For dilute nitride epitaxy, 1,1-dimethylhydrazine (UDMH) is the most established precursor. It has a N-N bond with one nitrogen having two methyl groups attached. This implies two strong N-C bonds. Three main decomposition paths were discussed in the literature, including homolytic fission and intramolecular coupling, which result in NCH_3 and CH_3 radicals. The strong carbon incorporation induced by UDMH is attributed to these decomposition products²⁰⁸ or to methyl or ethyl radicals originating from other precursors¹³⁸ that bond firmly to nitrogen. The third intramolecular coupling reaction leads to N_2 , which is too stable to decompose at the applied growth temperatures. Hence, the nitrogen incorporation efficiency is rather low and extremely high partial pressures must be applied. Necessarily, the gas phase is dominated by UDMH. Alternatively, di-*tert*-butyl-amino-arsane (DTBAA) can be used as nitrogen and arsenic precursor. It features two larger butyl groups and no N-C bonds, which promises less carbon incorporation²⁰⁹. It is still in an experimental stage, which means that the purity is low compared to UDMH. Especially oxygen contamination must be expected. Additionally, the incorporation efficiency of nitrogen is much better compared to UDMH, most

probably because no decomposition path leads to N_2 . Besides the nitrogen atom, DTBAA also exhibits an arsenic atom, making the use of TBAs for the epitaxial growth of dilute nitrides redundant.

Due to the materials grown in the following experiments, which require growth temperatures between 500 and 625°C, the precursors were chosen to be TEGa, TMIn, TESb, TBAs and UDMHy as gallium, indium, antimony, arsenic, and nitrogen precursors, respectively. UDMHy and TBAs are replaced by DTBAA during the dilute nitride layer growth for certain experiments. The explicit gas phase ratios depend strongly on this choice and will be discussed in the following chapter.

3.1.2 Technical implementation

The semiconductor industry demands low cost, low maintenance, high throughput, high material quality, and reproducibility for the production process. All these requirements can be satisfied by MOVPE. Planetary and showerhead reactor designs allow large wafer diameters or high throughput and homogeneous material properties. For research applications, the costs play an essential role hence the reactors used for these purposes are typically smaller horizontal reactors. However, all results obtained in these reactors can be upscaled for industry applications. A horizontal AIX 200 GFR reactor manufactured by AIXTRON SE was used in this work. It offers easy sample exchange and simple reactor cleaning procedures, making it well suited for research. The maximum substrate diameter is two inches, which drastically reduces the costs because the consumption of source molecules is minimized due to a small reactor volume. The consideration of the AIX 200 GFR MOVPE machine can be divided into three major parts. The most important part is of course the actual reactor. Additionally, a gas mixing cabinet and an exhaust module are required for operation. The reactor consists of a graphite susceptor on which the substrate is placed. It features a round plate that can be rotated to achieve homogeneous growth on the whole substrate. Inside the graphite susceptor, a thermocouple measures the reactor temperature. It is calibrated with the surface phase transition of the Al/Si eutectic formation at 577°C to the surface temperature on top of the rotatable sample plate. Heating is performed with six infrared heating lamps, that heat up the graphite susceptor from below. As already outlined in the previous section, the growth is performed with metalorganic molecules (MOs) out of a gas phase. Metal getter purified H_2 carries the MOs into the reactor. N_2 is also available, but in this case, it is only used as purging gas. To ensure homogeneity, the gas flow through the reactor is held constant at 6800 ml/min. Furthermore, the graphite susceptor is placed in a quartz liner that provides the shape ensuring a laminar gas flow above the substrate. The reactor pressure is set to 50 mbar for all growth experiments.

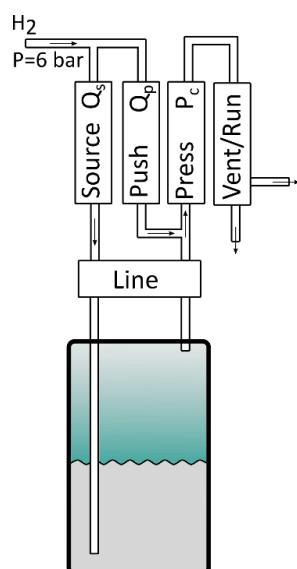


Figure 3.1 Schematic drawing of a bubbler (liquid precursor container). In grey, the liquid precursor is illustrated. A dip tube on the left operates as the gas inlet and is reaching towards the ground of the bubbler. The outlet tube begins at the ceiling of the bubbler and is depicted on the right. Above that, a line valve is present which is used to control if the gas flows through the bubbler. Above that, a source mass flow controller (MFC) and a push MFC control the total gas flow. The pressure is controlled by the pressure controller (PC) indicated as Press. If the Vent/Run valve is switched on, the gas flow reaches the reactor, and else it is led into the exhaust system.

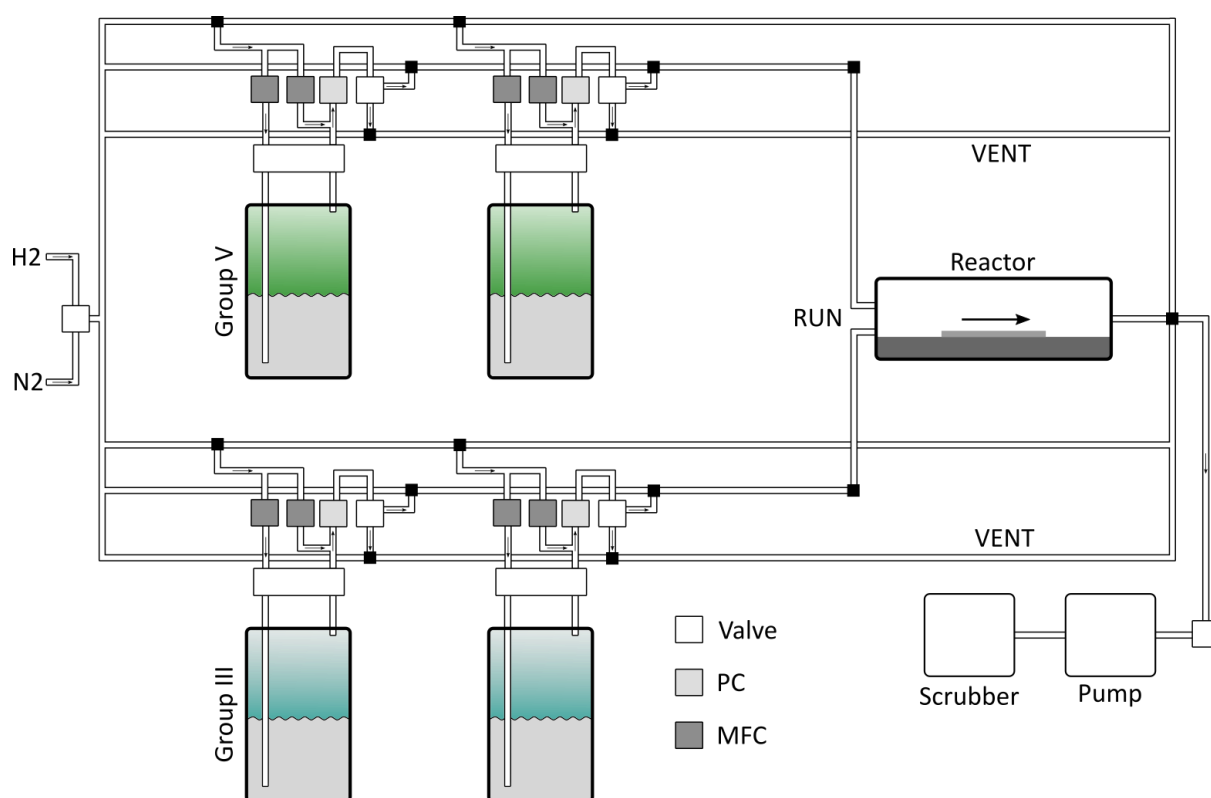


Figure 3.2 Schematic drawing of a MOVPE machine. The valve on the left side is responsible for supplying nitrogen or hydrogen as carrier gas. For group V and group III elements, a set of three tubes controls the gas flow, respectively. The upper tube supplies the source MFCs. More details on the connection of bubblers to the system can be found in Figure 3.1. The RUN tube leads the MO saturated carrier gas into the reactor. The third tube heads directly into the exhaust system. Behind the reactor chamber, a pump and a butterfly valve are responsible for maintaining the process pressure. Behind the pump, all gases are cleaned with the scrubber module.

To control the composition and growth rates of the deposited materials, the mixture of the different source molecules in the gas phase is crucial. Everything related to this technical challenge is carried out in the gas mixing cabinet, in which the liquid or solid sources are stored in stainless steel containers called bubblers. These bubblers feature an outlet and a dip tube. The vapor pressure of the respective precursor saturates the gas phase above the liquid or solid phase in the bubbler. Carrier gas flows through the bubblers, entering through the dip tube and saturates there with source molecules. The amount of source molecules in the reactor and accordingly the partial pressure P_p can be determined by the following equation:

$$\frac{P_p}{P_R} = \frac{Q_S}{Q_T} \frac{P_v}{P_B - P_v}$$

Where P_R , P_v , Q_S , Q_T describe the reactor pressure, the vapor pressure, the gas flow through the bubbler, and the total gas flow in the reactor, respectively. The vapor pressure of the source molecule defines the amount of source molecules in the gas phase of the bubbler. It is susceptible to temperature. Consequently, bubblers must be stored in temperature stabilizing water baths. It can be calculated by the following equation:

$$P_v = e^{A - \frac{B}{C+T}}$$

The parameters A, B and C are constant for the particular source material that must be experimentally determined and T is the source temperature.

Technically, pressures and gas flows must be controlled precisely to fulfill MOVPE growth requirements. Hence, every bubbler is connected to two mass flow controllers (MFC) and one pressure controller (PC), each of which can be electronically controlled. The gas flow through the bubbler is controlled by the source MFC Q_S . Since the source flow is regularly changed during epitaxy processes, an additional push MFC Q_P is added to dilute the source saturated carrier gas further to maintain a constant gas flow through the PC. In practice this means the sum of Q_P and Q_S remains constant during the process. The cumulated gas flow then passes the PC, which ensures a constant pressure in the bubbler. Possible setpoints are between 150 and 1800 mbar. Afterwards, the gas is switched between two different lines by the run valve connected to the gas collecting main lines differentiated in run and vent lines. The vent lines head directly into the exhaust system while the run lines lead the gas into the reactor. This way a stable gas flow can be maintained.

The machine is operated from a computer running AIXACT software. Within this software, it is possible to program recipes for all conducted experiments.

3.1.3 Experimental details

All experiments were carried out on 2'' GaAs substrates, either n-doped or semi insulating. The delivered substrates are specified as "epiready", which means that no wafer pre-treatment is necessary. However, for laser structures, an etching procedure was applied in order to remove potential oxidized layers. The etching procedure is based on a mixture of ultrapure water, hydrogen peroxide and a diluted amount of ammonia with a pH value of 7.5. The wafer is placed in a spin coater during the whole etching process. First the etching mixture is constantly poured over the wafer for 2 minutes. Then, the wafer is flushed with cleaned water for 5 minutes and in the end dried with N₂ for 3 minutes. Directly after this etching process, the substrates were transferred to the N₂ filled glovebox connected to the MOVPE reactor to avoid further contamination and oxidation of the substrate surface. Inside the glovebox, the substrates are eventually cleaved into four equal pieces to reduce the wafer consumption.

At the beginning of each MOVPE process, a pre-treatment of the substrate surface is carried out. It includes 10 minutes bake out at 350°C to remove water and a subsequent 5 minutes bake out at 750°C to remove all remaining oxidized layers and other contaminations. This heating procedure is followed by a 250 nm GaAs buffer growth at 625°C to ensure a reproducible clean growth surface. A pre-run of all precursors saturates all interior tube surfaces of the particular source to ensure a constant partial pressure in the reactor chamber when the process starts.

Some parameters were chosen to be constant in all epitaxy runs to reduce complexity. The partial pressure of the gallium precursor TEGa is 7.09E-3 mbar in all experiments and the reactor pressure 50 mbar. This results in typical growth rates between 0.25 to 0.40 nm/s. After finishing the last active layer, a GaAs cap layer between 20 and 60 nm is grown for all samples to protect the active layers and prevent loss of charge carriers, due to coupling into surface states during optical experiments. To ensure the compositional preciseness, at the beginning of each epitaxy session, the growth parameters for each alloy are adjusted by growing test structures. These test structures consist of 20 nm thick Ga(N,As) layers, if the nitrogen content is to be adjusted. All other alloys were adjusted by growing thin quantum well layers with the intended thickness with maximized number of repetitions without relaxation. The single quantum well layers are separated by 20 nm thick GaAs barrier layers.

3.2 High Resolution X-ray diffraction

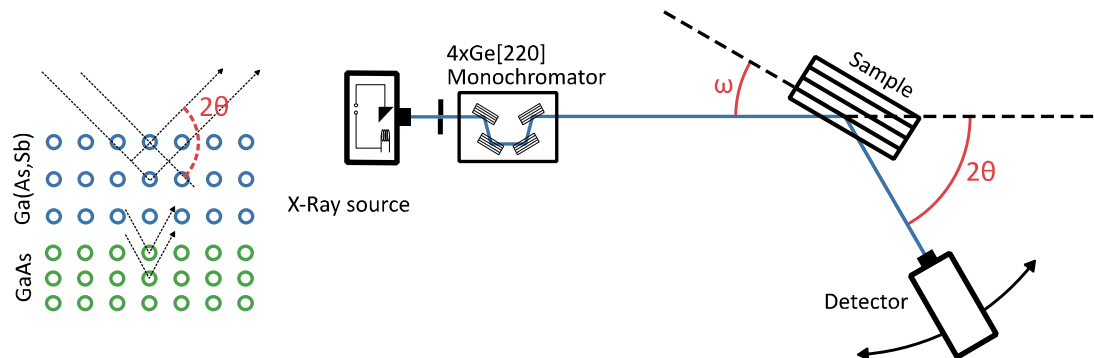


Figure 3.3 Left: Strained Ga(As,Sb) layer on GaAs substrate. Since the Sb atoms increase the lattice constant, the layer is compressively strained and the lattice elongated in growth direction. The scattering geometry at crystal lattices is shown with the dashed lines. The scattering angle is different for both materials. Right: HR-XRD setup with X-Ray source on the left side. From the X-Ray beam the K_{α} line of the copper anode is filtered with a monochromator. The sample and the detector are mounted on rotatable stages. During the measurement both are rotated.

The last section outlined the technical challenges in growing thin layers of semiconductor materials with high compositional control. These properties also induce the urge for a supplementary analysis technique that offers quick, non-destructive, and reliable feedback after each epitaxy run. Analyzed structures have dimensions in the range between nanometer and micrometer, which is why optical microscopes are not suitable because the wavelength of the probing beam is longer than the structural dimensions. Alternatively, appropriate wavelengths can be achieved with electrons and X-Rays. Techniques based on electron probe beams like scanning transmission electron microscopy (STEM) are not acceptable to be used as feedback for every sample because they are too complicated and due to the sophisticated sample preparation too slow to apply on every sample. Therefore, the most established structural analysis method in epitaxy labs is based on X-Rays and is called high-resolution X-ray diffraction (HR-XRD). The most important principles of HR-XRD will be discussed in this section. A thorough discussion can be found for instance in P. Fewsters book²¹⁰. Two models can describe the results obtained by HR-XRD, namely the kinematic and the dynamic diffraction theory. In the following, the kinematic diffraction model will be briefly discussed since it is well suited for showing the intuitive ideas of the technique.

In the kinematic model, an impinging X-Ray wave scatters elastically at the periodically ordered crystal atoms. Multiple scattering events are neglected in the kinematic approximation. The angular dependence of the scattering can be described by Bragg's law²¹¹ or Laue's condition⁸¹. The former can be derived by relating the path difference of the scattered X-Ray waves from neighboring lattice

planes to the constructive interference condition, considering the wavelength λ . The geometry of this case is shown on the left side of Figure 3.3.

$$2d_{hkl}\sin\theta = \frac{2a}{\sqrt{h^2 + k^2 + l^2}}\sin\theta = n\lambda \quad (3.1)$$

The integer n denotes the order of diffraction, a the lattice constant, and h, k, l are the Miller indices of the respective lattice planes with distance $d_{hkl} = \frac{a}{\sqrt{h^2 + k^2 + l^2}}$. From equation 3.1 it becomes obvious that the scattering angle depends on the distance between the lattice planes. Since the investigated structures exhibit pseudo morphically distorted layers in growth direction (see chapter 2.2.1), the scattering angle caused by the respective lattice planes are shifted compared to the substrate angle, if the lattice planes perpendicular to the growth direction are involved in scattering. The compressed or elongated lattice constant of the strained layer can thus be detected in angular dependent measurements. According to equation 2.16 and 2.17, the lattice constant of the unstrained alloy can be calculated. With this, Vegard's law (equation 2.12) leads to the composition of the alloy. Aside from fringes resulting from lattice planes, all layers can also form superlattices that cause fringes related to the layer thicknesses.

This kinematic model is successful in predicting the scattering angle for thick layers but is not sufficient for complicated heterostructures consisting of multiple thin layers. For instance, for thin layers a peak shift was reported²¹², that was contrary to the kinematic model. For such structures, the more advanced dynamic modeling approach must be chosen, which describes the X-Ray waves inside the periodic crystal potential, including multiple scattering events. Starting point of this modelling is the structure factor, which summarizes the effect of scattering on all atoms of a unit cell. Also, the scattering intensity at different atoms is included in these calculations, which opens the possibility to simulate the intensity of the scattering fringes, which is totally omitted in the kinematic model. In this work, the commercial software X'Pert Epitaxy and Smoothfit by Panalytical was used for retrieving the compositions and layer thicknesses by fitting simulated diffractograms to the measurements.²¹³

The X-Rays are generated with a copper anode, whose K_α line of the characteristic spectrum is selected with a 4xGe[220] monochromator and has a wavelength of 1.5405 Å making it well suited for investigations of crystal lattices²¹⁴. The sample and the detector are mounted on rotatable stages and a coupled scan of ω and 2θ (see Figure 3.3) is performed for all presented measurements in this work. The angular range in vicinity to the GaAs (004) reflex is investigated because GaAs (001) surfaces are utilized as substrates and the distortion in growth direction is to be investigated.

In practice the interpretation of such HR-XRD diffractograms is difficult. To observe all distinct features and fringes, diffractograms are typically plotted with a logarithmic intensity scale, as can be seen in Figure 3.4. One of the most prominent peaks is the substrate peak, which corresponds to the substrate's lattice constant. Quantum well fingerprint fringes can be used to extract the chemical composition and the layer thickness of the respective layers: The envelope function is defined by the chemical composition and the underlying smaller peaks are a result of diffraction at the internal interfaces, so called Pendellösung fringes. The higher the distance between these peaks, the smaller the layer thicknesses. Their shape gets determined by the thickness of the cap layer. If the defect density is high, the FWHM of the fringes increases. Since the simulation software assumes compositionally abrupt interfaces, slight deviations of the simulation from the measurement can hint to a gradient at the interface or even a bad interface quality. Exceeding the critical layer thickness of the epi layer, relaxation of lattice planes will result in a broadening of the peak. Error bars are estimated by changing the simulated sample structure, until measurement and simulation barely fit. Complex heterostructures like WQWH must be carefully simulated, in order to determine their structural parameters. Most of the time it is reasonable to use the result of other samples as a starting point.

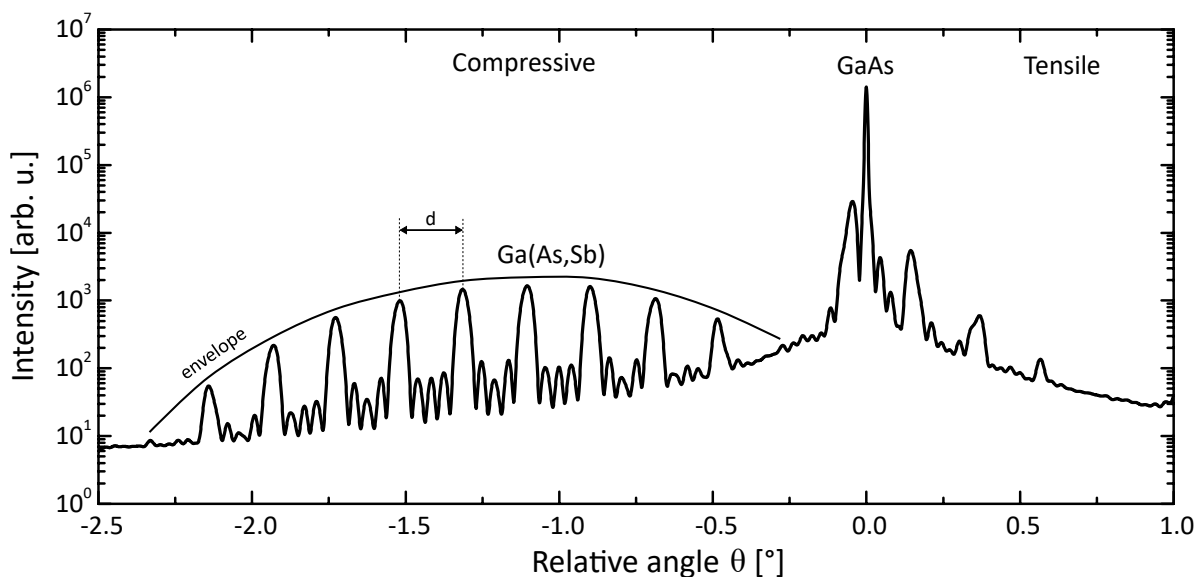


Figure 3.4 Simulated HR-XRD diffractogram of a sample with five repetitions of 5 nm Ga(As,Sb) quantum wells, separated by 20 nm GaAs barriers. On the left side of the GaAs substrate peak, the compressive side of the diffractogram exhibits the diffraction fringes of the Ga(As,Sb) quantum well layers. The position of the envelope function is a measure for the antimony content. The distance d depends on the thicknesses of all repeated layers of the structure.

3.3 Photoluminescence Spectroscopy

While HR-XRD measurements can provide quick feedback on the structural properties, a similarly quick and non-destructive technique must be used to determine the optical quality. CW

photoluminescence spectroscopy (PL) is a utile technique which satisfies these requirements exactly. Its working principle is based on a continuous wave (CW) laser focused on the sample surface to excite electrons. The wavelength of this laser has to be chosen in a way, that the photon energy is larger than the band gap energy of the investigated material. In samples containing quantum wells, the excitation takes most probably place in the barrier layers, because their thicknesses exceed the thickness of the quantum well layers. The process is illustrated in Figure 3.5. Due to excitation, the electron is lifted to a conduction band state, and a hole occupies a valence band state. Both charge carriers first relax into energetically lower states of the same band due to phonon scattering. This process typically happens on a faster timescale than band to band recombinations. Ideally, both charge carriers recombine radiatively when they occupy the energetically lowest possible states of their respective bands. As already outlined in section 2.5.1, multiple possible recombination paths can take place, and in some cases a photon is emitted. The photon energy corresponds to the energetic distance between the two involved states, which are either quantized states if the analyzed material contains a quantum well, or the band edges, if a bulk material is investigated.

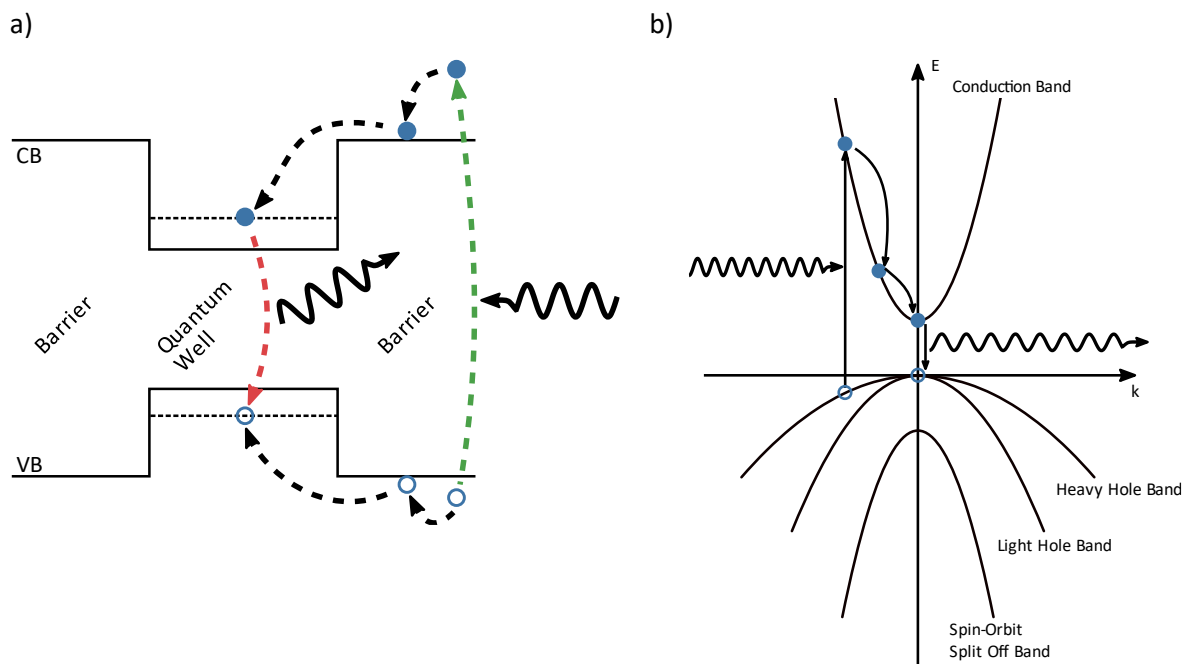


Figure 3.5 In both figures, the working principle of PL spectroscopy is illustrated. In a) the optical excitation of a sample containing a quantum well is shown. Due to its larger thickness, the charge carriers get excited in the surrounding barrier material. Then, the charge carriers relax under emission of phonons into the lowest possible state, where they recombine radiatively. In b) the same process is shown for a bulk layer in k-space.

During the excitation, the light emitted from the sample gets spectrally dispersed and the intensity is measured for each photon energy. With that, an emission spectrum is retrieved that shows several interesting features. For quantum well samples, the distance between the quantized states can be determined and for bulk layers at least a good measure for the band gap can be found. The band gap determination is limited by the fact that the density of states is lowest at the band edges. Hence, the

intensity peak in the emission spectrum will be above the band gap energy because more transitions occur for these higher transition energies with higher local density of states. Besides that, disorder states smear out the band edge of real semiconductors and strain effect come into play. If a high number of defect states are localized in the band gap, radiative recombinations related to these states also contribute to the emission spectrum. Especially highly doped crystals can form bands closely to the band edges that influence the emission spectrum. Apart from these effects, also all conceivable non-radiative recombination processes can lower the overall intensity of the emission spectrum. Therefore, PL offers the possibility to investigate the optical quality of the material directly after growth, without making too much effort. However, the comparability of laser device properties and the results of PL spectroscopy are limited because the excitation density is much lower in PL spectroscopy than in laser devices. Additionally, a laser device features a more sophisticated sample structure with SCH and cladding layers that also affect the device performance.

Low temperature measurements can typically reveal additional features. If the PL spectra are measured temperature dependent, the temperature dependent peak shift determines the disorder of the material. At low temperatures, the high energy flank of the peaks estimates the carrier temperature while the low energy flank hints for example to the characteristics of disorder.

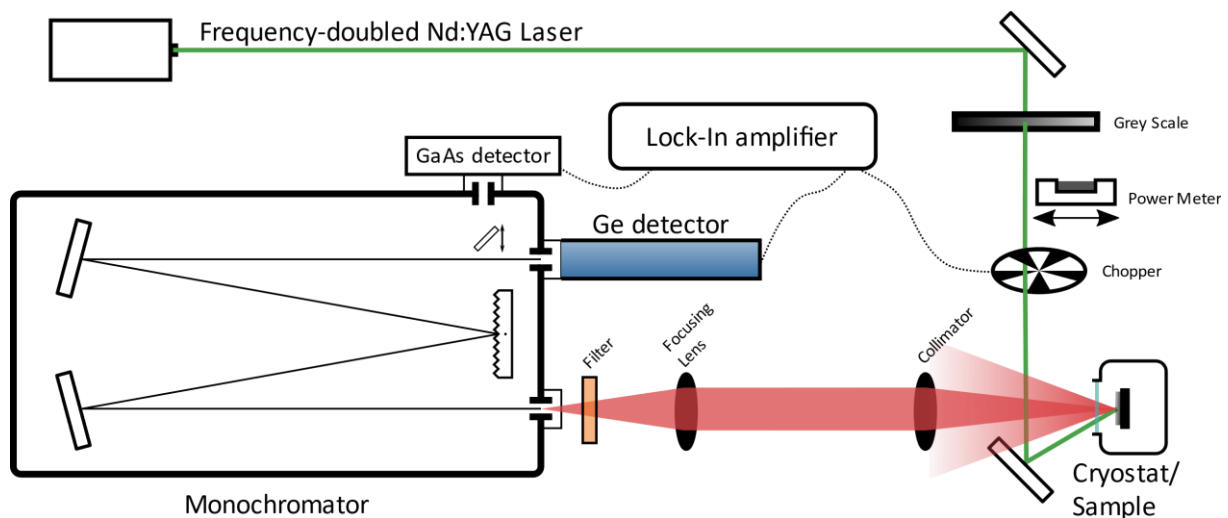


Figure 3.6 Photoluminescence spectroscopy setup. Excitation of the sample is done by a frequency doubled Nd:YAG Laser. The sample is placed inside a cryostat chamber that allows for low temperature measurements. The PL signal is dispersed by a monochromator and detected with a germanium detector using a lock-in technique for improved signal to noise ratio.

The custom build PL setup is schematically drawn in Figure 3.6. A frequency doubled neodymium-doped yttrium aluminum garnet (Nd:YAG) solid state laser (Laser Quantum Opus 532) excites the sample with an emission wavelength of 532 nm. This wavelength corresponds to a photon energy of 2.331 eV and is therefore well above the band gap of GaAs (1.42 eV). Alternatively, two additional laser sources are available but not used in this work. The laser line at 1064 nm is filtered out with a

short pass filter. A grey scale filter lowers the laser intensity to the intended excitation density. The laser intensity is measured by a subsequent power meter. The sample is placed inside a cryostat chamber, which can be cooled with liquid nitrogen to 85 K or with helium down to 10 K. Two achromatic lenses with focal lengths of 120 mm for collimating and 400 mm for focusing, collimate the PL signal and focus it into a monochromator (Jobin-Yvon THR 1000). The monochromator consists of two mirrors and a rotatable blazed grating with 600 lines per mm and a blaze angle optimized for a wavelength of 1000 nm. The maximum achievable resolution depends on the slit settings. A long pass filter is placed in front of the entrance slit to rule out any damage on the detector caused by the laser light. The variability of the entrance and outlet slit widths of the monochromator allows for measurements of samples of completely different optical quality. Inside the monochromator, a rotatable diffraction grid is dispersing the PL signal. Combined with the output slit, a precise wavelength selection is possible. The optical intensity is measured directly at the output slit with a liquid nitrogen cooled germanium detector (Applied Detector Corporation 403L). To improve the signal to noise ratio, the laser beam gets chopped with a mechanical chopper wheel which is connected to a lock-in amplifier (Stanford Research System SR510) that measures the signal of the germanium detector.

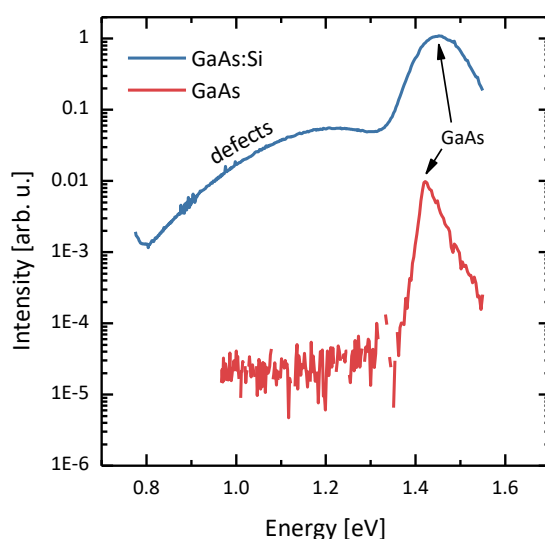


Figure 3.7 PL spectra measured for undoped GaAs substrate and n-doped GaAs substrate doped with silicon atoms. Compared to the undoped GaAs, a defect background originating from the silicon doping is observable for the silicon doped substrate. The GaAs peak itself is smeared out.

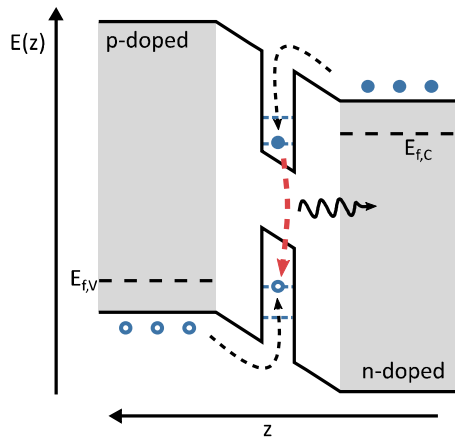
In Figure 3.7 two PL spectra are shown as an example. One of these spectra corresponds to a pure GaAs substrate, without any epitaxially grown layer, and the other spectrum originates from an n-doped substrate. A peak at 1.42 eV is visible in both spectra, which comes from radiative recombinations over the GaAs band gap. The shape of these peaks differs due to the dopant atoms acting as defects. As indicated in Figure 3.7, these defects also cause a different background at lower

energies. Spectra of undoped GaAs layers deposited on n-doped GaAs substrates, the GaAs is a superposition of both shapes illustrated in Figure 3.7.

3.4 Electroluminescence Spectroscopy

In the last section the limited possibility to draw a conclusion regarding laser devices with PL spectroscopy was outlined. To investigate the optical properties under the influence of high excitation densities, the considered materials must be electrically pumped. Therefore, special laser structure samples are deployed. The light emission process in laser diodes is based on electroluminescence and accordingly, the spectroscopy technique is called electroluminescence spectroscopy (EL). The basics of this electroluminescence process are already thoroughly discussed in section 2.5. Hence, this section will only focus on a brief repetition. The process is schematically plotted in Figure 3.8 a). Charge carriers get pumped into the active region utilizing a pn-junction. In the active region, they relax into the lowest possible states and recombine with various radiative and non-radiative processes.

a)



b)

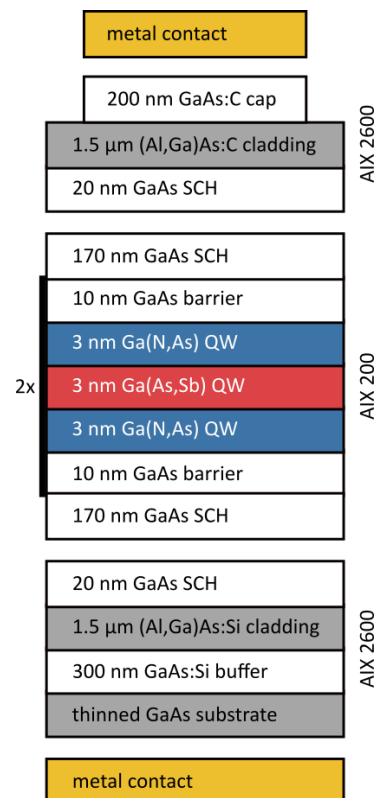


Figure 3.8 a) Schematic explanation of the EL process. Charge carriers get pumped into the active region via p- and n-doped cladding layers, where they relax into the quantized states of the quantum well. From these states they recombine with various recombination paths, eventually with the emission of a photon. b) Illustrates the laser sample structure.

The electrical pumping raises some requirements on the sample structure, as already outlined in section 2.5. In Figure 3.8 b) the layer stack of such laser structures is depicted. Besides the active region, GaAs SCH layers and (Al,Ga)As cladding layers have to be grown. The full layer structure is epitaxially grown in three separate processes on a n-doped GaAs substrate. The cladding layer growth, including 20 nm GaAs SCH, is carried out in an AIX 2600 G3 reactor with a 24x2'' configuration. This reactor is a production scale planetary reactor, which enables growth on 12 wafers simultaneously. These well-established cladding processes ensure a high comparability between laser structures grown in one epitaxy session, because only the active region varies. The gaps in the layer stack in Figure 3.8 b) illustrate the different epitaxy runs. All processes on these production machines exhibit reactor temperatures of 625°C during the growth of all layers.

In the first process, the n-doped cladding layer is grown. The standard wafer pre-treatment is performed, but in this case a 300 nm highly n-doped GaAs buffer realizes the flat growth surface. As n dopant, silicon atoms were incorporated with Di-tert-butyl silane (DTBSi) as precursor. To ensure low carbon incorporation, the GaAs buffer layer is grown with a V/III ratio of 10. The Si/III ratio is $1\text{E}-3$. Then, 1 μm n-doped (Al,Ga)As is deposited, employing DTBSi with a Si/III ratio of $3\text{E}-3$, resulting in a silicon content of $1\text{E}18\text{ 1/cm}^3$. After this 1 μm (Al,Ga)As layer, additional 500 μm (Al,Ga)As with a lower Si/III ratio provides a lower n-doping of approximately $5\text{E}17\text{ 1/cm}^3$. These cladding layers require a large V/III ratio, to avoid intrinsic carbon incorporation, which is therefore chosen to be 60. On top of the (Al,Ga)As cladding layers, the first 20 nm of the GaAs SCH act as cap layer.

The next step is the deposition of the active region. For that, the wafers are quickly transferred from the production machine into the N_2 filled glovebox, connected to the AIX 200 system. In the AIX 200 reactor, no special pre-treatment is performed, but 170 nm GaAs SCH is deposited prior to and after the active region growth at 625°C.

After transferring all wafers back to the production machine, a similar p-doped cladding structure is grown. To symmetrize the SCH layers, 20 nm GaAs is deposited first. The doping of the (Al,Ga)As layers is this time achieved by intrinsic carbon doping, using lower V/III ratios. The first 1200 nm (Al,Ga)As aim for a p dopant concentration of $5\text{E}17\text{ 1/cm}^3$ by using a V/III ratio of 50. Subsequently, 300 nm (Al,Ga)As with $1\text{E}18\text{ 1/cm}^3$ p dopant content is grown with a V/III ratio of 30. On top of these layers, a highly doped 50 nm (Al,Ga)As layer was grown, during which the V/III ratio was changed constantly from 30 to 10. A highly p-doped GaAs layer caps the full laser structure. Since the intrinsic carbon doping is not sufficient for GaAs layers, carbon tetrabromide (CBr_4) is applied as carbon source with a C/III ratio of $4.8\text{E}-2$.

Besides the epitaxial growth, the structures must be processed to full laser structures by first grinding the substrate thickness down to 150 μm . On the backside of the n-contact, a large area gold

contact is evaporated. On the top p-contact 50 μm and 100 μm thick gold stripes are build using lithography techniques, resulting in a laser bar with multiple contacts. The GaAs cap layer is removed by etching in regions without gold contacts. All processing steps are performed by Stephan Reinhard.

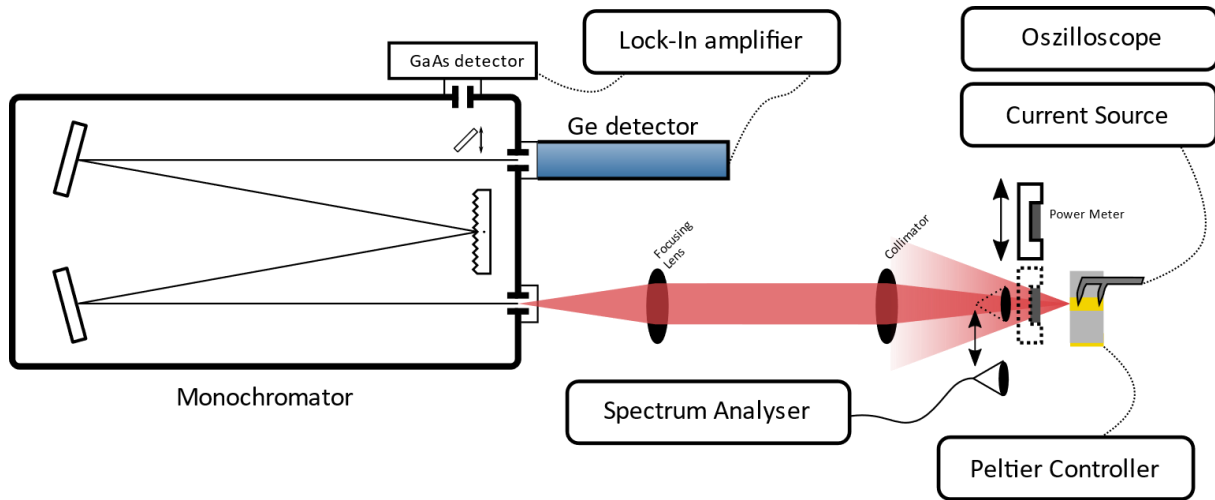


Figure 3.9 Depiction of the EL setup. The processed device is contacted with thin needles and the golden back contact. It is placed on a copper block, that features a temperature sensor and a Peltier element. These components stabilize the temperature of the device. Two different current sources apply a pulsed voltage and current to the measured gold contact. The optical output power can be measured with a power meter or spectrally analyzed with the optical spectrum analyzer or the monochromator setup in combination with the Ge detector. To ensure a high signal-to-noise ratio, the signal is measured with a lock-in amplifier.

The EL setup is schematically drawn in Figure 3.9. Since the technique is similar to PL, the setup is also partly shared with the PL setup. The laser structure is placed on a copper block, which is thermally stabilized using a Peltier element and a thermistor inside the copper block. Both are connected to a temperature controller that is used to stabilize the temperature to a fixed value between 5 and 100°C. The Peltier element transfers the heat between the copper block and a water-cooled heat sink. As current source, two pulsed voltage sources are used. The voltage applied by these sources is pulsed and approximately rectangular shaped. This way the laser device is operated in pulsed CW mode to reduce the heating. The duty cycle can be adjusted manually with the measurement software. A probe card with multiple needles with a spacing of 100 μm is placed on top of the p-contact stripes of the sample as positive pole and the ground potential is set to the copper block which is contacted to the backside n-contact. The current and the voltage applied to the laser structure is polled by an oscilloscope which is also connected to the measurement computer. A rectangle is fitted to the measured voltage and current signal to obtain the real forward voltage and current. Its trigger signal is connected to the trigger output of the current source. The measurement of the optical output power depends on the purpose of the measurement. In the case of determination of the characteristic power-current curve (P-I curve), a Newport 1835-C power meter is used together with a Newport 818-ST2-IR photodetector. The applied voltage is then varied, and the related optical output power is measured per facet. This measurement is repeated for all

contacts of each bar and the optical power output and voltage curves are averaged. The evaluation is conducted according to section 2.5 on the averaged data.

Analog to PL spectroscopy, the emitted signal can alternatively be measured by the liquid nitrogen cooled Ge detector after dispersing the signal into its spectral components with the monochromator. This way the emission spectrum (EL spectrum) can be obtained. During these measurements the voltage source is set to a constant voltage and the trigger signal of the current source is connected to the trigger input of the lock-in amplifier.

Two pulsed current sources are available. The first is called EΦMR UR19GR05 and provides a maximum voltage of 19 V, resulting in 4 V forward voltage across the device and nicely rectangular shaped voltage pulses. The maximum current achieved with the laser structures described above, is about 4 A. Standard values for the pulse length and the repetition rate are 400 ns and 10 kHz, respectively, which result in a duty cycle of 0.4%. All these parameters result in a dissipated electrical power of approximately 64 mW.

The second pulsed current source is commercially available from AVTech, which reaches voltages of up to 320 V, resulting in currents of about 20 A and forward voltages of about 40 V. The pulse width of 100 ns is typically shorter than that of the other pulse source and the pulse period is set to 200 μ s, which corresponds to a duty cycle of 0.05%. The dissipated electrical power is accordingly 400 mW.

The power meter exhibits different sensitivities at different wavelengths. This responsivity is plotted in Figure 3.10 as a function of the emission wavelength. Each determined optical output power must be corrected using the respective correction factor retrieved from this plot.

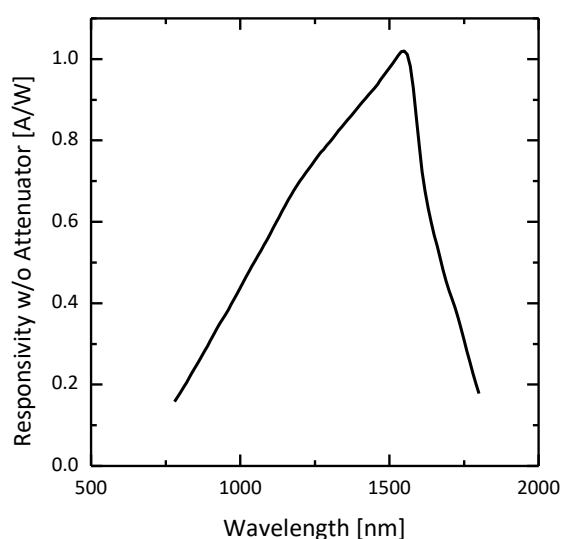


Figure 3.10 Wavelength depended responsivity of the Newport 1835-C power meter. The optical power output obtained in the characteristic P-I measurements must be corrected by a correction factor determined by the emission wavelength.

3.5 Atomic force microscopy

The atomic force microscopy (AFM) is a technique which allows for the investigation of microscopic surface morphology under ambient conditions. This is useful as a standard method for investigating the sample quality.

In Figure 3.11 the components of an AFM are schematically drawn. A cantilever whose oscillation can be excited mechanically with a given frequency is scanned over the sample. The tip of this cantilever is as small as possible, in the best case only one atom in size. A laser beam is conducted onto the cantilever where it gets reflected towards a detector with four different segments. By calculating the difference signals of these segments, the frequency of the cantilever oscillation can be determined. The sample is placed on piezo elements in order to electrically move the sample in x, y and z direction. In this work a Nanoscope IIIa by Digital Instruments was operated in tapping mode. In this most common AFM operating mode, the cantilever is excited with a frequency near the resonance frequency while being scanned in x and y direction closely over the sample. If the distance between the cantilever tip and the surface changes, the resonance frequency also changes due to the tip and surface interaction. The z-position of the sample is then tuned with a piezo element to maintain the same resonance frequency. Then, the signal needed at that piezo element corresponds to the surface height at the sampled xy position.

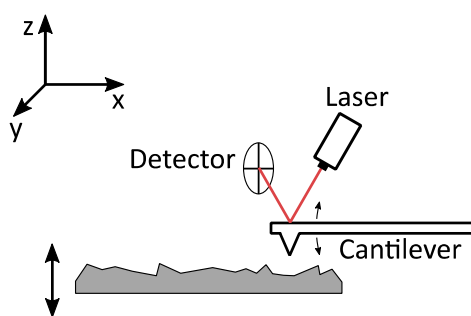


Figure 3.11 Working principle of atomic force microscopy. An oscillating cantilever is moved over the sample surface. The oscillation is tracked by the movement of a reflected laser spot on a detector.

In principle, two different types of sample surfaces can be analyzed by AFM. The first type is the sample surface as it comes out of the MOVPE reactor. In this case only the cooled cap layer surface can be investigated. The morphology of this surface does only indirectly represent the morphologies of the internal interfaces, making it a good measure of the overall growth quality. For example, defects and unfeasible growth parameters of underlying layers can be estimated by looking at the cap layer surface. Secondly, when applying a selective etching technique, special samples can be

prepared with whom the actual internal interface morphologies can be observed. More details on this technique will be discussed in section 5.3.2.

3.6 Rapid thermal annealing

In section 2.4.1, the basic processes of thermal annealing and the dependence on the optical quality of dilute nitride containing samples were discussed. In this section, the technical implementation is considered. The easiest way of annealing samples is by application of annealing steps directly after the growth in the MOVPE reactor. More common is the use of a rapid thermal annealing apparatus (RTA). For some annealing experiments, a JetFirst 200C RTA is used. It features a sample chamber with water cooled metal walls. All heating is performed by infrared halogen lamps. The samples are placed face to face on a GaAs wafer, to avoid arsenic desorption out of the sample surface. The annealing chamber can be filled with N₂ as ambient gas. Besides that, no other gas ambients, like for example arsenic stabilization, can be applied. With this setup, quick heating and cooling ramps can be run. The heating rates are between 10 and 30°C/s, before the annealing temperature is reached, at which the temperature is stabilized for several seconds. Then, the reactor can be quickly cooled down in a timescale between 2-3 minutes, utilizing the cooling water, that cools down all walls, including the plate on which the sample is placed.

Reactor and RTA annealing offer different features. Reactor annealing can be conducted under arbitrary gas ambients, including TBAs stabilizations, while RTA annealing is limited to N₂. In contrast to that, RTA annealing offers quick temperature ramps that cannot be achieved inside the MOVPE reactor, because no cooling technique is implemented there.

3.7 Simulation of laser devices

For interpreting experimental results, it is sometimes beneficial to compare experimental findings with theoretical predictions. All presented experiment-theory comparisons are based on simulations conducted by Dr. Ada Bäumner. To obtain reasonable predictions, a fully microscopic many-body theory was used in the scope of the commercially available software Simulase. It takes many-body effects like electron-electron scattering into account and additionally radiative and non-radiative recombinations like Auger recombinations. Furthermore, charge separation effects in type-II structures are addressed by solving the Schrödinger-Poisson equation.

Besides these comparisons, band edge diagrams together with energetic positions of quantized states were calculated by Dr. Ada Bäumner using the Simulase software. In this case, the band edges are given for strained layers in growth direction.

Chapter 4 Epitaxial growth of single quantum wells

In the first part of this chapter the growth parameters of single quantum wells will be discussed for Ga(N,As), Ga(As,Sb), (Ga,In)As and (Ga,In)(N,As) in the compositional ranges necessary for the realization of type-II WQWH laser devices. All growth parameters were already well studied in detail in the literature and will only be illustrated with samples grown in the scope of this thesis. The second part specifically investigates the influence of antimony on the nitrogen incorporation into Ga(N,As) by discussing studies not available in the literature, carried out originally for this thesis.

For the growth of III/V alloys, the resulting solid composition depends strongly on the composition of the vapor phase. Generally, group V atoms exhibit a more considerable volatility on the growth surface, requiring an overpressure of the group V source molecules. The parameter that accounts for that is the V/III ratio, which should be above 1 for most growth processes. Under these conditions, all group III atoms that reach the surface are incorporated into the solid. The number of group III atoms that reach the surface is determined by the mass transport to the surface, which is directly linked to the partial pressures of the respective precursors. The solid composition of an alloy $A_{1-x}B_xV$ is therefore linearly linked to the gas phase composition constituted by the ratio of the precursors' partial pressures $P_p(A)/P_p(B)$.⁹⁵

$$k_{A_{1-x}B_xV} = \frac{x/(1-x)}{P_p(A)/P_p(B)} \quad (4.1)$$

The number $k_{A_{1-x}B_xV}$ is the proportionality factor and takes values of about 1 for typical cases but can be temperature dependent. The ratio of partial pressures is the parameter that determines the composition at the group III sublattice. For most compounds alloyed on the group V sublattice, the situation is more complex than that for the group III sublattice because thermodynamic effects determine the incorporation behavior and can no longer be described with a linear model.⁹⁵

As already outlined in previous chapters, the growth temperatures that can be employed depend on the choice of the precursor molecules for all constituent atoms and should be chosen high enough so the parasitic carbon incorporation due to alkyl groups is reduced.²¹⁵

Another important concept is the concept of surface reconstructions. Depending on the ambient conditions, the dangling bonds on the growth surface are rearranging in a favorable way in terms of the total surface energy. For typical growth conditions, a GaAs surface is adopting $c(4 \times 4)\beta$

reconstruction, which is arsenic rich. This reconstruction changes if specific precursors are supplied to the reactor and to the surface. In some cases, the surface reconstruction determines the incorporation behavior.²¹⁶

4.1 Gallium indium arsenide (Ga,In)As

The growth of (Ga,In)As is comparatively simple, since the alloying takes place at the group III sublattice. This means that the linear dependency given above can be taken for granted. Indium is a relatively heavy atom, and hence it tends to segregate on the growth surface^{183,217,218}, meaning that the indium profiles of the (Ga,In)As quantum wells will have the typical segregation profile.¹⁸³ During

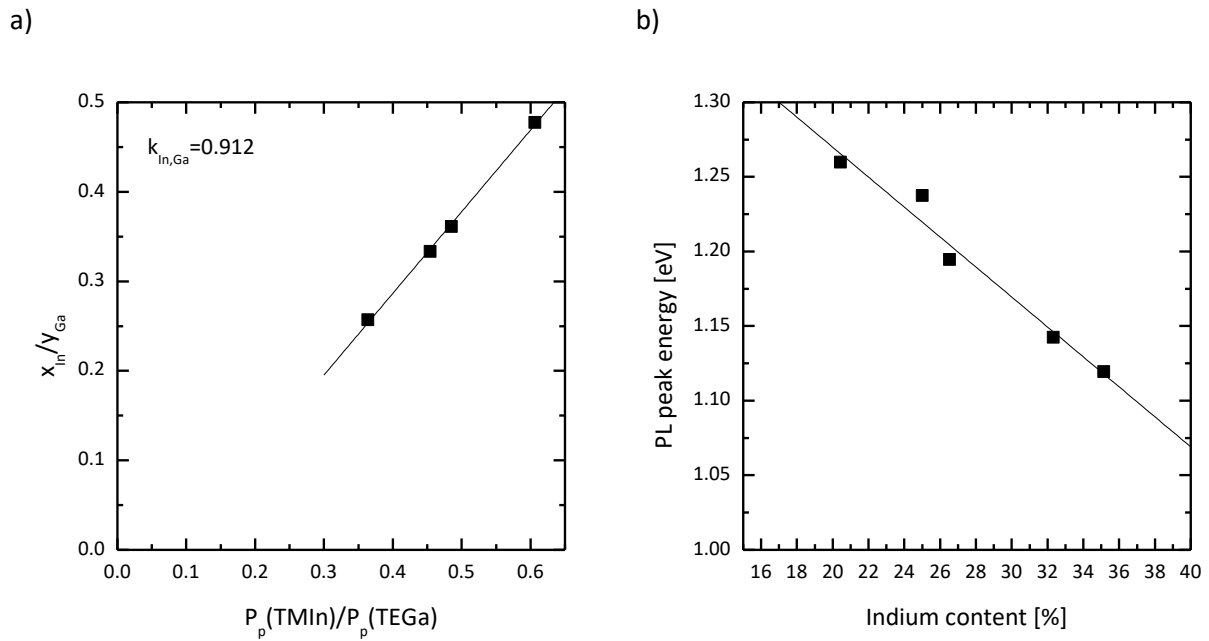


Figure 4.1 a) Solid phase ratio of indium to gallium as a function of the corresponding gas phase ratio. The samples show a linear dependency. b) The PL peak energy as a function of the indium content that was determined with HR-XRD. A redshift with increased indium content is visible. The line serves as a guide to the eye.

the epitaxial growth the indium incorporation increases slowly until the required indium surface coverage is reached. Then, the indium incorporation hits its intended value until the precursor supply is switched off. The remaining surface segregated indium is incorporated into the following layers until the surface is again totally depleted of indium atoms.

In order to adjust the growth parameters for a desired molar fraction, multiple type-I quantum well test samples were grown. The structures contain three repetitions of 5 nm thick (Ga,In)As quantum wells, separated by 50 nm GaAs barriers. A 50 nm GaAs cap layer capped the topmost quantum well. All quantum well and cap layers are grown at 550°C after the standard wafer treatment procedure described in section 3.1. The TMIn partial pressure was changed in the test structures while keeping

the TEGa and the TBAs partial pressures constant. Consequently, the TMIn/TEGa ratio and the V/III ratios are effectively changed for all samples. The TBAs/TEGa ratio is 5 for all samples, ensuring a sufficiently high TBAs supply for good growth quality without forming metallic droplets. Figure 4.1 a) relates the indium to gallium ratio in the solid phase, retrieved by HR-XRD simulations with diffractograms presented in Figure 4.2, to the equal ratio in the gas phase. A linear fit could be applied of which the slope was determined to be 0.912. This value corresponds to the proportionality factor $k_{In,Ga}$ and is below 1, suggesting that more gallium atoms are incorporated into the crystal than indium atoms if the supply is equal. This hints that a fraction of the supplied indium atoms segregates on the surface instead of being incorporated. The growth rate of the quantum well layers linearly depends on the TMIn supply and can be easily calculated by summing up the separate growth rates obtained if the other precursor would not be in the reactor at all:²¹⁹

$$v_{Ga,In} = v_{Ga} + v_{In} \quad (4.2)$$

All samples were characterized with photoluminescence spectroscopy. In Figure 4.1 b) the peak positions of all spectra are plotted as a function of the indium content. The spectra shift red with higher indium content, at 35% indium a PL emission wavelength of 1.12 eV can be observed. At 5 nm quantum well thickness, the quantization still plays a minor role for the transition energy.

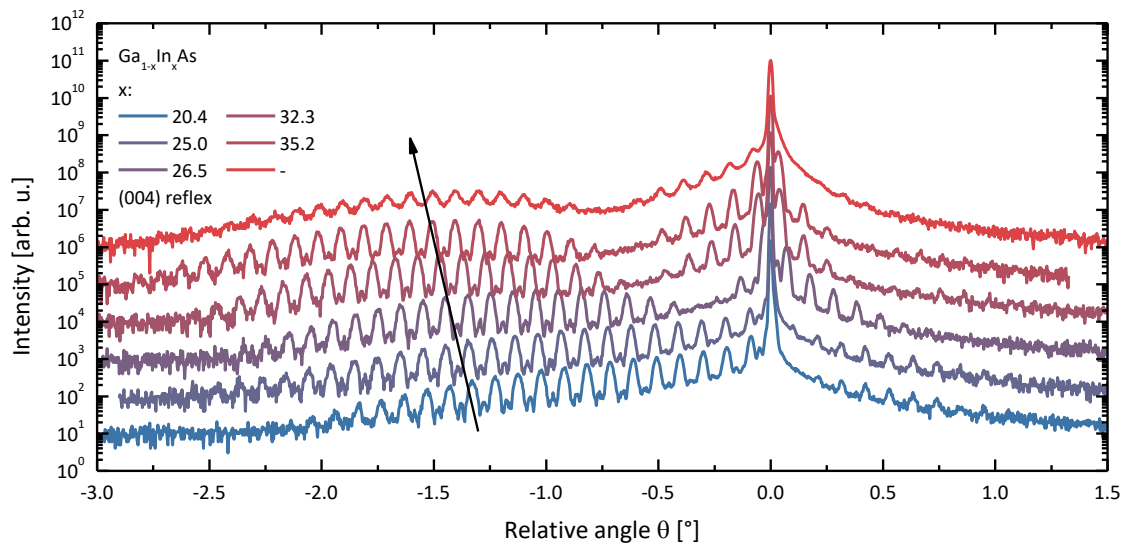


Figure 4.2 HR-XRD diffractograms of the investigated (Ga,In)As quantum well structures. On the compressive side on the left of the GaAs substrate peak, the diffraction peaks of the quantum well layers are prominently visible. With increasing indium content, the envelope of these peaks shifts to lower angles. The sample above the sample with 35% indium exhibits less distinct peaks than all other samples. This indicates excessive strain of the structure resulting in partly relaxation.

The HR-XRD diffractograms of all structures are displayed in Figure 4.2, which show a shift of the peak envelope to lower relative angles caused by the higher indium incorporation. The sample that

should contain the highest indium content has less distinct diffraction peaks compared to all other samples. In this sample, the strain energy exceeded the energy required for the formation of dislocations, causing the structure to partly relax. This illustrates that the emission wavelength of (Ga,In)As quantum wells is limited by strain. Incorporation of 28% indium leads to a lattice mismatch of 2%, according to equation 2.17, already.

4.2 Dilute incorporation of nitrogen into GaAs: gallium nitride arsenide Ga(N,As)

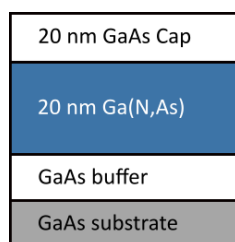


Figure 4.3 Schematic representation of the sample structures investigated in this section. A single 20 nm thick Ga(N,As) layer is grown on the 250 nm GaAs buffer layer. The structure is capped by a 20 nm GaAs cap layer.

The epitaxial growth of dilute nitride layers is challenging since the covalent radius and the electronegativity of the nitrogen atom differ drastically from those of arsenic or antimony atoms. Moreover, pure GaN exhibits a hexagonal lattice, while dilute nitrides are grown with a Zincblende structure. Therefore, being metastable, the alloying as a random alloy is difficult.⁹⁷

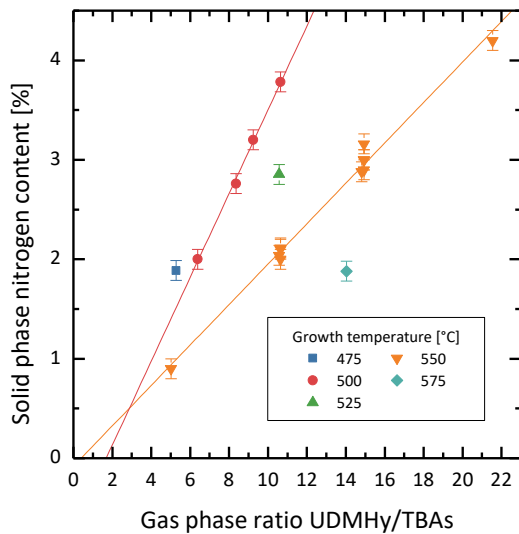
It is known to form chain like ordering of nitrogen. Additionally, the bonding of nitrogen with carbon is firm, which leads to parasitic carbon incorporation due to bonding to alkyl groups. More details regarding dilute nitrides can be found in section 2.4.

In this section the nitrogen incorporation behavior will be studied. Since the nitrogen content determination accuracy should be maximized, 20 nm thick Ga(N,As) layers are chosen as sample structures, schematically illustrated in Figure 4.3. A 20 nm GaAs cap layer caps the Ga(N,As) layer. The layer thicknesses were obtained by measuring the HR-XRD diffractograms around the GaAs (004) reflection peak and fitting a dynamical simulation to the measurement.

The electric properties of dilute nitride compounds were already discussed in detail in section 2.4. Hence, in this section it must only be noted that 5% of nitrogen introduces a lattice mismatch of only 1%. However, at these 5% already, a strong band gap reduction can be observed. Compared to Ga(As,Sb) and (Ga,In)As quantum wells, Ga(N,As) quantum wells enable the most substantial reduction of the band gap energy while inducing the weakest strain.

4.2.1 Dimethylhydrazine (UDMHy) as nitrogen source

a)



b)

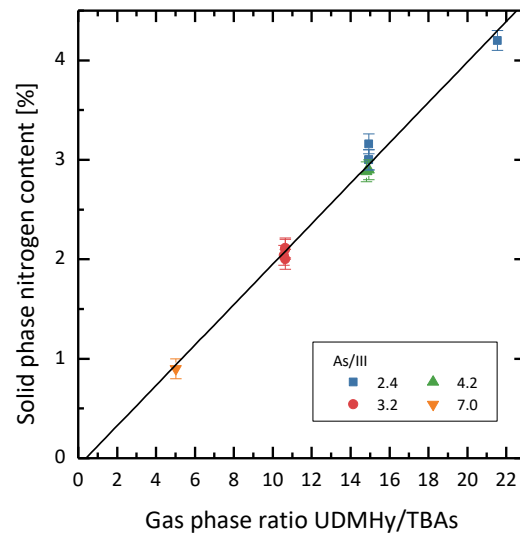


Figure 4.4 a) Solid phase nitrogen content as a function of the gas phase ratio of UDMHy to TBAs for growth temperatures between 475°C and 575°C. For all temperatures the relation between gas and solid composition is linear. b) Solid phase nitrogen content as a function of the gas phase ratio of UDMHy to TBAs for different As/III ratios. The solid phase nitrogen composition is only dependent on the UDMHy/TBAs ratio, not on the As/III ratio.

The standard nitrogen precursor is 1,1-dimethylhydrazine (UDMHy). A discussion of this precursor can be found in section 3.1.1. All samples were grown with a constant TEGa partial pressure of 7.09E-03 mbar and varying partial pressures of TBAs and UDMHy. The nitrogen incorporation as a function of the gas phase ratio of UDMHy/TBAs is plotted in Figure 4.4 a) for different growth temperatures and b) for different As/III ratios. The error of the nitrogen determination was estimated to be 0.1%. All investigated temperatures show a linear dependency of the solid phase nitrogen content and the gas phase ratio of UDMHy/TBAs^{219,220} which hints that the competition of group V atoms determines the composition of the solid. For 1% nitrogen incorporation an UDMHy/TBAs ratio of approximately 6 must be set, which means that the number of UDMHy molecules must be six times higher than that of TBAs molecules even to achieve only 1% of nitrogen incorporation, highlighting that the overall incorporation efficiency of UDMHy is low.

This efficiency gets even worse if the growth temperature is increased^{221,222}. No change in nitrogen incorporation should be expected when changing the As/III ratio while letting the UDMHy/TBAs ratio constant. This is what can be seen in Figure 4.4 b), in which the solid phase nitrogen content is plotted as a function of the gas phase ratio UDMHy/TBAs for different As/III ratios.²²⁰

Because of the incongruent evaporation of group V and III atoms, the group V partial pressure must be set higher than the group III partial pressure. For Ga(N,As) growth with UDMHy it is reasonable to introduce the As/III ratio as growth parameter²²³ since the partial pressure of UDMHy would be

higher than the group III partial pressure, even if the growth is gallium rich. To ensure random alloying, a large As/III should be chosen. However, to maintain the target nitrogen incorporation, the UDMHy/TBAs ratio must be constant, resulting in a drastic increase of the UDMHy partial pressure. Due to the low incorporation efficiency, the gas phase is dominated by UDMHy leading to unwanted effects during the growth in the gas phase as well as on the surface.

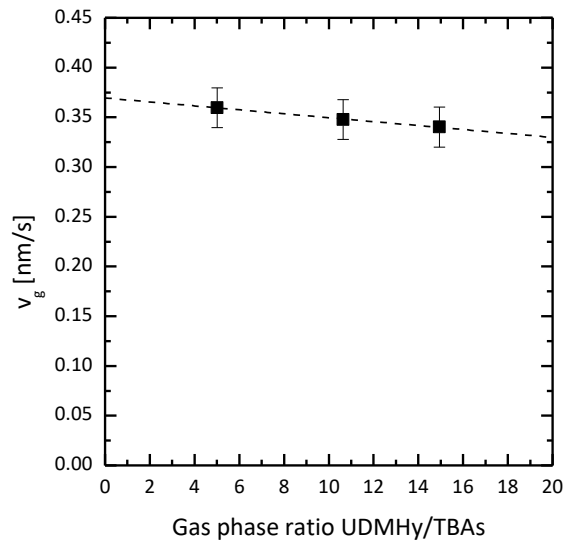


Figure 4.5 Growth rate of Ga(N,As) grown at 550°C in dependence on the UDMHy/TBAs gas phase ratio. Overall, the growth rate decreases with increased UDMHy/TBAs ratio. This can be explained by etching of the surface by UDMHy.

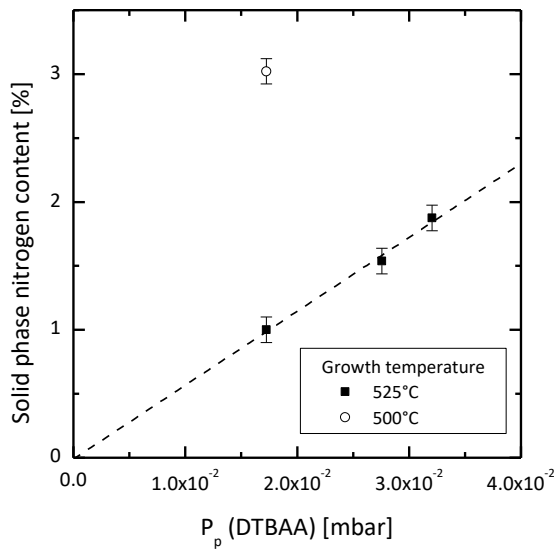
When changing the amount of UDMHy inside the reactor, the growth rate is changed. The growth rate of the samples grown at 550°C are plotted as a function of UDMHy/TBAs in Figure 4.5 and a linear decrease with increasing UDMHy/TBAs ratio can be seen. This is contrary to the fact that for most III/V MOVPE growth only the supply of group III precursor molecules determines the growth rate, while the group V supply shows no influence. The reason for the growth rate reduction can be found in the formation of N_2 as a decomposition product of UDMHy. Due to the high UDMHy partial pressure, a high concentration of N_2 can be found near the growth surface. As pure N_2 as carrier gas reduces the growth rate in comparison to H_2 , the growth rate gets reduced with increasing N_2 gas phase content.²¹⁹

The influence of UDMHy on the surface reconstruction was investigated for example by Maßmeyer et al.²¹⁶ The authors stated that a GaAs surface exhibits typically an arsenic rich $c(4 \times 4)\beta$ surface reconstruction at ordinary growth temperatures, but changes to a $(2 \times 6)/(6 \times 6)$ surface reconstruction that is much more gallium rich during Ga(N,As) deposition. Depending on the N/As ratio, the surface reconstruction is a linear combination of these two reconstructions. This was attributed to the enhanced arsenic desorption under UDMHy ambient or the incorporation of nitrogen into the

surface reconstruction. The authors summarize that nitrogen incorporation strongly depends on the surface reconstruction. Other authors came to similar conclusions, using different techniques.²²⁴

4.2.2 Di-*tert*-butyl-amino-arsane as nitrogen and arsenic source

a)



b)

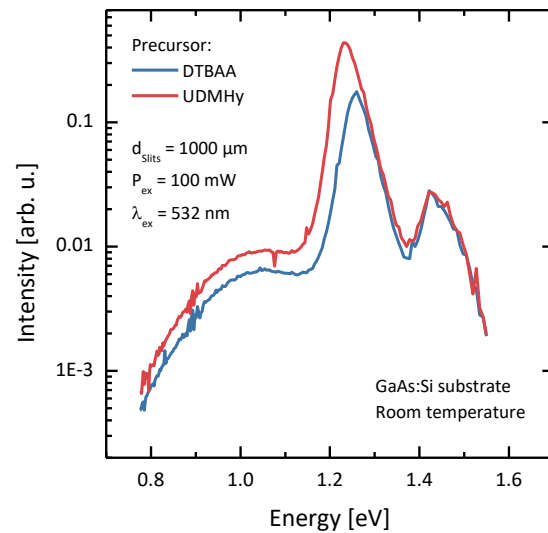


Figure 4.6 In a) the nitrogen content of the investigated Ga(N,As) samples is given as a function of the DTBAA partial pressure. A linear fit describes all 525°C data points well. The nitrogen incorporation depends strongly on the growth temperature, the sample grown at 500°C exhibits a significantly larger nitrogen content than the sample grown at 525°C. Figure b) shows PL spectra of two similar samples, grown with DTBAA and UDMHy. The UDMHy grown sample shows a superior intensity.

As alternative nitrogen precursor for Ga(N,As) growth, the novel precursor Di-*tert*-butyl-amino-arsane (DTBAA) can be utilized, bringing the advantage that no direct nitrogen-carbon bond is present, which should lead to a reduced carbon incorporation. Additionally, the nitrogen incorporation was shown to be much more efficient compared to UDMHy and the partial pressures used for DTBAA are comparable to other precursors making it not as influential in the gas phase as UDMHy. Besides from nitrogen, DTBAA also contains an arsenic atom. Hence, no further arsenic precursor must be used in order to grow Ga(N,As). The nitrogen incorporation was found to be linearly dependent on the DTBAA partial pressure. The growth rate is not influenced by the DTBAA supply.²²⁵

In Figure 4.6 a) the solid phase nitrogen content is plotted with respect to the DTBAA partial pressure for 500°C and 525°C. In principle higher growth temperatures are also possible, but due to the small vapor pressure, unreasonably high source flows must be applied to achieve nitrogen contents up to 3% at elevated temperatures. A linear dependency is observed between the DTBAA partial pressure

and the nitrogen incorporation. Similar to the incorporation behavior of UDMHy, the incorporation efficiency increases exponentially with a lower growth temperature.²²⁵

Since DTBAA is a novel precursor that is not yet produced in industry scale production plants, it still contains a large number of impurities like oxygen atoms. These impurities will reduce the optical quality of the finished sample structures. Similar carbon incorporation was found, when the carbon incorporation induced by UDMHy and DTBAA was compared, which was attributed to contaminations.¹³⁸ In Figure 4.6 b) a PL spectrum of an UDMHy grown sample is compared to a PL spectrum of a DTBAA grown sample. The UDMHy grown sample shows a better intensity, although it also shows a longer wavelength, indicating a slightly larger nitrogen content. This verifies the worse purity of the novel precursor. However, the peak intensities of both samples are still in the same order of magnitude, implying at least similar optical material qualities.

If DTBAA is used as nitrogen precursor, the surface reconstruction also changes to a (2x6)/(6x6) reconstruction. However, the transition is shown to be much more efficient than UDMHy, meaning that the amount of DTBAA supplied to the surface can be much less for the surface reconstruction to change.²²⁶

4.2.3 Nitrogen profiles in thin quantum wells

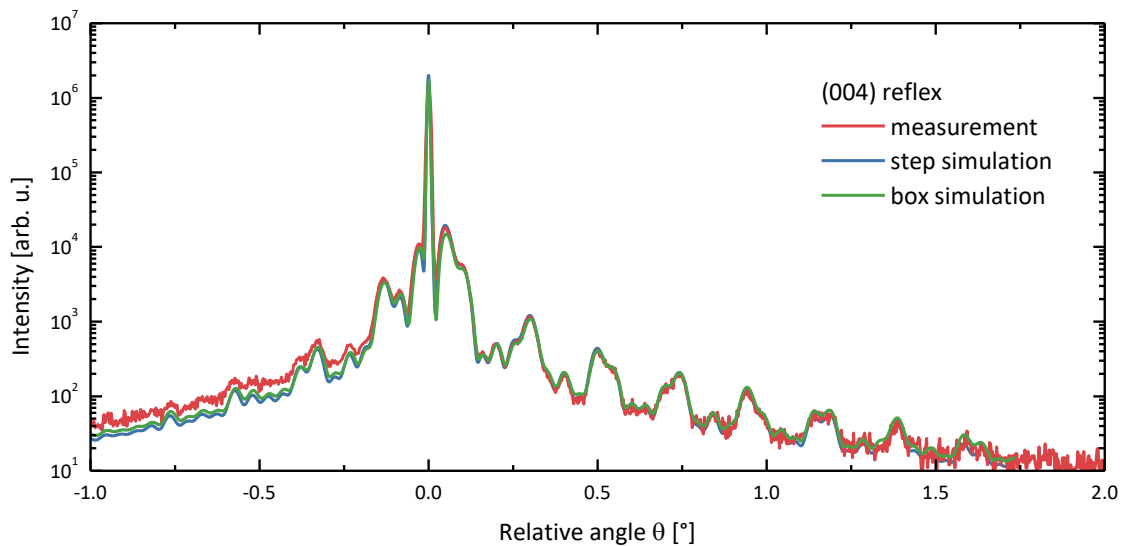


Figure 4.7 HR-XRD diffractogram measured for the Ga(N,As) quantum well sample. The green curve represents a simulation based on a box-like shape of the nitrogen composition. The blue curve is the simulation based on multiple 0.5 nm thin Ga(N,As) layers stacked for forming the full Ga(N,As) quantum well. Each has a different nitrogen content determined by the novel EFSTEM technique, developed and conducted by Saleh Firoozabadi.

So far only 20 nm thick Ga(N,As) layers were investigated. If the thickness is reduced, effects at the interface play a more significant role. Thus, the effect of thickness reduction will be analyzed in this section. The sample investigated for this purpose was grown at 550°C with UDMHy as nitrogen

precursor. 3 nm thin Ga(N,As) quantum well layers embedded in GaAs barriers with 20 nm thickness were repeated three times and capped with 60 nm GaAs. The TBAs/TEGa ratio of 1.8 was relatively low and the UDMHy/TBAs ratio was about 19.2.

In Figure 4.7 the HR-XRD diffractogram of this sample is shown in red. As expected, the diffraction peaks emerge on the tensile side on the right of the substrate peak. A standard box-shaped nitrogen composition profile is assumed for the fit simulation shown in green. The simulation fits well and shows only minor differences to the measurement in the range of the expected errors. The nitrogen composition and the Ga(N,As) layer thickness obtained by this simulation are 4.9% N and 2.8 nm, respectively. The error in nitrogen composition determination should be considered as high since the layer thickness is low and slightly changing the nitrogen content of the simulated structure only insignificantly changes the diffractogram. Given the growth parameters, the composition is expected to be about 4% compared to the 20 nm thick samples analyzed in section 4.2.1.

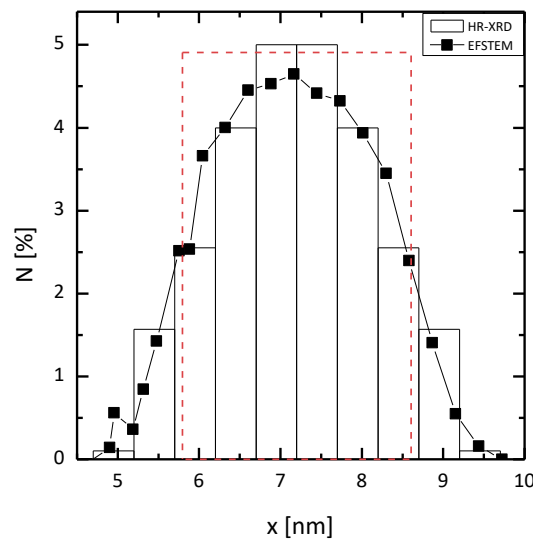


Figure 4.8 Compositional profile obtained by EFSTEM measurements. The dashed red profile indicates the box profile assumed for the HR-XRD simulation. The black boxes show the compositions of the thin stacked Ga(N,As) layers used for the graded simulation. It fits well to the profile obtained by EFSTEM.

Energy filtered scanning transmission electron microscopy measurements (EFSTEM) and quantitative determination of the nitrogen content in each atomic column were performed by Saleh Firoozabadi. This technique is still in an experimental stage and further details will be delivered in Saleh Firoozabadi's work. It allows the examination of a nitrogen content profile as a function of the position in growth direction. The result is shown in Figure 4.8 together with the compositional profiles obtained by box-shaped and graded HR-XRD simulations. The profile obtained by EFSTEM shows the formation of a strong gradient and an almost gaussian-shaped profile differing strongly from the box shape. The graded HR-XRD simulation fits very well with the EFSTEM profile. Given that

the graded HR-XRD simulation also nicely fits the measurement, the nitrogen content of the given quantum well should be assumed to be graded.

The nitrogen profile evidences a symmetric gradient in both growth directions with a peak nitrogen content in the center of the quantum well. This is not intuitive from the epitaxial point of view since both interfaces exhibit a similar nitrogen profile. Generally, graded interface profiles occur for example in alloys with antimony because antimony atoms segregate on the growth surface and the typical segregation profile appears in the chemical composition profile. However, in this kind of profile both heterointerfaces are different¹⁸³. Therefore, an explanation that is not related to the gas switching during the MOVPE process is conceivable. For instance, thermodynamically induced clustering of nitrogen atoms could be an explanation. Due to diffusion, nitrogen clusters and chains could be formed with a higher probability in the center of the quantum well. These clusters raise the average nitrogen content per atomic column determined for the quantum well center. Similar nitrogen profiles were already presented in the literature for annealed Ga(N,As) sample¹⁵.

The main result of this short discussion is that the composition profile of thin Ga(N,As) quantum well layers can only be approximated by HR-XRD measurements and nitrogen composition changes drastically over the full quantum well.

4.3 Gallium arsenide antimonide Ga(As,Sb)

The growth of antimony containing alloys proves to be challenging. Due to the large size of the antimony atoms, they are well known for segregating on the growth surface for MOVPE^{205,227–230} and MBE²³⁰ growth, where they show a low volatility meaning that the duration for total desorption required for one full antimony layer is high.

The volatility is so low that Ga(As,Sb) can be grown by depositing antimony atoms on the growth surface during a growth pause and overgrowing these with GaAs. The surface reconstruction changes because of the antimony segregation to a (3x8) reconstruction. This means that the surface is antimony terminated, and arsenic dimers are reduced while antimony dimers are formed.²²⁹

Almost all antimony alloys are unstable under thermodynamic aspects and the growth must be carried out far from equilibrium conditions but still at comparably low temperatures between 350°C and 600°C. Due to the low solubility, phase separation and ordering can be observed.²⁰⁵ TESb is employed for Ga(As,Sb) growth in this work. Important growth parameters for Ga(As,Sb) are the Sb/V ratio and the V/III ratio. The Sb/V ratio describes the TESb antimony precursor partial pressure fraction of all group V precursors' partial pressures.^{231,232}

$$\text{Sb/V} = \frac{P_p(\text{TESb})}{P_p(\text{TESb}) + P_p(\text{TBAs})} \quad (4.3)$$

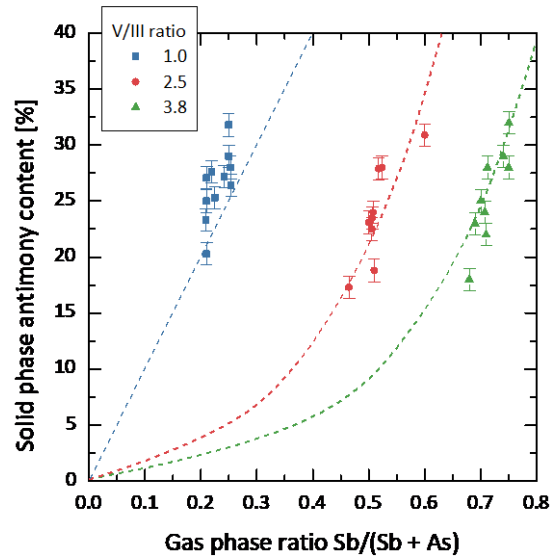


Figure 4.9 Solid phase antimony content as a function of the Sb/V ratio for three different V/III ratios. With higher V/III ratio the antimony incorporation efficiency is reduced drastically. The best efficiency can be obtained if a V/III ratio of 1 is employed, for which the solid phase antimony content shows a linear dependency on the gas phase composition. All solid lines serve as guides for the eye.

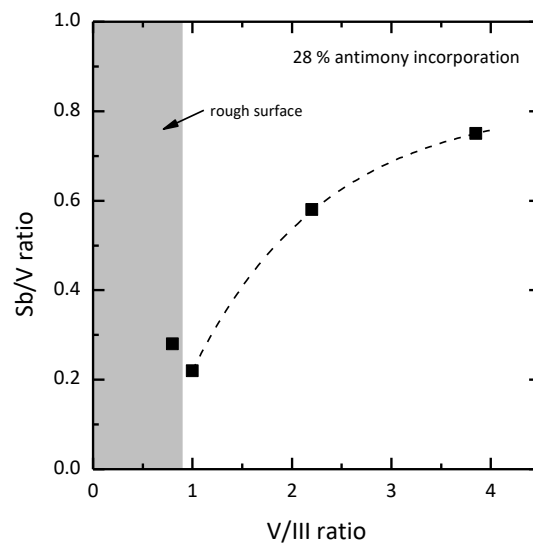


Figure 4.10 The Sb/V ratio required to obtain an antimony content of 28% as a function of the V/III ratio. V/III ratios below 1 result in metallic gallium droplets on the surface and, hence, insufficient material quality. A V/III ratio of 1 can be used if the highest antimony incorporation efficiency is needed. The incorporation efficiency quickly decreases with increasing V/III ratio but the reduction is saturated with higher V/III ratio.

To adjust the Sb/V and the V/III ratio, multiple samples with several Ga(As,Sb) quantum wells divided by 20 nm GaAs barriers and capped by 60 nm GaAs cap layers are deposited. The quantum well layer thicknesses vary in a range between 3 nm and 6 nm and the number of repetitions between 3 and 5. The structural analysis is done by HR-XRD simulation with an accuracy of approximately $\pm 1\%$ antimony. In Figure 4.9 the solid phase antimony content as a function of the Sb/V ratio reveals a strong dependency on the V/III ratio. A V/III ratio of 1 means, that an equal amount of group V precursor is supplied to the reactor as it is for the gallium precursor. Thus, as a good approximation all supplied atoms get incorporated into the crystal. As a result, the given incorporation relation is a straight line and the solid and vapor composition is equal, as it is the case for alloys on the group III sublattice like (Ga,In)As. If the V/III ratio is increased, thermodynamic effects come into play and the straight line becomes what is depicted as the green and the red curve. The antimony incorporation efficiency decreases strongly with increased V/III ratio and an unproportional amount of antimony precursor must be supplied in order to achieve significant solid composition. In Figure 4.10 the Sb/V ratio that must be adjusted for a given V/III ratio to obtain 28% antimony composition in the solid is shown. For V/III ratios below 1, excess gallium segregates on the growth surface and metallic gallium droplets form. This results in a deterioration of the sample quality which is indicated by rough surfaces. At V/III ratio of 1, the surface looked smooth, and an excellent layer quality can be assumed. If the V/III ratio is raised, the Sb/V ratio which is needed to achieve 28% of antimony is rapidly increasing saturated with higher V/III ratios. For the highest V/III ratio investigated in this sample series, the group V gas phase consisted of up to 75% of antimony precursor while only incorporating 28% into the solid.

For the sake of incorporation efficiency, lower V/III ratios should be preferred. The dependence of the optical quality on the V/III ratio will be investigated later in this work in the framework of type-II structures.

In MBE and in MOVPE growth processes that aim for thin quantum wells consisting of antimony containing alloys, the compositional abruptness must be considered. Due to antimony segregation effects the compositional profile will resemble the typical segregation profile.^{233,234}

Also, arsenic and antimony exchange processes are reported to be an issue but will be discussed in depth at a later stage in this work.²³³

In the end it should be noted that the antimony incorporation behavior depends strongly on the temperature. This means, that the antimony incorporation is different for differently doped GaAs wafers and changes with the wafer size due to the temperature calibration method. Additionally, the composition can significantly vary over the wafer due to slight temperature gradients. All these effects require careful readjustment of all growth parameters separately for each epitaxy session.

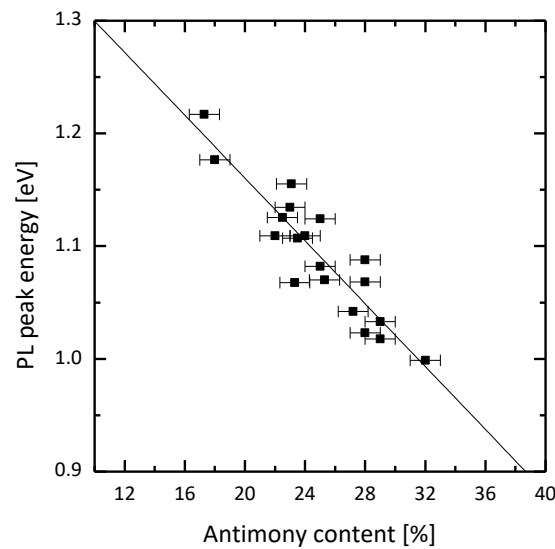


Figure 4.11 PL peak energies of the Ga(As,Sb) transition for several samples containing Ga(As,Sb) quantum wells. The straight line serves as a guide to the eye.

In Figure 4.11 the transition energies obtained by PL spectroscopy of the samples discussed in Figure 4.9 are plotted as a function of the antimony content. All investigated samples contained quantum wells of different widths, which adds a variety of quantization energies to the band gap transition energies. Therefore, the PL peak energies given in the figure are only a measure of the wavelengths that can be achieved with Ga(As,Sb) quantum wells. It can be seen that a PL peak energy of up to 1 eV can be reached if antimony contents of 32% are employed. However, the lattice mismatch at 32% antimony corresponds already to 2.5%. A mismatch of 2% is reached at antimony contents of 26%. Consequently, a slightly larger fraction of indium can be incorporated into GaAs compared to antimony, however, a longer wavelength can be achieved with Ga(As,Sb) at equal lattice mismatch values. Thus, Ga(As,Sb) gained attention for laser applications but due to a low barrier height in the conduction band, these lasers could not be brought into production.³⁸

4.4 Quaternary material: gallium indium nitride arsenide (Ga,In)(N,As)

The last III/V compound semiconductor described in this chapter is (Ga,In)(N,As). In the past a lot of effort has been made to grow this material in high quality, because it is highly intriguing for long wavelength applications like diode lasers⁵⁹. Additionally, it can be deposited lattice matched on Ge substrates to realize the 1 eV absorption layer of solar cells¹³⁸.

It was shown that the band gap reduction of (Ga,In)As is limited by strain¹⁸. A possibility to further increase the emission wavelength is to incorporate nitrogen into (Ga,In)As, to form the quaternary alloy (Ga,In)(N,As) while reducing the overall strain²³. When growing this alloy with MOVPE, a strong

reduction of the nitrogen uptake is unavoidable. This reduction depends exponentially on the growth temperature and the indium content, when UDMHy and TMIn are utilized as precursors for nitrogen and indium^{223,235}. The reason is not apparent yet, but several explanations were given in the literature. The most obvious cause is gas phase reactions between the NH_2 and the CH_2 radicals, which arise as decomposition products from UDMHy and TMIn, respectively. However, this claim is easily falsified by the fact that the use of TMGa as gallium precursor does not show a reduction of nitrogen incorporation, compared to TEGa²²³. Surface processes give another explanation. Indium is well known to segregate on the surface, producing the common segregation profile in the indium incorporation. This means, that the surface reconstruction during the growth is changed by indium atoms, causing already a reduction of the nitrogen content, which is highly sensitive to the surface reconstruction²²⁴. The In-N bond is weaker than the Ga-N bond, which could induce nitrogen desorption if the surface is indium terminated and which corroborates this surface explanation²²³. On the surface, the nitrogen atoms were proposed to diffuse and interact with multiple indium atoms, increasing the strength of the desorption effect²²³. However, these explanations seem to disagree with the findings of other authors, who show that the nitrogen incorporation into (Ga,In)As is not affected if DTBAA is employed as nitrogen precursor¹³⁷, or if the epitaxial growth is conducted with other epitaxy techniques like MBE^{51,236}. Overall, the reason for reduced nitrogen incorporation into (Ga,In)(N,As) found in MOVPE growth is not yet fully understood.

F. Höhnsdorf and other authors propose a critical nitrogen content, which depends on the indium content and is well above 2%. Above this nitrogen content, the structure begins to deteriorate, which seems to be a self-sufficient process since it prevails for lattice matched samples. He additionally stated that the indium content does not change if nitrogen is incorporated. This assumption will be accepted for all experiments regarding (Ga,In)(N,As) in this work.^{219,223}

The most critical parameter for (Ga,In)(N,As) growth is the N/As ratio, corresponding to the UDMHy partial pressure divided by the arsenic partial pressure. For significant nitrogen incorporations, this gas phase ratio must be chosen to be very large.²²³

The HR-XRD results obtained for (Ga,In)(N,As) test structures grown at 525°C with 7 nm quantum well thicknesses and three repetitions are plotted in Figure 4.12. The TMIn/TEGa vapor ratio was chosen to be 0.4 for all samples, resulting in an indium uptake of 25%. If the N/As ratio is raised, the solid phase nitrogen content increases exponentially²¹⁹. However, the exponential dependency between nitrogen incorporation and the growth temperature as well as the indium content must be additionally considered. To adjust the indium and the nitrogen content for a specific growth temperature, the first step is to adjust the indium content of (Ga,In)As under consideration of the As/III ratio, according to section 4.1. Then, the N/As ratio must be adjusted until the intended

nitrogen content is reached. Since (Ga,In)(N,As) is a quaternary material, HR-XRD measurements are not distinct, and no change of the indium content must be assumed when determining the nitrogen content.

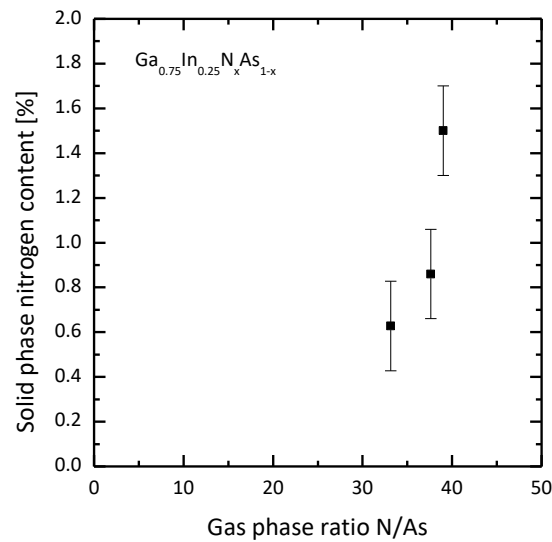


Figure 4.12 Relation between the solid phase nitrogen composition and the gas phase composition resembles an exponential function.

As mentioned above, the nitrogen incorporation is not affected by indium if DTBAA is used as nitrogen precursor. If a DTBAA partial pressure of $3.2\text{E-}2$ mbar replaces the UDMHy and TBAs supply with otherwise the same growth parameters like in the samples above, a nitrogen content of 1.9% is determined by HR-XRD. The measured diffractogram and the respective fit are plotted in Figure 4.13. The simulation fits well to the measurement, indicating that the sample contains 1.9% nitrogen. This value is also expected for this partial pressure for Ga(N,As) growth. Hence, the nitrogen incorporation is verified to remain constant under the presence of indium, compared to Ga(N,As), when using DTBAA as precursor.

In section 2.4.1 the paramount importance of annealing for (Ga,In)(N,As) samples was outlined, which drastically improves the optical quality of these structures by improving the distribution of atoms.

(Ga,In)(N,As) quantum wells are typically compressively strained, considering the commonly utilized nitrogen and indium fractions. As already mentioned, 5% nitrogen introduce a lattice mismatch of only 1% in GaAs. However, the common nitrogen contents in (Ga,In)(N,As) are expected to be in the range between 1 and 2%, causing a much lower tensile strain. The largest possible indium content should be used to achieve the lowest possible band gap while avoiding nitrogen induced defects. Hence, indium contents of about 28% are used, exhibiting already a lattice mismatch of 2%.

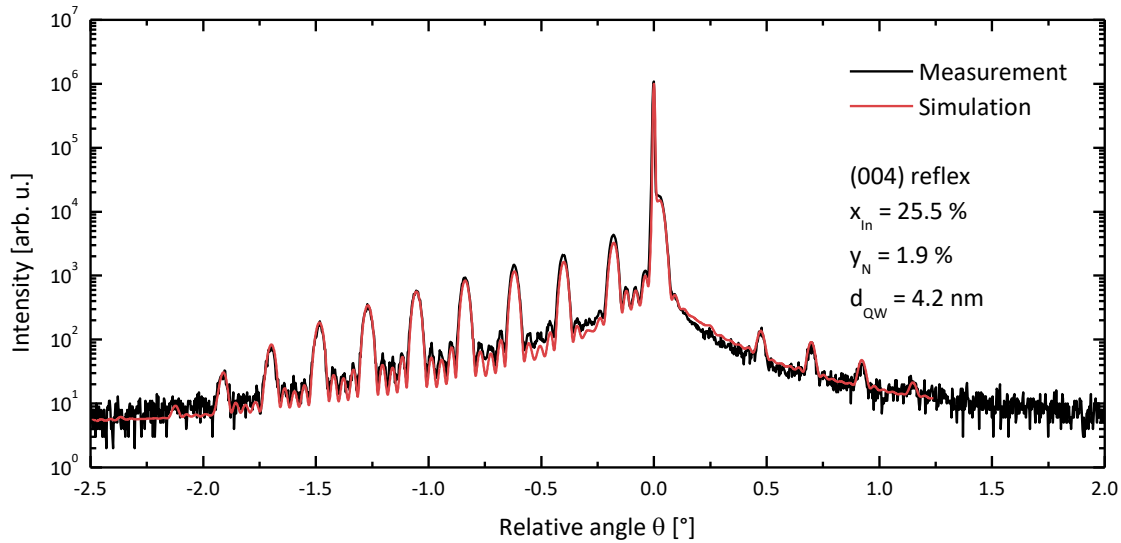


Figure 4.13 HR-XRD of a triple (Ga,In)(N,As) quantum well structure. The sample features equal growth parameters as the sample presented in Figure 4.12. However, as nitrogen and arsenic precursor DTBAA was chosen.

4.5 Influence of antimony on nitrogen incorporation into Ga(N,As)

Before discussing the growth of full WQWH, the incorporation behavior of nitrogen into GaAs under the influence of antimony must be examined. From the literature it is well known that nitrogen incorporation gets drastically reduced when heavier atoms like antimony or indium are present and UDMHy is used as nitrogen precursor²³⁷. To overcome the mentioned problems caused by this fact, the reason for this behavior is studied in the following sections. The first section will deal with the gas phase effects that are already postulated but not understood in the literature²³⁸. In the following section the dependency of the nitrogen content with the antimony surface coverage is studied for two different nitrogen precursors. In the end all results are discussed and strategies to tackle these growth problems are proposed.

4.5.1 Gas phase effects

During the investigation of Ga(As,N,Sb) as active material for laser devices, a strong reduction of the nitrogen incorporation was found, if TESb was supplied as antimony precursor and UDMHy as nitrogen precursor²³⁸. When the authors of that study applied TMSb instead of TESb, they declared, that the nitrogen incorporation increases. For both precursor combinations, they showed a shift to smaller lattice constants, if UDMHy was additionally supplied, indicating either less antimony incorporation or increased nitrogen incorporation. The PL emission wavelength shifted blue for the TEGa/TESb combination and red for the TMGa/TMSb combination. They concluded that the TEGa/TESb sample reduced its antimony incorporation, while the TMGa/TMSb sample incorporated

nitrogen, due to gas phase effects. In other papers, this effect was confirmed^{52,239}. However, no real explanation was given besides that, and these experiments could not be reproduced in our reactor. Other authors claimed an improved nitrogen content when TriSb was used as antimony precursor^{240,241}. Indeed, they did not show convincing proof in their paper. The in-situ mass spectrometer setup was utilized to investigate these gas phase effects further. It is based on a quadrupole ion trap mass spectrometer from Carl Zeiss SMT GmbH, which functions as a Paul trap. A Paul trap confines ions into it by applying an oscillating electric field. A quartz nozzle aspirates process gas several millimeters above the susceptor into the mass spectrometer. More technical details can be found in the literature^{226,242}. The frequency response of the moving ionized molecules inside this Paul trap indicates the mass of these molecules.

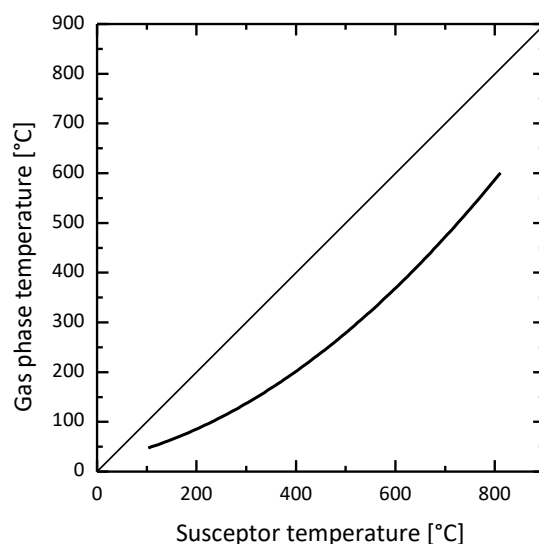


Figure 4.14 Calibration curve which gives the gas phase temperature at the position of the nozzle entrance as a function of the susceptor temperature. Using this curve, exact decomposition temperatures can be determined.

Before discussing gas phase measurements, the ambient conditions and the preconditioning of the reactor and the nozzle are discussed. The temperature differs strongly with the position in the reactor. Therefore, calibration measurements were carried out, where the well-known decomposition products of TBAs were used to find the gas temperature at the position of the nozzle entrance. The calibration curve is given in Figure 4.14. At susceptor temperatures of 800°C, gas phase temperatures of about 600°C can be expected.

Since the decomposition behavior of metal organic precursors was proven to depend strongly on catalytic surface effects, the quartz nozzle must be overgrown with GaAs for realistic decomposition experiments. As the temperature in the reactor changes with the position, the decomposition observed with mass spectrometry takes place at the nozzle. Prior to the decomposition experiments

the reactor was heated to a susceptor temperature corresponding to a gas phase temperature at the nozzle of about 625°C. Then, TEGa and TBAs were supplied into the reactor with typical partial pressures and several nanometers of GaAs were deposited on the nozzle. To control the effect of this deposition, tiny flakes of the grown material were scraped off with a tweezer and investigated with a scanning electron microscope (SEM) and EDX together with Johannes Glowatzki. The result can be seen in Figure 4.15.

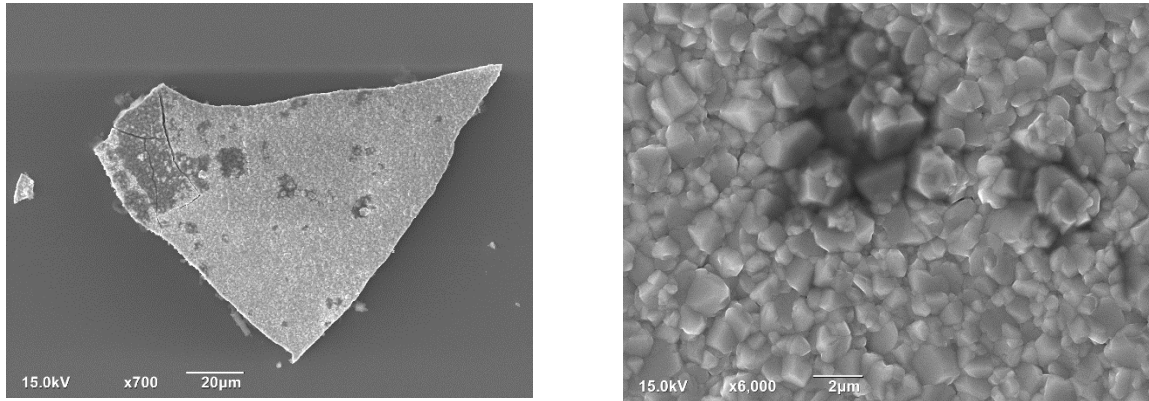
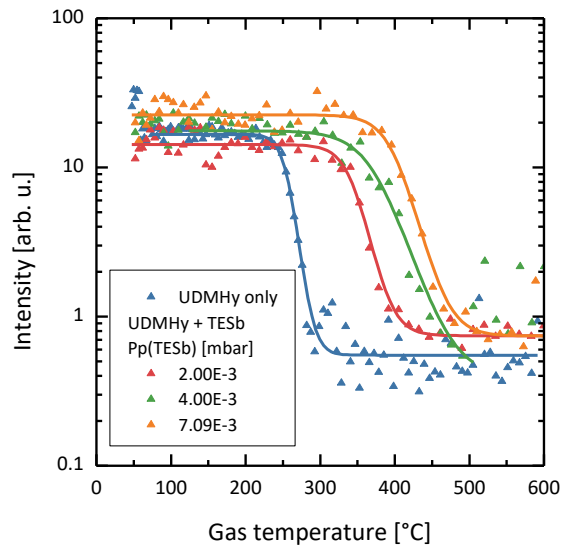


Figure 4.15 SEM images taken from tiny flakes of material deposited on the mass spectrometer nozzle. EDX analysis revealed that polycrystalline GaAs was deposited. Images taken together with Johannes Glowatzki.

a)



b)

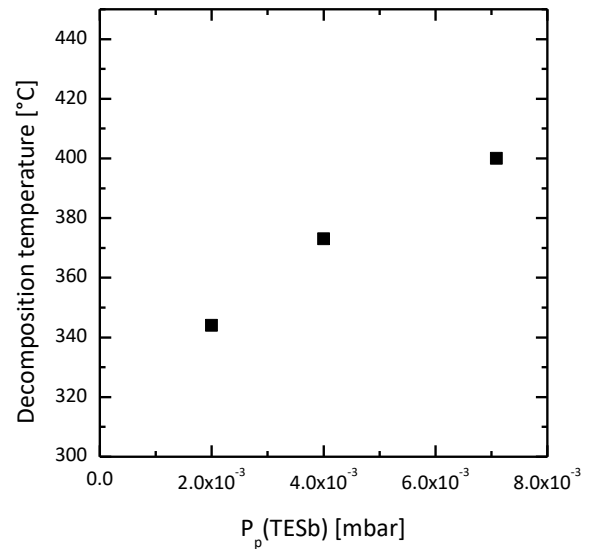


Figure 4.16 In a) the decomposition curves of UDMHy (61 u). They are formed by measuring the signal obtained by the mass spectrometer for the given atomic mass as a function of the gas temperature. In b) the decomposition temperature of UDMHy is plotted with respect to the TESb partial pressure. It shifts to higher temperatures with increasing TESb partial pressure.

The material deposited turned out to be polycrystalline GaAs which means that all possible microscopic surface orientations are present on the macroscopic surface. This implies that only averaged surface effects can be considered with this kind of experiments. However, the results

obtained with deposited polycrystalline GaAs should be much more realistic compared to the plain quartz glass nozzle.

To investigate the influence of TESb on the UDMHy decomposition, four decomposition curves are measured for different process parameters. First, only UDMHy was led into the reactor with a partial pressure of $4\text{E-}2$ mbar. The mass spectrometer detected molecules with an atomic mass of 61 u, which corresponds to the full UDMHy molecule. The reactor temperature was slowly ramped up to 800°C , which is 600°C in the gas phase at the nozzle position. For these conditions, a decomposition temperature at which half the molecules decompose of 255°C was determined, which is much lower compared to the value of 440°C given in the literature²²⁶. This deviation in temperature could be caused by multiple reasons. For example, the gas temperature calibration could be wrong or catalytic effects on GaAs surfaces could lower the decomposition temperature.

When TESb is added during this experiment, the decomposition curve shifts to higher temperatures, depending on the TESb partial pressure, up to 150 K limited only by the measured range of TESb partial pressures.

The determined decomposition temperatures may not be correct. However, the qualitative trend towards higher decomposition temperatures is significant. This shift could be explained by different surface reconstructions depending on the antimony surface configuration. It seems like the UDMHy decomposition process is taking place on the growth surface and hence, is highly dependent on the surface. This finding agrees with literature results, in which a surface sensitivity of the nitrogen incorporation was observed²¹⁶.

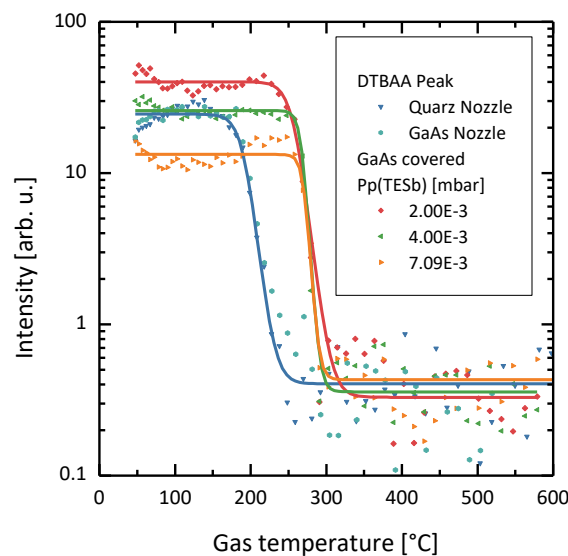


Figure 4.17 Decomposition curves of DTBAA with different TESb supply. The decomposition temperature remains equal if the surface is changed from quartz to GaAs. It shifts to higher temperatures if TESb is added.

Similar experiments were carried out with DTBAA instead of UDMHy, tracking the DTBAA mass of 205 u. The respective decomposition curves are depicted in Figure 4.17. For DTBAA measured on GaAs and quartz surfaces, a decomposition temperature of 195°C was obtained, which again deviates from the value found in the literature of 160°C²⁰⁹.

When TESb is supplied additionally with the DTBAA molecules, the decomposition temperatures of DTBAA shift to higher temperatures. However, no dependency on the TESb partial pressure can be found.

These experiments reveal the strong influence of the surface structure on the decomposition of UDMHy molecules but not on the decomposition of DTBAA. The origin for the deviation of the presented decomposition temperatures and the literature values is not clear yet. Nevertheless, a qualitative shift to higher temperatures can indeed be derived from the presented data.

However, further investigations will be conducted, particularly the parallel investigation of UDMHy decomposition products like $\text{HN}(\text{CH}_3)_2$ or HNCH_3 will lead to a much better understanding of the nitrogen incorporation behavior when antimony is present. In these further experiments a focus will be laid on the precise determination of the decomposition temperatures. Additionally, similar experiments carried out with indium could clarify if the same mechanism reduces the nitrogen incorporation efficiency for indium and for antimony.

4.5.2 Influence of antimony surface coverage on nitrogen incorporation

The second proposed explanation that can be found in the literature is related to surface effects. Dimroth et al. discussed the influence of substrate misorientation on the nitrogen incorporation. The misorientation determines the number of steps and their characteristics regarding bond configurations. They found that the nitrogen incorporation changes drastically with the misorientation. This led to the conclusion that nitrogen atoms are preferably incorporating at particular surface lattice sites. Additionally, these authors epitaxially deposited Ga(N,As) layers in which they varied the supplementary TESb partial pressure. They found a correlation of the TESb partial pressure to the surface occupation of antimony atoms. A Langmuir model, assuming a constant number of possible lattice sites that can be used for group V chemisorption, matched the experimental results very well, implying that antimony atoms occupied these lattice sites.²³⁷

Maßmeyer et al. found that the surface reconstruction must be gallium rich for nitrogen to incorporate²¹⁶ and hence this number of lattice sites is undoubtedly determined by the surface reconstruction.

The findings indicate clearly that a surface effect reduces the nitrogen uptake. In this section relatively thick Ga(N,As) layers are investigated with particular focus on the influence of small amounts of TESb on the nitrogen incorporation behavior, similar to the experiments of Dimroth et al.²³⁷ Especially, the difference between UDMHy and DTBAA will be investigated, in order to harmonize these surface effects with the results of last section. For that, the structure shown on the left of Figure 4.18 is grown as reference sample. A 20 nm Ga(N,As) layer is deposited at 550°C with a As/III ratio of 3.3 and a N/As ratio of 10.6 utilizing UDMHy as nitrogen precursor. The structure was capped with a 20 nm GaAs cap layer that was also grown at 550°C.



Figure 4.18 Investigated sample structures. On the left side the reference sample is shown. It contains a 20 nm thick Ga(N,As) layer capped by 20 nm GaAs. On the right side the sample structure for all other samples is depicted. In contrast to the reference sample, TESb was supplied with various partial pressures in these samples.

The HR-XRD analysis of this sample disclosed a nitrogen content of 2.1%. In similar structures illustrated on the right of Figure 4.18, an extra supply of TESb was introduced during the growth of the Ga(N,As) layer with a partial pressure of one order of magnitude lower than what would be used for Ga(As,Sb) growth. The TESb partial pressure was varied for different samples from $7.8\text{E-}5$ to $8.0\text{E-}4$ mbar. These experiments assume that the antimony surface coverage links directly to the TESb partial pressure and the antimony atoms act as surfactant. The HR-XRD diffractograms obtained for these samples are depicted in Figure 4.19. The diffraction patterns owing to the tensile strain of Ga(N,As) can be seen on the right side besides the GaAs substrate peak for different TESb partial pressures. With increasing TESb partial pressure, this diffraction pattern is shifted to lower relative angles, which hints to a lower nitrogen incorporation into the Ga(N,As) layer or an antimony incorporation. However, the partial pressures of TESb are too low, so no to almost no antimony incorporation should be expected.

Photoluminescence spectroscopy measurements were carried out for all structures to further analyze the optical properties. The acquired spectra are summarized in Figure 4.20. The left peak that is shifted with the TESb partial pressure is the peak that belongs to the Ga(N,As) transition. Matching to the HR-XRD results, the shift of the emission wavelength to higher energies indicates less nitrogen incorporation with increasing TESb partial pressure. In Figure 4.21 b) the peak energies of all PL spectra are depicted together with values obtained for Ga(N,As) samples grown without TESb. Both

samples compose a consistent curve, indicating that no antimony is incorporated into the Ga(N,As) layers grown with additional TESb. It can be assumed that antimony is only acting as surfactant.

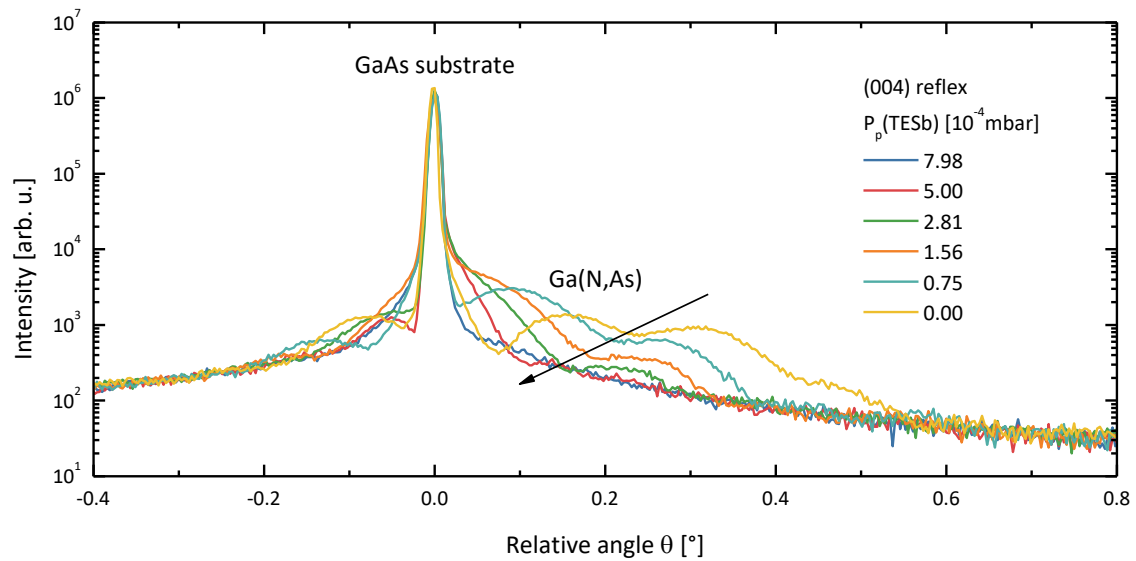


Figure 4.19 HR-XRD diffractograms of 20 nm thick Ga(N,As) containing samples. The growth parameters were constant for all samples, except the TESb partial pressure supplied during the Ga(N,As) deposition. Antimony acts as surfactant and does not get incorporated. With higher antimony supply the tensile strain of the entire structure gets reduced, hinting less nitrogen content.

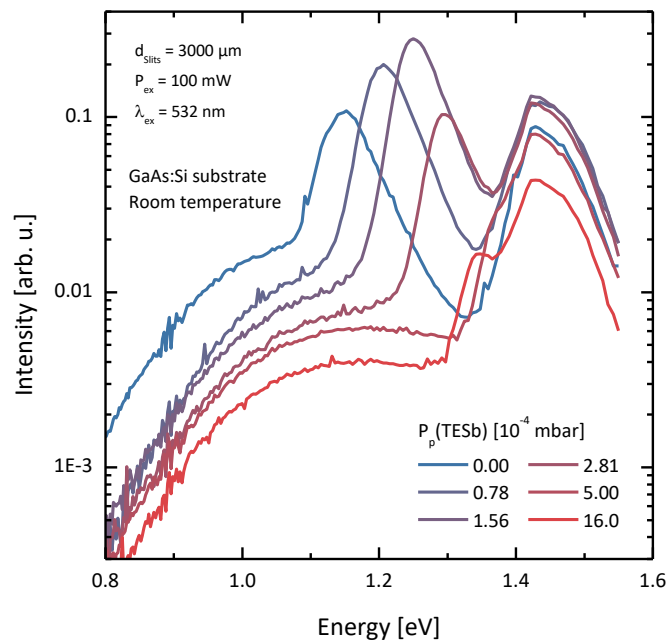


Figure 4.20 PL spectra of 20 nm thick Ga(N,As) samples grown with varied TESb partial pressures. All samples have the same typical background caused by the n-doped GaAs substrates. The low energy peak conforms to the Ga(N,As) transition and the peak at 1.42 eV to the GaAs substrate transition.

In Figure 4.21 a) the relative nitrogen content determined by simulating and fitting HR-XRD diffractograms is plotted with respect to the TESb partial pressure applied during the growth of Ga(N,As). Relative means in this case that it is compared to the value determined for the undisturbed growth of the reference sample. A relative nitrogen content value of 1 means, that the full nitrogen content is achieved. For the UDMHy sample series, the resulting curve shows a strong decay, which agrees with the findings of older studies that were explained by a simple Langmuir model^{237,243} that links the nitrogen content to the antimony surface coverage. From this model it could be concluded that the nitrogen incorporation reduction under the presence of antimony can be attributed to group V competition on the growth surface. However, in the same figure similar data points obtained for samples grown with DTBAA are shown. These samples were grown at 525°C and with DTBAA as nitrogen and arsenic precursor. The targeted nitrogen incorporation was 1.5% nitrogen, making the error bars of the relative HR-XRD composition determination more considerable compared to the UDMHy sample series. The partial pressure of DTBAA was chosen to be 2.76E-2 mbar. In contrast to the UDMHy sample series, the DTBAA grown samples indicate no influence on the presence of the antimony precursor. The nitrogen composition of all samples is in the vicinity of 1 and does not change significantly.

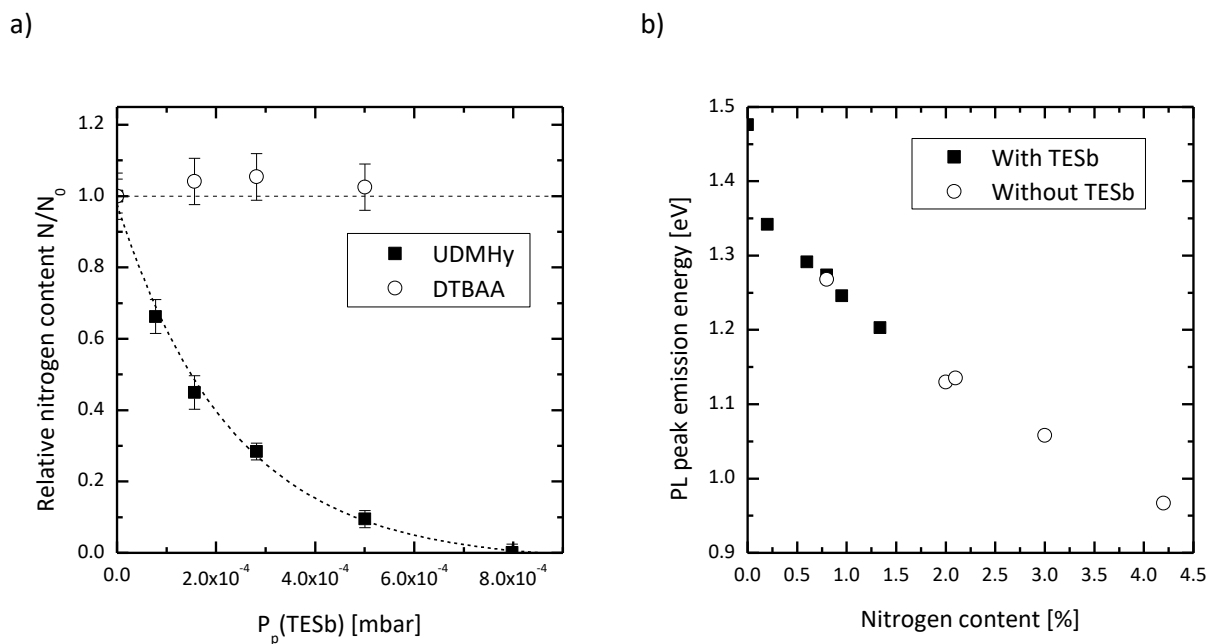


Figure 4.21 The relative nitrogen content of 20 nm thick Ga(N,As) samples is plotted as a function of the TESb partial pressure. The diffractograms used for the composition determination are shown in Figure 4.19. The samples grown with UDMHy as nitrogen precursor indicate an exponential reduction of nitrogen content with TESb partial pressure, while the nitrogen contents of the DTBAA grown samples remain unchanged. Figure b) demonstrates that no antimony incorporates into the Ga(N,As) layers, by comparing the PL peak wavelengths of samples grown with and without TESb. The PL peak wavelengths of both sample types agree.

Hence, it can be concluded, that the proposed group V surface competition is not only the reason for the reduced nitrogen incorporation because if this were the case, the same reduction would be

observable for both nitrogen precursors. Antimony seems not to influence the nitrogen incorporation efficiency if DTBAA is used.

4.5.3 Compensation of reduced incorporation efficiency

In the last section it was shown that the nitrogen incorporation efficiency decreases strongly, if UMDHy is used as nitrogen precursor and antimony is present in the reactor or on the surface. This section aims to investigate if this efficiency reduction can be compensated by adjusting the UMDHy partial pressure. For this, similar samples as last section were grown. 20 nm thick Ga(N,As) layers grown with an As/III ratio of 3.3, a fixed TESb partial pressure of $2.81 \cdot 10^{-4}$ mbar and varying N/As ratios. The variation of the N/As ratio was done by changing the UMDHy partial pressure. All samples were grown at 550°C reactor temperature. The nitrogen composition determined by HR-XRD measurements are shown in Figure 4.22 a).

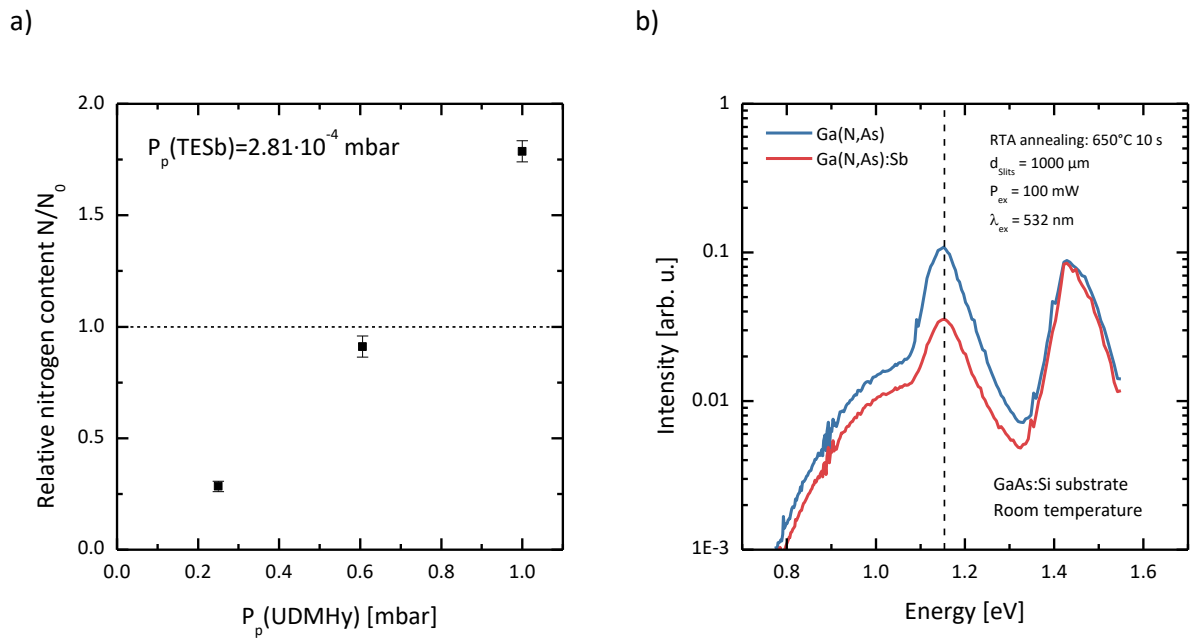


Figure 4.22 a) shows the relative nitrogen content as a function of the UMDHy partial pressure. A linear behavior is visible, similar to the undisturbed nitrogen incorporation behavior. The full nitrogen content compared to the undisturbed case can be achieved. In b) the PL spectra of two samples are compared. The blue spectrum originates from the undisturbed sample, and the red curve with TESb supply, but also with adjusted UMDHy partial pressure. If TESb is supplied, the intensity drops in the same order of magnitude.

In this plot, the data point with the lowest UMDHy partial pressure can be also found in Figure 4.20. The dashed horizontal line is representing the target nitrogen content, which corresponds to the nitrogen content that would be achieved if the growth was carried out undisturbed by TESb. With increasing UMDHy partial pressure, the relative nitrogen content is also increasing. All datapoints resemble a straight line, which agrees with the nitrogen incorporation behavior of undisturbed Ga(N,As). The sample grown with 0.6 mbar UMDHy is near the target nitrogen content. If this sample is compared to the undisturbed reference sample, the PL spectra look almost the same. The PL

spectra of these samples are depicted in Figure 4.22 b) after 10 s RTA annealing at 650°C, to enhance the optical properties. The dashed vertical line illustrates the peak position of the Ga(N,As) peak determined for the undisturbed reference sample. It can be seen that also the sample in which an increased UDMHy partial pressure compensated the reduced nitrogen incorporation exhibits the same Ga(N,As) peak position. However, the intensity is decreased almost one order of magnitude. To conclude, the compensation of the reduced nitrogen incorporation efficiency by tuning the UDMHy partial pressure is successful, but the optical quality of the grown layer is reduced for the structure with applied TESb. This could be due to an increased number of defects for example, which is counterintuitive, since Sb surfactant was shown to reduce the carbon incorporation in different III/V compounds²⁴⁴. However, the number of alkyl groups is increasing with the UDMHy partial pressure, which could lead to this increased number of defects.

If this technique is used to grow Ga(N,As) layers under the influence of antimony, a careful consideration of the growth rate must be taken into account, because the growth rate gets reduced linearly with increasing UDMHy partial pressure.

4.5.4 Discussion

In the last sections, the reason behind the reduced nitrogen incorporation efficiency if antimony is present was analyzed. Two explanations were investigated: Gas phase effects and surface effects. The possible gas phase effects were examined using an in-line mass spectrometer setup that investigates the molecular masses of molecules constituting the process gas. In these experiments a shift of the decomposition temperature was observed for UDMHy but not for DTBAA. Surface effects were investigated by reproducing the results of Dimroth et al., who fitted the reduction of the nitrogen content using UDMHy to a Langmuir model. This model relates the number of occupied lattice sites suitable for incorporation of group V atoms to the actual nitrogen content²³⁷. In contrast to that, the nitrogen content was not reduced at all if DTBAA was used.

To interpret these results, it is beneficial to also taking a closer look at the MBE growth of Ga(N,As,Sb). In MBE experiments, no reduction and even an increase of the nitrogen content was found^{50,51}. In fact, antimony even improved the material quality because the formation of deep level traps and other nitrogen related defects was suppressed^{245,246}. Antimony segregation was reported to play a severe role in MBE based growth of antimony containing compounds. Therefore, the surface reconstruction will be different compared to Ga(N,As) growth. However, the surface reconstructions can be totally different for different growth methods²⁴⁷. The fact that no reduction of nitrogen incorporation is visible for MBE growth can explain that strain does not affect the nitrogen incorporation too much. Due to the different surface reconstructions, the number of lattice sites

available could be larger compared to the surface during the MOVPE process. Additionally, MBE does not rely on metal organic precursor molecules, corroborating the thesis of increased UDMHy decomposition temperatures.

The comparison between MBE and MOVPE growth together with the fact that the nitrogen incorporation is not affected if DTBAA is used indicate that a gas phase effect causes the nitrogen incorporation to drop. However, also surface effects seem to play a role. A proposed mechanism could be that UDMHy decomposition is heavily dependent on the surface properties. Further mass spectrometry measurements will be conducted to clarify this point. All in all, antimony affects mainly the efficiency of nitrogen incorporation. As was shown in section 4.5.3, this efficiency drop can be compensated by increasing the supply of UDMHy.

The next chapter will deal with Ga(N,As)/Ga(As,Sb)/Ga(N,As) WQWH. In these structures the segregated antimony of the center Ga(As,Sb) quantum well reduces the nitrogen content of the following Ga(N,As) quantum well drastically, if UDMHy is used as nitrogen precursor. A strategy to overcome this issue could include compensating this effect by adjusting the UDMHy partial pressure.

Chapter 5 Ga(N,As)/Ga(As,Sb)/Ga(N,As)

“W” type-II heterostructures

5.1 Band alignments and challenges

In the last chapter the growth of single quantum well structures on GaAs substrates was discussed. The emission wavelength was found to be limited by strain. Type-II band alignments are a viable option to red shift the emission wavelength even further. In this chapter, the type-II band alignment of the Ga(N,As)/Ga(As,Sb) heterostructures is exploited to shift the emission to longer wavelengths. A “W” type structure is composed of two Ga(N,As) quantum wells that surround a Ga(As,Sb) quantum well. According to chapter 2.4, incorporating diluted amounts of nitrogen into GaAs will cause a strong reduction of the band gap, which acts in the conduction band. Hence, the Ga(N,As) quantum wells confine electrons and the Ga(As,Sb) quantum well confines holes.

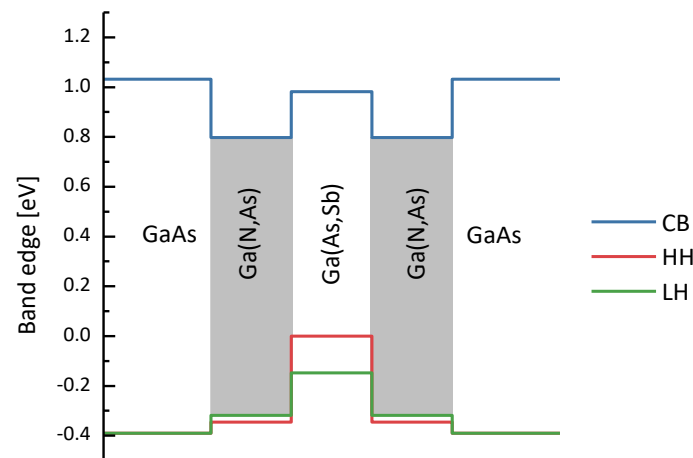


Figure 5.1 Band edge diagram of a Ga(N,As)/Ga(As,Sb)/Ga(N,As) WQWH, calculated by Dr. Ada Bäumner. The Ga(N,As) to Ga(As,Sb) heterojunction forms a type-II structure, enabling electron confinement in the Ga(N,As) layers and hole confinement in the Ga(As,Sb) layer.

In Figure 5.1 the band edge diagram of such a WQWH is illustrated. In the conduction band the Ga(N,As) layers provide deep potential wells for electrons and the center Ga(As,Sb) layer exhibits a slightly reduced barrier compared to GaAs, raising the wavefunction leakage into the Ga(As,Sb) layers. However, the wavefunction leakage is reduced by the comparatively heavy electron masses in the Ga(N,As) material. Two valence bands are plotted in the figure, indicating the heavy hole and the light hole bands.

To investigate the suitability for laser applications in the telecommunication wavelength ranges, the theoretically expected emission wavelengths of these structures, which correspond to the type-II transitions, are shown in Figure 5.2 a) in the low excitation regime. It can be seen that a wavelength of 1.3 μm can be easily reached with about 2% of nitrogen. 1.5 μm requires as much as 4% nitrogen but can also be reached. It must be noted that the uncertainty of the heterostructures assumed for these simulations may be high, so a shift of up to 0.1 eV is still viable. For larger excitation densities, as it is the case for laser devices, a blueshift is expected (see section 2.6). To quantify this blueshift, the emission peak energy is theoretically analyzed as a function of the charge carrier density inside the quantum wells and depicted in Figure 5.2 b). For very low carrier densities, the blueshift is weak. For carrier densities above $2 \times 10^{12} / \text{cm}^2$ it becomes linear with a slope of 0.009 to 0.01 eV/ 10^{12}cm^2 . In the following sections, this plot will be used for approximating the carrier density based on the experimentally determined blueshift.

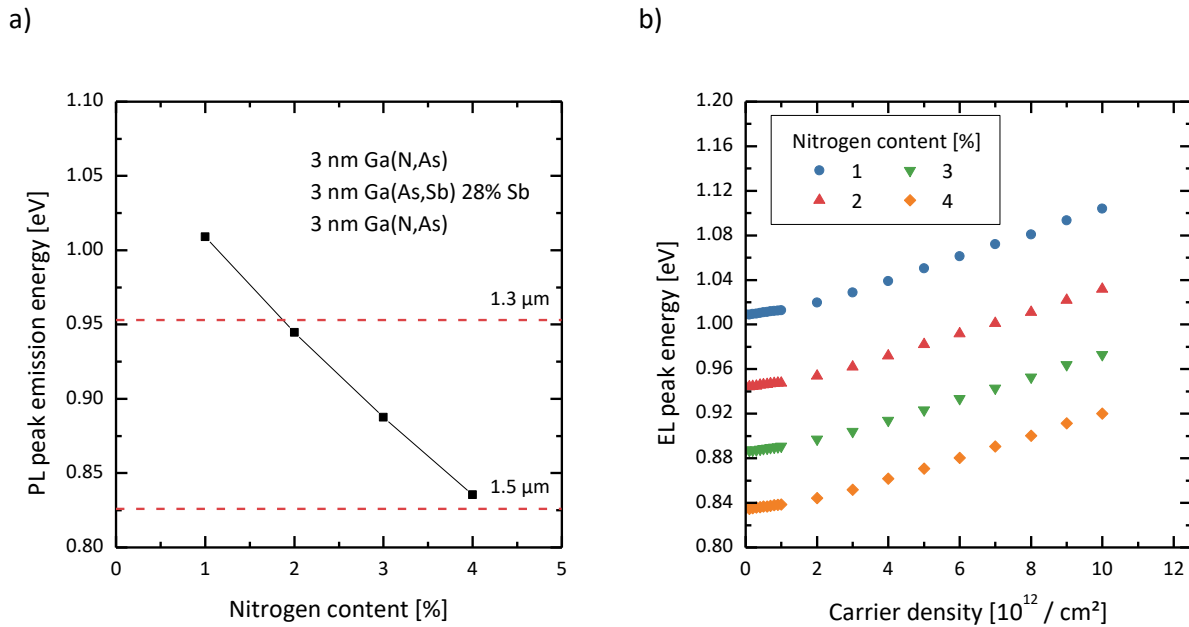


Figure 5.2 Calculated low excitation density emission energies are plotted as a function of the nitrogen content in a) for room temperature. As quantum well layer thicknesses 3 nm was chosen. As antimony content 28% was used. If the excitation density is increased the typical blueshift can be observed, as it is illustrated in b), in which the peak energy is illustrated with respect to the carrier density in the quantum wells. Dr. Ada Bäumner provided both data sets.

Besides these theoretical properties the challenges regarding the epitaxial growth must be considered. In the last chapter the reduction of the nitrogen incorporation under the influence of antimony was discussed in detail. The realization of the WQWH mentioned above is affected by this reduction because the second Ga(N,As) quantum well that is deposited on the Ga(As,Sb) quantum well is influenced by the segregated antimony atoms, resulting in a substantial reduction of the nitrogen content in this quantum well. Thus, a compositional asymmetry between the two Ga(N,As) layers exists. This structural asymmetry reduces the wavefunction overlap of the electron and hole

states and hence the achievable gain. In this chapter these growth challenges will be addressed, and in the end laser devices based on these preliminary investigations will be discussed.

5.2 Epitaxial growth of consecutive Ga(As,Sb)/Ga(N,As) quantum well layers

As a first step towards the realization of full Ga(N,As)/Ga(As,Sb)/Ga(N,As) WQWH, type-II quantum well heterostructures (QWH) are investigated. These feature two quantum wells that form a type-II band alignment. In this section both possible orders of the Ga(As,Sb)/Ga(N,As) layer growth sequence are analyzed, as illustrated in Figure 5.3. These structures have the advantage that compositional and thickness information can be retrieved much more precisely since the degrees of freedom in the HR-XRD fit are reduced. First, the growth of these structures with UDMHy and DTBAA is presented. Then, a study regarding the growth parameters like V/III ratio is conducted for both quantum wells separately to find the optimum parameters.

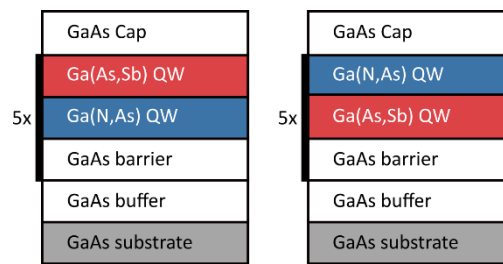


Figure 5.3 Layer stacks of type-II quantum well heterostructures (type-II QWH) that will be used in this section are schematically shown. Two possible stacking orders are possible. If the Ga(N,As) layer is deposited on the Ga(As,Sb) layer, antimony will affect it.

5.2.1 Growth with UDMHy as nitrogen source

The type-II QWH structures mentioned above are grown with UDMHy as nitrogen precursor. What should be expected is almost no influence of the Ga(N,As) layer on the growth of the following Ga(As,Sb) layer, besides a neglectable lattice pulling effect. However, if the growth order is reversed, the antimony segregation influences the following Ga(N,As) layer by reducing the nitrogen incorporation. To investigate this effect, two type-II QWH samples were grown at 550°C each with a different ordering of the 4 nm thick quantum wells. The nitrogen content was aimed to be 2.1% with an As/III ratio of 3.3 and a N/As ratio of 10.6. The Ga(As,Sb) quantum well was grown with a V/III ratio of 1 and a Sb/V ratio of 0.24. Test structures revealed an antimony content of approximately 28%.

In Figure 5.4 the HR-XRD diffractograms measured for these samples are shown with their fitted simulation and the determined thickness and composition values. The reduced intensity of the peaks on the tensile side of the diffractograms suggests that less nitrogen is incorporated into the sample in which the Ga(N,As) quantum well is grown onto the Ga(As,Sb) quantum well. The simulation yields that only 40% of the targeted nitrogen composition is reached for this sample. Also, the antimony content seems to be lowered in this sample, but this reduction is still within the scope of the HR-XRD composition determination errors. However, the thickness of the Ga(N,As) layer is reduced slightly, so it can be concluded that the growth rate is also slightly changing. Compared to this sample, the sample grown in a different order showed exactly the compositional and thickness values obtained for the test structures.

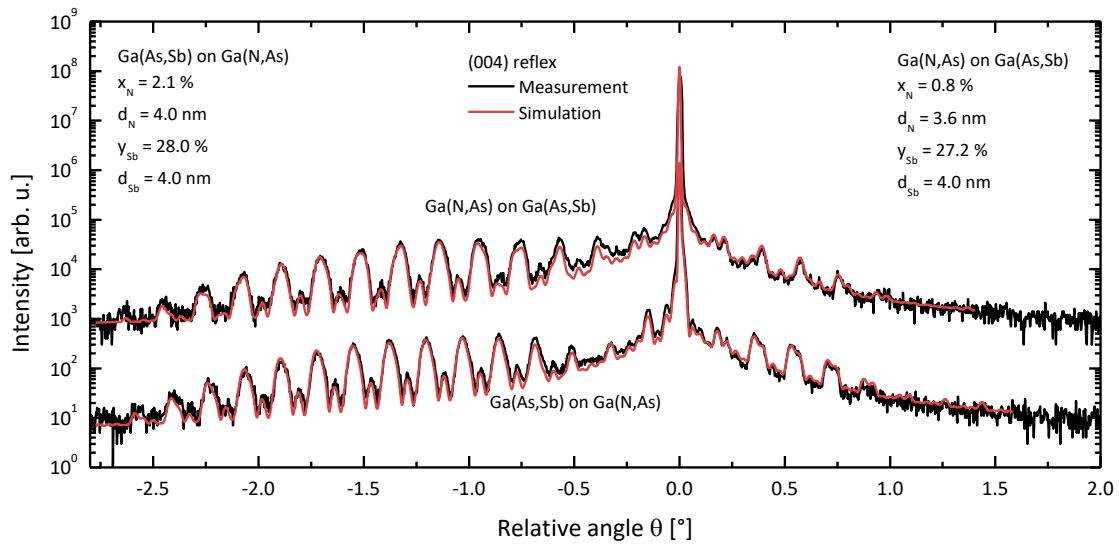


Figure 5.4 HR-XRD diffractograms of two type-II QWH grown with different quantum well orders. If Ga(N,As) is grown on Ga(As,Sb), the peaks on the tensile side of the diffractogram are much less pronounced compared to the sample where Ga(As,Sb) is grown on Ga(N,As). This indicates that the nitrogen incorporation into the sample in which the Ga(N,As) layer was grown first is more significant. The upper diffractogram is multiplied by 100 to improve the comprehensibility of the image.

To further clarify this behavior, PL measurements are conducted. The spectra of both samples are shown in Figure 5.5. The sample with the higher nitrogen composition (blue color) shows the lowest energy peak, which can be correlated to the type-II transition. A second peak is present next to the type-II transition in the same spectrum that could originate from higher order transitions.

Only one distinct peak can be seen in the other sample (red color), which is assumed to be the type-II transition of this type-II QWH structure. The energetic position far from the peak of the other sample indicates again that the nitrogen incorporation is drastically reduced. Also, the increase in intensity hints to that fact.

In conclusion, the nitrogen incorporation is drastically reduced if Ga(N,As) is grown on a Ga(As,Sb) layer if UDMHy is used as precursor. In WQWH structures this results in an unfavorable asymmetry.

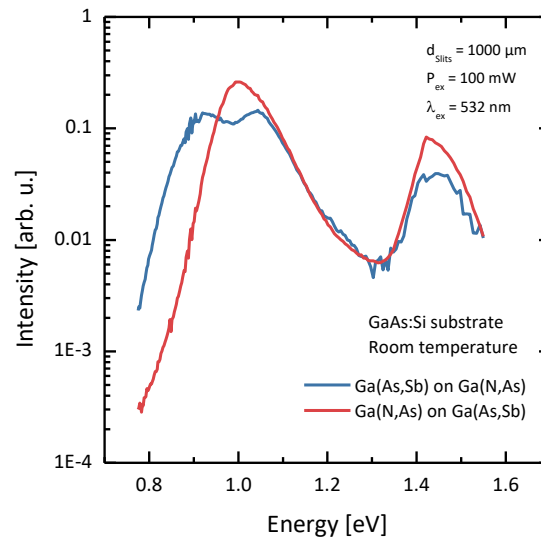


Figure 5.5 PL spectra of the two type-II QWH samples discussed above. The peak on the low energy side of the spectrum corresponds to the type-II transition. Both samples were grown on n-doped GaAs substrates.

5.2.2 Growth with DTBAA as nitrogen and arsenic source for Ga(N,As) growth

To compare the influence of different nitrogen precursors, the same experiment is executed with DTBAA as nitrogen and arsenic precursor for the Ga(N,As) quantum well layer. Because DTBAA needs lower growth temperatures, the samples were grown at 525°C. The DTBAA partial pressure was chosen to be 3.2E-2 mbar, which resulted in a nitrogen incorporation of about 2% in test structures. The Ga(As,Sb) quantum well was grown with a V/III ratio of 3.85 and a Sb/V ratio of 0.58. In the sample in which Ga(N,As) was grown on Ga(As,Sb), the individual layer thicknesses were aimed to be 3 nm thin, while in the other sample thicknesses of 5 nm were intended because both samples were grown in different epitaxy sessions. However, both samples are still well comparable. The HR-XRD measurements and analysis are shown in Figure 5.6. Both samples have similar nitrogen contents in the Ga(N,As) layers that both reach their intended thicknesses. Although the growth conditions of the Ga(As,Sb) layer growth were equal in both samples, the thinner sample exhibited a smaller antimony content. This could be explained by gradient effects in the antimony composition profiles produced by segregation effects.

The antimony segregation does not seem to influence the nitrogen incorporation of Ga(N,As) layers grown on top of Ga(As,Sb) layers at all. This can be expected from the results concluded in the last chapter, where no change of the nitrogen incorporation was observed if DTBAA was used and antimony was present in the reactor. Similar samples were grown at 500°C and the same effect of

equal nitrogen incorporation was seen. However, since DTBAA is an experimental nitrogen precursor that contains still a comparatively large amount of oxygen in its purest form, it is not yet well suited for laser applications. Thus, the following sections will mainly deal with the growth of Ga(N,As) layers using the conventional precursor UDMHy.

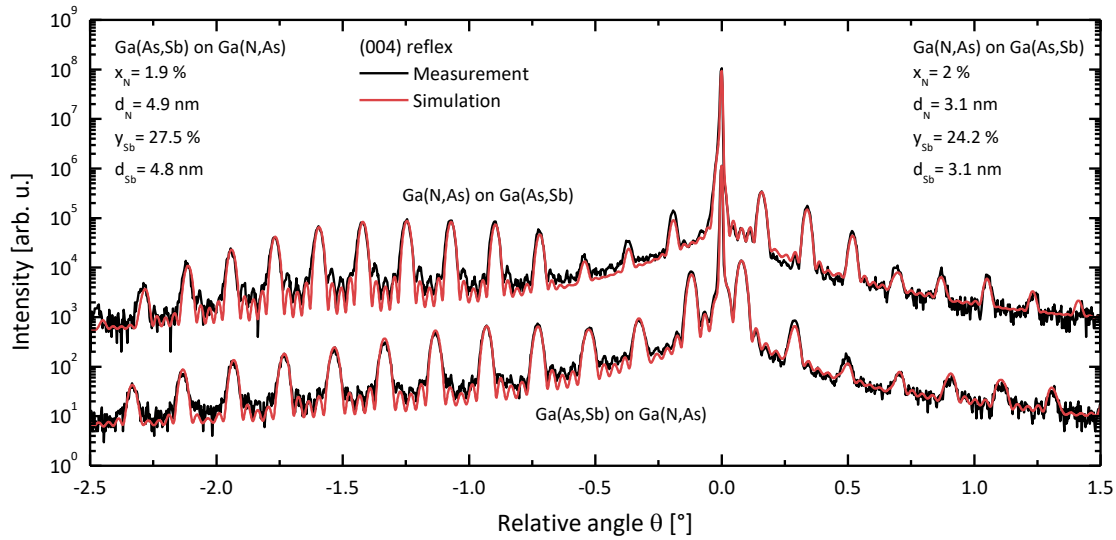


Figure 5.6 Measured and simulated HR-XRD diffractograms of two type-II QWH grown with DTBAA as nitrogen precursor. No change in nitrogen content is visible, meaning that segregated antimony atoms do not influence the nitrogen incorporation efficiency. The upper diffractogram is multiplied by 100 to improve the comprehensibility of the image.

5.2.3 Growth parameters of single quantum well layers

The optical properties depend heavily on the gas phase ratios of the precursors. Therefore, this section is dedicated to investigating their influence on the optical properties of type-II QWH. A major interest is also the influence on the nitrogen incorporation efficiency under the effect of antimony segregation.

5.2.3.1 Ga(N,As)

In this section a sample series containing type-II QWH in which the Ga(As,Sb) quantum well was grown first is presented. The As/III ratio used for the growth of the Ga(N,As) quantum wells was changed between 2 and 8 for all samples while the N/As ratio was constant with a value of 14.9. In the undisturbed growth of the test structure, these parameters led to a nitrogen content of 3%. In the Ga(As,Sb) quantum wells a V/III ratio of 1 together with a Sb/V ratio of 0.22 led to an antimony content of 26%. The individual layer thicknesses were 3 nm for the Ga(As,Sb) quantum well and 5 nm for the Ga(N,As) quantum well.

The HR-XRD analysis of these samples showed no significant influence of the As/III ratio on the nitrogen content. The review of the PL spectra in Figure 5.7 indicates that the intensity of the

samples grown with As/III ratios of 2 and 4.12 are comparable, while the sample with an As/III ratio of 8 produces an intensity that is more than one order of magnitude larger. If a closer look is taken at the peak shapes, the FWHM seems to be wider for the sample with As/III of 2. Also, the peak shape of the substrate peak at 1.42 eV seems to be wider. This could be attributed to defects introduced with low As/III ratios.

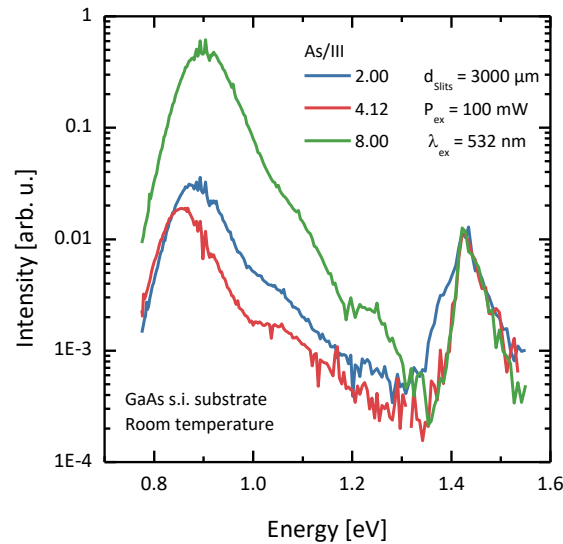


Figure 5.7 PL spectra of Ga(As,Sb)/Ga(N,As) type-II QWH samples grown with different As/III ratios for the Ga(N,As) quantum well. The As/III ratio was varied between 2 and 8, while the N/As ratio stayed constant at 14.9.

In conclusion, the effect of the As/III parameter for Ga(N,As) growth was investigated. The nitrogen content does not depend on it, but the optical properties seem to be improved for higher As/III ratios. Therefore, a high As/III ratio should be chosen for device applications if a UDMHy partial pressure below 1 mbar can be selected and still sufficiently high nitrogen incorporation can be expected.

5.2.3.2 Growth of Ga(As,Sb)

More interesting than the As/III influence on the Ga(N,As) growth is the influence of the V/III ratio of the Ga(As,Sb) layer on the nitrogen incorporation into the following Ga(N,As) quantum well layer as well as on the optical properties of the whole type-II QWH structure. The idea behind this experiment is that a V/III ratio of 1 means that exactly one group V atom is supplied for each gallium atom. If then all antimony atoms are incorporated into the crystal, no antimony segregation layer can be formed and the Ga(N,As) growth can take place in an undisturbed way. If this were the case, the nitrogen incorporation efficiency would be decreased for higher V/III values.

To investigate this dependency, six samples were grown at 550°C growth temperature with 5 repetitions of the type-II QWH, in which the Ga(As,Sb) layer was grown first. The 5 nm thick Ga(N,As) layer was deposited with a As/III ratio of 4.12 and a N/As ratio of 14.8 leading to 3% nitrogen incorporation for the undisturbed case, while the Ga(As,Sb) layer was aimed to be only 3 nm thick. The V/III ratio, as well as the Sb/V ratio of the Ga(As,Sb) layer were carefully adjusted to obtain 28% Sb content.

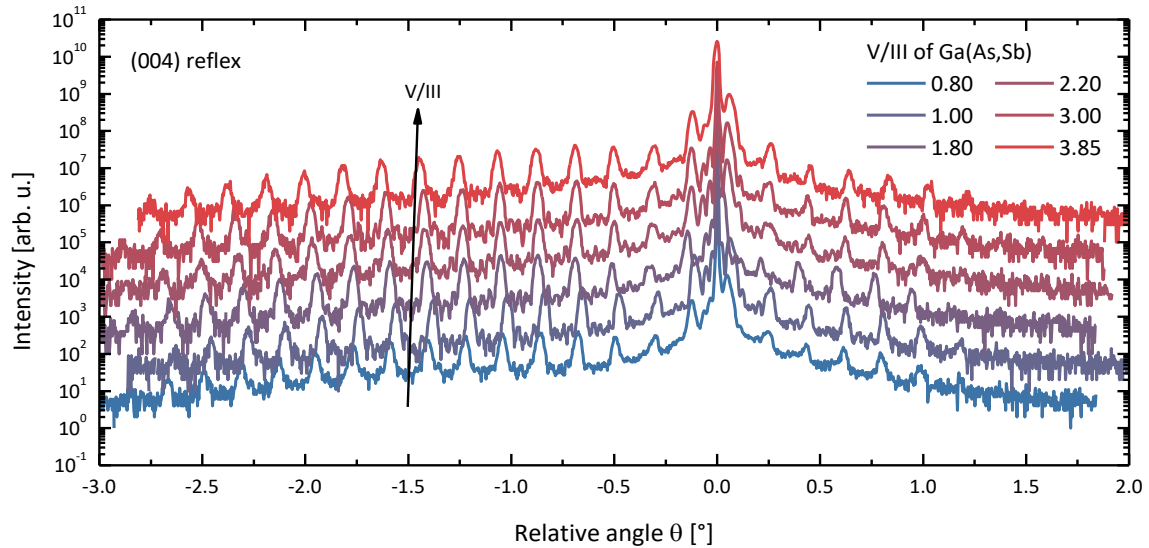


Figure 5.8 HR-XRD measurements of type-II QWH samples with varying V/III ratios as parameter for the Ga(As,Sb) layer growth. The Ga(As,Sb) layers look similar, as can be seen in the similar diffraction patterns on the compressive side of the diffractogram.

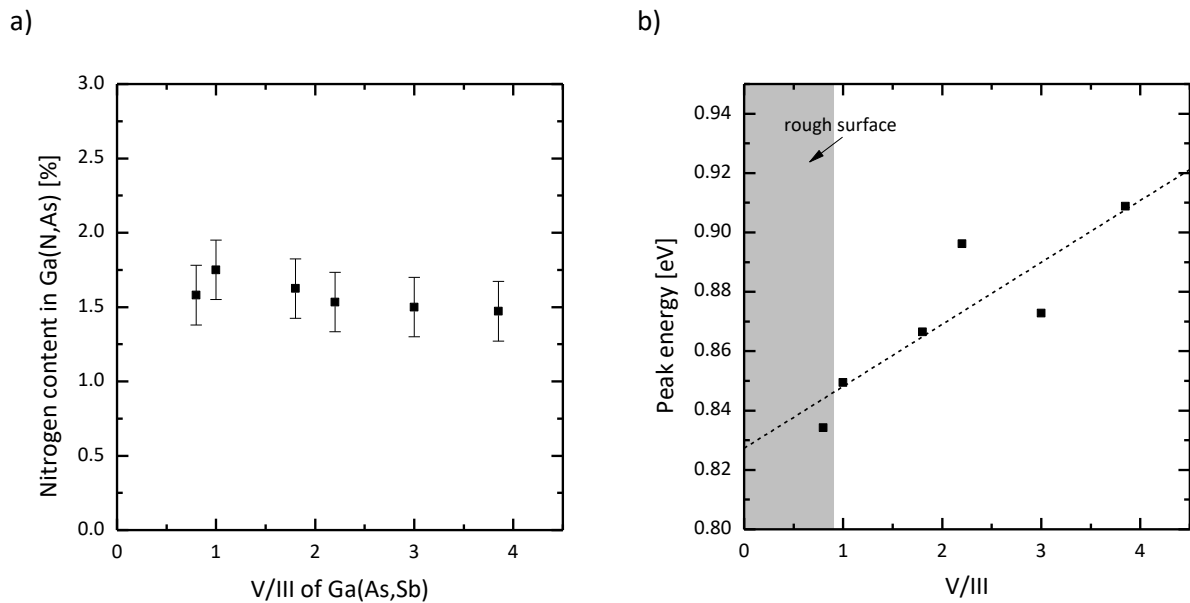


Figure 5.9 a) Nitrogen content of the Ga(N,As) layer as a function of the V/III ratio used for the Ga(As,Sb) quantum well growth. The error bars stem from the variation of the nitrogen content under careful observation of the HR-XRD simulation in comparison to the measurement. The PL peak energies of these samples were evaluated in b). The straight line serves as a guide to the eye.

The measured HR-XRD diffractograms of these samples are plotted in Figure 5.8. On the compressive side of these diffractograms all samples except the one with a V/III ratio of 0.8 seem to be similar in terms of diffraction peak envelope. This indicates that roughly the same antimony composition is achieved in all samples. The positions of the peaks are shifting slightly with respect to each other, showing that the Ga(As,Sb) quantum well thickness or other layer thicknesses are slightly changing. However, the diffraction patterns look quite similar, so the thickness difference should not be overestimated. The exceptional sample with a V/III ratio of 0.8 shows less distinct diffraction peaks. This stems from the formation of metallic gallium droplets on the surface due to the excess gallium deposition.

The peaks on the tensile side of the diffractogram look also similar, but to analyze the influence of the V/III ratio on the nitrogen incorporation, the diffractograms were analyzed by fitting simulations to the measurements. The nitrogen contents obtained by these fits can be seen in Figure 5.9 a) as a function of the V/III ratio used for the Ga(As,Sb) layer growth. At first it looks like the nitrogen incorporation is increasing, but if also the error bars of the HR-XRD composition determination are taken into consideration, the difference vanishes. The respective PL peak energies evaluated from the spectra depicted in Figure 5.10 are plotted as a function of the V/III ratio in Figure 5.9 b). In this plot a shift in wavelength can be seen that amounts to 80 meV from V/III ratios of 0.8 to 3.85. In this plot a grey area is highlighted for which the surfaces are rough and the PL spectrum that corresponds to these samples is deteriorated due to the formation of metallic gallium droplets. The redshift observed with lower V/III ratio could be explained by the increase of the nitrogen content, which would be contrary to the observations in the HR-XRD analysis.

The peak intensities of the PL spectra show no clear dependency. However, the intensity reduction seems to correlate with the redshift, indicating increased nitrogen incorporation. The highest intensity shows the sample grown with a V/III ratio of 2.2 and the lowest intensity the sample grown with a V/III ratio of 1.0.

All in all, it must be concluded that the V/III ratio of the Ga(As,Sb) layer does not show a clear influence on the nitrogen content and on the optical properties of the full type-II QWH, so no clear recommendation regarding the V/III ratio can be given for future experiments. The assumed improvement of the nitrogen incorporation due to reduced segregation cannot be unambiguously verified. However, a reduction of the antimony surface coverage is not in contrast with the discussed results since the surface reconstruction can still be antimony dominated in the case of V/III ratios close to 1. Because these results were not available when all other laser structures and samples were deposited and for the sake of antimony incorporation efficiency, most further experiments will be

carried out with V/III ratios close to 1. In future experiments V/III ratios of 2.2 will be employed to achieve superior optical quality.

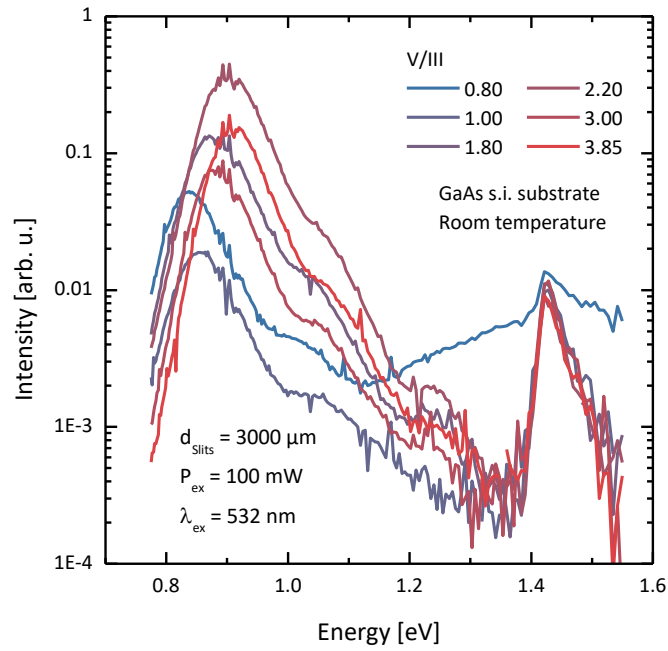


Figure 5.10 PL spectra of type-II QWH samples with varying V/III ratio for the Ga(As,Sb) layer growth. The strong background signal observed for the sample with a V/III ratio of 0.8 is referred to the formation of gallium droplets due to the excess gallium offering.

5.3 Preparation of internal interfaces

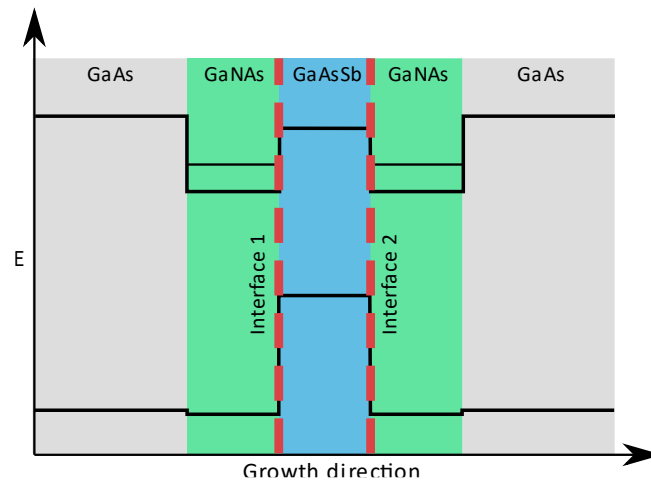


Figure 5.11 Band edge diagram of the full Ga(N,As)/Ga(As,Sb)/Ga(N,As) WQWH with highlighted interfaces. Two interfaces play a major role in these structures. Interface 1 is defined as the interface between the first Ga(N,As) quantum well to the Ga(As,Sb) hole quantum well. Interface 2 corresponds to the interface between the Ga(As,Sb) quantum well and the second Ga(N,As) quantum well.

In section 2.6 the importance of internal interfaces for type-II based devices was discussed thoroughly^{177,178}. Thus, the interface quality will be investigated in this section. The results obtained in this section and in section 5.4 were already published²⁴⁸. In the full WQWH two interfaces are present that contribute notably to the optical quality of the WQWH because the charge carrier recombination takes place across these interfaces. To make the discussion more comprehensive, interface 1 is defined as the interface between the first Ga(N,As) layer and the Ga(As,Sb) layer and interface 2 as the interface between the Ga(As,Sb) layer and the second Ga(N,As) layer as illustrated with the dashed red vertical lines in Figure 5.11. Both interfaces pose a challenge to the epitaxial growth process related to antimony segregation.

5.3.1 Interface 1

At interface 1 the growth challenge is related to a sufficient antimony surface coverage for the antimony incorporation to start. To be more precise, if the antimony precursor run valve is switched on, the antimony precursor gets supplied into the reactor. Then, antimony surface coverage is built up while the growth continues until adequate surface coverage is achieved. Until then, the grown layers consist of GaAs which is depleted of antimony atoms. This effect is expected to be most severe for small V/III ratios since the TESb partial pressure and hence the supplied antimony atoms are pretty low. To counteract this problem, a short growth interruption can be implemented, in which the run valve of the gallium precursor is closed and all other precursors are normally supplied. If this is done for a short amount of time, the antimony surface coverage is built up and the growth can continue. This way a much more abrupt composition profile can be obtained. For most following samples an antimony predeposition time of 3 s was used.

5.3.2 Interface 2

The challenge posed by interface 2 is much more critical than for interface 1. After the growth of the Ga(As,Sb) layer, an antimony surface coverage must be expected to be still present. As discussed in the last sections, this antimony film or the surface reconstruction induced by antimony atoms changes the incorporation efficiency of nitrogen into Ga(N,As), if UDMHy is used as nitrogen precursor. The most apparent countermeasure is introducing a desorption step to desorb excess antimony atoms from the surface. This desorption step will be called growth interruption (GI) in the following. The gas switching during this growth interruption is rather simple: the run valve of the gallium and antimony precursors is switched to closed while the arsenic precursor is still supplied to the reactor because the antimony surface atoms must be replaced by arsenic atoms. Furthermore, the vapor pressure of group V elements is much higher than that of group III atoms, so arsenic vacancies could be formed due to arsenic desorption if no TBAs stabilization was supplied. The

samples grown by Dr. Christian Fuchs presented in this section contain a Ga(As,Sb) quantum well to which a TBAs stabilized growth interruption of varying length is applied. For comparison purposes, similar samples with GIs applied to GaAs layers were grown.

The quality of an internal interface is considered good, if it is atomically flat, which means big and well-defined terraces are forming. In contrast, an internal interface is considered bad, if holes and hillocks are forming for example. To investigate the quality of the surface, AFM images are taken on specially prepared samples. In these images, the RMS value is a measure for the quality of the interface. Since the Ga(As,Sb) quantum wells are grown at 550°C, the surfaces have to endure a cooldown procedure which changes the surface morphology drastically, perishing the effect of the GIs. Thus, the surface morphology must be frozen directly after the GIs. This was done by growing 150 nm AlAs layer immediately after the GI followed by a 10 nm GaAs cap layer to protect the whole structure while cooling down. In order to uncover the buried interface, a selective etching technique was applied,²⁴⁹ in which the GaAs and AlAs layers were etched off with highly selective acids. Selective means, that acids are chosen that etch GaAs or AlAs strongly but show almost no effect on the respective other material, causing no change of the uncovered interface. The GaAs etching solution used for the GaAs cap layer was a mixture of cleaned water, hydrogen peroxide (31%), and ammonia solution (28%) with a pH value of 7. The AlAs surface freezing layer can be etched by 2 percent hydrofluoric acid. The selective etching and the AFM measurements of these samples depicted in Figure 5.12 were performed by Lukas Hellweg in the scope of research assistant work.

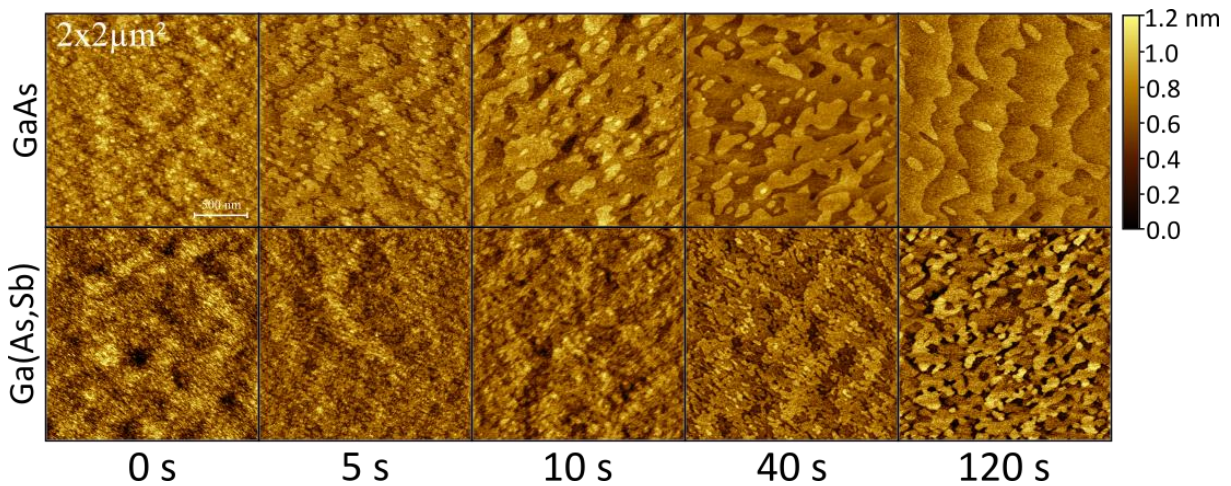


Figure 5.12 AFM images of internal interfaces uncovered by a selective etching technique. The numbers below correspond to the duration of the TBAs stabilized growth interruption applied before the surface freezing layer was grown. The top row shows the effect of these GIs on GaAs while the lower row shows the effect on Ga(As,Sb). The GaAs surface gets flatter and nicer in quality while the Ga(As,Sb) surface first improves its quality but after a particular duration, holes emerge and the quality gets worse. Lukas Hellweg measured the AFM images.

The AFM images presented in Figure 5.12 demonstrate two different behaviors, depending on the internal interface that was treated with GIs. In the simple case of GaAs, the interface is smoothing out with longer GI duration, until after 120 s atomically flat terraces emerge due to a rearrangement

of the surface caused by surface diffusion. To make this clearer, the RMS values obtained from these images are depicted in Figure 5.13. As expected, the RMS values for the GaAs interface decrease with longer growth interruption duration. The analysis of the Ga(As,Sb) interfaces provides a different result. For short GIs, the Ga(As,Sb) interface gets smoother. In this regime, antimony atoms desorb from the surface and the surface has time to rearrange itself. After a specific GI duration, the surface becomes rougher again. At that point, the excess antimony atoms are mostly desorbed from the surface and the buried antimony atoms that were already incorporated into the bulk crystal close to the surface get desorbed. This is particularly distinct for 120 s GI duration, where relatively large holes are present in the AFM image. A further indicator for the worsening of the interface is the RMS value. The grey box in Figure 5.13 highlights the GI durations for which only surface atoms are desorbed. A turning point can be approximately determined at 20 s, making this the recommended GI duration for samples grown at 550°C. Since the desorption is expected to be weaker at lower temperatures, a GI duration of 30 s is used for 525°C grown samples.

In the literature this roughening effect was already observed and interpreted as arsenic to antimony exchange process.^{234,250} Also the desorption of antimony under the presence of arsenic precursor was observed.²²⁹ The next section is dedicated to investigating the effect of these GIs on the nitrogen incorporation into the subsequent Ga(N,As) quantum well.

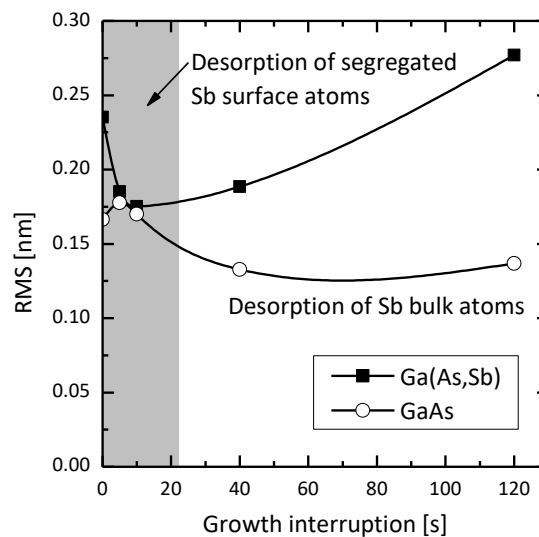


Figure 5.13 RMS values obtained from the AFM images shown in Figure 5.12 as a function of the growth interruption duration. As already made clear from the AFM images, the GaAs interface gets smoother with increasing GI duration while the Ga(As,Sb) interface produces holes with increasing GI duration, after a particular duration is exceeded. Antimony atoms are desorbing from the surface below this duration (illustrated with a grey area). Above this duration the desorption of antimony atoms happens from the bulk crystal.

5.4 Nitrogen incorporation symmetry optimization using growth interruptions

The radiative transition rates in WQWH depend heavily on the wavefunction overlap. If the nitrogen content in both Ga(N,As) quantum wells is not equal, the wavefunction overlap will be reduced drastically. Therefore, the symmetry of the whole structure must be optimized before growing laser devices. The effect of growth interruptions on Ga(As,Sb) quantum well layers on the nitrogen incorporation into the following Ga(N,As) quantum well is analyzed using similar type-II QWH samples. The full structure is grown at 550°C with three repetitions separated by 20 nm GaAs barriers. The thickness of the cap layer was set to be 60 nm. The V/III ratio of the Ga(As,Sb) layers was set to 1 and the Sb/V ratio was tuned in a way that the antimony incorporation is 24%. During the Ga(N,As) growth, an As/III ratio of 3.27 and a N/As ratio of 10.8 was applied, resulting in 2% nitrogen incorporation under undisturbed test structure conditions. The individual layer thickness is 4 nm for both quantum wells. TBAs stabilized growth interruptions under a TBAs partial pressure of 2.3E-2 mbar were applied on the Ga(As,Sb) quantum wells with different durations between 0 and 120 s. The tensile side of the HR-XRD diffractograms shown in Figure 5.14 indicates an increase in nitrogen content with longer GI duration because the diffraction peaks highlighted with the black box are rising in intensity with longer GI duration. Besides the tensile side, the compressive side reveals that the thicknesses of the Ga(As,Sb) quantum wells are decreasing slightly. This can be seen by the shift of the angular position of the diffraction peaks. The envelope and therefore the antimony composition seems to be equal for all samples. The nitrogen composition relative to the nitrogen content of the test structure determined by HR-XRD simulation fitting can be found in Figure 5.15 b). For a GI duration of 120 s, full nitrogen incorporation can be achieved. The dependency between GI duration and nitrogen content is a function that converges to the nitrogen composition of the undisturbed growth after quickly increasing the nitrogen content for short GI durations.

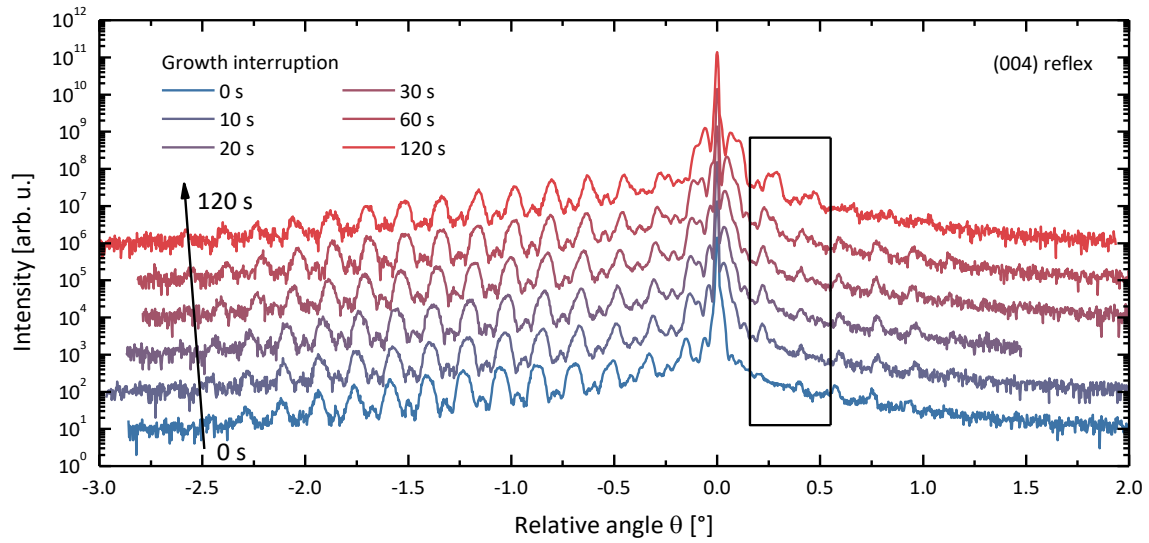
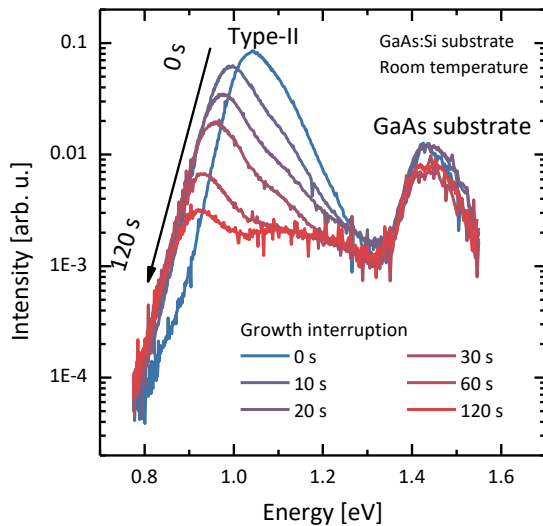


Figure 5.14 HR-XRD diffractograms measured for samples with different growth interruption durations. The diffraction peaks on the compressive side shift towards the GaAs substrate peak with longer growth interruption durations, hinting a thinner Ga(As,Sb) quantum well. The highlighted peaks on the tensile side increase in intensity, which indicates a more significant nitrogen content in the samples with longer growth interruption duration.

a)



b)

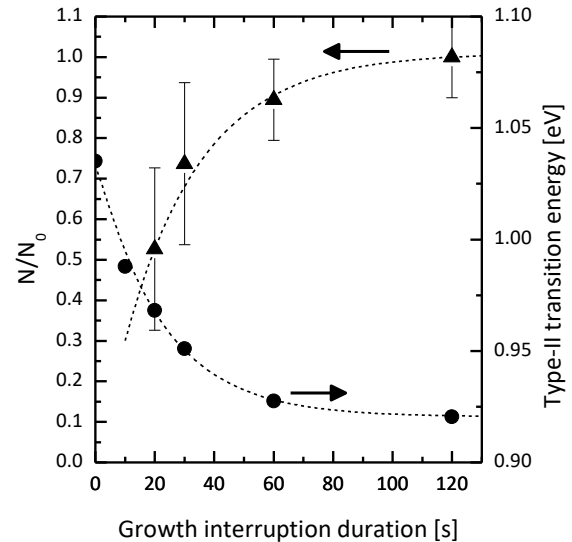


Figure 5.15 The PL spectra depicted in a) exhibit a redshift and a loss of intensity of the type-II peak with increased growth interruption duration, both indicating an increase of nitrogen incorporation. The corresponding type-II transition energies are plotted as a function of the growth interruption duration in b). Additionally, the relative nitrogen content obtained by HR-XRD fits is given.

Besides HR-XRD analysis, the PL spectra of these samples were measured as grown and plotted in Figure 5.15 a). In these spectra, the GaAs substrate and barrier peak is present at 1.42 eV, and a clear type-II peak is located at lower energies. Two features of these spectra are interesting: The intensity of the type-II peak gets reduced with longer GI duration. The peak position of these peaks is

redshifted, as depicted in Figure 5.15 b). As for the nitrogen content, the effect of GI is more severe for short GI durations and saturates around 120 s. Both of these effects can be related to higher nitrogen incorporation with longer GI.

To further verify the improvement of the nitrogen incorporation with longer GI duration, complementary scanning transmission electron microscopy (STEM) measurements were carried out by Yurii Radiev and Pirmin K  kelhan. The sample investigated with STEM was prepared explicitly for these investigations. It contains multiple stacked WQWH structures with a 20 nm GaAs barrier. A different GI duration was chosen for each WQWH included in this sample. This way, only one sample must be elaborately prepared.

The STEM analysis was conducted in a double aberration-corrected JEOL JEM 2200 FS operating at 200 kV. To obtain contrast between GaAs and Ga(N,As) layers, the camera length must be chosen to collect low scattering angles of 33-132 mrad with the annular dark field (ADF) detector²⁵¹. With this imaging technique, a contrast between GaAs and Ga(N,As) can be achieved. However, no quantification of the nitrogen content can be performed, contrary to the energy filtered STEM presented in section 4.2.3.

Figure 5.16 a) presents the atomically resolved ADF STEM image of the WQWH with no GI. The box inset highlights the high resolution obtained for the whole field of view. The brightest layer in the center of the image corresponds to the Ga(As,Sb) quantum well. Due to the high atomic number, the contrast is especially high for antimony containing layers. Left to it, showing a darker contrast, the Ga(N,As) layer grown on top of the GaAs barrier is shown. On the right of the Ga(As,Sb) quantum, the second Ga(N,As) layer is located. In this case the contrast is low, indicating low nitrogen incorporation. To improve the visibility of the effect of GIs on the nitrogen composition of the second Ga(N,As) quantum well, the averaged cross sections of all grown WQWH are depicted in Figure 5.16 b). In this image, only the group V atomic columns were considered. For 0 s GI, a large difference in the measured intensity suggests a strong asymmetry of nitrogen incorporation in this WQWH. For increasing GI duration, the intensity of the second Ga(N,As) quantum well is improving its contrast with respect to GaAs. This means that the nitrogen incorporation gets improved with a longer GI duration. For 120 s, the nitrogen content approaches the same nitrogen level as in the first Ga(N,As) quantum well, indicating symmetric nitrogen incorporation. At the second Ga(As,Sb) to Ga(N,As) interface, the slope of the intensity profile hints the reduction of antimony in the interface region. All these findings agree with the results obtained with HR-XRD and PL analysis. The reduction of antimony directly at the interface matches the result of the AFM investigations, showing that holes in the surface are forming due to antimony desorption.

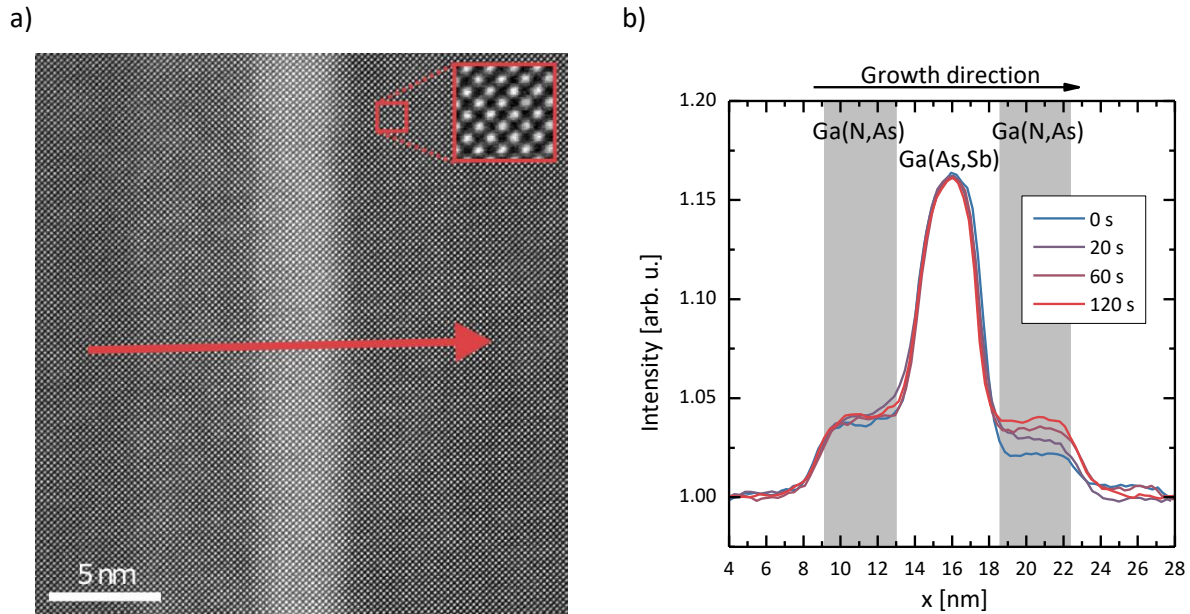


Figure 5.16 In a) the atomically resolved ADF STEM image is depicted. It was acquired for the sample without any growth interruption. The inset highlights the high resolution achieved for the whole picture. The averaged cross section considering only group V columns of all WQWH with different growth interruption duration are shown in b). STEM analysis was conducted by Yurii Radiev and Pirmin K  kelhan.

To conclude, a long growth interruption of 120 s would be preferred in terms of nitrogen incorporation symmetry. After the desorption of antimony atoms for this GI duration, the surface is most probable GaAs like, and nitrogen can be incorporated in an undisturbed way. This effect starts already for short GI durations and gets more pronounced for longer GI. This means that the surface reconstruction gets more and more GaAs like. However, the introduction of a TBAs stabilized GI can lead to a significant roughening of the surface due to antimony to arsenic exchange or the desorption of antimony atoms out of the near surface layers of the already grown crystal. For a similar sample series not presented in this section, even an antimony depleted GaAs like layer of several monolayers thickness was observed for very long GI durations. Nevertheless, the surface morphology improves for short GI while the effect on the nitrogen incorporation is strongest in the same time range. Thus, a short GI should be introduced for WQWH growth in laser devices to improve the nitrogen incorporation as much as possible while at the same time improving the morphology of the internal interface. As already proposed in the last section, this optimum GI duration is approximately 20 s for 550°C and 30 s for 525°C.

5.5 Symmetry optimization of “W”-quantum well heterostructures

The symmetry optimization executed alone with the application of GI at interface 2 resulted in symmetric nitrogen incorporation but, unfortunately, also in a strong reduction of the interface

quality. The optimum GI duration in terms of surface morphology is not sufficient to fully overcome the nitrogen incorporation reduction. As this reduction of nitrogen incorporation by antimony was shown to be compensated by supplying higher UDMHy partial pressures, the other optimization route committed in this section is the careful optimization of the UDMHy partial pressure supplied during the growth of the second Ga(N,As) quantum well. Since this optimization is very delicate, it will be done with full WQWH to be able to transfer the resulting growth parameters directly to laser device growth processes.

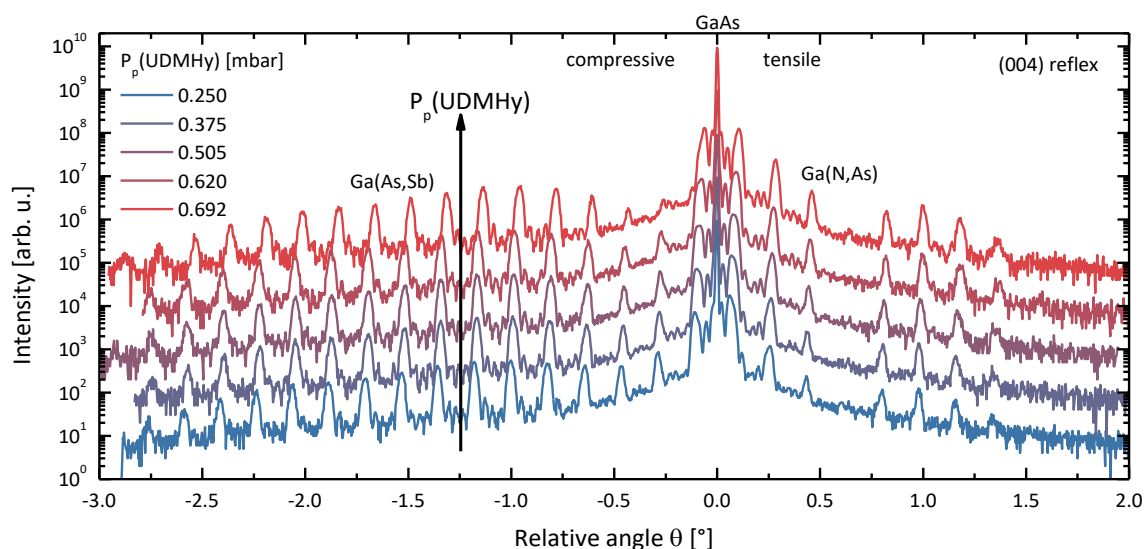


Figure 5.17 Diffractograms of WQWH samples grown with different UDMHy partial pressure during the growth of the second Ga(N,As) quantum well. The diffraction peaks on the compressive side indicating that the Ga(As,Sb) layers exhibit similar compositions and thicknesses. The increasing peaks on the tensile side suggesting an raised nitrogen content.

The 3 nm Ga(N,As) quantum well grown first was grown with an N/V ratio of 10.55 and an As/III ratio of 3.3, which resulted in nitrogen incorporation of 2%. The subsequent 3 nm Ga(As,Sb) quantum well with 28% antimony was grown with a V/III ratio of 1 and a Sb/V ratio of 25.5. The antimony predeposition described in a previous section was applied for 3 s while the following TBAs stabilized growth interruption as desorption and smoothing step accounted to 20 s. The second Ga(N,As) quantum well that followed the growth interruption was also grown with an As/III ratio of 3.3 while the N/V ratio was varied by changing the UDMHy partial pressure for different samples. The whole WQWH is repeated 5 times to ensure a high accuracy in HR-XRD composition and thickness determination. All samples were grown at 550°C reactor temperature.

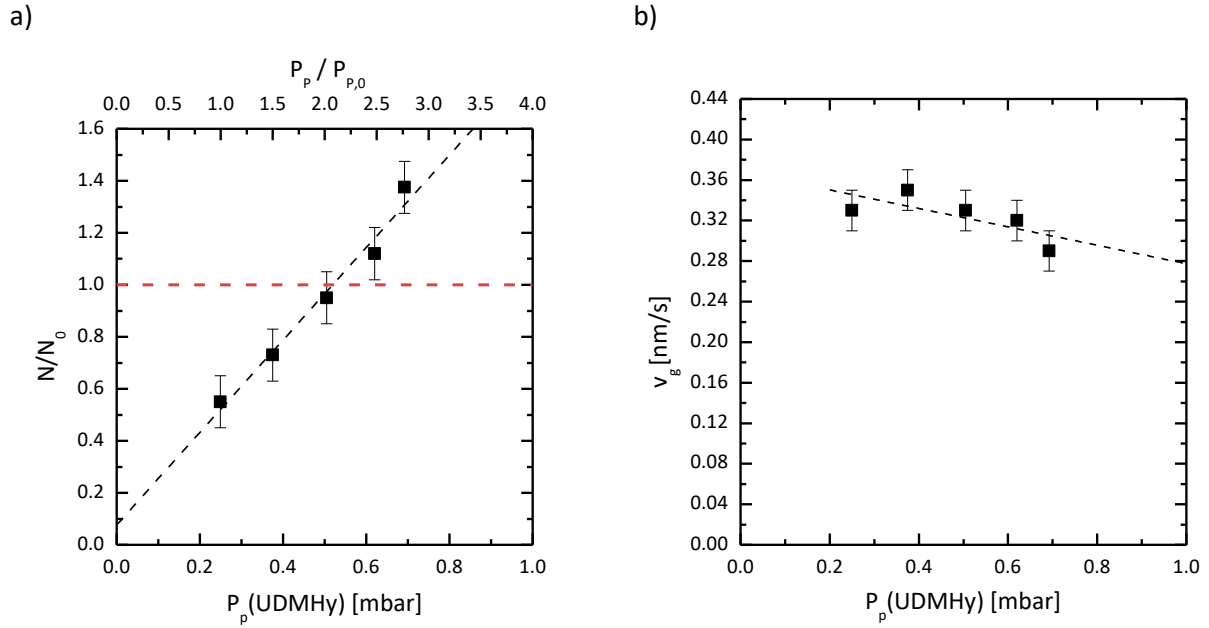


Figure 5.18 a) The nitrogen content of the second Ga(N,As) quantum well relative to the nitrogen content of the first Ga(N,As) quantum well N_0 is plotted with respect to the UDMHy partial pressure. The dashed red line indicates equal nitrogen contents in both quantum wells. To achieve similar nitrogen content, the UDMHy partial pressure must be approximately doubled (top x-axis). The respective growth rates are depicted in b).

The partial pressure of UDMHy is changed between 0.25 and 0.692 mbar, which equals to N/As ratios of 10.55 and 29.3, respectively. The HR-XRD diffractograms of these samples displayed in Figure 5.17 show uniform Ga(As,Sb) diffraction peaks implying no modification of the Ga(As,Sb) layers in dependence of the UDMHy partial pressure. Peaks arising from the Ga(N,As) layers are averaged over both individual Ga(N,As) layers. This means that only the averaged nitrogen incorporation can be measured with this method. However, if the peak intensities increase on the tensile side, as it is the case here for more supplied UDMHy, the nitrogen content is also higher. The relative nitrogen content of the second Ga(N,As) quantum well as a function of the UDMHy partial pressure can be found in Figure 5.18 a). The relative nitrogen content is the nitrogen content of the second Ga(N,As) quantum well divided by the nitrogen content of the first Ga(N,As) quantum well. Owing to the nitrogen determination strategy discussed in section 3.2, which is based on growing multiple samples with an advancing number of quantum wells until the full WQWH is achieved, the error bars of the nitrogen content are reasonably small. In the figure, the linear trend of the nitrogen content suggests that the nitrogen content of the second Ga(N,As) quantum well can be adjusted by changing its UDMHy supply. For optimization purposes, it is beneficial to grow multiple samples and determine the optimum UDMHy partial pressure by applying a linear fit as executed in Figure 5.18 a). The intersection of this linear fit with the horizontal red dashed line coincides with the optimum growth parameters.

While optimizing the nitrogen content of the second Ga(N,As) quantum well, the growth rate of this layer must be kept in mind. If the N/As ratio is changed, the growth rate changes linearly. To account for that, the growth rate can be plotted as a function of the UDMHy partial pressure in Figure 5.18 b), and then a linear curve can be fitted. The growth rate that must be chosen for a given UDMHy partial pressure can be determined from this fit. However, for thin quantum well layers, the HR-XRD thickness determination error bars are severe.

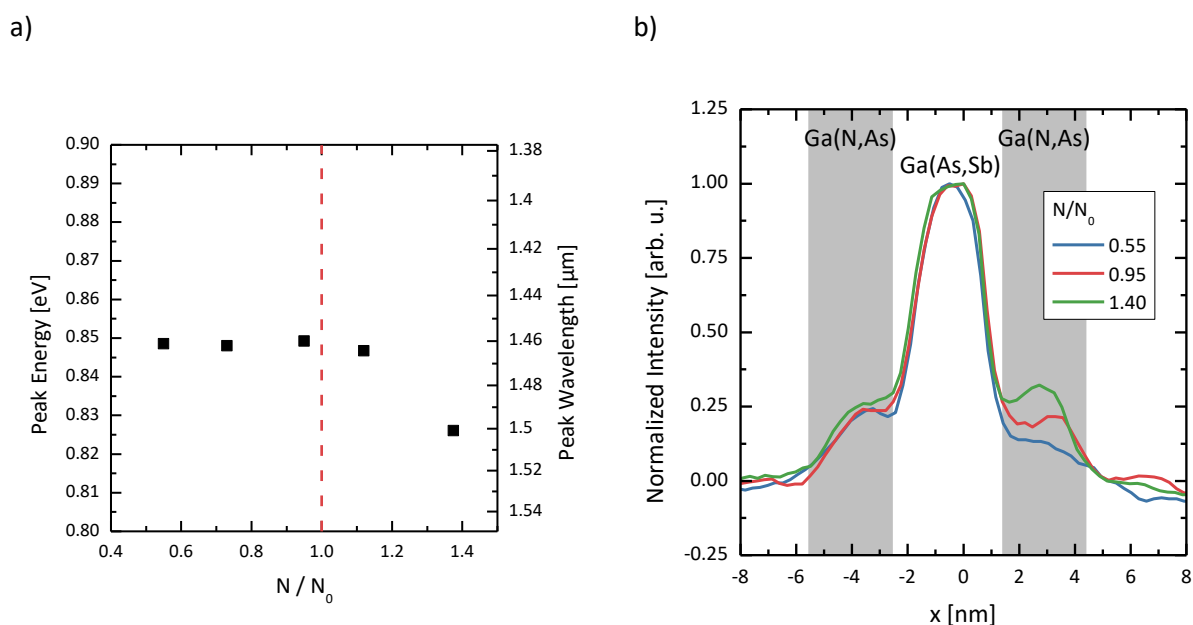


Figure 5.19 a) The PL peak energies of the samples analyzed in Figure 5.18 are depicted in dependence on the relative nitrogen content of the second Ga(N,As) quantum well. b) ADF STEM cross section images considering only the group V columns. The technique used to obtain the related images was described in the last section. STEM measurements were conducted by Varun Shankar Chejarla.

PL spectroscopy and STEM measurements are consulted to confirm this optimization scheme further. The PL peak positions of the type-II transition of the respective samples are drawn as a function of the relative nitrogen incorporation into the second Ga(N,As) quantum well in Figure 5.19 a). The type-II transition is occurring for highly unsymmetric WQWH from the first Ga(N,As) to the Ga(As,Sb) quantum well without involving the second Ga(N,As) quantum well in the process. If the symmetry is high, both electron Ga(N,As) quantum wells are coupling, and the transition is happening from the first coupled quantized state of the Ga(N,As) electron potentials. If the nitrogen content of the second Ga(N,As) quantum well exceeds the nitrogen content of the first, both will decouple again, and the type-II transition occurs from the second Ga(N,As) quantum well to the Ga(As,Sb) quantum well. For the plot in Figure 5.19 a) this means that the type-II peak position does not change until the WQWH structure is symmetrized (N/N_0 of about 1). Then the peak position shifts red with increased nitrogen content in the second Ga(N,As) quantum well. At this transition point, symmetry is

achieved. This behavior can be seen in the measurements, indicating that the optimization scheme is working.

The most precise way to determine the symmetry of the nitrogen incorporation is by analyzing the WQWH with the same STEM method as used in section 5.4. However, the sophisticated sample preparation is consuming too much time to use this technique for optimizing growth parameters before growing laser devices. To show that the method developed here is sufficient, a sample is grown in which WQWH are stacked that are grown with the same growth parameters like for the samples given above. The STEM analysis was carried out by Varun Shankar Chejarla. In Figure 5.19 b) the averaged cross section plots of the images obtained by STEM, only considering group V atomic columns, are shown for three different WQWH. Each WQWH corresponds to a different N/N_0 fraction determined for the same growth conditions with HR-XRD. The sample with a fraction of 0.95 was determined by HR-XRD to be the most symmetric WQWH. This is confirmed by the STEM analysis if the cross section is compared to the sample in which the UMDHy supply was too high (green curve, 1.40) and which is clearly unsymmetric. The small dip in intensity that is located at the interface 2 indicates an incorporation gradient but considering the small structural size of 3 nm quantum well thickness, this gradient can be omitted.

In summary, the optimization procedure of WQWH includes the introduction of a short GI of 20 s followed by the growth of a sample series with varying UDMHy partial pressure for the growth of the second Ga(N,As) quantum well layer. This way an excellent WQWH structure was achieved that will be applied to laser structures in the next section.

5.6 Investigation of Laser structures

In this section, the growth strategies developed in the previous sections were applied to grow laser structures with Ga(N,As)/Ga(As,Sb)/Ga(N,As) WQWH as active regions. First, the electrical properties of the full laser structures, including cladding and SCH layers are presented. Since the nitrogen content has been proven to be a critical parameter for dilute nitride-based laser materials, the influence of the nitrogen content on the device performance will be investigated in the following section. To analyse the loss channels further, the following sections are concerned with the influence of the device performance on the number of WQWH repetitions inside the active region and the comparison of WQWH based laser devices with the properties of “M” quantum well heterostructures (MQWH). These MQWH are similar to WQWH, but the layers are exchanged, which means that two Ga(As,Sb) hole QWs are surrounding a single Ga(N,As) electron QW. Analogous to WQWH, the conduction band edge diagram of such structures resembles an “M”. In the last sections, the nitrogen

precursor used during the Ga(N,As) QW growth showed to have a major impact on the incorporation behavior of nitrogen under the influence of heavy atoms that tend to segregate on the growth surface like indium or antimony. Hence, a further section of this chapter will deal with the influence of these precursors on the device performance. Comparable devices are presented that are grown with either DTBAA or UDMHy. In the end of this section the effect of annealing is discussed because similar dilute nitride-based laser materials showed a drastic optimization in important figures of merit after post growth annealing.

To ensure comparability of the presented laser devices, the cladding layers were grown in a planetary MOVPE reactor that can produce up to 12 claddings on 2” substrates during one process. Since this reactor is dedicated to growing these cladding layers, the processes are optimized and well established. This way a good cladding quality can be ensured. Further details on the device structures can be found in section 3.4.

5.6.1 Double quantum well heterostructure laser device

As first experiment regarding laser devices, a double type-II QWH stack is utilized as the active region (Figure 5.20). It is pumped with the AVTech pulser device described in-depth in section 3.4. The 4 nm Ga(N,As) quantum well contains 2% nitrogen, and the 3.4 nm Ga(As,Sb) quantum well 25% antimony. No additional growth steps like growth interruptions or antimony predepositions were applied.

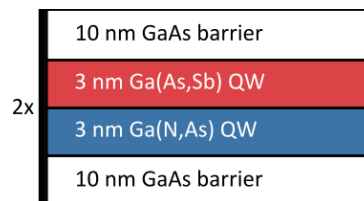


Figure 5.20 Layer structure of the active region. A type-II QWH in which the Ga(N,As) quantum well is deposited first was repeated twice. The repetitions were divided by a 20 nm GaAs barrier.

The dimensions of the devices discussed here are 100 μm as contact width and 700 μm as cavity length. The output power-current (P-I) characteristic is shown in Figure 5.21. In a) the entire curve is plotted, and in b) a zoom to lower pump currents is depicted.

The devices reach lasing threshold at 6.3 A. Below threshold, the optical efficiency is 0.14 mW/A achieving an optical output power of 0.9 mW at threshold. Above threshold, the optical efficiency is 20 mW/A which relates to a differential efficiency of 3.7%. The fits used to obtain these values are marked as red dashed lines in Figure 5.21.

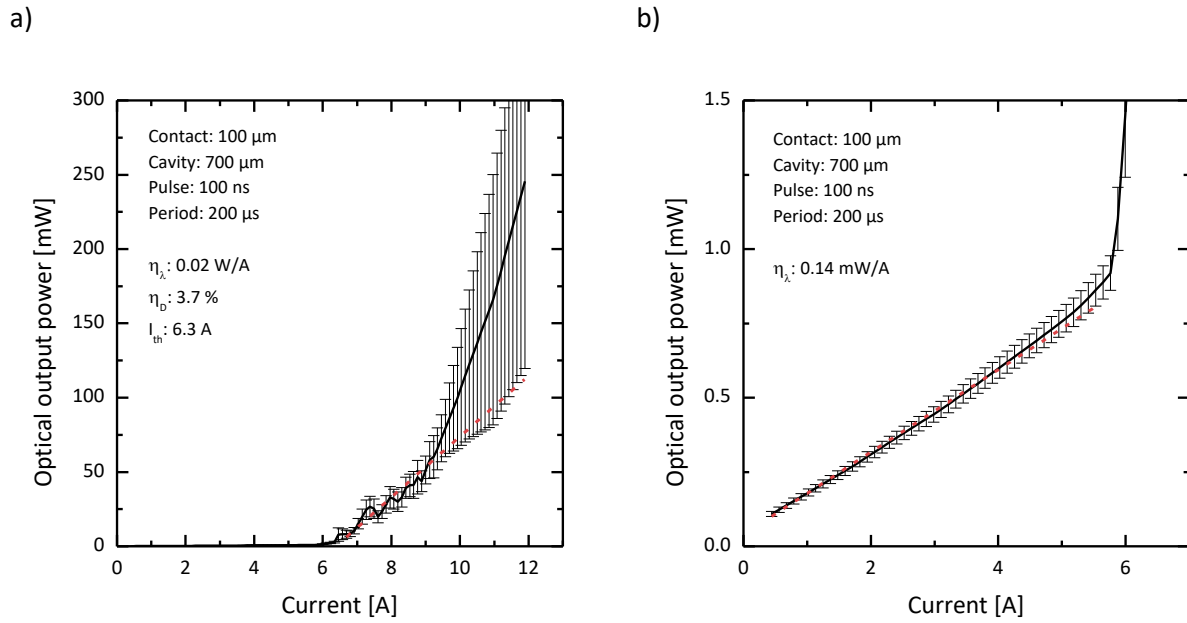
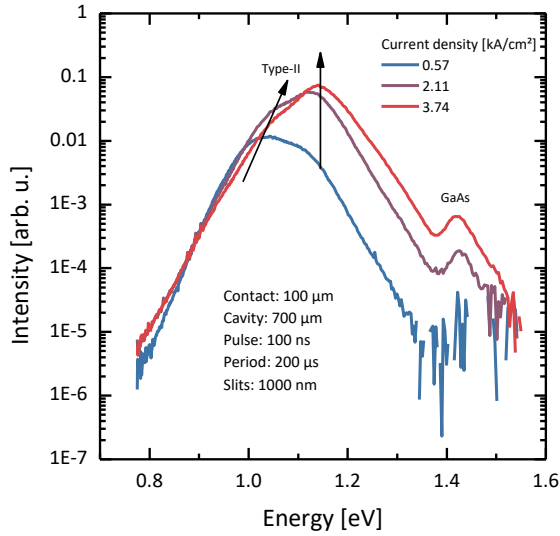


Figure 5.21 P-I characteristics of a laser device containing type-II QWH active regions (Figure 5.20). In a) the full measurement range is depicted, exhibiting the lasing threshold and relatively high output powers. In b) the zoom to the range before reaching the threshold current is shown.

To further interpret these P-I data, complementary EL spectroscopy is carried out. Figure 5.22 a) depicts the spectra retrieved below lasing threshold for three different current densities. A black arrow illustrates the type-II transition. The typical blueshift is present, however, even for small pump current densities a striking second peak emerges, first increasing the FWHM of the emission peak and then exceeding the type-II peak and quickly becoming more distinct. Also, a GaAs substrate or barrier peak is prominently visible. The additional peak slightly changes its position and is located at 1.15 eV. Due to the additional peak exceeding the e1h1 type-II peak at higher pump current densities suggests that the lasing mode is originating from this rather than from the e1h1 type-II transition. An EL spectrum is measured above threshold using the optical spectrum analyzer to verify this further. The spectrum shown in Figure 5.22 b) indicates that the lasing mode is around 1060 nm and can therefore not be related to the e1h1 type-II transition.

All these findings imply that the transition probability for the type-II e1h1 transition is low due to the low wavefunction overlap expected for this type-II QWH. The transition responsible for lasing could be a higher order transition that is more probable because the wavefunction of the electron state is strongly leaking into the Ga(As,Sb) layer. The intensity increase of the GaAs peak is also pointing towards substantial carrier leakage in the structure. For following laser devices, a WQWH must be employed due to its larger wavefunction overlap of the first quantized states.

a)



b)

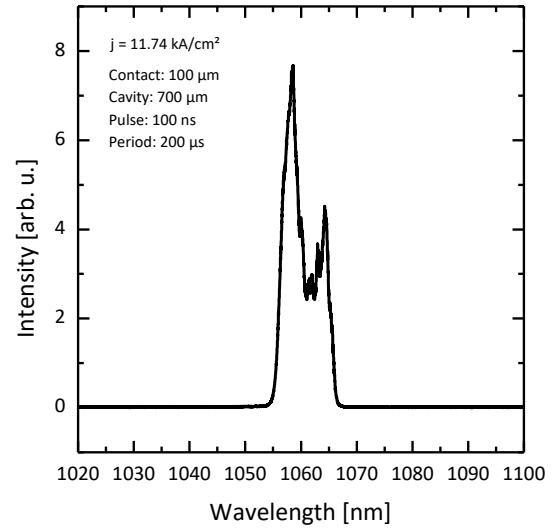


Figure 5.22 a) The EL spectra of a type-II QWH device measured for three different current densities. The type-II peak shifts blue, as indicated by the left arrow. With higher current densities, a second peak raises from the high energy shoulder of the type-II peak. b) The spectrum above lasing threshold suggests that lasing is not based on the e1h1 transition.

5.6.2 Dependence of device properties on nitrogen content

In this section the influence of the nitrogen content on the device performance and properties is investigated. For that, samples from multiple epitaxy sessions are combined. If not stated otherwise, all samples presented in this and all following sections are pumped with the UR19 pulse source. As cavity length and widths 1000 μ m and 50 μ m are used in all presented laser structures in the following of this chapter. In the first part, four samples are discussed in-depth, of which the growth parameters are summarized in Table 5.1.

All P-I curves are plotted in Figure 5.23. The device with the highest optical output power and the highest optical efficiency is the one with 1.7% nitrogen. Both of these parameters seem to decrease stronger than linear with increased nitrogen content. Exceeding lasing threshold was not accomplished by any of the presented structures. The shape of the P-I curves bends for higher excitations, and the optical efficiency at those currents gets lower, which means that the optical output power saturates.

Table 5.1 Summary of growth parameters of samples analyzed in this section.

Sample	A	B	C	D
Ga(As,Sb)				
V/III, Sb/V	4, 0.67	1, 0.26	4, 0.67	4, 0.67
d [nm]	4	3	2.4	3
Sb [%]	27.6	28	28	28
Ga(N,As)				
As/III, N/As	4.8, 7.3	3.3, 10.57	3, 14.62	3, 17.00
d [nm]	4	3	3	3
N [%]	1.7	2	3.3	4.6
Symmetry optimization	20 s GI	20 s GI + N/As optimization	120 s GI	120 s GI

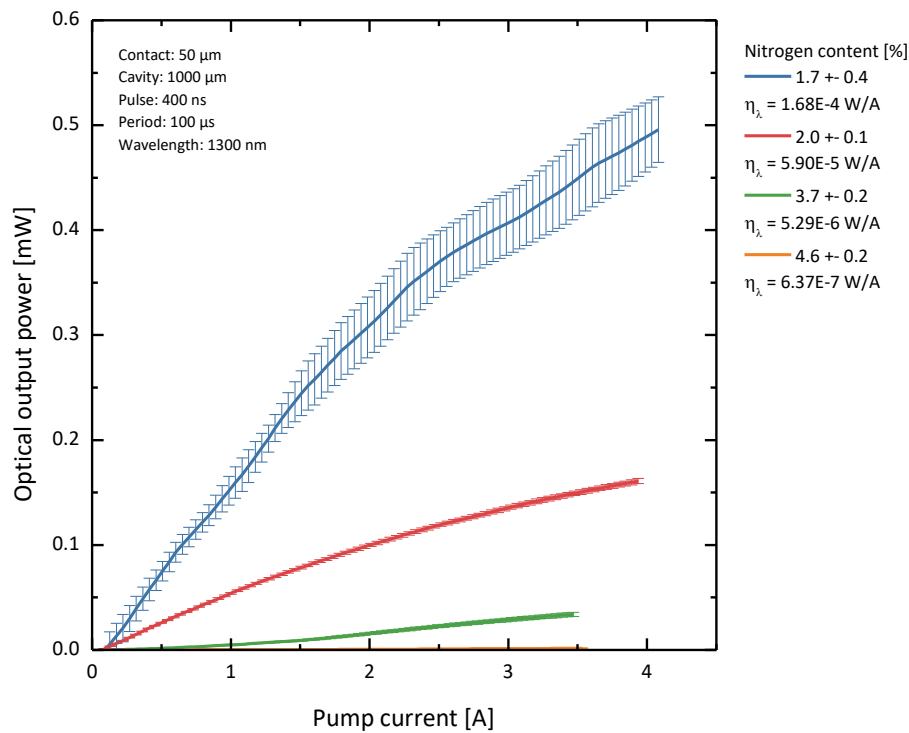


Figure 5.23 P-I characteristic measured at room temperature for four different devices with the UR19 pulser. In these structures, the nitrogen content of the Ga(N,As) layers was varied. All samples exhibit a different order of magnitude for their optical efficiency. The red and the blue curve show a strong saturation at higher pump currents starting from around 2 A.

Despite the significant change of the optical properties of the devices with changing nitrogen content, the electric properties that are depicted in Figure 5.24 do not depend on the nitrogen content at all. Two different electrical characteristics can be identified. The onset voltage and the

differential resistance of the samples with 1.7 and 2.0% nitrogen content are 1.44 to 1.66 V and 0.53 to 0.46 Ω , respectively. This difference is small and can be neglected. The electrical properties of the two other samples were 2.7 V and 0.88 Ω . Changing the active region seems not to change the electrical properties, but they depend strongly on the cladding layers. The cladding layers of the first two samples were grown in the AIX 2600 G3 production reactor, at which these processes are well established, while the other two claddings were grown with less established processes at the AIX 200 GFR reactor.

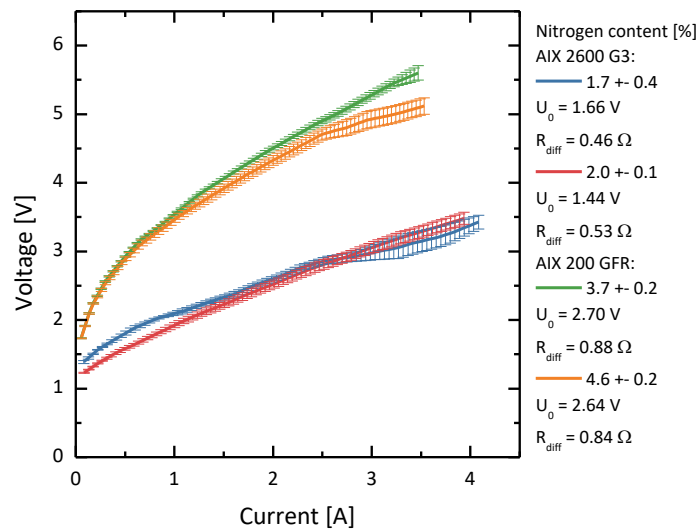


Figure 5.24 Voltage-Current characteristics of samples with different nitrogen contents. Two characteristics can be distinguished, which can be attributed to two different growth processes established at two different MOVPE reactors. The electrical characteristics do not depend on the material of the active region.

To further analyze the devices, their P-I characteristics and electroluminescence spectroscopy measurements are illustrated in detail in Figure 5.25 to Figure 5.28. The pump current density was varied for all devices to investigate the wavelength shift. The green and the orange curve do not show a saturation of the optical output power, but they exhibit the typical behavior of almost no emission for low currents and a higher slope for higher currents, which is expected for LED devices with a major amount of non-radiative losses. Hence, the determination of optical efficiencies is difficult because multiple possibilities exist to fit a linear line into each curve. The fits of P-I curves that get saturated at larger currents are applied from low currents to the point where the saturation sets in to maintain reasonable comparability. In low power P-I curves, these fits are applied beginning from the point where the optical output sets in.

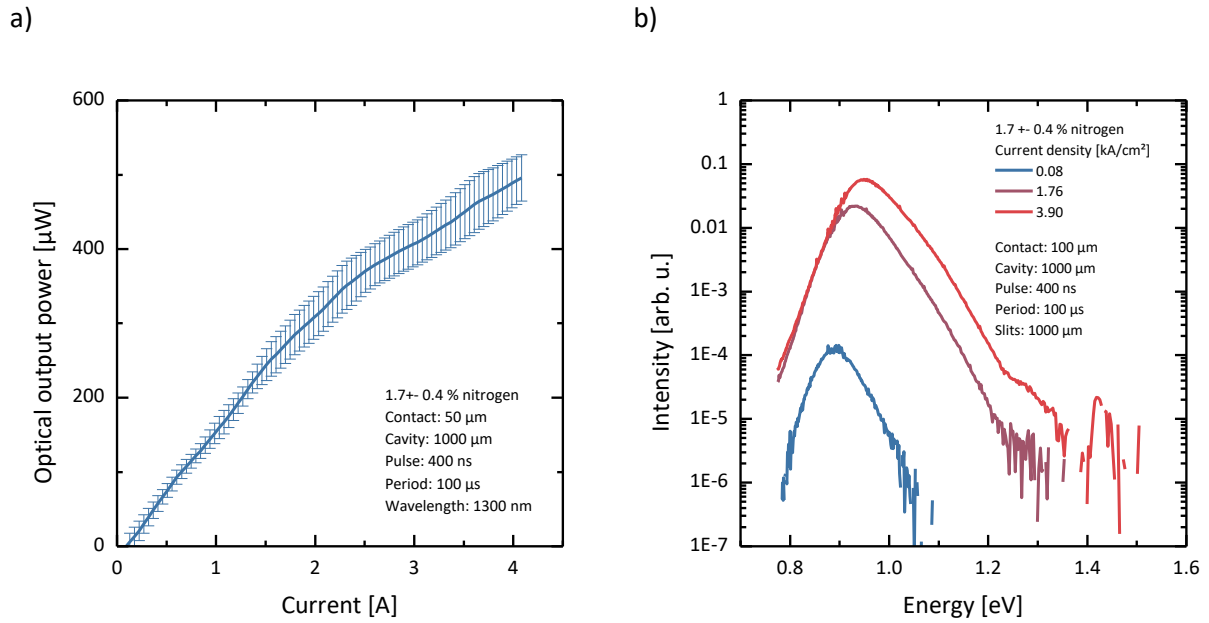


Figure 5.25 Characteristics of the device with 1.7% nitrogen incorporated into the Ga(N,As) quantum wells. a) P-I characteristics. An optical output power of approximately 500 μW is reached with an optical efficiency of $1.68\text{E}-4$ W/A, but a saturation of the optical output power reduces the overall device performance. b) EL spectra for different pump current densities.

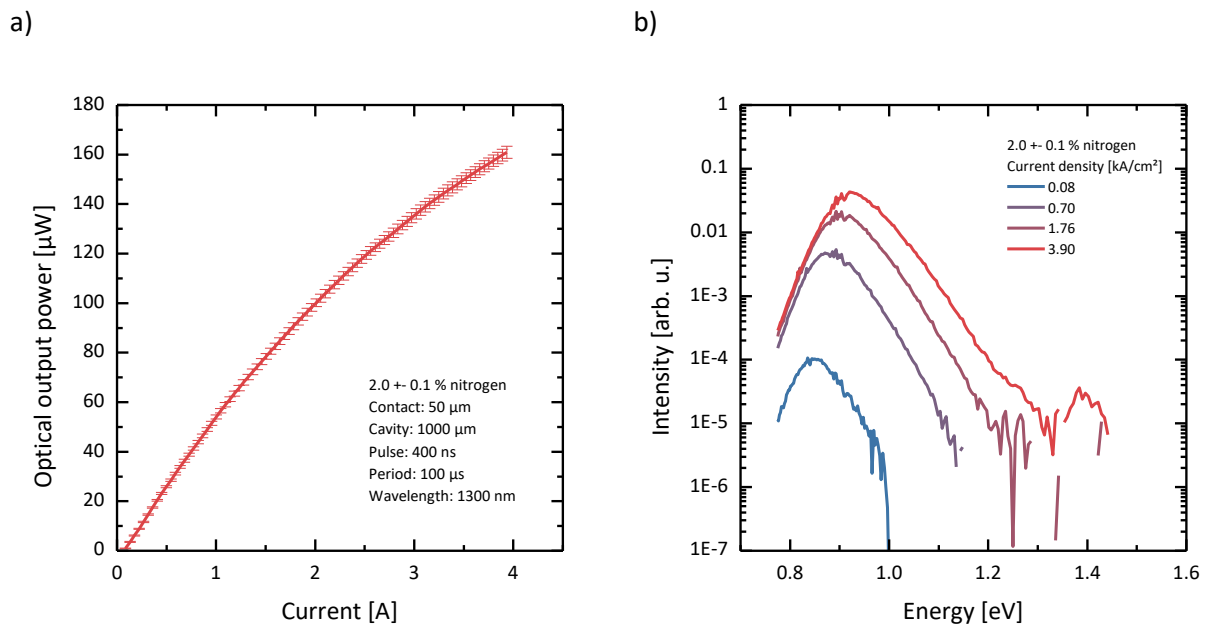


Figure 5.26 Characteristics of the device with 2.0% nitrogen incorporated into the Ga(N,As) quantum wells. a) P-I characteristics. An optical output power of approximately 160 μW is reached with an optical efficiency of $5.90\text{E}-5$ W/A, but a saturation of the optical output power reduces the overall device performance. b) EL spectra for different pump current densities.

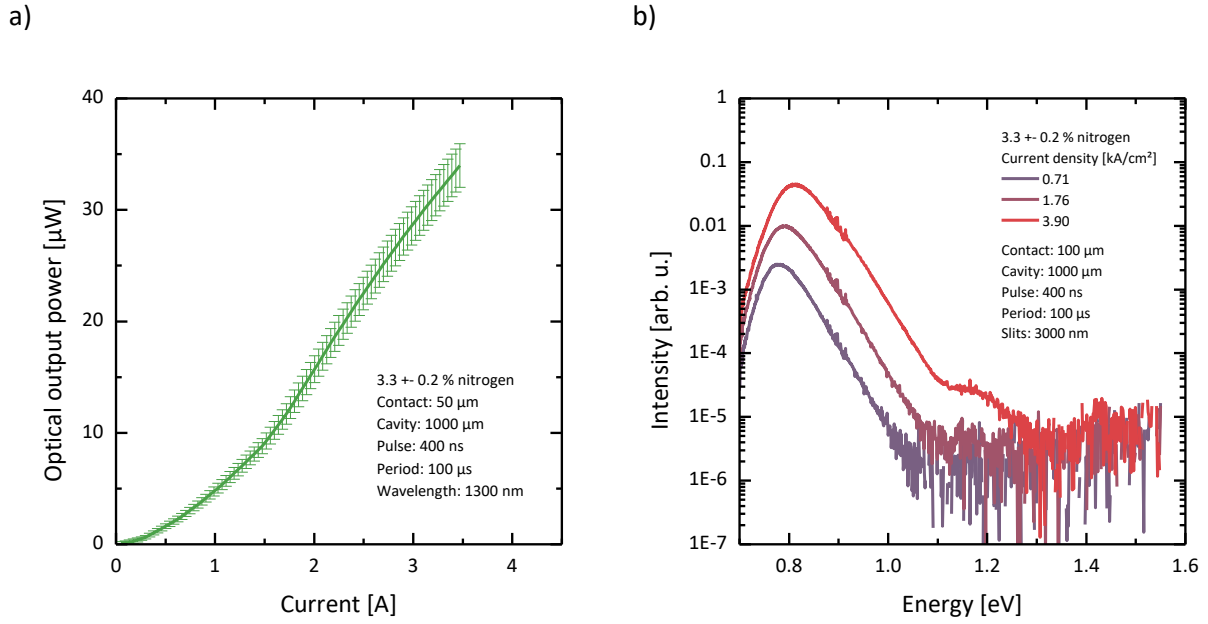


Figure 5.27 Characteristics of the device with 3.3% nitrogen incorporated into the Ga(N,As) quantum wells. a) P-I characteristics. An optical output power of approximately 35 μW is reached with an optical efficiency of $1.28\text{E}-5$ W/A. b) EL spectra for different pump currents densities.

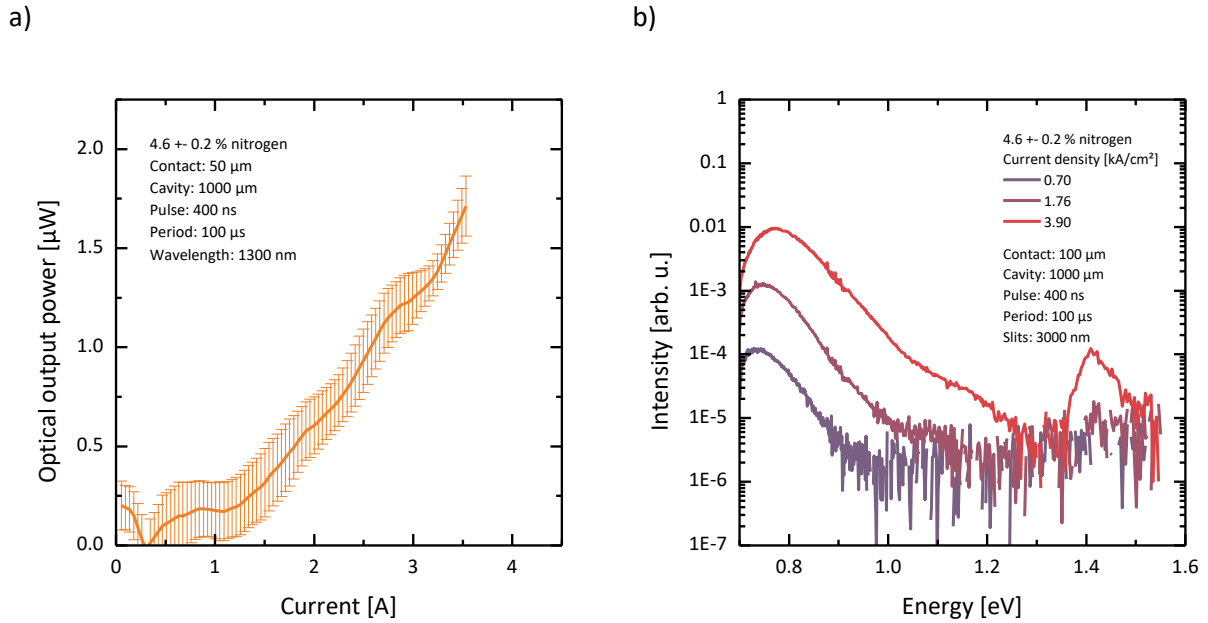


Figure 5.28 Characteristics of the device with 4.6% nitrogen incorporated into the Ga(N,As) quantum wells. a) P-I characteristics. An optical output power of approximately 1.75 μW is reached with an optical efficiency of $6.37\text{E}-7$ W/A. The optical output power is so low that the signal to noise ratio is bad. b) EL spectra for different pump currents densities.

In all EL spectra distinct type-II peaks are visible that are shifted red with larger nitrogen content. In contrast to the device discussed in the previous section, no higher order transition emerges. However, a peak at 1.42 eV arises for almost all devices, representing the luminescence from the GaAs barriers or the GaAs SCH layers. To make the shift in emission wavelength clearer, the peak

energy of these type-II peaks is plotted in Figure 5.29 as a function of the pump current density. In this figure, the heavy linkage between nitrogen content and emission wavelength is pointed out. All devices achieve at least emission wavelengths above $1.3\ \mu\text{m}$ and the samples with nitrogen contents above 3% exceeded $1.55\ \mu\text{m}$ as well, contrary to the theoretical predictions given in Figure 5.2. The deviation between experiment and theory could be explained by different hetero offsets used in the simulations. Alternatively, the real nitrogen composition profile could be different than the ideal box profile assumed in the simulations. Apart from that, the emission spectra get blue-shifted with larger pump current density. This unique feature of type-II-based devices is discussed in depth in section 2.6. It is related to the charge carrier separation and many particle properties. The blueshift is larger for the samples with nitrogen contents below 3.0%. For these samples, the blueshift seems to saturate at higher pump current densities. The other two blueshift curves of samples above 3% nitrogen show a linear dependency between emission wavelength and current density, and no saturation takes place for the considered current densities. This can be explained by the much lower effective carrier density in these structures due to nitrogen induced defects and the resulting non-radiative recombinations. If the optical quality of all structures were similar, the current density dependent blueshift would be equal.

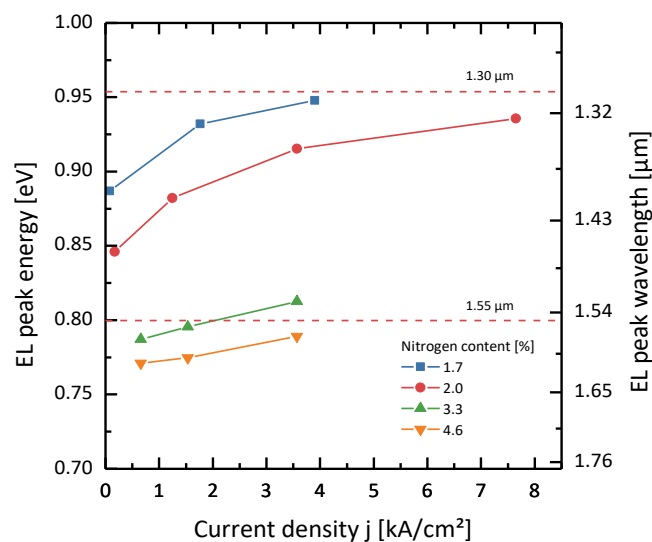


Figure 5.29 Type-II transition peak positions obtained by EL with respect to the applied current density. The peaks are blue shifted for all samples, as expected devices based on type-II transitions. However, the strength of the blueshift is lower for larger nitrogen contents. This can be attributed to the higher density of nitrogen related non-radiative recombination centers.

In order to find out more about these loss processes, an experiment-theory comparison is conducted. The predicted blueshift as a function of the carrier density shown in Figure 5.2 is used to approximate the real carrier density in the realized structures by comparing the amount of blueshift of the experiment with these theoretical values. Since the theory values are shifted due to errors in

the utilized hetero offsets, only the energetic difference to low excitation is considered. This means that the developed algorithm first calculates the blueshift with respect to the low excitation density and builds a function that returns the carrier density as a function of this blueshift. Then, the same blueshift is calculated for the experimental data. This requires measured low excitation EL spectra. The function described above is then evaluated with the obtained experimental blueshift. As a result, the carrier density can be determined as a function of the current density for all different samples. In Figure 5.30 this evaluation is presented for the data given in Figure 5.29. Below 2 kA/cm² the correlation between the current density and the carrier density is equal for the samples with 1.7 and 2.0% nitrogen. Then, the carrier density reached in the sample with 2.0% nitrogen exceeds the value obtained for the 1.7% nitrogen sample. Carrier densities far below these values are determined for the samples with nitrogen contents larger than 3%. These curves are almost linear, however, no measurements at low excitation energies are available, so the accuracy of these curves is limited. Based on these results, the principal loss channel is different for different nitrogen contents. For low nitrogen contents below 3%, the carrier injection is efficient, suggesting only a minor number of charge carriers get lost by defect recombination. If the current density is further increased, the injection efficiency gets reduced, indicating that carriers get lost because of low barriers in the conduction band. If the nitrogen content is increased above 3%, a major number of charge carriers get lost by defect recombinations, resulting in a lower charge carrier injection efficiency.

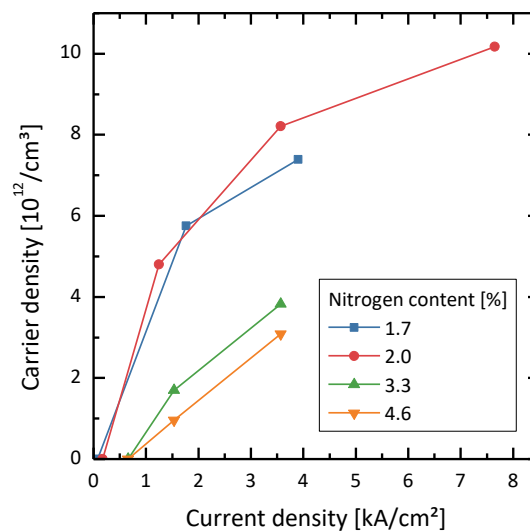


Figure 5.30 Correlation between current density and carrier density inside the WQWH. The values were obtained by comparing the amount of blueshift of the experimental data with the blueshift expected from theory, simulated by Dr. Ada Bäumer. Since no low excitation EL spectra of the 3.3% nitrogen and the 4.6% nitrogen samples are available, the respective curves should be shifted to slightly higher carrier densities.

To gain a more definite picture of the dependency between nitrogen content and device properties, the optical efficiencies as a function of the nitrogen content of all suitable devices, including devices

that are possibly asymmetric in nitrogen content, are plotted in Figure 5.31 a). Due to the dissimilarity of these values in terms of order of magnitude, a logarithmic representation is chosen. In this figure, a linear fit nicely describes the dependence between optical efficiency and the nitrogen content of the device, suggesting an exponential decay as the interrelationship between these two parameters. In comparison, the simulated peak absorption minima are plotted in Figure 5.31 b) for different nitrogen contents and as a function of the carrier density. Negative values indicate gain instead of absorption. The gain is highest for samples with lower nitrogen contents. This is intuitively the case because the barrier height to the Ga(As,Sb) quantum well is lowest for low nitrogen contents, and hence a stronger coupling between the Ga(N,As) quantum well states results in a more significant wavefunction overlap. This supports the overall larger optical efficiencies of samples with lower nitrogen content to some extent, but it cannot explain the drastic exponential decay behavior, which must be accounted for the large number of nitrogen induced defects. When comparing the transparency carrier density with the carrier densities determined in Figure 5.30, the question arises why no gain was observed in the experimental devices. This can be explained by the fact that most loss processes or non-radiative recombination paths depend strongly on the carrier density, which increases the threshold current density. These effects were not taken into account by the simulation software. One exception is Auger recombination, which is included in the simulation. Since the gain is highest for lower nitrogen contents, a reduced influence of Auger recombinations can be expected for these samples indicating that Auger recombination is not a limiting factor.

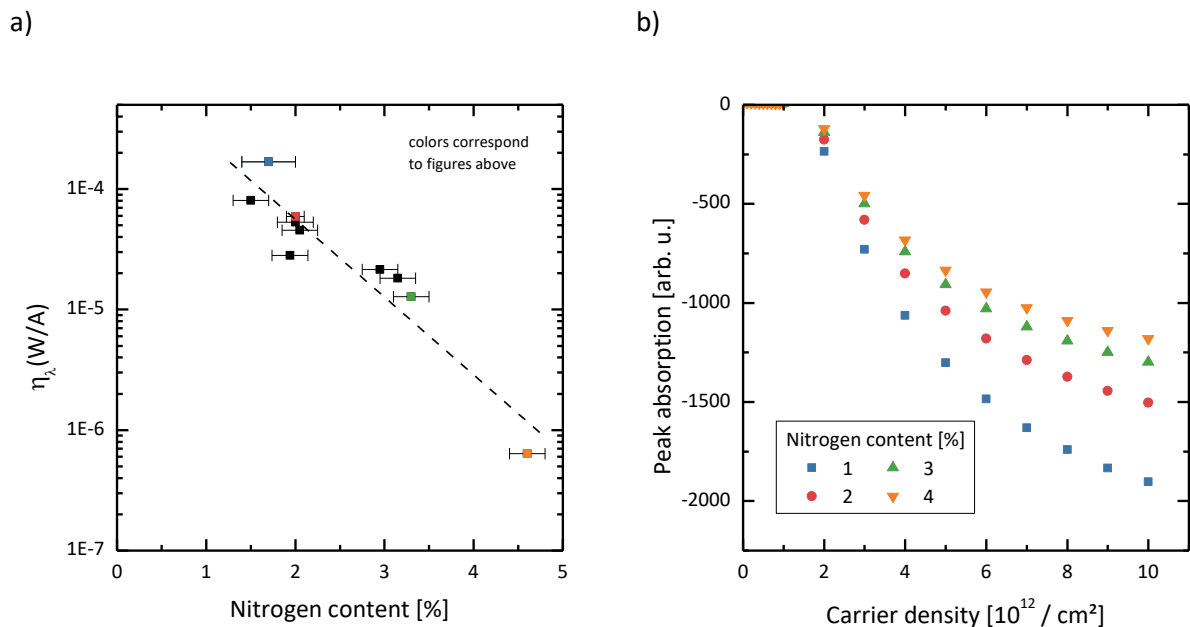


Figure 5.31 a) Optical efficiency of all measured devices as a function of the nitrogen content in the Ga(N,As) quantum wells. All data points can be described by a linear function in this logarithmic graph, indicating an exponential decay of the optical efficiency with nitrogen content. As comparison, the simulated peak absorption values in dependence on the carrier densities are depicted in b). A negative absorption means gain. All simulated values are provided by Dr. Ada Bäumner and calculated for a WQWH structure with an individual layer thickness of 3 nm and an antimony content of 28%.

In Figure 5.32 the type-II transition energies measured for pump currents between 3 and 4 kA/cm² of the same samples are depicted with respect to the nitrogen content. Here, an approximately linear correlation between the emission wavelength and the nitrogen content is found. An emission wavelength of 1.55 μm can be achieved with nitrogen contents of about 3 to 4%, while 2% nitrogen yields 1.3 μm .

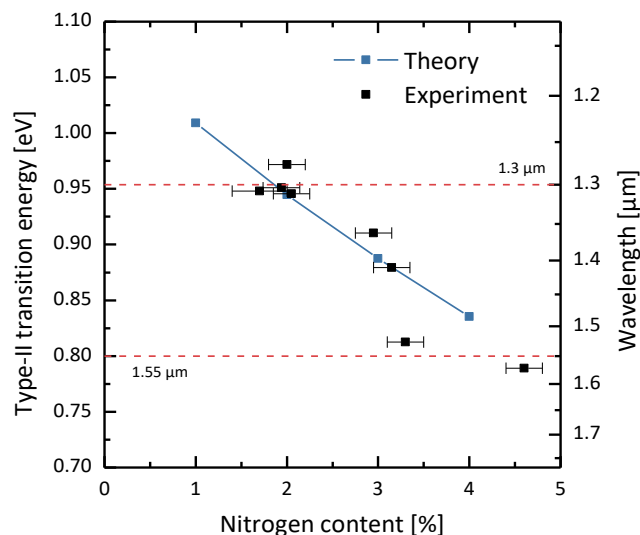


Figure 5.32 Energetic position of the type-II transition measured in EL with current densities between 3 and 4 kA/cm². All data points create a line that shows that an emission wavelength of 1.55 μm can be reached with nitrogen contents in the Ga(N,As) quantum wells between 3 and 4%, while 1.3 μm can already be reached with nitrogen contents as low as 2%. The experimental data was obtained for relatively high excitation densities. However, it agrees nicely with the simulated values, besides the fact that they were simulated for very low excitation densities, highlighting the error in the assumed hetero offset. The theory dataset was simulated by Dr. Ada Bäumner. The blue line serves as a guide to the eye.

The experimental findings indicate a fundamental problem with Ga(N,As) for laser device applications. The optical efficiency in the LED regime is decreasing exponentially with the nitrogen content in the Ga(N,As) layers. All samples investigated fit into this exponential decay behavior, despite the nitrogen symmetry and other vital parameters were not optimized, suggesting that the optical properties depend mostly on the total nitrogen content. As already known from literature, nitrogen induced effects like nitrogen clustering and carbon incorporation give rise to non-radiative recombinations as a competing recombination process. These non-radiative recombination processes are expected to be more prominent for higher nitrogen contents, and since the number of non-radiative recombination centers is limited, they can be saturated. If the two samples with 3.3 and 4.6% nitrogen are considered, they are expected to exhibit the largest number of non-radiative recombination centers. These are draining charge carriers out of the active region, leading to a much lower charge carrier density in the active region. This affects that the blueshift is much weaker than for other samples since the blueshift is dependent on the real charge carrier density. Their P-I

characteristics also show the lowest optical efficiencies and no saturation of the optical output power.

The optical output power saturates for lower nitrogen contents, below 3%. In these samples the effect of non-radiative recombination centers is not as severe as in the samples with higher nitrogen contents. Hence, the charge carrier density is higher than for the samples with a higher nitrogen content than 3%. This gets backed up by the larger blueshift of the respective EL spectra and the much larger optical efficiency. However, a second major loss channel is becoming the dominant loss process. The saturation of the P-I curves and the blueshift indicates that the charge carrier densities in the active region are saturating as well. This hints to a strong carrier leakage due to low quantum well barriers and high carrier densities. Since this effect is only present for lower nitrogen contents, the conduction band offset is assumed to be too low. Combined, both suggested loss processes attain that no room temperature lasing can be observed for these WQWH structures. It should be noted that the device with the lowest nitrogen content achieved an optical output power of 500 μW . As highlighted in section 2.5, lasing is a process that depends on the interplay between carrier density in the active region and the photon density in the cavity. The type-II QWH laser device discussed in the last section showed an optical output power in the same order of magnitude as 500 μW . This strongly indicates that the photon density in both devices is similar and is not an issue for the WQWH device with 1.7% nitrogen. However, the charge carrier density is not high enough due to carrier leakage, so charge carrier population inversion cannot be achieved. If the nitrogen content is raised, a sufficiently high photon density cannot be achieved and lasing threshold fails to be reached.

In summary, nitrogen incorporation introduces non-radiative recombination centers that reduce the charge carrier density of the active region and the optical efficiency in the LED regime. For higher nitrogen contents this effect is more severe, leading to an exponential decay of the optical efficiency with nitrogen incorporation. For lower nitrogen contents, the conduction band hetero offset is assumed to be too low to achieve population inversion because due to the still considerable amount of non-radiative recombinations, high pump currents must be used.

5.6.3 Number of “W” quantum well heterostructures

Since the modal gain can be optimized by introducing multiple repetitions of the active WQWH²⁵², the influence of the number of WQWH on the optical properties is investigated based on the structure with 2.0% nitrogen content presented already with two repetitions in the last section. A sample series consisting of three samples with WQWH counts between 1 and 3 is grown. The Ga(As,Sb) quantum wells were deposited with 3 s predeposition of antimony prior to the quantum

well growth and 20 s interface treatment by TBAs stabilized growth interruptions. The thickness of these layer is 3 nm and the antimony content 28%, while the 3 nm thick Ga(N,As) layers contain 2% nitrogen. The nitrogen incorporation symmetry is optimized by adjusting the UDMHy partial pressure during the growth of the second Ga(N,As) quantum well, according to section 5.5.

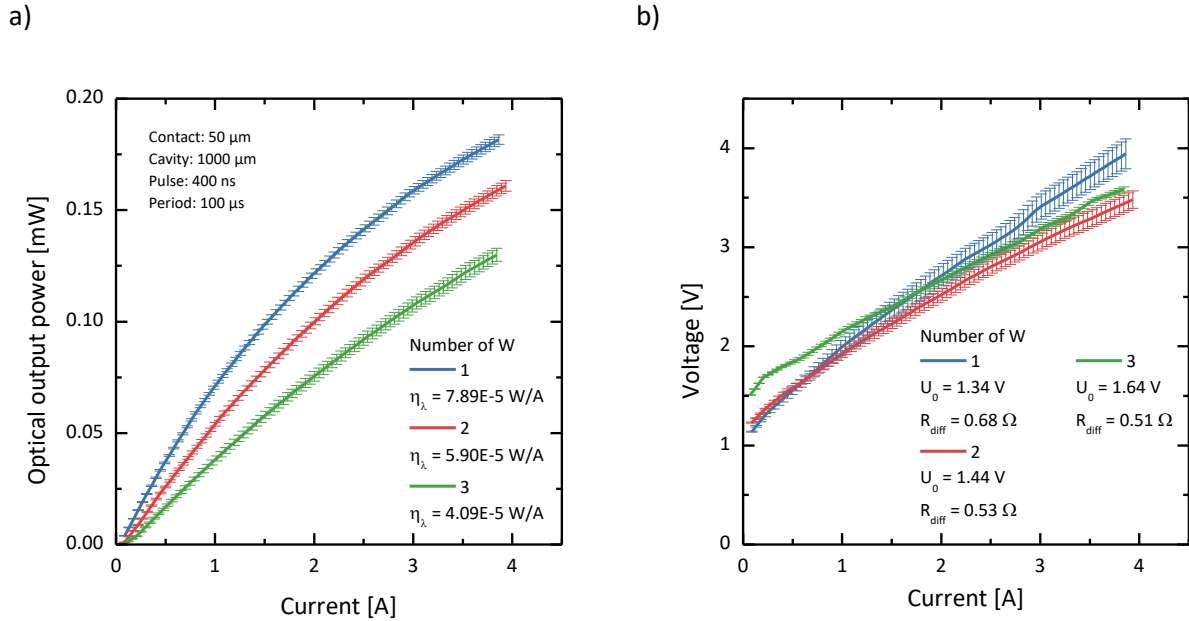


Figure 5.33 a) P-I curves for devices with varying count of WQWH as active region. The current is divided by the number of WQWH. In b) the respective V-I curves are shown.

The P-I characteristics for all three samples pumped with the UR19 current source are depicted in Figure 5.33 a) and the V-I characteristics in b). In a) a drawback of multiple WQWH is shown: If the number is raised and multiple WQWHs are stacked, the charge carriers supplied by the current flow are divided by the number of WQWH, resulting in lower charge carrier density per WQWH for equal pump currents and lower output power. To account for that, the optical output power is plotted as a function of the current density per WQWH in Figure 5.34 b). All P-I curves exhibit a saturation of the output power already discussed in the previous section. This saturation becomes less pronounced if the number of WQWH is increased.

The cladding layers of all three samples were not only grown in the same reactor, but also during the exact same process. Thus, all modifications of the V-I curves by the number of WQWH must be attributed to these. The number of WQWH modifies mainly the onset voltage U_0 , which could be due to the thicker intrinsic active region stack, while the differential resistivity is only slightly decreased with a higher number of WQWH. Hence, the overall influence of the number of WQWH on the electrical properties is low and can be neglected.

Owing to the saturation effect, it is difficult to determine optical efficiencies for the P-I curves. Therefore, the differential optical efficiency is given in Figure 5.34 a) by the first derivative of the

respective P-I curves. Because of the already discussed division of the pump current densities, the optical efficiency of the sample with only one WQWH is the highest, while the peak optical efficiencies drop with the number of WQWH repetitions. However, the drop of this differential optical efficiency with pump current is highest for the sample with only one WQWH. These effects can all be attributed to the lower charge carrier density if a larger number of WQWH is deployed as active region, as the same pump current corresponds to different pump current densities per WQWH.

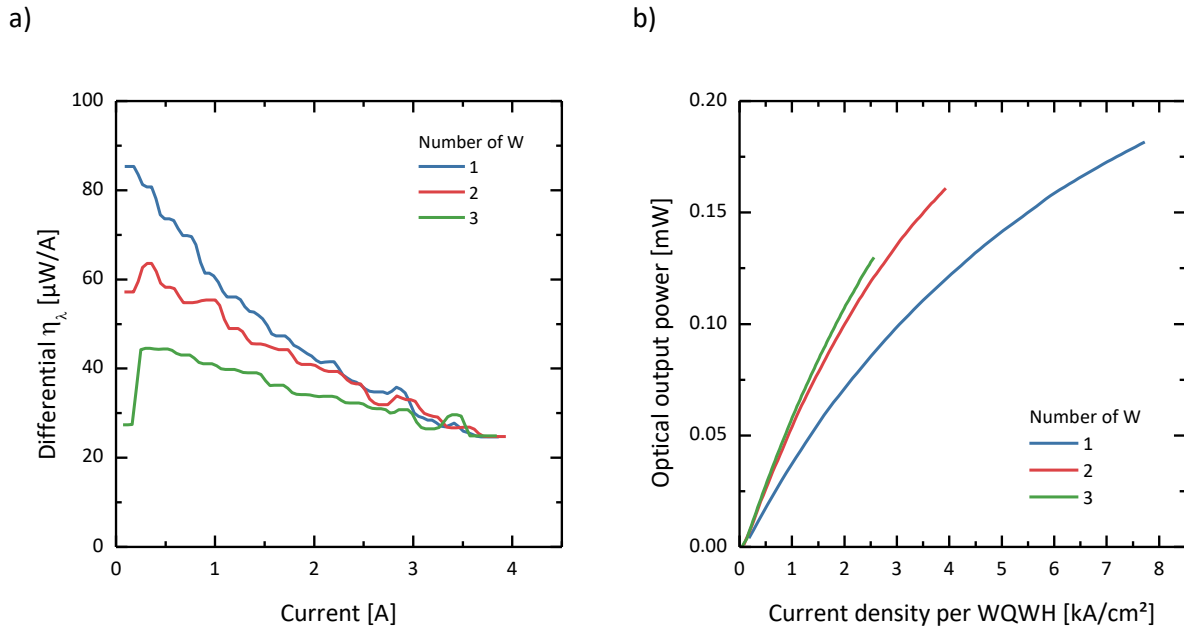


Figure 5.34 In a) the differential optical efficiencies are plotted as a function of the pump current. The differential optical efficiency can be determined by calculating the first derivative of the P-I curves given in Figure 5.33 a). In b) the optical output power is given as a function of the current density per WQWH. With this, the effect of reduced carrier density per WQWH can be ruled out for further analysis.

The optical output power as a function of the current density per WQWH can be seen in Figure 5.34 b). Here, the effect of different charge carrier densities is ruled out. The most important feature of this plot is the fact that the optical output power per WQWH is higher for a larger number of WQWH if an equal current density per WQWH is considered. This is beneficial for the overall device performance. However, the total optical output power gets reduced with the number of WQWH, and the photon density required for lasing could eventually not be achieved. The bowing of the curve for 1 WQWH is drastically higher than the bowing for the other samples, indicating that the charge carrier leakage really is a major loss process, as already proposed in the previous section.

To prove the theory of carrier leakage even further, the EL spectra for different pump current densities are measured for all samples. They are depicted in Figure 5.35. In all these spectra, a clear type-II transition peak is present. Besides that, the GaAs barrier and SCH peak at 1.42 eV is observable for higher pump current densities. It gets more distinct if the number of WQWH in the

sample is low. This means that the charge carrier density in the quantum wells is too high, and due to band filling effects, the charge carriers leak into the barrier layers. For the sample with 1 WQWH, the EL spectrum measured with 7.54 kA/cm^2 current density, a shoulder on the higher energy flank of the type-II peak emerges, which could be a higher order transition that emerges because of the larger current density.

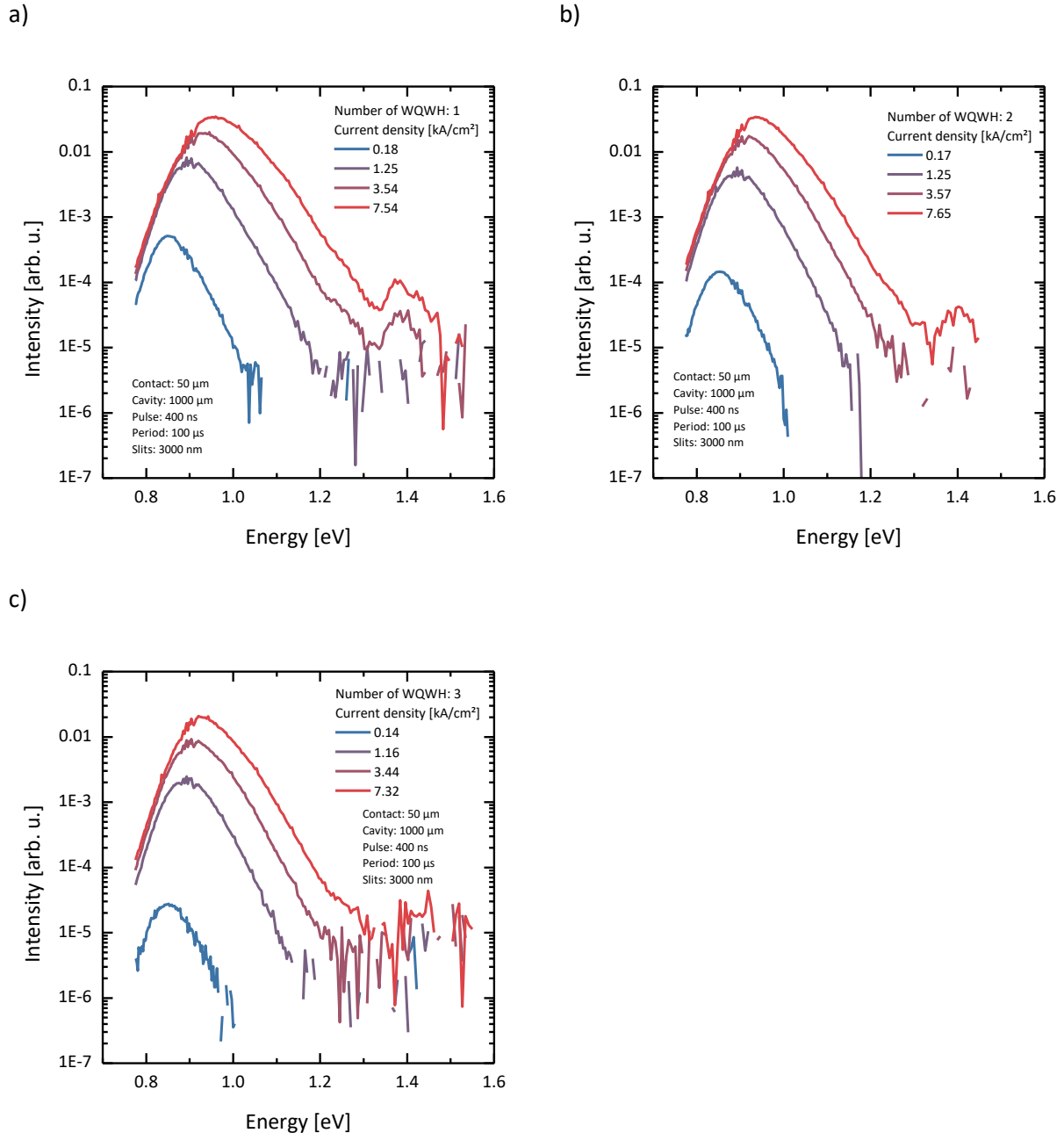


Figure 5.35 EL spectra measured for different numbers of WQWH as active region. a) 1 WQWH, b) 2 WQWH, c) 3 WQWH. The type-II peak is visible for all samples and all pump current densities. For higher pump current densities above 7 kA/cm^2 , the GaAs barrier and SCH luminescence emerges at 1.42 eV. For the sample with only 1 WQWH this is already true for 3.54 kA/cm^2 .

To further analyze the current density per WQWH, the blueshift of the type-II transition visible in the EL spectra of Figure 5.35 is plotted as a function of the current density per WQWH in Figure 5.36. All

type-II peaks shift blue in a similar strength, which means that the current density per WQWH is approximately equal for all stacked WQWH. It could have been the case that the center WQWH is not receiving the same number of charge carriers as the outer two, but this seems not to be the case. However, the saturation of the blueshift is present in all samples with similar strength, suggesting carrier leakage in all samples.

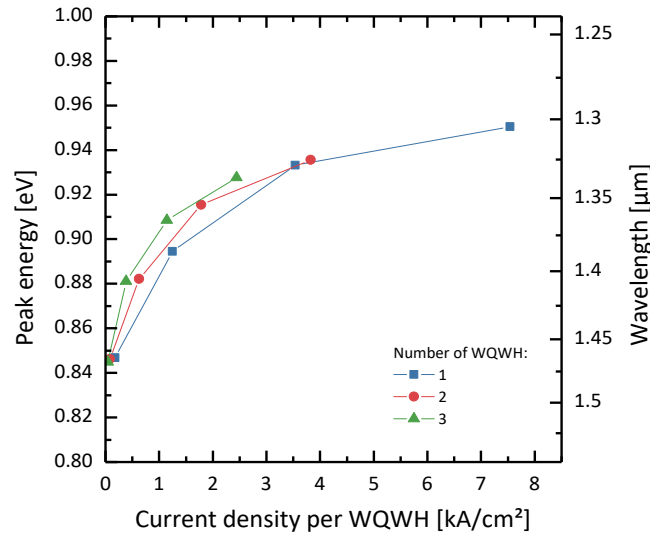


Figure 5.36 Blueshift of the type-II peak energy as a function of the current density per WQWH. A strong blueshift from 1.45 μm to 1.3 μm emission wavelength can be observed. All samples show approximately the same blueshift behavior, indicating that all WQWH get supplied by equal numbers of charge carriers.

In conclusion, the number of WQWH employed as active region is critical for device performance. On the one hand, a higher number of WQWH is advantageous for the optical output power per WQWH, but on the other hand, the total optical output power decreases. The charge carrier leakage process counteracts the lasing process, especially for low numbers of WQWH. A trade-off between reduced charge carrier leakage and reduced optical output power must be found in order to achieve a sufficiently high photon density and population inversion. This compromise is recommended to be two WQWH. Thus, most presented devices consist of two WQWH.

5.6.4 Nitrogen precursor comparison: DTBAA and UDMHy

In section 5.2.2, the advantage of DTBAA compared to UDMHy as nitrogen precursor for the investigated WQWH was discussed. The main advantage is the highly improved nitrogen incorporation efficiency, even if larger elements like antimony or indium are present during the growth. Therefore, no further symmetry optimization is required to grow Ga(N,As)/Ga(As,Sb)/Ga(N,As) WQWH laser devices. In this section, the influence of the nitrogen precursor on the device performance is investigated for one particular device. The device presented already in the previous sections with 2% nitrogen, 28% antimony, and an individual layer thickness of

3 nm will be used as the sample grown with UDMHy. Growth temperatures of 550°C were used, and 3 s of antimony predeposition combined with 20 s of TBAs stabilized growth interruption were implemented for the Ga(As,Sb) layer growth. Two repetitions of the full WQWH were employed. A similar sample exhibiting equal compositions and thicknesses was deposited with DTBAA as precursor. Due to the necessity of lower temperature epitaxial growth with this precursor, the sample was grown at 525°C, and the duration of the TBAs stabilized growth interruption was increased to 30 s because antimony desorption is assumed to be weaker at these temperatures.

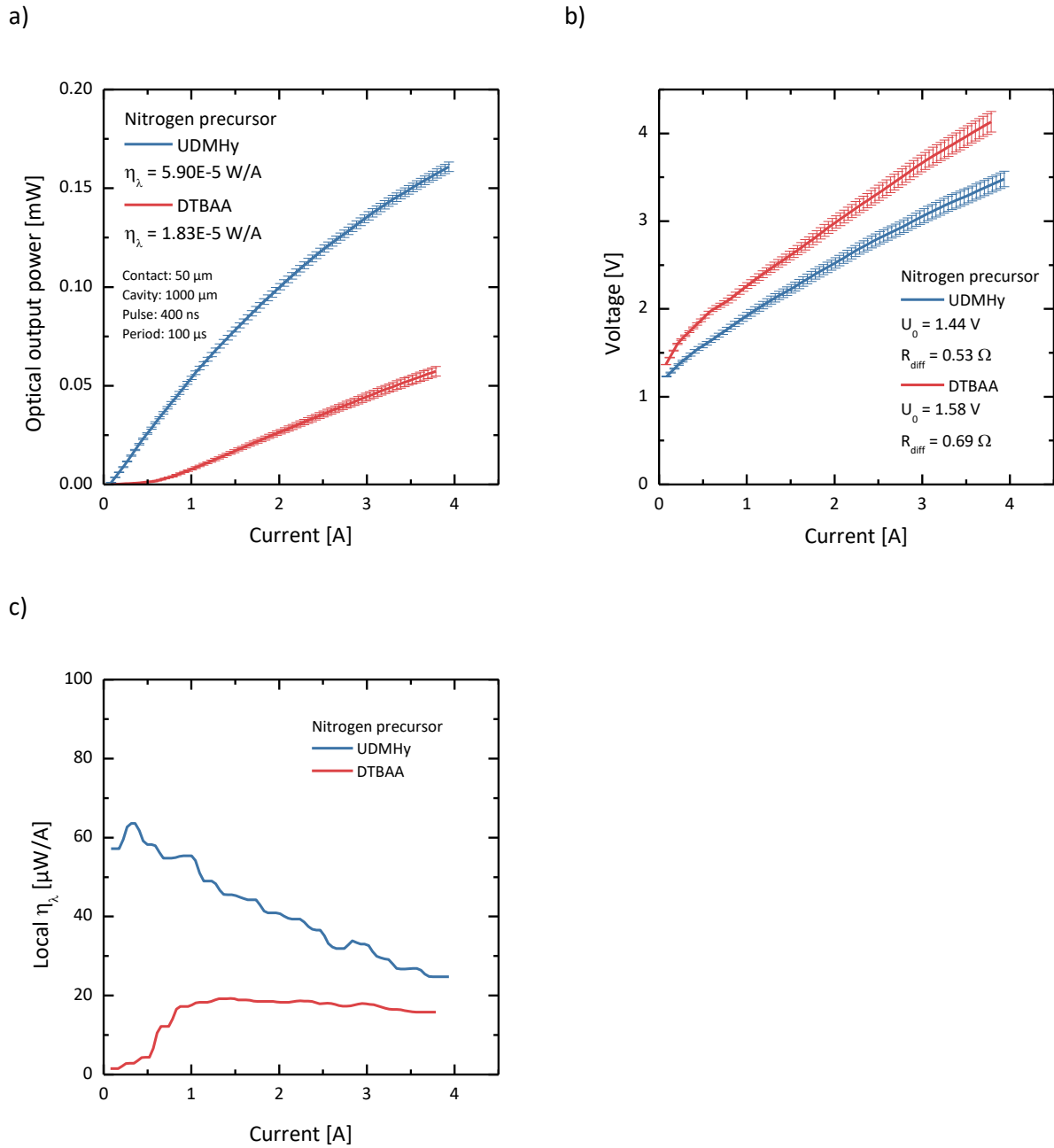


Figure 5.37 The optical and electrical properties of a sample grown with DTBAA and one grown with UDMHy are compared in this figure. In a) the P-I characteristics are plotted, in b) the V-I curves are illustrated, and in c) the differential optical efficiencies are given as a function of the pump current, which are the first derivatives of the curves in a).

The P-I characteristics of both samples are compared in Figure 5.37 a). The optical output power achieved for the UDMHy grown sample is much higher than 50 μW achieved for the DTBAA grown sample. Additionally, the optical efficiency of $5.90\text{E-}5 \text{ W/A}$ is reduced drastically by a factor of 3.2 for the DTBAA sample to $1.83\text{E-}5 \text{ W/A}$. The shape of the DTBAA P-I curve shows no saturation effect but also no optical output power for very low pump currents. These effects can also be seen if the differential optical efficiency as a function of the pump current that is plotted in Figure 5.37 c) is considered. From this figure, it gets clear that the P-I curve of the UDMHy sample is saturating strongly, as already discussed in the previous sections, and the DTBAA sample is first not emitting any light, and after a certain current is reached, the slope of this curve is only changing slightly. Since the DTBAA precursor is still in an experimental stage, the purity is expected to be low. This means that especially oxygen incorporation is expected if this precursor is used, which gives rise to non-radiative recombination as a competing process to the radiative recombination. These non-radiative recombinations lower the charge carrier density in the WQWH resulting in lower output power and lower optical efficiency. On the other hand, the carrier leakage only plays a minor role causing the saturation of the optical output power not to be as significant as for the UDMHy grown sample.

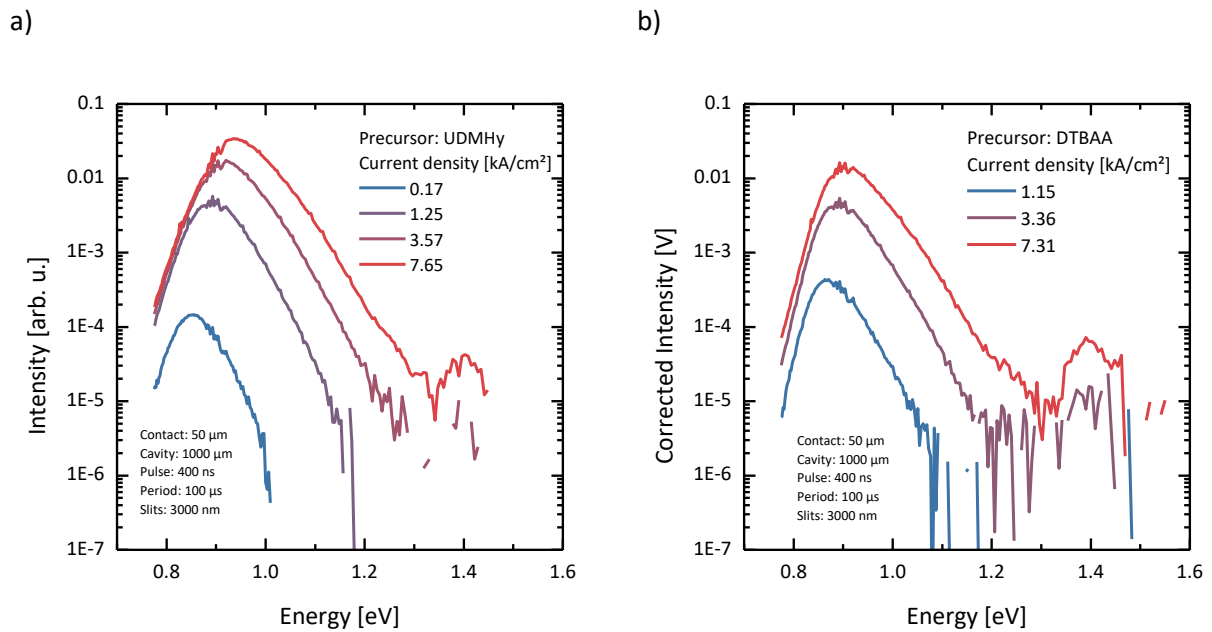


Figure 5.38 EL spectra for different pump current densities of similar samples grown with a) UDMHy or b) DTBAA as nitrogen precursor.

Figure 5.38 shows the EL spectra of both samples, that show a clear type-II transition peak as the main optical emission. Besides that, a GaAs barrier and SCH peak is present for pump current densities above 7 kA/cm^2 for both samples. Peak energies as a function of the current densities are plotted in Figure 5.39. Based on these experimental results, the carrier density is correlated to the current densities by applying an experiment-theory comparison, depicted in Figure 5.40. As expected, the charge carrier density is much lower in the DTBAA grown sample compared to the

UDMH_y grown sample due to DTBAA induced defects that drain the charge carriers out of the active region. A further reduction of the optical quality is caused by the lower growth temperature and the resulting larger carbon incorporation due to alkyl groups.

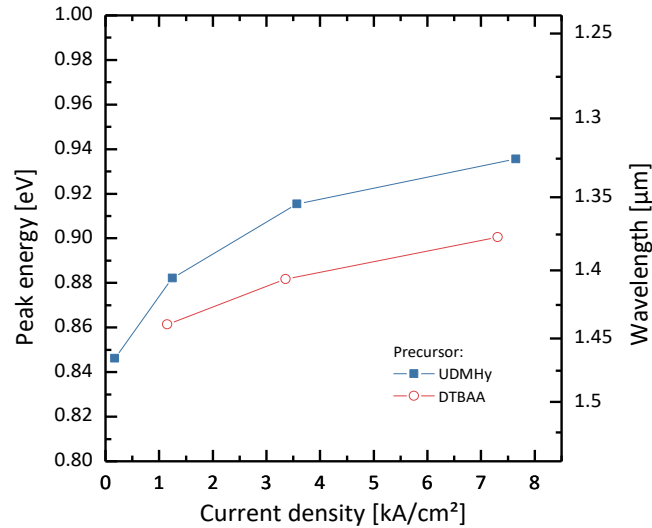


Figure 5.39 Peak energies of the type-II transitions as a function of the current density taken from Figure 5.38 for two samples grown with UDMHy or DTBAA as nitrogen precursor. The type-II peak of the UDMHy grown sample blueshifts stronger compared to the DTBAA grown sample, indicating a reduced charge carrier density in the DTBAA sample due to non-radiative recombination processes.

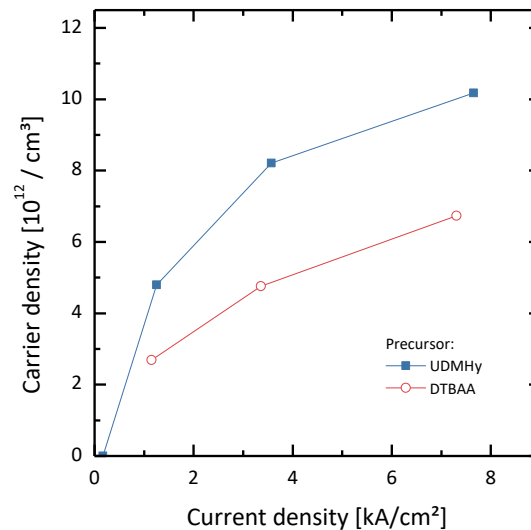


Figure 5.40 Carrier density as a function of the current density is plotted. The carrier density is determined by comparing the blueshift obtained in simulations by Dr. Ada Bäumner and the experimentally observed blueshift. The carrier density of the DTBAA grown sample is reduced due to DTBAA induced defects.

In summary, DTBAA exhibits still a worse purity compared to UDMHy, making it the less suitable choice for the nitrogen precursor, when aiming at the growth of laser devices. Defects like oxygen and carbon lower the charge carrier density in the WQWH.

5.6.5 Comparison of WQWH and “M” quantum well heterostructures

An alternative approach for “W” type-II structures are “M” type-II quantum well heterostructures (MQWH). Analogously to WQWH, the band edge structure of the valence band looks like an M. This means that the material systems of the quantum wells have to be exchanged because the outer quantum wells must be hole quantum wells and the center quantum well an electron well. In this particular case discussed here, this means the following stacking order: Ga(As,Sb)/Ga(N,As)/Ga(As,Sb). In Figure 5.41 the layers of this kind of structure are represented in a) while the band edge diagram to illustrate the band structure is shown in b).

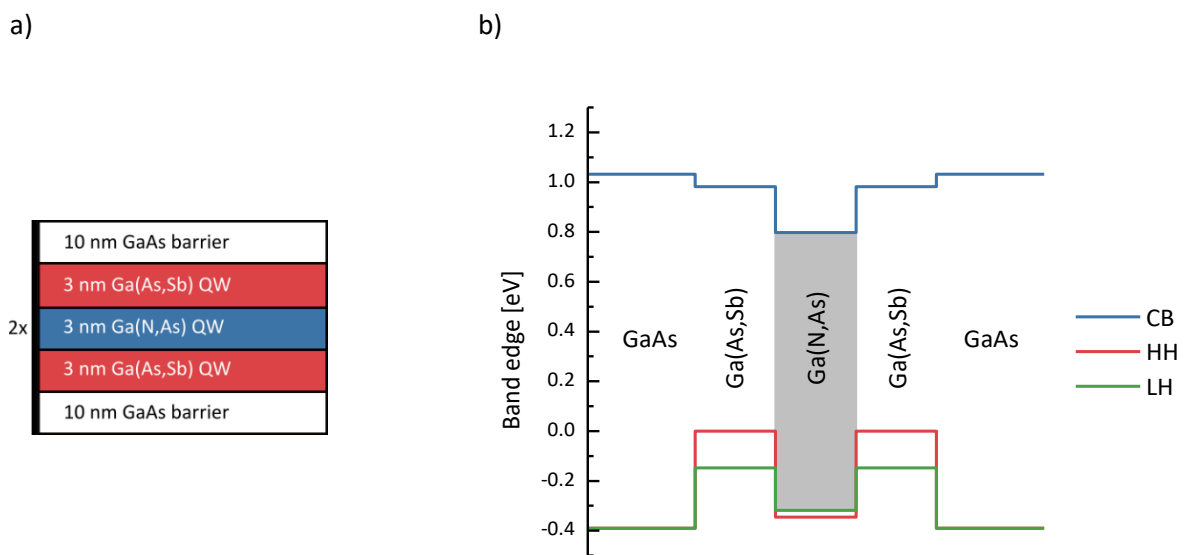


Figure 5.41 Schematic representation of a “M” type-II quantum well heterostructure. Two Ga(As,Sb) hole quantum wells sandwich a Ga(N,As) electron quantum well. a) Epitaxial layer stack b) band edge diagram determined by Dr. Ada Bäumner illustrating that the valence band edges resemble a “M”.

Overall, the WQWH design is expected to be superior to a MQWH design due to the lighter electron effective masses compared to hole effective masses. Hence, the wavefunction overlap in a WQWH design is more significant than for MQWH, since the coupling between the two outer quantum wells depends on the effective masses. Higher effective masses result in stronger localization of the wavefunctions in the center of the quantum well, while lower effective masses strengthen the tunneling into the barriers. In the material system investigated here, a further disadvantage of MQWH is the lower barrier in the conduction band of the Ga(N,As) quantum well, as can be seen in Figure 5.41 b). In a similar type-II material system theoretic studies revealed that WQWH show strongly enhanced gain compared to MQWH¹⁷³. However, in this section, the properties of a device based on MQWH are compared to a WQWH device with equal nitrogen and antimony content because in section 5.6.2, a strong dependence on the nitrogen content was demonstrated, and the overall nitrogen content of an MQWH is only half the amount of a WQWH. The WQWH sample

compared in this section is again the device with 2% nitrogen, 28% antimony, and 3 nm individual layer thickness. Accordingly, the MQWH was designed to also have the same compositions and layer thicknesses. The number of repetitions is 2 for both samples. From the epitaxial point of view, the realization of MQWH structures is comparatively undemanding since the symmetry issues are not existent.

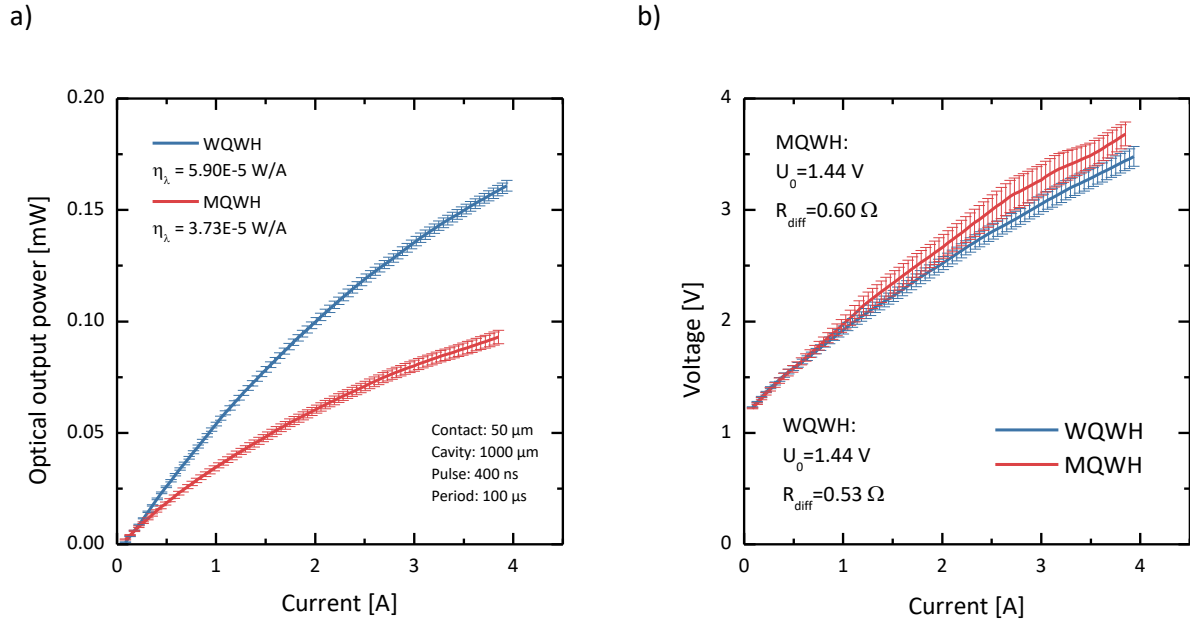


Figure 5.42 Comparison of the properties of WQWH and MQWH based devices. In a) the P-I characteristics are plotted and in b) the respective V-I characteristics. The claddings of both devices were grown with the same growth processes in the production scale reactor.

The pump current limited optical output power achieved for the MQWH is 90 μW , which is less than 165 μW obtained for the WQWH device. However, the P-I curves look similar in terms of bending. Slightly worse optical properties of the MQWH are represented by the optical efficiencies determined to be $3.73 \times 10^{-5} \text{ W/A}$ for the MQWH and $5.90 \times 10^{-5} \text{ W/A}$ for the WQWH. As the strong saturation effect of the optical output power is present in both samples, the differential efficiency is additionally plotted in Figure 5.43. Both curves seem to be parallel with respect to each other, but the differential optical efficiencies of the MQWH are shifted to lower values of η_{λ} . These lower optical efficiencies can be attributed to the lower wavefunction overlap expected due to the heavier effective masses. Since the reduction of the optical efficiency with larger pump currents looks similar for both structures, the loss process responsible for the saturation of the optical output power is probably equal and attributed to be charge carrier leakage in the last sections.

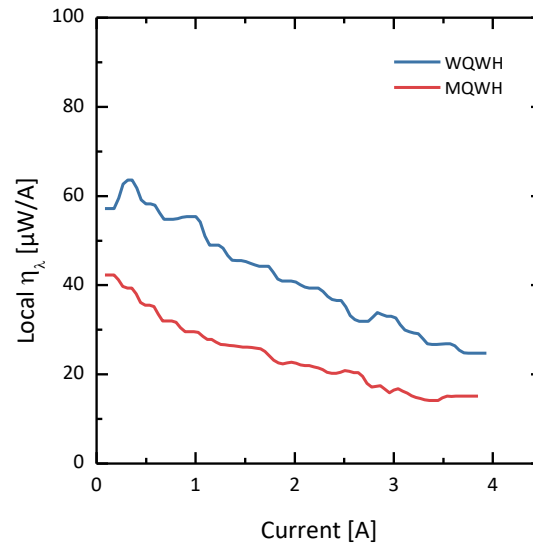


Figure 5.43 Differential optical efficiencies calculated for the P-I curves of Figure 5.42 a) as a comparison between WQWH and MQWH. Both structures exhibit remarkably similar differential optical efficiency curves but the curve of the MQWH device is translated to lower optical efficiencies.

In the following, the spectral properties of both structures will be compared and discussed. The spectral measurements are carried out at 85 K in order to make the charge carrier leakage due to band filling effects more evident. In Figure 5.44 spectra of both structures are plotted for different pump current densities. The most distinct low energy peak is the type-II transition. The GaAs barrier and SCH peak is present for both samples at 1.42 eV. The intensities of this GaAs peak are higher for the MQWH sample compared to the same pump current densities and the WQWH sample. Additionally, a higher order transition, most probably the e2h2 transition, emerges in the high energy flank of the e1h1 type-II transition peak. The background level between the type-II and the GaAs transitions can be attributed to impurity luminescence. As the luminescence of the higher order transitions is improved in the investigated spectra, the charge carrier leakage must be higher in the MQWH device. This is clear due to the electric properties of the MQWH compared to the WQWH: The barrier height of the conduction band Ga(N,As) quantum well is lower because of the adjacent Ga(As,Sb) quantum wells. Due to band filling, charge carriers occupy higher quantized states or even leak into the GaAs layers surrounding the MQWH. Similar EL measurements were also conducted at room temperature. The blueshift of the room temperature type-II transition is illustrated in Figure 5.45. In total, only a small discrepancy between both samples can be seen in this plot. The emission wavelength of the WQWH starts at low current densities at a longer wavelength, and shifts blue faster than the MQWH. At higher current densities above 7 kA/cm² the difference in emission wavelength is reduced compared to low excitation.

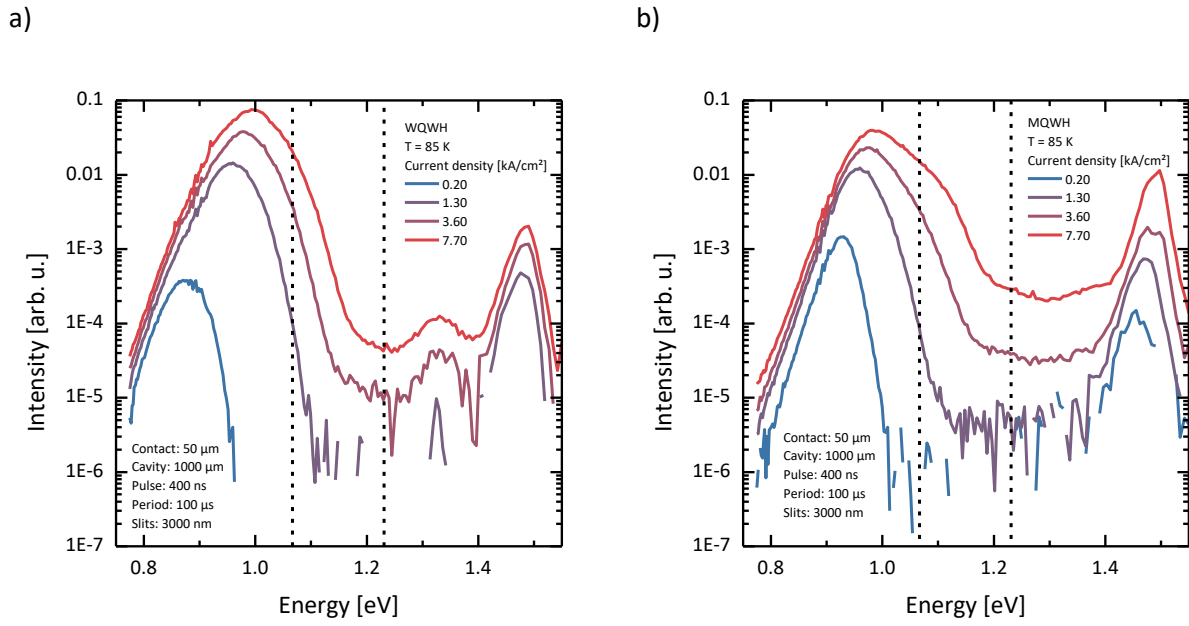


Figure 5.44 Low temperature (85 K) EL spectra of a) the WQWH device and b) the MQWH device.

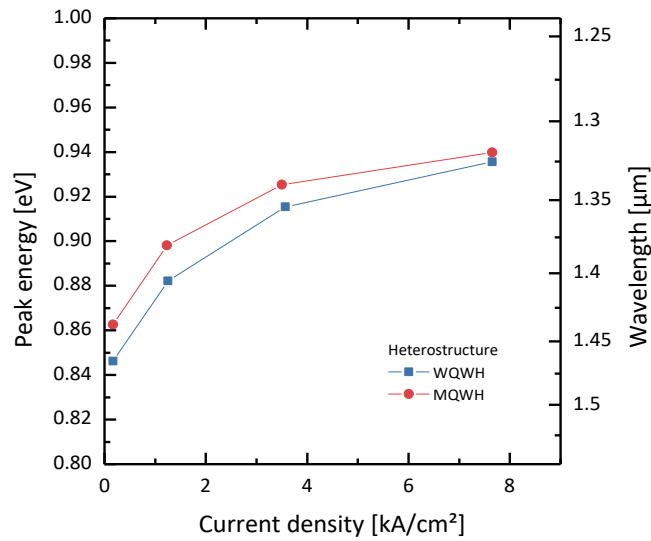


Figure 5.45 Type-II peak energy as a function of current density measured at room temperature. The EL spectra which were used to obtain these data points are not shown.

In total, the MQWH structure exhibits worse optical properties compared to the WQWH, because carrier leakage seems to be much more significant. Furthermore, the properties expected for MQWH are worse than that of WQWH since the effective masses of valence band holes in Ga(As,Sb) are heavier than the electron effective masses in Ga(N,As), leading to a weaker coupling between the Ga(As,Sb) quantum wells and a reduced wavefunction overlap.

5.6.6 RTA annealing

The critical influence of annealing on the optical quality of dilute nitrides was discussed in depth in section 2.4.1. Thus, optimized annealing steps are expected to improve the material quality of the device structures discussed in this chapter. As sample structure, a device with 3.3% nitrogen is used (sample C of Table 5.1). Two separate pieces were cut out of the raw wafer and annealed in the RTA at 650°C and 700°C for 10 s. Afterward, the samples were processed to full devices and measured in the EL setup. The P-I characteristics are shown in Figure 5.46 in comparison to the unannealed or “as-grown” sample.

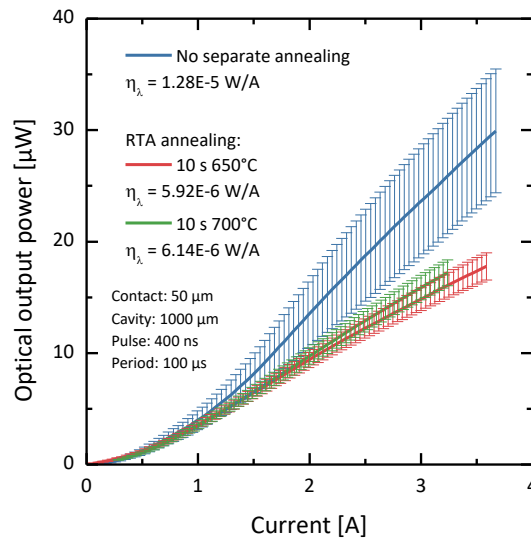


Figure 5.46 Optical output power measured for different pump currents. The as-grown device shows the highest optical output power, while the RTA annealed samples exhibit similar behavior and lower optical output power. The optical efficiency is slightly improved at 700°C.

Although an improvement of the optical quality was expected, the as-grown sample still exhibits the highest optical output power and optical efficiency compared to the RTA annealed structures. The RTA annealed devices show similar optical properties, but the 700°C annealed sample has a slightly higher optical efficiency. The related voltage-current curves that are plotted in Figure 5.47 are similar, but the 700°C annealed sample exhibits slightly worse electrical properties. In conclusion, RTA annealing seems to worsen the optical as well as the electrical properties. To further investigate the reason, EL spectra of RTA annealed devices were measured for different pump current densities and depicted in Figure 5.48. The corresponding peak energies are displayed in Figure 5.49.

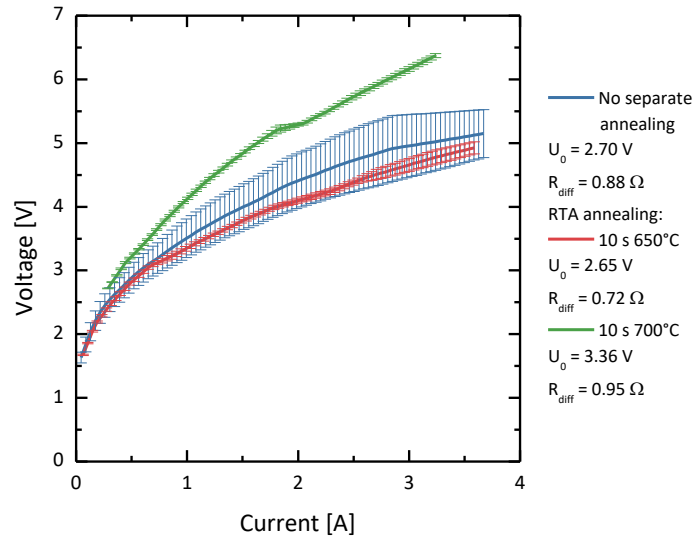
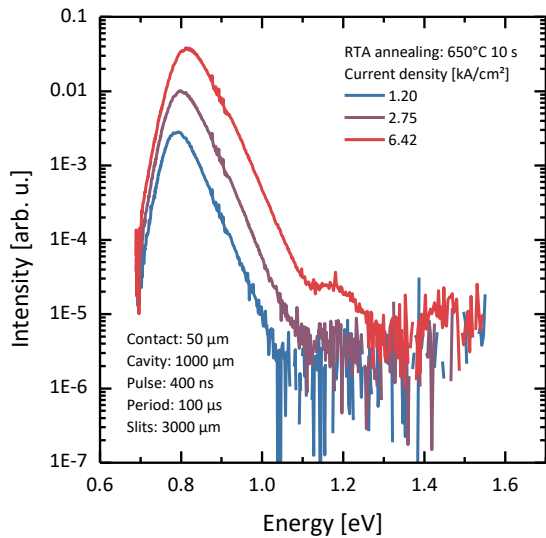


Figure 5.47 Voltage-Current characteristics of all investigated samples. Annealing at 700°C seems to lower the electrical quality of the devices.

a)



b)

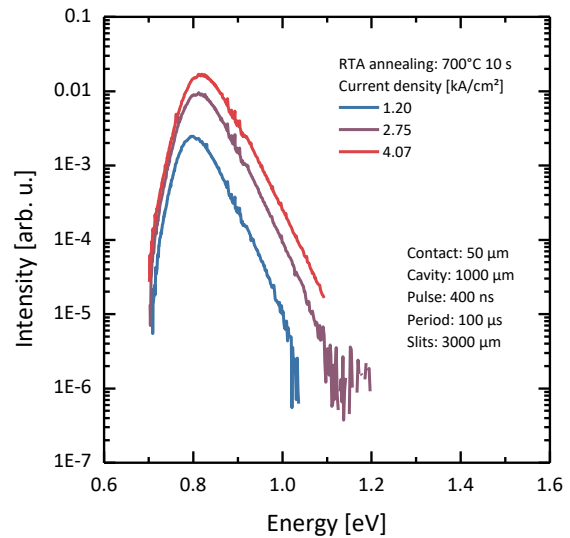


Figure 5.48 EL spectra measured at different current densities. The device presented in a) was RTA annealed at 650°C for 10 s. The device in b) at 700°C for 10 s.

All peaks look similar if similar current densities are applied. If the peak positions are considered, they still get shifted blue after RTA annealing. It is remarkable that the EL spectra are blue shifted in total but exhibiting a weaker blueshift compared to the as-grown sample, indicating a fundamental blueshift originating from the annealing process, like microscopic reordering, but also less efficient charge carrier injection due to defects.

To conclude, all results point towards an increase in defect density if RTA annealing in the investigated temperature range is considered, possibly due to over-annealing. All devices get

overgrown with (Al,Ga)As cladding layers at 625°C for roughly an hour, which should already act as annealing. Hence, the as-grown sample was in fact already annealed. All further annealing steps could result in nitrogen clustering, which introduces large numbers of non-radiative recombination centers, as was already outlined in section 2.4.1. Additionally, out-diffusion of nitrogen atoms out of the Ga(N,As) quantum wells could be a possible explanation. This could be clarified by further STEM analysis.

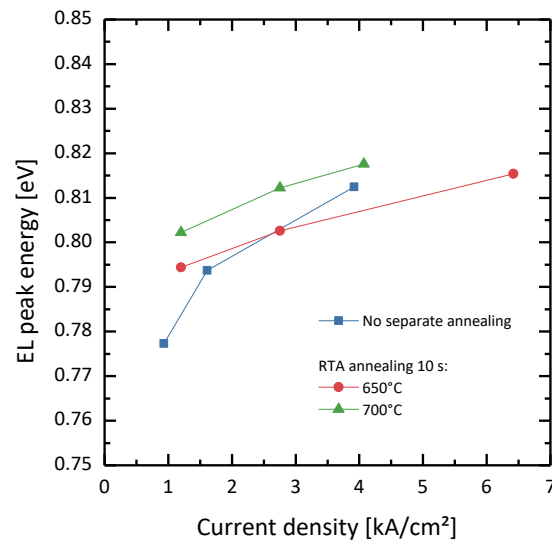


Figure 5.49 The EL peak energy is plotted as a function of the current density of the annealed samples depicted in Figure 5.48. In comparison, the peak energies of the as-grown sample are shown.

5.7 Summary and discussion

All in all, several challenges that accompany the deposition of Ga(N,As)/Ga(As,Sb)/Ga(N,As) WQWH were presented, including a substantial reduction of nitrogen incorporation if surface segregated antimony atoms are present. This reduction was compensated by carefully tuning the UDMHy partial pressure supplied during the growth of the second Ga(N,As) quantum well, and entirely nitrogen symmetric WQWH structures were realized. Furthermore, internal interfaces determine how many charge carriers get lost before they recombine over the type-II transition. Thus, the morphology of the internal interfaces was optimized by applying a short antimony predeposition prior to the Ga(As,Sb) growth and a short TBAs stabilized desorption step afterwards, resulting in flat interfaces. Devices were grown based on these optimization strategies. So far, no lasing was achieved when these optimized WQWH were employed as active region, but valuable insights regarding the loss processes and limitations were gained. For example, the nitrogen content of the Ga(N,As) layers turned out to be the crucial factor determining the optical properties. Device structures with low nitrogen contents are limited by leakage of electrons due to low conduction band barriers with

respect to GaAs barrier layers and high charge carrier densities. No hint for carrier leakage can be found if the nitrogen content is raised because necessary charge carrier densities cannot be reached. However, non-radiative recombination centers originating from nitrogen induced defects lower the charge carrier density in the quantum wells as well as the overall optical output power. As correlation between optical efficiency and nitrogen content, an exponentially decreasing function was found. The investigated devices exhibited emission wavelengths between 1.25 to 1.55 μm utilizing Ga(N,As) nitrogen contents between 1.7 to 4.6%. Choosing the suitable precursor for nitrogen is of major importance. With DTBAA, it is easier to achieve symmetric nitrogen incorporations, but it introduces even more defects, causing the charge carrier density to be drained stronger. As UDMHy is the more established precursor, the defect density of Ga(N,As) seems to be lower if grown with this precursor. Usually, nitrogen induced defects can be thermally annealed, so different RTA annealing conditions were tried out with the result that the defect density increases, which was attributed to an over-annealing that comes with clustering of nitrogen atoms. No further optimization was observed by changing the number of WQWH implemented in one device. Also, the exchange of WQWH with MQWH led to a deterioration of the optical properties.

Nevertheless, valuable knowledge was gained. In order to realize functioning laser devices utilizing this material system in the future, nitrogen contents below 2.5% should be used. Additionally, a different barrier material should be applied, which features a higher conduction band barrier than GaAs. Suitable materials could be Ga(P,As) or (Al,Ga)As. Ga(P,As) would have additionally the advantage to also reduce the strain of the entire layer structure. From the spectroscopic point of view, a more in-depth analysis of these structures must be performed to find out more about the limiting factors, particularly the influence of non-radiative loss channels like Auger recombination. To improve the structures even further and to enable high photon densities even for larger nitrogen contents, high reflection coatings could be applied to at least one facet.

Chapter 6 Ga(N,As)/(Ga,In)As/Ga(N,As)

“W” type-II heterostructures

6.1 Introduction and band structure

The next material system being investigated is Ga(N,As)/(Ga,In)As/Ga(N,As) type-II WQWH. In the past, type-II transitions of (Ga,In)As/Ga(As,Sb) heterojunctions were utilized for realizing laser structures. In this case, (Ga,In)As is used as electron quantum well due to its relatively high conduction band hetero offset, and Ga(As,Sb) as hole quantum well. However, (Ga,In)As can form a type-II heterostructure with Ga(N,As) in which electrons are confined in Ga(N,As) quantum wells and holes in the (Ga,In)As quantum well. Such structures form a type-II alignment if a sufficiently high nitrogen content is incorporated that the conduction band edge of Ga(N,As) is lower than the (Ga,In)As conduction band edge, as can be seen in Figure 6.1. This change occurs at nitrogen contents of about 1%.¹⁹⁰

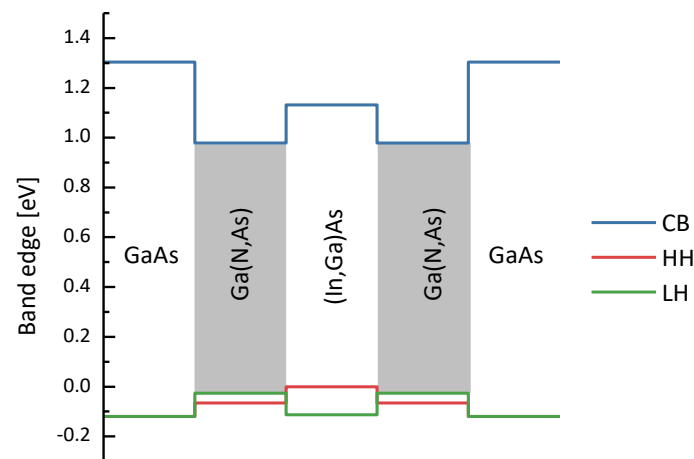


Figure 6.1 Band edge diagram of a Ga(N,As)/(Ga,In)As/Ga(N,As) WQWH with GaAs barriers.

Compared to Ga(As,Sb), which was used as hole quantum well in the last chapter, the light hole mass of (Ga,In)As is lower, resulting in less confined carriers and thus probably in a more considerable wavefunction overlap. Since (Ga,In)As and Ga(N,As) are compressively, and tensilely strained, an advantage of such heterostructures is the possibility to reduce to total strain of the structure. Until now, no further experiments regarding the growth of laser devices based on these structures have been conducted. In this chapter, this gap of knowledge will be closed.

6.2 Epitaxial growth of consecutive (Ga,In)As/Ga(N,As) quantum wells

In the last chapter, a significant challenge dealt with the reduction of nitrogen incorporation by antimony. As similar effects come into play if (Ga,In)(N,As) is deposited, an effect of surface segregated indium atoms is expected for (Ga,In)As/Ga(N,As) structures. To investigate this effect, two type-II QWH samples were grown in different order at 550°C. An As/III ratio of 2.36 during the growth of Ga(N,As) quantum wells combined with a N/As ratio of 14.94 led to an undisturbed nitrogen incorporation into test structures of 3.2%. An indium content of 25% was reached with a In/Ga ratio of 0.45 and a good material quality was ensured by an As/III ratio of 3.45. The type-II QWH features individual layer thicknesses of 4 nm, 3 repetitions, and 20 nm GaAs barriers. HR-XRD diffractograms of both growth orders in combination with fitted simulations and the individual fit results are depicted in Figure 6.2.

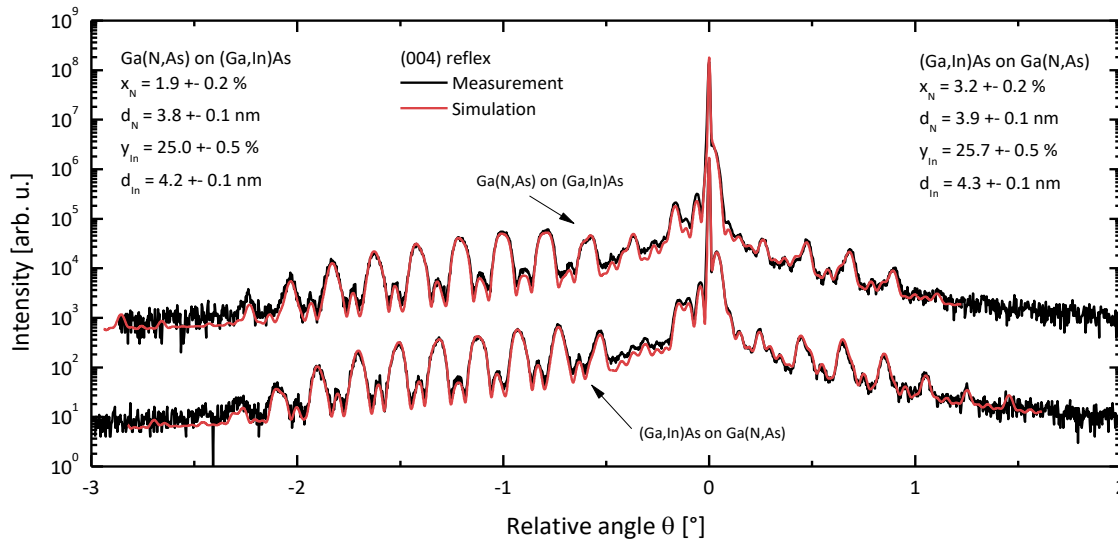


Figure 6.2 HR-XRD diffractograms measured for two type-II QWH containing samples with both possible growth orders. The lower diffractogram correlates to (Ga,In)As deposited on Ga(N,As) and the upper to Ga(N,As) grown on (Ga,In)As. The latter was multiplied with a factor of 100 to ensure good visibility. In red, the fitted simulations are plotted.

While the Ga(N,As) quantum well grown on GaAs has a nitrogen content of 3.2%, the nitrogen incorporation gets reduced to 1.9% if it is grown on (Ga,In)As, which corresponds to only 60% of the original nitrogen incorporation. Further analysis of this effect is done by measuring the room temperature PL spectra of these samples, plotted in Figure 6.3. A clear type-II e1h1 transition peak is visible but also one probably higher order transition with a weaker intensity, compared to the e1h1 transition. The lower intensity together with the redshift of the sample with (Ga,In)As grown on Ga(N,As) is in agreement with the result of a larger nitrogen content already obtained by HR-XRD.

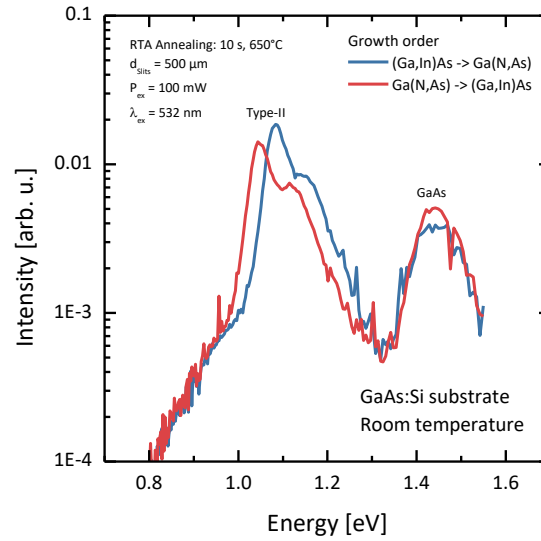


Figure 6.3 PL spectra of type-II QWH samples grown in different growth order. The intensity of the type-II peak is higher for the sample in which Ga(N,As) is grown on (Ga,In)As. An additional blueshift suggests less nitrogen incorporation. Besides the type-II peak, a second peak is present, which could be a higher order transition, like the e2h2 transition. Furthermore, a distinct GaAs substrate peak is visible.

To conclude, the nitrogen incorporation efficiency is decreased in this particular case by 40% if Ga(N,As) is grown on (Ga,In)As. In comparison to Ga(N,As) deposition on Ga(As,Sb), the reduction seems to be lower. Still, a structural asymmetry should be expected when a full WQWH is deposited. Compared to the influence of antimony on nitrogen incorporation, indium is incorporated on group III lattice sites, so arguing that a group V competition takes place is not possible. A change of surface reconstruction changing the nitrogen incorporation efficiency due to surface segregated indium appears reasonable. Hence, a strategy for increasing the nitrogen incorporation of the second Ga(N,As) quantum well must be found, similar to the strategies developed in the last chapter.

6.3 Optical properties

Since no experimental overview data of type-II transition energies is available until now, type-II QWH samples were grown with varying indium and nitrogen contents. To not be affected by the reduction of nitrogen incorporation due to indium, only one growth order was chosen in which the Ga(N,As) layer is grown first. Room temperature PL spectra were measured for all samples to estimate the reachable wavelengths with realistic compositional values. All samples used individual layer thicknesses of 4 nm. In Figure 6.4 the respective PL spectra are depicted, sorted for the indium content: a) 20%, b) 25%, and c) 32.5% indium. It is noticeable that all samples feature multiple peaks, besides the GaAs substrate peak at 1.42. All other peaks originate from type-II transitions of higher orders because the transition energies are lower than that of type-I samples described in Chapter 4.

The intensity of the type-II transitions decreases if the nitrogen content increases due to nitrogen induced defects. An indium content of 32.5% combined with a nitrogen content of 2% shows the highest intensity of all investigated samples. If the band edge diagram in Figure 6.1 is considered, the reason for the appearance of higher order transitions gets clearer, because even for relatively high nitrogen and indium contents, the barrier heights in the conduction as well as of the valence band are low, causing a weak energetic separation of the quantized states.

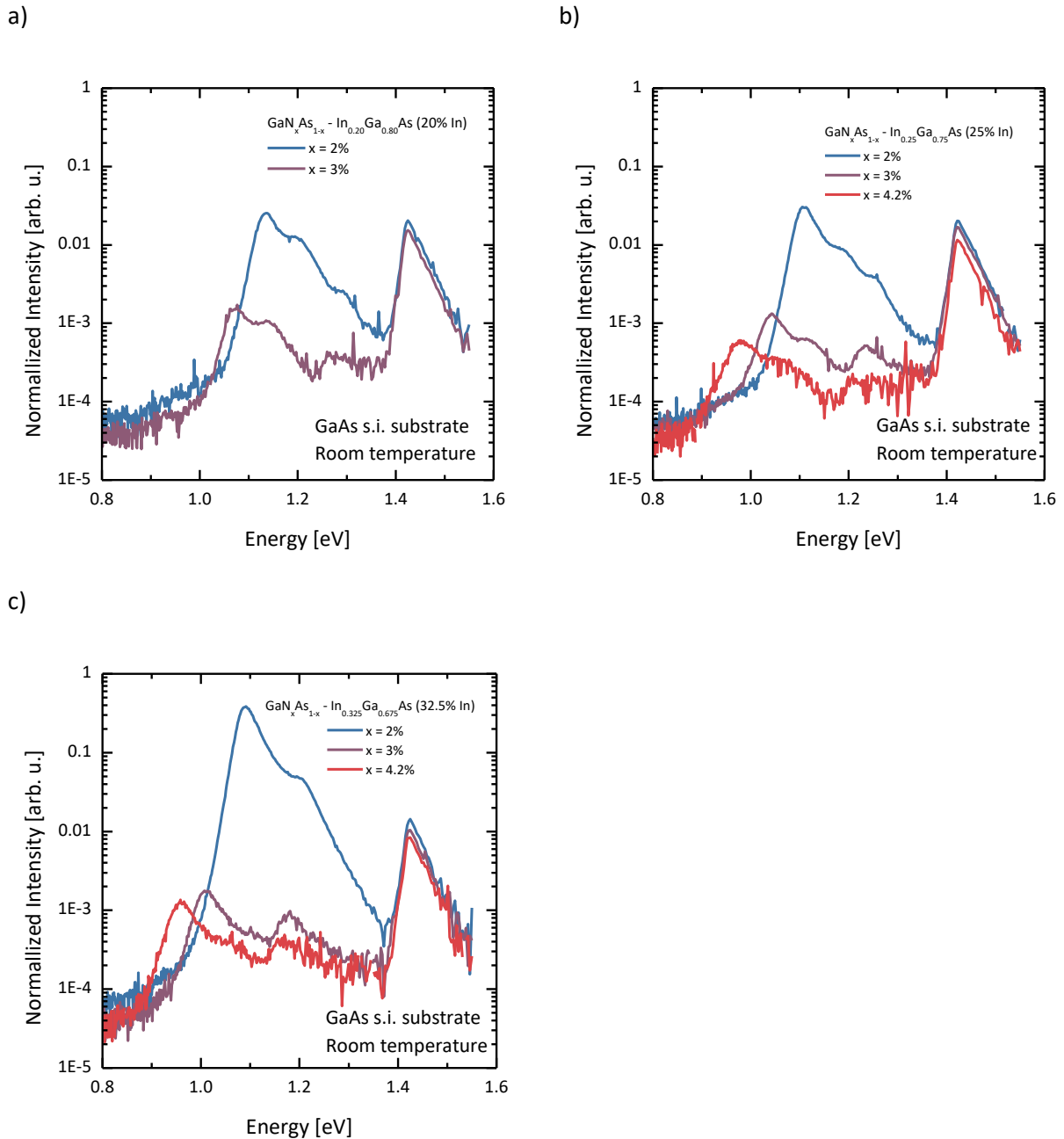


Figure 6.4 Room temperature PL spectra measured of samples with different indium and nitrogen contents.

For creating a comprehensive overview of the reachable wavelengths, the peak energies of the e1h1 transitions are plotted as a function of the nitrogen content in Figure 6.5. The wavelength range achieved is between 1.1 μm and 1.3 μm . An indium content of 32.5% reached the longest

wavelength with a nitrogen content of 4.2%. In conclusion, the first desirable wavelength of 1.3 μm was achieved with a very high nitrogen content of 4.2%, which undoubtedly results in large amounts of nitrogen induced defects. Longer wavelengths are principally possible but come with an even higher strain. Considering the blueshift with higher carrier density, a longer wavelength must be aimed for if a device emitting at 1.3 μm is desired. Hence, a wavelength of 1.5 μm cannot be achieved utilizing this material system.

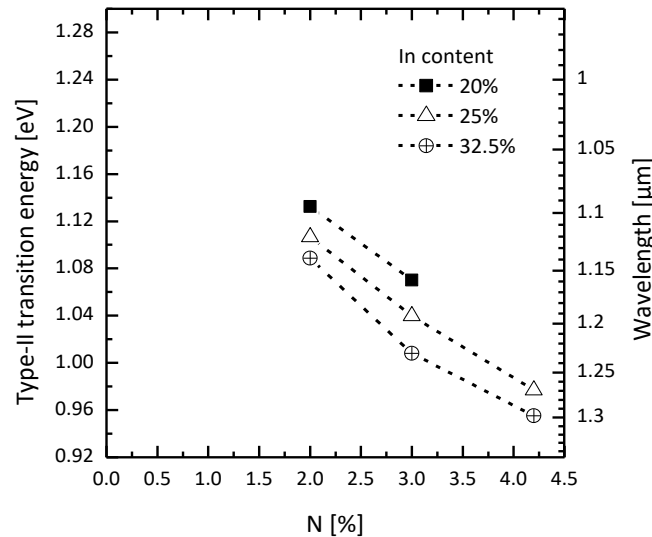


Figure 6.5 Type-II transition energies obtained for the e1h1 transitions of all samples presented in Figure 6.4. The longest reachable wavelength is considered to be 1.3 μm because (Ga,In)As is limited by strain.

As for all dilute nitride-based material systems, RTA annealing is expected to increase the optical quality drastically. Thus, a separate RTA annealing step is applied after sample growth. To compare the properties of as-grown samples and annealed samples, pieces were cut out of the same wafers used for the PL measurements of the as-grown 32.5% indium series, which were annealed with RTA at 650°C for 10 s. A comparison of these samples can be found in Figure 6.6. Of course, the intensity of the type-II peaks gets improved for all samples, up to two orders of magnitudes, if annealing was applied. The intensity increase is weakest for the sample with 2% nitrogen due to its already high as-grown intensity. Overall, the intensity of samples with lower nitrogen contents remains higher, even for the annealed samples. A blueshift is visible after annealing for all samples, as indicated with the vertical black lines. This blueshift could be for instance explained by nitrogen atoms rearranging to more indium rich interface regions or diffusing out of the Ga(N,As) layer.

All in all, annealing is essential regarding the optical quality of the material. Even for unoptimized annealing conditions, an improvement of up to two orders of magnitudes of the PL intensity was achieved.

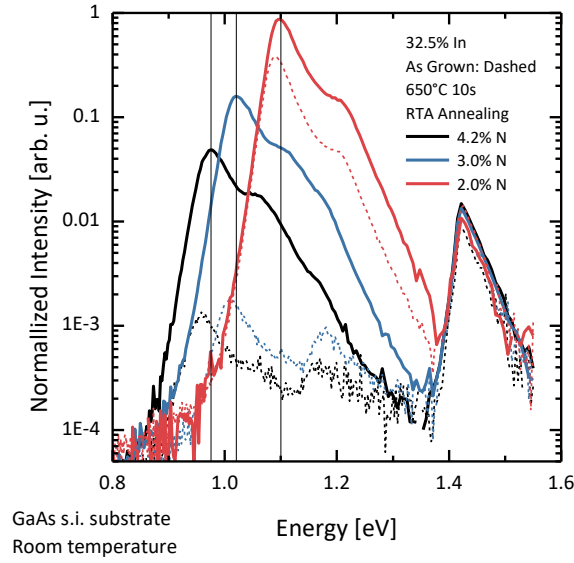


Figure 6.6 Comparison of room temperature PL spectra of as-grown samples and RTA annealed samples. The RTA annealing was carried out for 10 s at 650°C. Vertical lines were added at the peak positions of the annealed samples to highlight the blueshift induced by annealing.

6.4 Preparation of internal interface

Similar to the preparation of the internal interfaces of the previous material system, the internal interface of these structures will be investigated in this section. In the literature, a smoothing of the internal interface was observed if a TBAs stabilized growth interruption is applied on a (Ga,In)As surface.¹⁷⁸

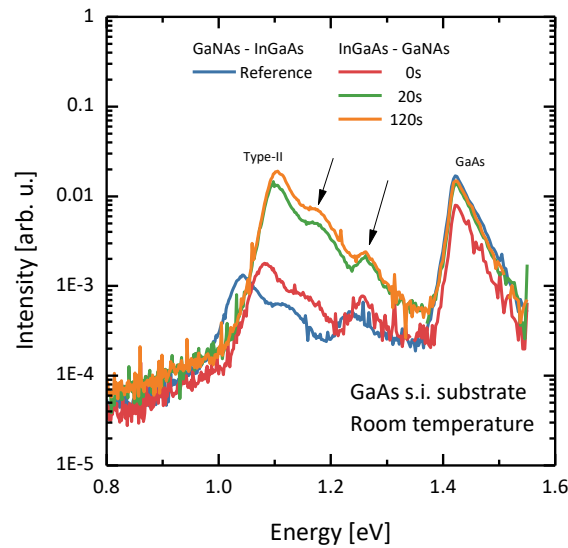


Figure 6.7 Room temperature PL spectra of type-II QWH structures in which different TBAs stabilized growth interruptions were implemented. In blue, the reference sample is shown in which Ga(N,As) was grown first. If the growth interruption changes the nitrogen content, the type-II peak will shift towards the type-II peak of the reference sample. Higher order type-II transitions are marked with black arrows.

To analyze the effect of such TBAs stabilized growth interruptions, samples were grown with 25% indium ($\text{As/III} = 3.45$, $\text{In/Ga} = 0.45$) and 3% nitrogen ($\text{As/Ga} = 2.36$, $\text{N/As} = 14.94$) at 550°C . Three repetitions are separated by 20 nm GaAs barriers. In between the growth of 4 nm thick (Ga,In)As and Ga(N,As) layers, a TBAs stabilized growth interruption was implemented, which means that all group III precursor run valves were closed. The duration of this growth interruptions was chosen to be 0 s, 20 s, or 120 s. The same nitrogen reduction was observed in the HR-XRD measurements, as presented in section 6.2. Interesting features of these growth interruptions can be derived if the room temperature PL spectra in Figure 6.7 are considered. The intensity of the type-II peaks drastically increases more than one order of magnitude due to improved surface morphology. Almost the full improvement is already achieved after 20 s of growth interruption. Compared to the Ga(As,Sb)/Ga(N,As) material system, no change in nitrogen incorporation was observed as a function of the growth interruption duration. This is due to the much lower desorption rate of group III atoms in general, which must be clarified in future experiments with longer growth interruption durations.

6.5 Laser structures

In this section laser structures based on Ga(N,As)/(Ga,In)As/Ga(N,As) WQWH will be examined. For that, two different device structures were deposited. Target nitrogen and indium compositions were 3% and 24% while the layer thicknesses were set to 4 nm. To improve the symmetry of nitrogen incorporation, a GaAs interlayer was introduced, which was grown for 2 s, corresponding to 0.7 nm. With this GaAs interlayer, the number of surface segregated indium atoms is reduced by incorporating these atoms into the GaAs interlayer. Thus, a thin (Ga,In)As layer instead of a GaAs layer is forming. The second sample was grown continuously. Both samples are certainly not fully symmetric, but they can give valuable insights into the suitability of the given material system for laser applications. If the result of this study suggests a good suitability, further optimization studies will be conducted. In Figure 6.8, the P-I and the V-I characteristics are depicted, showing a maximum optical output power of only $80\text{ }\mu\text{W}$ for the continuously grown device and even less $50\text{ }\mu\text{W}$ for the device employing an interlayer. The corresponding optical efficiencies are with $2.3\text{E-}5\text{ W/A}$ and $1.6\text{E-}5\text{ W/A}$ also relatively low and fit well into Figure 5.31 a), in which the optical efficiencies of several devices are plotted as a function of the nitrogen content. This highlights that the nitrogen content determines the optical efficiency, independent of the remaining material. Both samples show similar electrical behaviors, according to Figure 6.8 b).

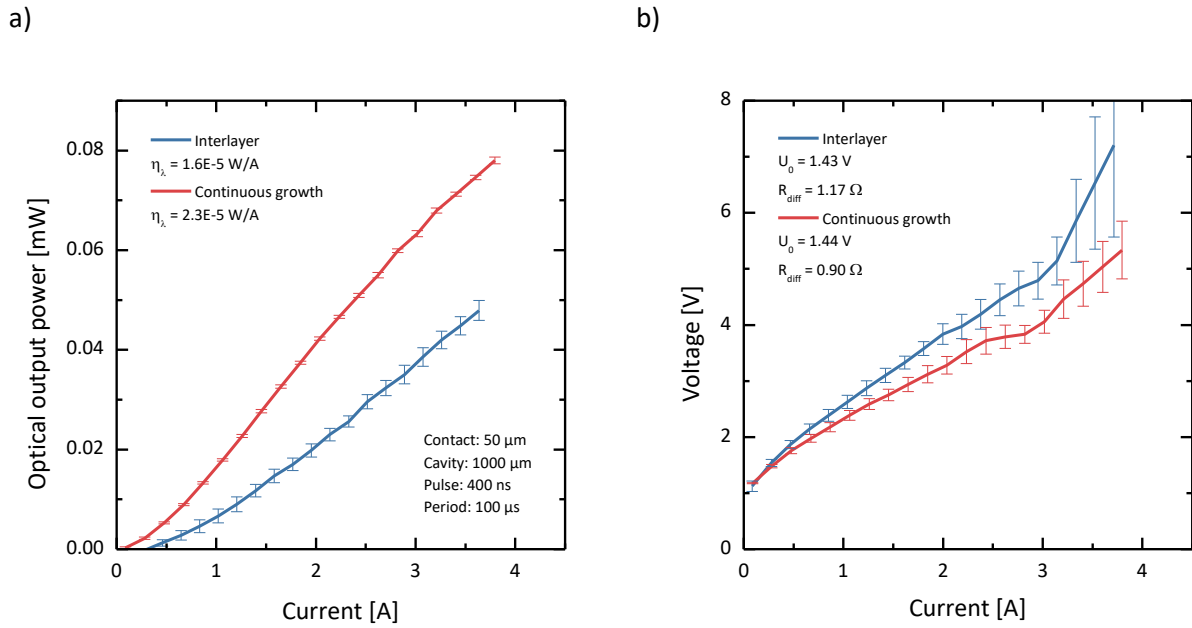


Figure 6.8 a) P-I characteristics of two WQWH based devices. b) The respective V-I characteristics.

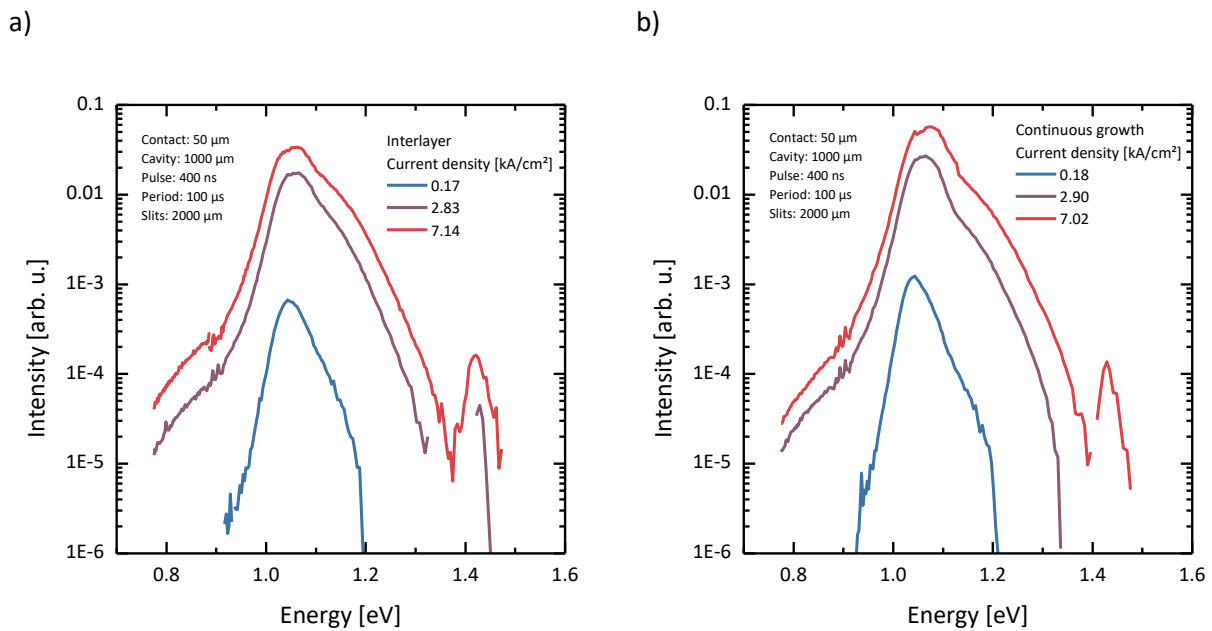


Figure 6.9 In a) room temperature EL spectra measured for the device which utilized a GaAs interlayer are depicted. In b) the spectra obtained for the continuously grown device are shown.

Spectral analysis is carried out with current density dependent room temperature EL measurements, resulting in the spectra displayed in Figure 6.9. For low excitation densities, one single e1h1 type-II peak is present in both samples. Due to the small separation of quantized levels, higher order peaks emerge in the high energy flank of the ground state transition, resulting in an increase of the FWHM. Still, the e1h1 transition remains the most intense peak in the investigated excitation range. Besides that, a GaAs peak at 1.42 eV becomes more intense at high excitation densities above 7 kA/cm^2 . The e1h1 peak position is plotted in Figure 6.10 as a function of the current density.

Both devices exhibit almost equal emission wavelengths with a very weak blue shift of about 20 meV, as shown in Figure 6.10. This is so far the weakest blueshift observed in this thesis, indicating a type-I transition character. If the band edge structure is taken into account, this effect could come from the low barrier heights and the small energy separation.

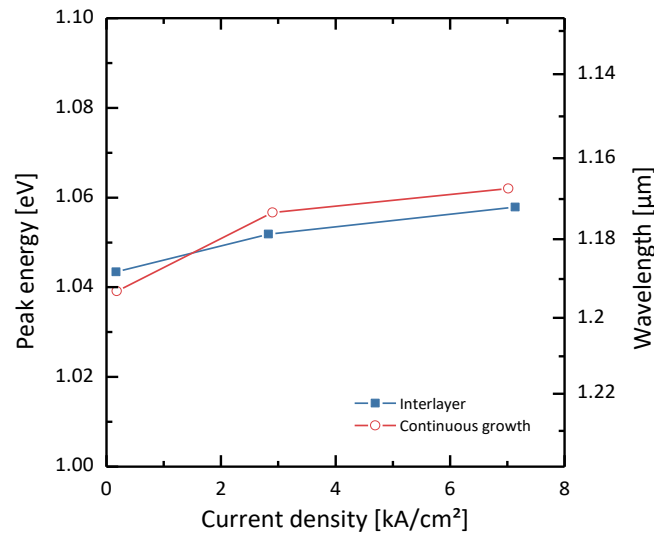


Figure 6.10 Blueshift of the EL spectra displayed in Figure 6.9. The blueshift with the current density is comparatively weak and is about 20 meV over the measured current density range.

6.6 Conclusion and discussion

To conclude this chapter, the suitability of (Ga,In)As/Ga(N,As) type-II heterostructures for laser applications was investigated. For that, the influence of indium on the nitrogen incorporation into the consecutive Ga(N,As) quantum well was examined and found to be severe. Only about 60% of the original nitrogen content was achieved when Ga(N,As) was grown on (Ga,In)As, resulting in a nitrogen asymmetry in WQWH, without further measures. Indium desorption steps applied on the (Ga,In)As surface were not valuable in terms of nitrogen incorporation in reasonable timescales but improved the optical properties of the structures due to an improvement of the interface morphology. So far, no symmetric WQWH could be achieved. It was shown that wavelengths up to 1.3 μm can be reached, however, a comparatively high nitrogen content of about 4.2% and an indium content of 32.5% are necessary. Compared to Ga(N,As)/Ga(As,Sb) heterostructures this relates to about twice the amount of nitrogen, with almost no room for shifting the wavelength even further. Due to unfavorable band alignments, the PL spectra exhibited higher order transitions with high intensities.

When it comes to device structures, two samples were investigated to analyze the optical properties under high excitation densities. Maximum pump current limited output powers of 50 to 80 μW were

achieved with an optical efficiency between 1.6 to 2.3E-5 W/A. Hence, the photon density in the device cavity for lasing was not reached, and no lasing threshold behavior was observed. Both devices featured nitrogen contents of 3%, which is already relatively high, but the detected emission wavelength was determined to be 1.19 μm . A comparatively weak blueshift of the type-II transitions may be attributed to the low band energy barriers in the conduction as well as the valence band.

All in all, (Ga,In)As/Ga(N,As) type-II heterostructures are less suitable for device applications compared to Ga(As,Sb)/Ga(N,As) quantum wells. When comparing the optical efficiency of both devices discussed in this chapter with the devices presented in section 5.6.2, the optical efficiencies are similar for equal nitrogen contents. Thus, it seems like the optical efficiency is mainly determined by the nitrogen content of Ga(N,As) quantum wells, independent of the additional material used to form a type-II heterostructure. This points out that the nitrogen content should be reduced if efficient lasers must be developed. Therefore, the next chapter will deal with (Ga,In)(N,As)/Ga(As,Sb) heterostructures.

Chapter 7

(Ga,In)(N,As)/Ga(As,Sb)/(Ga,In)(N,As) “W” type-II heterostructures

7.1 Introduction and electronic properties

Investigations on Ga(N,As) containing type-II heterostructures revealed that nitrogen determines the optical properties of devices with an exponential deterioration of the optical efficiency with nitrogen content. For lower nitrogen contents, carrier leakage becomes more significant and hinders devices to reach lasing threshold. Thus, it is reasonable to utilize the quaternary material (Ga,In)(N,As) for the purpose of electron confinement due to its increased electron barrier if equal nitrogen contents are compared. Highly efficient (Ga,In)As/Ga(As,Sb) laser structures were presented, emitting at 1.2 μm , highlighting that carrier leakage is not an issue if about 25% indium is used. However, the achieved threshold currents were admittedly lower. A full band edge diagram of such WQWH is shown in Figure 7.1. A good hole confinement is ensured by the deep Ga(As,Sb) quantum well, while the conduction band edge lies slightly below the GaAs band edge, resulting in stronger coupling of the (Ga,In)(N,As) quantum wells. (Ga,In)(N,As) offers a strong shift of the conduction band edge and a weaker shift of the valence band, resulting in a stepwise increase of the valence band edge favorable for wavefunction overlap.

Regarding the quantized states that are depicted with horizontal dashed lines, the third conduction band state is on one level with the GaAs conduction band edge. Consequently, electrons occupying this state can efficiently leak out of the quantum well into the GaAs barrier layers. However, the energetic separation between the second and the third state is relatively high, enabling higher excitation densities to achieve population inversion without leaking into the third state. Compared to Ga(N,As), the effective conduction band masses are lower for (Ga,In)(N,As) under the same wavelength conditions, which is beneficial for the wavefunction overlap and hence the optical gain. Since both quantum wells are compressively strained, no strain compensation can be achieved, in contrast to Ga(N,As)/Ga(As,Sb) heterostructures.

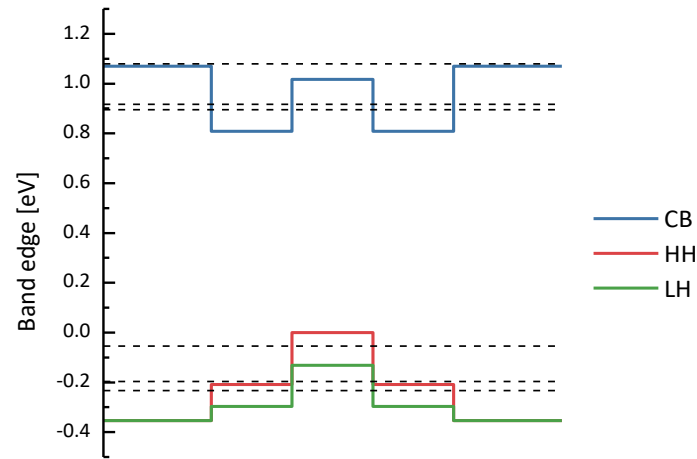


Figure 7.1 Band edge diagram of a WQWH calculated by Dr. Ada Bäumner. Horizontal dashed lines indicate the quantized states. As indium content 24% and as nitrogen content 1.1% was assumed. The individual layer thickness was set to 3 nm.

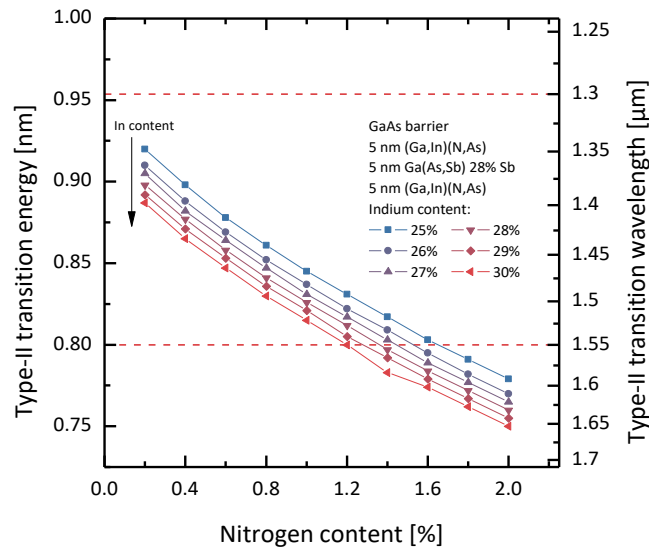


Figure 7.2 Type-II transition energies as a function of the nitrogen content incorporated into the 5 nm thick (Ga,In)(N,As) quantum wells for different indium contents between 25 and 30%. As antimony content 28% was used in the Ga(As,Sb) quantum well. Values determined by Dr. Ada Bäumner.

Theoretical simulations by Dr. Ada Bäumner led to the dependence between low excitation type-II transition energy and nitrogen content presented in Figure 7.2. Emission wavelengths above 1.3 μm are achieved for all simulated nitrogen contents. For low nitrogen contents starting at 1.2% even 1.55 μm are reached, which was only the case for nitrogen contents above 4% if Ga(N,As) was used. Considering the large number of nitrogen induced defects, this material system is thus promising for longer wavelength devices. However, layer thicknesses below 5 nm are preferred due to the larger wavefunction overlap and gain, causing shorter emission wavelengths due to quantization effects.

Calculations concerning the Ga(N,As)/Ga(As,Sb) system exhibited a quite large error in the wavelength determination. Hence, the simulated data should only be understood as a general trend.

7.2 Epitaxial growth

In the previous chapters, a severe reduction of the nitrogen incorporation was shown if antimony or indium are present during the growth of Ga(N,As), if UDMHy is employed as nitrogen precursor. For growing Ga(N,As)/Ga(As,Sb) WQWH, a sophisticated optimization of the nitrogen content of the second Ga(N,As) quantum well must be applied. For that, a precise determination of the nitrogen content is a prerequisite. However, determining the nitrogen content is not trivial if other degrees of freedom are introduced by the indium fraction or antimony fraction. Thus, convincing proof of nitrogen incorporation into (Ga,In)(N,As) layers deposited on Ga(As,Sb) layer could not be given due to the very low nitrogen incorporation. Hence, no WQWH were realized so far using UDMHy as nitrogen precursor.

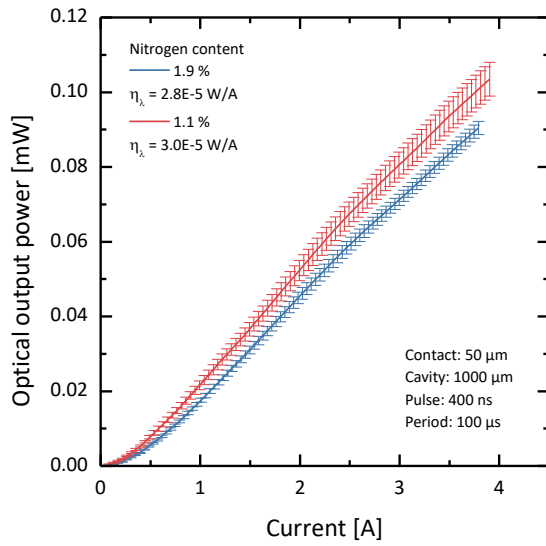
In several experiments, no influence of antimony and indium on the incorporation efficiency of nitrogen was observed when DTBAA is used. Thus, all the growth issues discussed above vanish if DTBAA is used as nitrogen precursor. Due to the immense complexity of (Ga,In)(N,As)/Ga(As,Sb) heterostructure growth with UDMHy, the following laser devices have been grown with DTBAA, despite a larger number of defects and a lower material quality.

7.3 Laser structures

Based on the conclusion of the last section, laser structures were deposited with DTBAA to investigate the optical properties under high excitation conditions. Both sample structures consist of two repetitions of the active region separated by a 20 nm GaAs barrier. Due to special requirements of DTBAA based deposition, the full active region was grown at a reactor temperature of 525°C. An In/Ga ratio of 0.4 combined with the standard TEGa partial pressure resulted in an indium fraction of 24% under an additional DTBAA supply of 0.02 mbar, which caused nitrogen incorporation of 1.1% in both quantum wells. The 3 nm thick Ga(As,Sb) layer was grown with a V/III ratio of 3.79 and a Sb/V ratio of 0.57, corresponding to 25% antimony incorporation. In a second sample, the DTBAA supply was raised to 3.2E-2 mbar, increasing the nitrogen incorporation to 1.9%. Thin individual layer thicknesses of 3 nm per quantum well were chosen in order to maximize the expected gain of the devices. The deposition of the full device was split into three parts according to section 3.4.

7.3.1 Nitrogen content

a)



b)

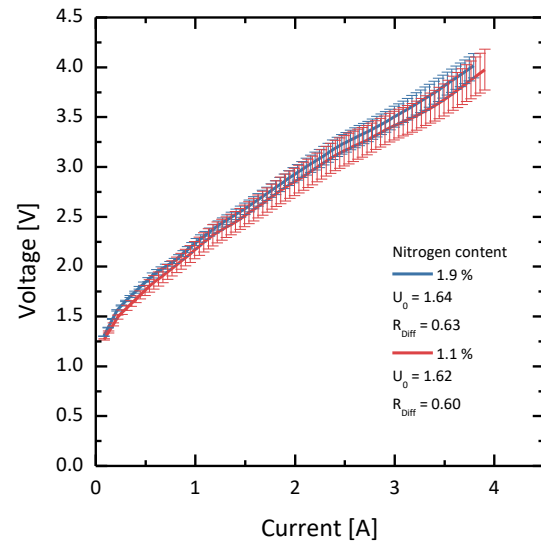
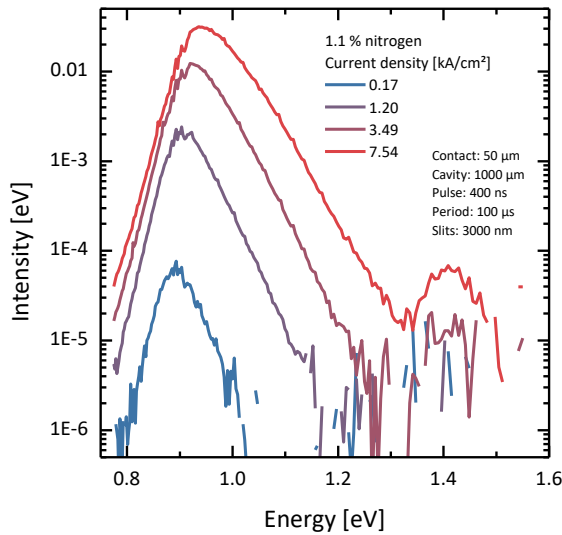


Figure 7.3 Results of the electrical pumping. In a) the optical output power (P-I curve) is depicted, while in b) the respective electrical behavior (V-I) is shown.

a)



b)

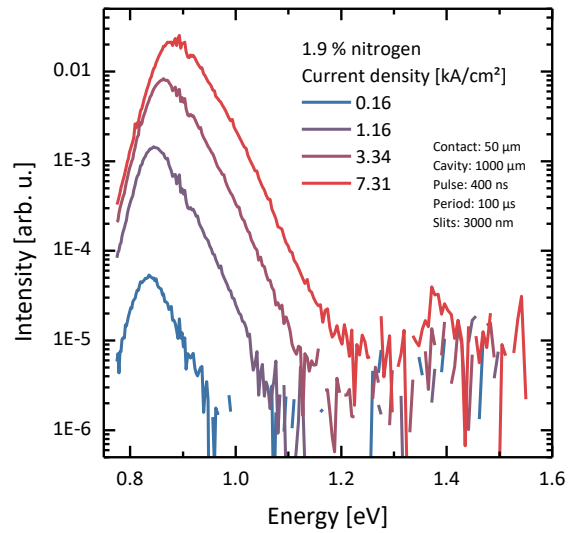


Figure 7.4 EL spectra obtained for different pump current densities. In a) the results measured for the 1.1% nitrogen containing device are shown. In b) for the 1.9% nitrogen device.

Since a strong dependence on the nitrogen content was found for all other investigated materials, the dependence of these device properties on the nitrogen content is examined in this section. As already given above, two almost identical samples with 1.1 and 1.9% nitrogen contents are investigated. Both devices were electrically pumped using the UR19 current source, as depicted in Figure 7.3. A closer look at the P-I characteristics reveals that the optical efficiency is $3.0\text{E-}5 \text{ W/A}$ for

the 1.1% nitrogen sample and 2.8×10^{-5} W/A for the 1.9% nitrogen device. Because the n- as well as the p-doped cladding layers were grown during the same process in the production reactor, the electrical properties are very similar, suggesting no influence of the nitrogen, as can be seen in b).

Both optical efficiencies are slightly worse than what would be expected from Ga(N,As)/Ga(As,Sb) heterostructures employing equal amounts of nitrogen, according to the evaluation presented in Figure 5.31 a). Only about 10 μ W optical output power was reached at pump currents of about 4 A, which is estimated to be one order of magnitude too low for lasing to set in due to a too low photon density inside the cavity. However, the shape of both P-I characteristics is a straight line, which is very promising because no saturation effects set in, and it can be expected that even higher charge carrier densities can be reached. If the room temperature EL spectra depicted in Figure 7.4 are considered, the narrow shapes of the spectra get obvious, which hints less luminescence from higher order transitions. Besides the single type-II peak, a GaAs barrier or SCH peak is visible for higher current densities above 7 kA/cm², indicating carrier leakage at least to some extent. With higher excitation density, the type-II peaks shift blue. To quantify this blueshift, the type-II peak position is plotted as a function of the current density in Figure 7.5. For comparison, the blueshift of a device with 2% nitrogen based on Ga(N,As)/Ga(As,Sb) heterostructures is shown in the same graph, which shows a stronger blueshift over the investigated current density.

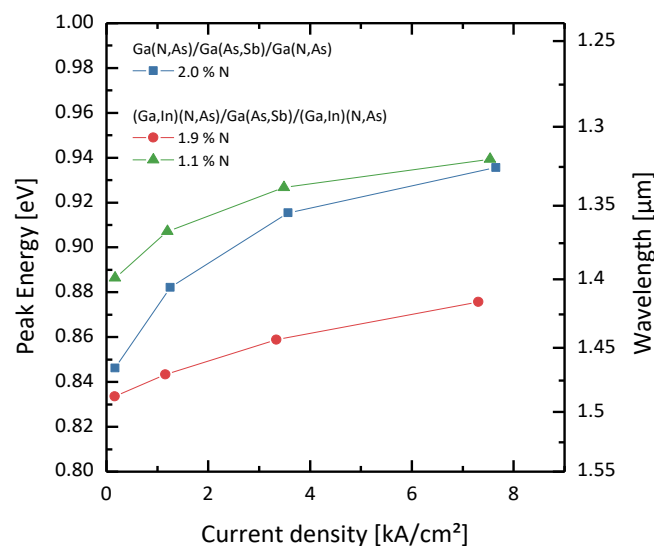


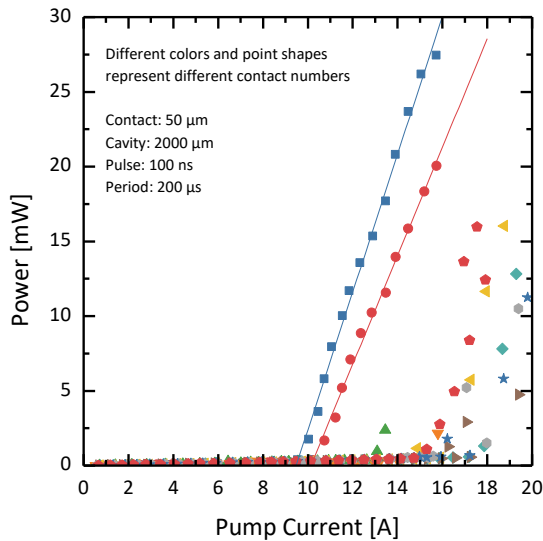
Figure 7.5 Blueshift visualization of the type-II peak of EL spectra depicted in Figure 7.4. In blue the blueshift of a similar Ga(N,As)/Ga(As,Sb) based device is shown for comparison purposes. It can be seen that a higher nitrogen content equals to a shift to longer wavelengths.

As expected, 1.1% nitrogen content results in a shorter wavelength than 1.9%, but the blueshift of both samples is very similar. Given the relatively small blueshift combined with the approximately linear shape, conclusions about the loss processes can be drawn. A linear behavior of the blueshift

indicates a constant carrier injection into the active material, suggesting that carrier leakage plays a minor role for both devices but still a higher role in the 1.1% nitrogen sample, given the higher discrepancy of the blueshift regarding a perfectly straight line. Besides the relatively high electron barriers, charge carrier leakage can still occur at such high excitation densities. The overall weak blueshift is a sign for a process draining charge carriers out of the active region, for example Shockley-Read-Hall recombinations over nitrogen induced defects as well as over precursor impurity induced defects. Additional more sophisticated spectroscopy methods will be applied to examine the influence of other loss processes such as Auger recombination.

7.3.2 Lasing characteristics

a)



b)

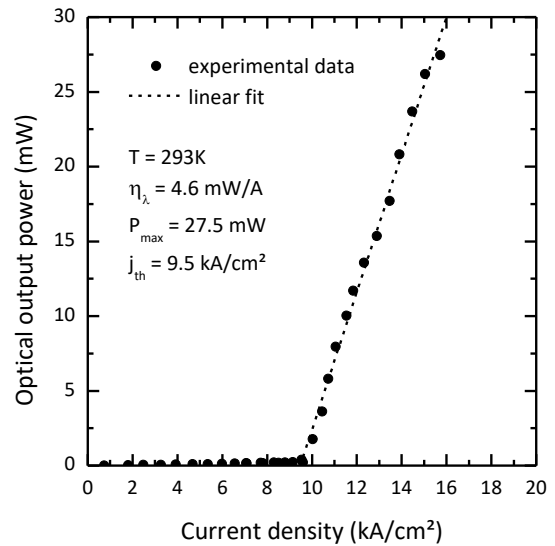


Figure 7.6 P-I characteristics measured with the AVTech current source and the device with 1.1% nitrogen content. In a) the exceeding of the lasing threshold is visible for all contacts. The threshold current varies significantly for all devices, but the optical efficiencies seem to be similar. In b) the best contact is separately shown and evaluated.

As the straight-line P-I characteristics obtained with the UR19 current source were promising, higher excitation densities were applied using the AVTech current source, as can be seen in Figure 7.6 a), in which P-I curves of several contacts are plotted. All results presented in this section were already published²⁵³. In contrast to all other electrically pumped structures presented in this work, devices with cavity lengths of 2000 μm will be used in this section. However, most other devices were also analyzed at different cavity lengths, but for the sake of reduced complexity, only 1000 μm cavities were discussed. All presented measurements exhibit the typical threshold behavior found in semiconductor lasers meaning that all contacts reach lasing threshold. At threshold, optical output powers between 200 μW and 600 μW were observed, which correspond to the values of the Ga(N,As)/Ga(As,Sb) type-II QWH laser presented in section 5.6.1, indicating that this order of power

output is needed to find a sufficiently large photon density in the cavity. Up to these values the power-current relation is perfectly linear. Above threshold, the optical efficiency is drastically increased for all contacts. Although the threshold current is different for all contacts, the optical efficiencies above and below threshold are similar. To further exemplify the lasing characteristics, one specific contact is selected and shown in Figure 7.6 b), this time with respect to the current density instead of pump current. It exhibits an excitation limited maximum output power of about 27.5 mW and an optical efficiency of 4.6 mW/A corresponding to a differential quantum efficiency of 1%. A threshold current density of 9.5 kA/cm² was found.

Due to the comparatively high threshold current density, the material must exhibit a large defect density induced by nitrogen or impurities caused by DTBAA, which is known for incorporating relatively large numbers of oxygen atoms. Additionally, no separate annealing procedure was implemented, suggesting that the external quantum efficiency, as well as the threshold current density, can be improved by finding ideal annealing steps. So far, the devices presented in this chapter were only annealed by the deposition of the cladding layer.

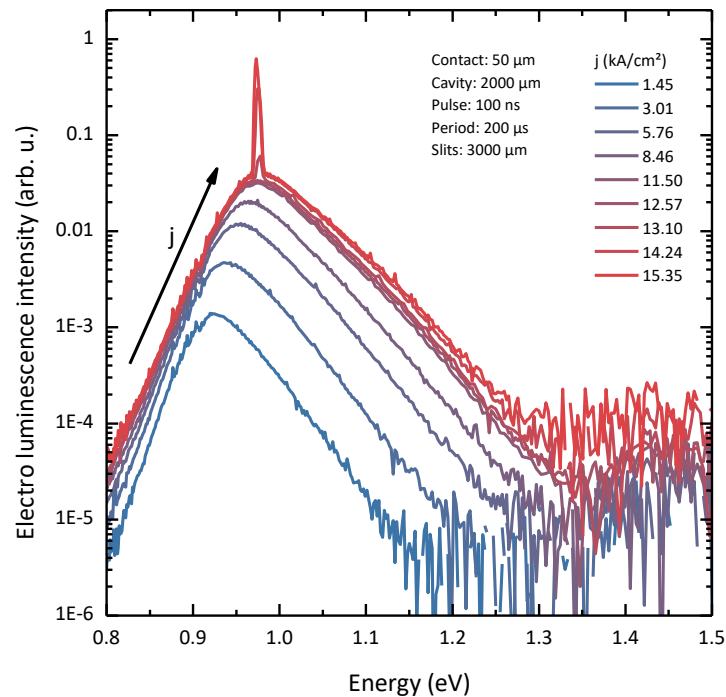


Figure 7.7 EL spectra of one of the devices characterized in Figure 7.6 measured with the AVTech current source. A strong blueshift is visible, indicating that the emission is based on the type-II transition. Above threshold, a narrow peak emerges from the type-II peak, suggesting that the lasing process is also based on the type-II transition. The emission wavelength is significantly red shifted compared to the emission wavelengths of the individual single quantum wells.

A further contact of the investigated device was used to measure EL spectra for different pump current densities to expose the radiative transition responsible for lasing. The measured spectra can

be found in Figure 7.7. A blueshift of the emission spectra with higher pump current density indicates the type-II character. Above threshold, the charge carrier density clamps, and the spectra are slightly shifted red, most probably due to competition of various LO-modes. The emission wavelength corresponds to 1.28 μm . Furthermore, the significant redshift compared to the expected type-I transitions of the individual quantum wells strongly suggests that lasing is based on the type-II transition.

Emission wavelength limiting factors arise for example from the high threshold current density. Higher threshold current density means that a higher charge carrier density is present inside the active region, causing the emission wavelength to shift blue. Hence, a longer wavelength can be reached if the threshold current density is lowered. The investigated laser device opens up a lot of room for improvement. First, the experimental precursor DTBAA can be further purified to reduce incorporation of these impurities, like oxygen atoms forming deep level traps and an efficient loss process. Besides that, no separate annealing was implemented, which is assumed to improve the optical quality drastically. Furthermore, a parameter study of chemical compositions and individual quantum well thicknesses will certainly improve lasing characteristics of the presented devices. Since the morphology of the internal interfaces plays a significant role for type-II recombinations, studies regarding the optimization of the internal interfaces will be conducted in the future. However, the presented laser devices constitute an excellent starting point for further investigations and represent the first room temperature laser emission ever observed for this particular material system.

7.3.3 Cavity length

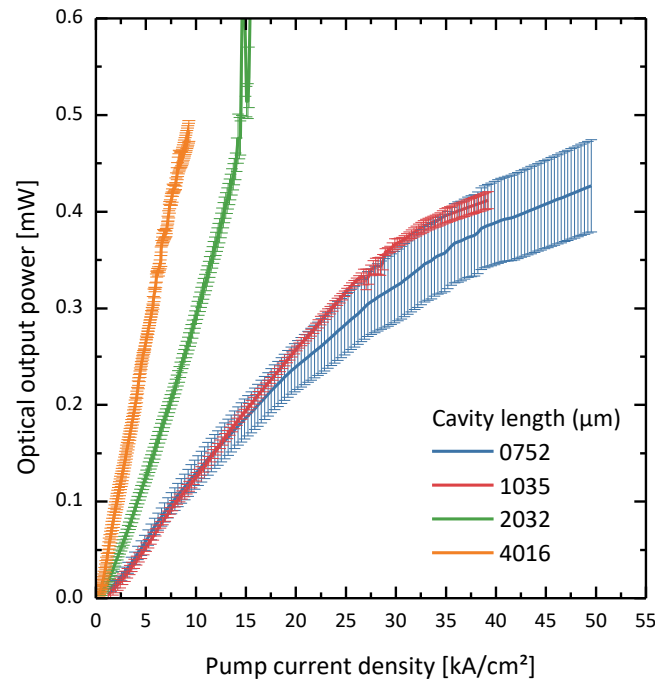


Figure 7.8 P-I characteristics measured for devices with different cavity lengths processed from the same wafer. A higher pump current density can be achieved with short cavity lengths, resulting in a saturation effect at high currents due to carrier leakage. Since shorter cavities cause the mirror losses to be more severe, lasing cannot be observed. For more extended cavities, the reachable current density is too low for lasing to set in. Thus, only for the 2032 μm cavity length lasing is observed.

As pointed out at the beginning of the last section, most devices presented in this work were shown with 1000 μm cavity lengths. A study in which laser bars with different cavity lengths are processed and measured was conducted in order to find the most suitable cavity length. If the cavity length is changed, two main properties are changing. First, the current density changes for constant pump current due to the changed contact length. Hence, stronger excitation can be investigated with shorter cavities. Additionally, the significance of mirror losses gets reduced when longer cavities are employed because these mirror losses are constant and only dependent on the properties of the cleaved facets, while the material loss or gain of one round-trip is changed in dependence on the cavity length. Thus, the mirror losses are far less significant if long cavities are used. From the experimental point of view, short cavities are easier to pump homogeneously.

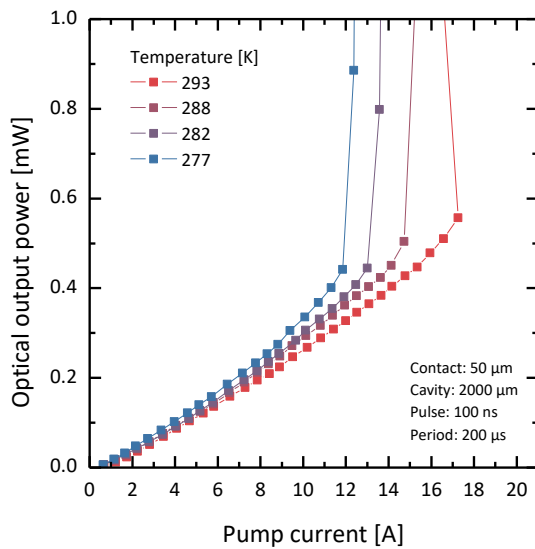
When comparing the P-I characteristics of different cavity lengths in Figure 7.8, it can be seen that larger pump current densities can be achieved for shorter cavities. For the 4016 μm long cavity, only about 10 kA/cm^2 can be reached, while about 50 kA/cm^2 can be achieved with the 752 μm long cavity. Interestingly, only the 2032 μm long cavity reached the lasing threshold, while different

processes limited all other devices. The 4016 μm long cavity is limited by too less pump current density, while the 752 μm and 1035 μm long cavities are limited by their stronger contribution of mirror losses. In this case, the mirror losses are so high that a larger photon density must be reached to start the lasing process. Unfortunately, the P-I curves are only linear up to pump current densities of about 15-20 kA/cm^2 . Above these current densities, the charge carrier density in the active regions can only be hardly increased due to band filling induced carrier leakage. Thus, the modal gain is too small for lasing.

All in all, 2 mm long cavities resemble a sweet spot mediating between optical mirror losses and sufficiently high carrier densities. Despite different cavity lengths were investigated also for devices discussed in previous chapters lasing was not found for any cavity lengths.

7.3.4 Temperature dependency

a)



b)

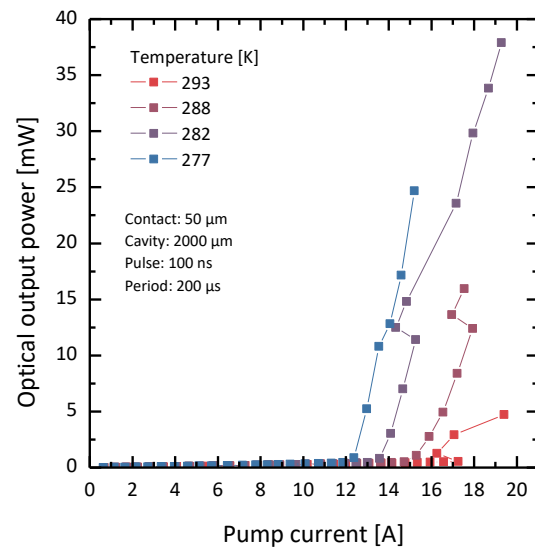


Figure 7.9 Temperature dependent P-I measurements. In a) a zoomed image detailing the LED regime is plotted, while in b) the full P-I data is shown. The threshold current shifts about 5.75 kA/cm^2 in the investigated 16 K temperature range slightly below room temperature.

Characteristics of semiconductor lasers are very dependent on the temperature under which they are used. Therefore, the discussed laser device is examined temperature dependent utilizing the Peltier element, which is typically used to stabilize the temperature to room temperature. Due to condensed water, only temperatures above 4°C can be reached. The P-I characteristics for various temperatures are plotted in Figure 7.9. A strong shift to lower threshold currents can be seen with lower temperatures. Even though the temperature was only reduced to about 4°C, the threshold current was reduced by 4.75 A or 28%. To illustrate the threshold current shift further it is plotted in Figure 7.10. Additionally, the differential quantum efficiency increases.

The overall substantial performance increase due to slightly cooling the device can be attributed to the reduction of carrier leakage as loss process due to reduction of thermal excitation. In section 7.3.1 a minor influence of carrier leakage on the device due to the high excitation density was found.

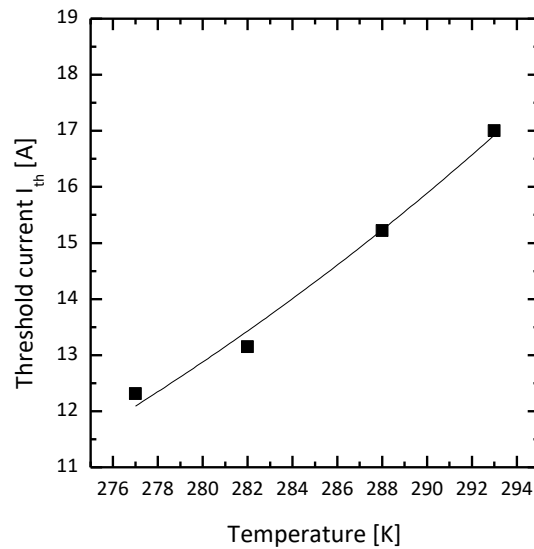


Figure 7.10 Threshold current as a function of the temperature. At room temperature the threshold current is about 17 A, which gets reduced to 12.25 A at 4°C, corresponding to a total decrease of 4.75 A.

7.3.5 Influence of annealing

In this section the laser device with 1.1% nitrogen content will undergo additional annealing steps carried out in-situ in the MOVPE reactor. For that, several smaller pieces were cut out of the full wafer. Then, these pieces were annealed in separate annealing processes with different temperatures. The annealing processes itself are divided into two subprocesses with different purposes, including a 30 min step at 650°C, 675°C, 700°C or 725°C under H₂ and TBAs ambient to allow atomic reordering to occur. A second annealing step 30 min under N₂ ambient was applied at 650°C to remove atomic hydrogen that forms interstitial defects.

To ensure a good structural quality after annealing, HR-XRD diffractograms of all pieces were measured before and after annealing, as can be seen in Figure 7.11. For lower TBAs annealing temperatures of 650°C to 675°C no difference between the measurements before and after annealing can be seen. In contrast, TBAs annealing at 700°C slightly changed the structure, as can be seen in the small shift towards less compressive strain in the red diffractogram, compared to the yellow diffractogram. What caused this shift cannot be ultimately determined because all possible options are in principle conceivable. Removal of hydrogen atoms bonding to nitrogen atoms that act as passivation could introduce a higher tensile strain in the structure. Additionally, compositional changes of indium and antimony by clustering or diffusion out of the quantum wells are possible.

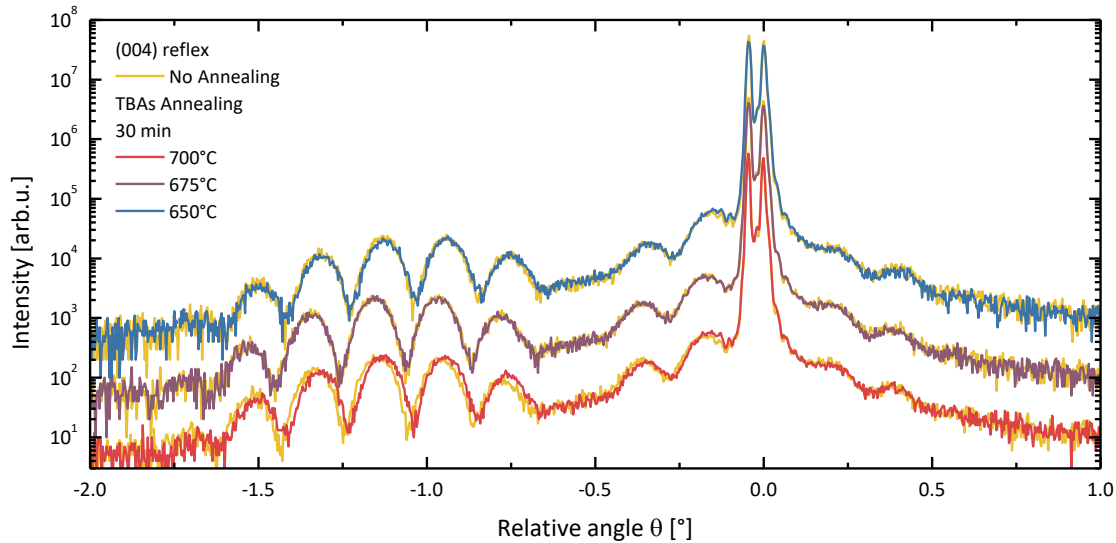


Figure 7.11 HR-XRD diffractograms measured before (yellow lines) and after annealing. To ensure a good comparability each piece cut from the full wafer was measured before and after annealing. At lower annealing temperatures no change is visible, while at 700°C a slight change towards less compressive strain is observable.

After the HR-XRD examination, the annealed samples were processed to full laser devices and measured using the AVTech current source. The P-I characteristics of 2000 μm long cavities are depicted in Figure 7.12 showing that the optical properties of the annealed samples deteriorate in comparison to the as-grown device. In particular, the optical output power and the optical efficiencies are much lower if annealed devices are considered. Furthermore, no lasing can be observed. To ensure that no unlikely changes of the cladding layers occurred, the V-I curves are plotted in Figure 7.13. As expected, no change of the electrical properties can be observed for all annealing temperatures, and the changes of the optical properties can be attributed to the active region.

Without further STEM analysis of the microscopic structure and ordering, only assumptions can be made explaining the deterioration of the optical properties. However, the effect of annealing on (Ga,In)(N,As) layers was thoroughly investigated, concluding in a microscopic reordering of nitrogen atoms to indium rich regions, causing the emission wavelength to shift blue and nitrogen induced defects like nitrogen clusters to reduce¹⁵. Annealing of Ga(As,Sb) was reported to improve the optical quality by reducing defects and a more homogeneous distribution of antimony^{188,254}.

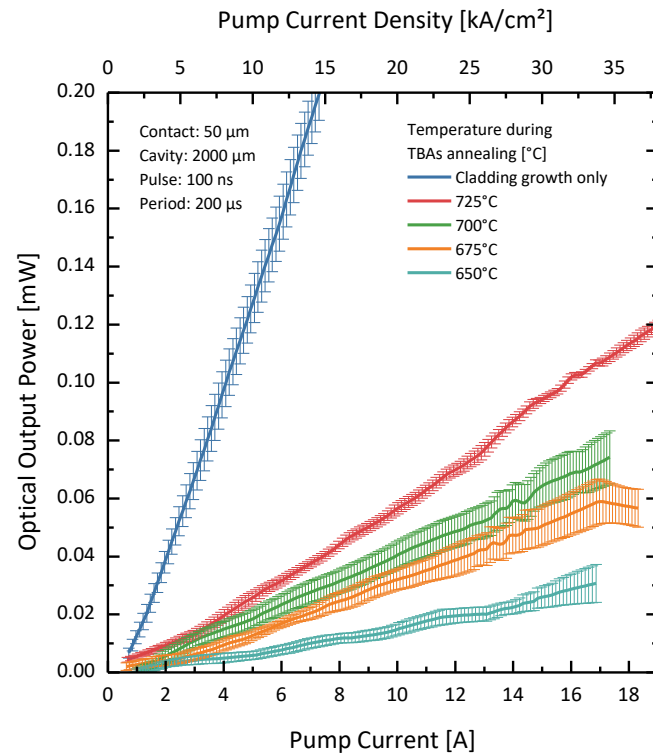


Figure 7.12 P-I characteristics of 2000 μm long cavities of annealed material compared to the as-grown samples. In comparison, the as-grown device depicted in blue exhibits a much higher optical output power and optical efficiency.

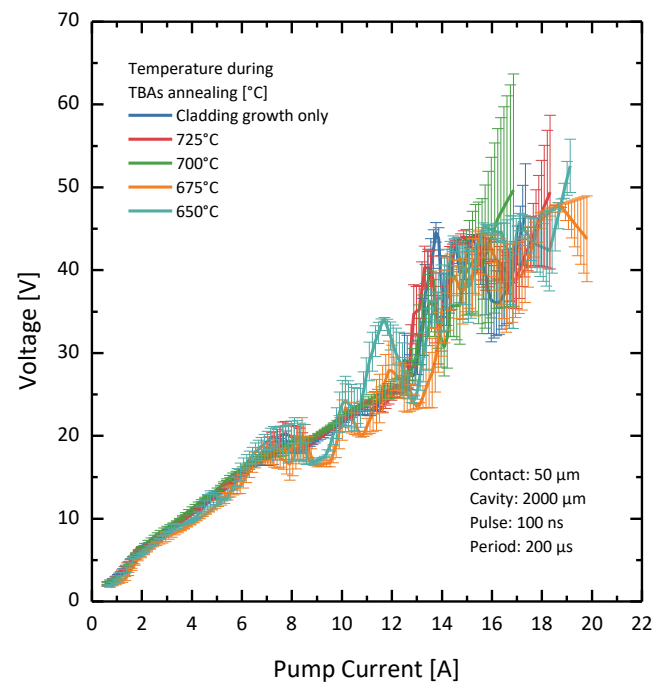


Figure 7.13 V-I characteristics measured for the devices presented in Figure 7.12. Due to the AVTech pulser, the determination of current and voltage by fitting a rectangular shape to the measured curves is difficult.

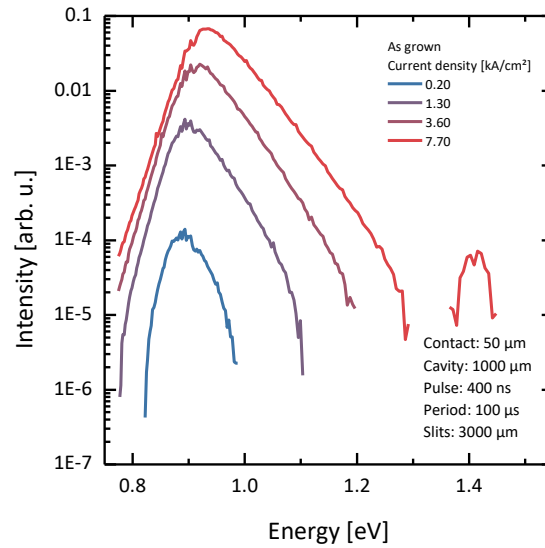


Figure 7.14 EL spectra of the as-grown device for different pump current densities below lasing threshold. A significant blueshift can be observed due to the charge carrier density inside the active region.

In the following, the effect of annealing on the spectral properties are analyzed with EL using the weaker UR19 current source. For repetition, the spectra measured for the as-grown device are depicted in Figure 7.14. All spectra of annealed devices are shown in Figure 7.15. As expected, the intensities raise with annealing temperature but are all below the intensities obtained for the as-grown sample. For lower annealing temperatures, a striking change of the low energy flank of the spectra can be seen that could be attributed to a larger defect density. However, to find a more convincing explanation, the samples will be measured at low temperatures in the future. In addition, a lower blueshift is observed for all annealing conditions, which is also illustrated in Figure 7.16. As already supposed by literature, a shift to shorter wavelengths can be measured after applying all investigated annealing conditions due to the microscopic rearrangement of nitrogen atoms. The extremely weak blueshift of about 20 meV caused by the type-II band alignment, suggesting an interdiffusion of indium or antimony atoms into neighboring layers. Therefore, the overall reduction of the optical efficiencies due to annealing could also be attributed to a deteriorated interface quality of all internal interfaces.

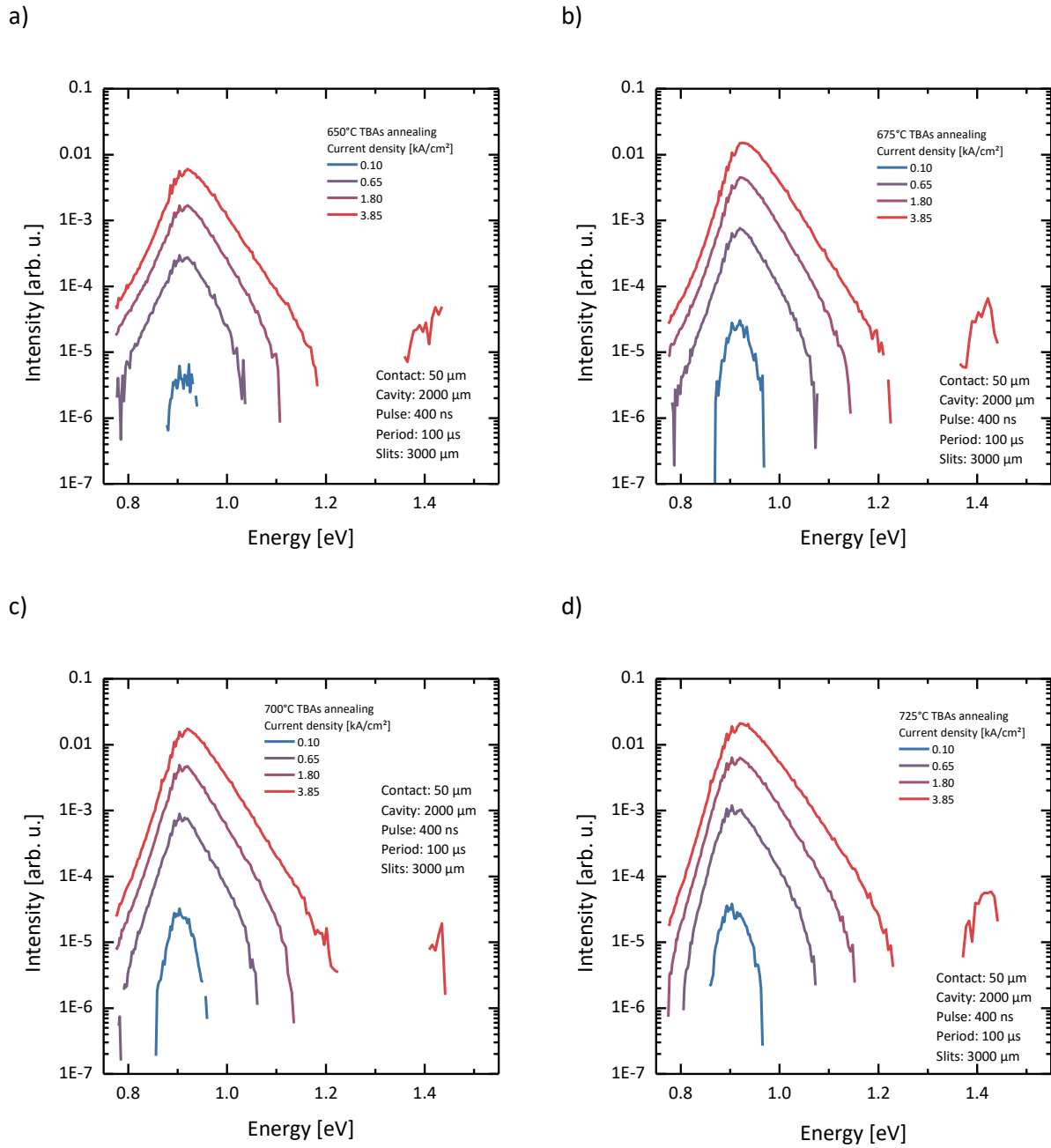


Figure 7.15 Room temperature EL spectra of annealed devices. All spectra are blue shifted compared to the as-grown sample. For the investigated pump current density range, no to almost no change of the emission energies can be seen. Especially low annealing temperatures led to a changing of the peak shape.

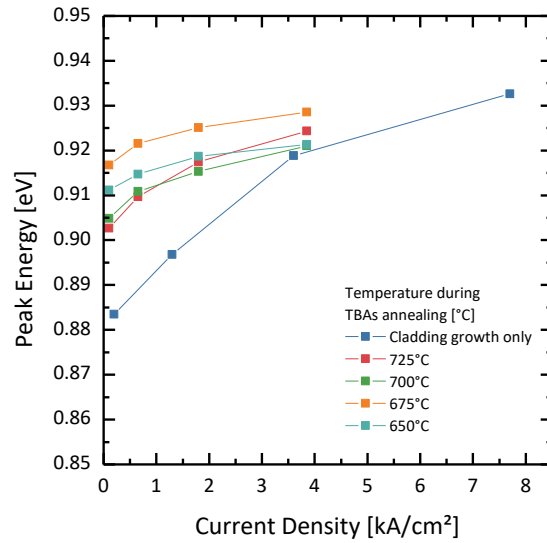


Figure 7.16 Blueshift of the EL spectra depicted in Figure 7.15. All peak emission energies of the annealed samples are blue shifted compared to the as-grown sample. However, the overall blueshift caused by charge carrier density is reduced.

If the optical efficiencies obtained for all annealed samples are plotted with respect to the TBAs annealing temperatures, the optical efficiencies form a straight line, as can be seen in Figure 7.17, indicating that a higher annealing temperature is better than lower temperatures.

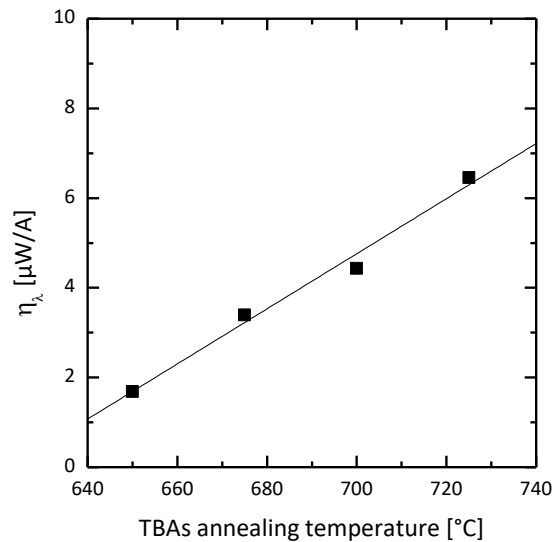


Figure 7.17 The optical efficiencies plotted as a function of the annealing temperature form a straight line. All of these optical efficiencies are worse than that of the as-grown device. Contrary to that, this plot suggests a higher annealing temperature.

This finding contradicts the fact that all annealing temperatures lead to worse optical properties. Maybe two competing processes cause the material to deteriorate for annealing in general but for higher temperatures to improve. For example, an interdiffusion process of antimony, nitrogen, or indium atoms could cause a worsening for all annealing temperatures due to the formation of highly

graded layers, as suggested by the weak blueshift as a function of the excitation density. However, these highly graded layers could benefit from higher annealing temperatures due to the usual annealing effects like microscopic reordering of nitrogen atoms into more indium rich environments or breaking of nitrogen chain like ordering and clusters, backed up by the blueshift caused by annealing.

To conclude, the effect of annealing on the discussed WQWH laser device is not clear yet. Contrary to all expectations, a severe deterioration of the optical properties was observed. More detailed studies investigating the effect of annealing on the microscopic ordering of atoms with a particular focus on the interdiffusion of antimony, indium, and nitrogen atoms must be carried out to further understand these effects and to improve the optical properties of the presented laser devices by annealing.

7.4 Conclusion and discussion

In conclusion, the epitaxial growth of (Ga,In)(N,As)/Ga(As,Sb) based type-II heterostructures for device applications is difficult to achieve with the conventional nitrogen precursor UDMHy. Instead, the experimental precursor DTBAA must be employed because it features no dependence on the presence of heavier elements like indium or antimony. Hence, two DTBAA grown laser structures were discussed in this chapter, containing 1.1% and 1.9% nitrogen. As expected, a higher nitrogen content causes the emission wavelength to shift to longer wavelengths. The reachable wavelength is still longer for all nitrogen contents than that of Ga(N,As)/Ga(As,Sb) heterostructures if equal nitrogen contents are compared. This makes the (Ga,In)(N,As)/Ga(As,Sb) material system superior due to the strong exponential dependence of the optical properties like output power and optical efficiency on the nitrogen content. However, due to the worse material quality caused by worse DTBAA purity, the optical efficiency was found to be below the values obtained for Ga(N,As)/Ga(As,Sb). Contrary, the shape of the P-I curves suggested less influence by charge carrier leakage, resulting in exceeding of the lasing threshold and the first presentation of room temperature lasing of dilute nitride containing type-II heterostructures. The temperature dependent determination of the threshold currents suggested again at least a worsening of the threshold current by carrier leakage, which is not unexpected considering the high excitation density. An in-depth study of different cavity lengths revealed that too long cavities do not reach the required threshold current density due to the large contact area, and too short cavities cannot achieve a sufficiently large photon density in the cavity. Although annealing is predicted to improve the optical properties of the devices, the applied in-situ reactor annealing caused a deterioration of the material

quality. The reasons for that are not fully understood yet, but the reason was assumed to be interdiffusion of indium, antimony, or nitrogen atoms.

Despite the superior optical efficiencies of laser devices utilizing materials from Chapter 5 and Chapter 6, the presented (Ga,In)(N,As)/Ga(As,Sb) heterostructures were still the only material that showed lasing at room temperature. In the following the possible reasons for that will be discussed. It was proven that the nitrogen content comes with introduction of defects like carbon and nitrogen clusters that act as non-radiative recombination centers. In the case of DTBAA oxygen atoms are assumed to incorporate additionally. These defects reduce the number of radiative recombination in the active region and hence decrease the photon density inside the cavity. Simultaneously, the non-radiative recombination centers drain charge carriers out of the active region, causing a lower charge carrier injection efficiency. It is likely that these non-radiative recombinations occur with a higher probability than the radiative recombination across the type-II transitions because the wavefunction overlap is undoubtedly smaller. In order to increase the photon density to a sufficient value, the pump current must be drastically raised to overcome the effects of non-radiative recombinations. At some point, the pump current either reaches a value at which it exceeds lasing threshold or carriers leak into higher states due to band filling effects. Then, the charge carrier injection efficiency gets decreased drastically, and no population inversion could be achieved. It seems like the increase of threshold current with nitrogen content, and carrier leakage are their respective antagonists for each other. If the nitrogen content is too low, carrier leakage is possible. If the nitrogen content is too high, the threshold current is shifted to high values causing carrier leakage to occur before lasing threshold is reached. Especially the photon density is too low in these high nitrogen containing devices.

The compositional profiles of Ga(N,As) quantum wells were shown to be inhomogeneous in section 4.2.3, which was found in the literature to worsen if annealing is applied. Contrary, a homogeneous distribution of nitrogen atoms was observed even after annealing for (Ga,In)(N,As).¹⁵ Thus, a further reason for lasing in (Ga,In)(N,As) containing WQWH could be the improved nitrogen distribution.

Ga(N,As) quantum wells must provide electron confinement only by incorporation of nitrogen, which is unfavorable for lasing due to the abovementioned reasons. Additionally, the quantum wells are tensilely strained, causing the valence band effective hole mass to be heavy and hence the density of states to be comparatively large. If holes leak into these states, shifting the quasi Fermi levels is difficult, so reaching population inversion is hindered.

The usage of (Ga,In)(N,As) instead of Ga(N,As) enables stronger carrier confinement combined with less nitrogen incorporation needed for reaching this carrier confinement. Together with a reduced effective mass of confined conduction band electrons, which leads to more extensive wavefunction

overlap and gain, an exceeding of lasing threshold could be experimentally achieved. In addition, a compressive strain causes the effective valence band masses to be light and the density of states small.

Chapter 8 Conclusion and Outlook

In this present thesis, the growth by metal organic vapor phase epitaxy (MOVPE) of GaAs-based materials is investigated to shift the emission wavelength to longer wavelengths. This was addressed by incorporating dilute amounts of nitrogen into “W” type-II heterostructures (WQWH). As materials, studies regarding Ga(N,As)/Ga(As,Sb)/Ga(N,As), Ga(N,As)/(Ga,In)As/Ga(N,As), and (Ga,In)(N,As)/Ga(As,Sb)/(Ga,In)(N,As) WQWH were detailed, ultimately leading to the very first dilute nitride based WQWH laser device exhibiting room temperature lasing.

At first, the respective single quantum wells were analyzed with a particular focus on the possible interactions between the epitaxial growth of the entire “W” heterostructures, especially the influence of surface segregated antimony on the nitrogen incorporation in the subsequent dilute nitride containing layer. For that, the consideration was divided into gas phase and surface effects. Investigations of gas phase effects were carried out using an in-situ mass spectrometer integrated into the MOVPE reactor and examining the decomposition temperatures of the respective nitrogen precursors under the application of different amounts of antimony precursor supply. In detail, the nozzle of the mass spectrometer was overgrown with polycrystalline GaAs to comprise catalytic effects. The decomposition as a function of the ambient temperature while supplying varying amounts of antimony precursor was analyzed. For the conventional most established nitrogen precursor 1,1-dimethylhydrazine (UDMHy), an elevated decomposition temperature was observed for increased antimony precursor supply, indicating that UDMHy decomposition is highly dependent on the underlying surface due to significant changes of surface reconstructions occurring because of surface segregation of antimony atoms. In contrast to that, the novel combined nitrogen and arsenic precursor di-*tert*-butyl-amino-arsane (DTBAA) showed a much weaker sensitivity on the surface and no influence on the antimony supply. Besides that, surface effects were investigated by growing relatively thick Ga(N,As) layers under a constant supply of antimony. As a result, no influence of this antimony on the incorporation efficiency was found when DTBAA was used, while a strong reduction to almost no nitrogen incorporation occurred when UDMHy was utilized. However, the effect of reduced nitrogen incorporation of UDMHy combined with antimony was reported to be perfectly compensable with an application of higher UDMHy supplies. All in all, the effect of antimony could not be exhaustively clarified, but first hints point towards a decomposition effect occurring at the growth surface. Future experiments will be conducted investigating the precise changes of precursor decomposition paths under antimony influence.

These insights were exploited for growing the full Ga(N,As)/Ga(As,Sb)/Ga(N,As) WQWH in which the first Ga(N,As) quantum well can be deposited undisturbed while the growth of the second Ga(N,As) quantum well suffers from the influence of surface segregated antimony from the previous Ga(As,Sb) layer deposition causing the nitrogen incorporation to drop by 60%. An optimization process was developed to overcome this issue, which included a compensation of the reduced nitrogen incorporation by adjusting the UDMHy supply. Besides that, optimization of the internal interfaces between Ga(N,As) quantum wells to the Ga(As,Sb) quantum well was carried out. For that, an antimony predeposition before growing Ga(As,Sb) layers helped to achieve an abrupt chemical composition profile. The second internal interface was prepared by applying TBAs stabilized growth interruptions, smoothing the surface while desorbing excess antimony. However, the duration of such growth interruptions must be carefully chosen since too long durations induce the effect of antimony desorption from the already grown crystal, hence worsening the interface morphology. As optimized durations, 20 s or 30 s were determined for growth at 550°C or 525°C, respectively. Unfortunately, the full antimony surface coverage cannot be abolished within 20 s but only after a growth interruption of 120 s. Nevertheless, the antimony surface coverage is already significantly reduced after 20 s long growth interruptions, and the compensation of the reduced nitrogen incorporation can easily be achieved. Alternatively, DTBAA can be used as nitrogen precursor removing the need for further optimization of the nitrogen incorporation equality because the incorporation efficiency was not influenced by antimony.

The epitaxial growth of Ga(N,As)/(Ga,In)As/Ga(N,As) WQWH raises a similar challenge, namely a reduction of nitrogen incorporation due to segregated indium atoms. An application of TBAs stabilized growth interruption after the (Ga,In)As quantum well growth of up to 120 s resulted in improved optical properties but showed no effect on the nitrogen incorporation into the subsequent Ga(N,As) quantum well due to the lower volatility of indium atoms, compared to antimony atoms.

So far, the nitrogen incorporation issue was not solved for (Ga,In)(N,As)/Ga(As,Sb)/(Ga,In)(N,As) WQWH if UDMHy is used due to even more severe effects if indium and antimony atoms affect the nitrogen incorporation simultaneously. Thus, DTBAA was successfully employed for growing these structures resulting in symmetric nitrogen incorporation.

For all the above-mentioned material systems, laser devices were fabricated according to the insights gained by all epitaxial growth experiments. All materials have in common that they feature diluted amounts of nitrogen as an essential element for reducing the conduction band edge. Experimental determination of the optical efficiency of multiple laser devices reveals a strong dependence of the optical efficiency on the nitrogen content which was attributed to the formation of nitrogen clusters and carbon incorporation that act as non-radiative recombination centers. The investigation of

Ga(N,As)/(Ga,In)As/Ga(N,As) based laser structures exhibited the least suitability for laser applications due to too low band offsets while requiring relatively large nitrogen contents. Better suitability was found for Ga(N,As)/Ga(As,Sb)/Ga(N,As) WQWH because only 2% nitrogen is necessary to reach emission at 1.3 μm . Even less nitrogen (less than 1%) is needed if (Ga,In)(N,As) replaces Ga(N,As) as electron quantum well material. With this, even 1.5 μm are reachable with reasonable nitrogen contents, as can be seen in Figure 8.1 a).

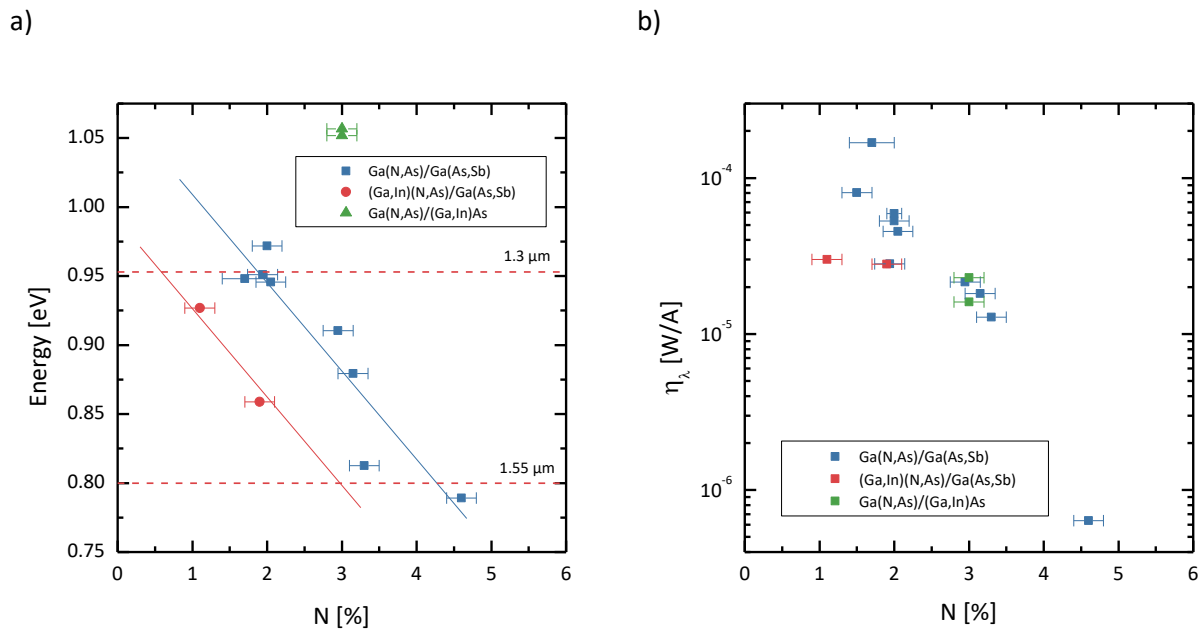


Figure 8.1 In a) the peak emission energies of the respective devices are depicted. The lines serve as a guide to the eye. b) Combined plot of optical efficiencies as a function of the nitrogen content covering all three investigated material systems.

Valuable insights were gained when examining the device properties of Ga(N,As)/Ga(As,Sb)/Ga(N,As) WQWH based devices. The optical efficiencies determined as a function of the nitrogen content were illustrated in Figure 8.1 b), highlighting the exponential dependency between nitrogen content and optical efficiency. For relatively low nitrogen contents, a significant saturation of the optical output power was observed, while for higher nitrogen contents above 3%, the optical output power was found to be weak. These effects were attributed to two different major loss channels that come into play at different nitrogen contents. Under low nitrogen conditions non-radiative recombination paths increase the threshold current density to comparatively high values. Before sufficient photon densities could be reached, electrons occupy energetically higher states facilitating electron leakage to conduction band barrier states. In the case of large nitrogen contents, the non-radiative recombination processes become the major limiting factor. Carrier leakage was additionally proven by realization of Ga(As,Sb)/Ga(N,As)/Ga(As,Sb) “M” type-II structures in which one instead of two Ga(N,As) quantum wells provide confined electron states.

These issues can be partly overcome by replacing Ga(N,As) by (Ga,In)(N,As). It was found that less nitrogen content is required to achieve a sufficiently high conduction band barrier due to the band edge reduction introduced already by indium incorporation alone. This reduced requirement of nitrogen incorporation enables a reduced non-radiative recombination path. Finally, these structures led to the outstanding result of first room temperature lasing for this material class. A device containing 1.1% nitrogen showed lasing above a current density of 9.5 kA/cm^2 with a differential efficiency of 1% and an optical efficiency of 4.6 mW/A. A pump current limited maximum pulse output power of 27.5 mW was reached. Spectral characterization revealed a lasing wavelength of $1.28 \mu\text{m}$, which could be shifted to longer wavelengths by further optimizing this structure.

When considering Ga(N,As)/(Ga,In)As/Ga(N,As) WQWH devices, the barriers especially in the valence band are too low and thus electronic states spanning over the full WQWH are forming, as indicated by the weak blueshift at high excitation densities.

When all possible GaAs based dilute nitride materials are reviewed, the fact that only very specific materials showed laser emission is notable. While (Ga,In)(N,As)⁵⁹, (Ga,In)(N,As,Sb)⁷¹ and (Ga,In)(N,As)/Ga(As,Sb)/(Ga,In)(N,As) showed laser emission at room temperature, materials like Ga(N,As,Sb) or Ga(N,As) could never successfully be employed in laser devices. The striking difference between these materials is the incorporation of indium. Besides the deliberate considerations about the nitrogen content in Ga(N,As) and its influence on the main loss channel, the influence of nitrogen induced defects must not be underestimated. One explanation could be that thermal annealing is generally required to reduce these defects and achieve a microscopic rearrangement. In an excellent study Volz et al. showed that annealing induces an improvement of nitrogen homogeneity in (Ga,In)(N,As) quantum wells while it can induce cluster formation in Ga(N,As) quantum wells¹⁵. These clusters can reduce the optical quality drastically. Indium may be required for achieving homogeneity of nitrogen distribution and consequently lasing.

First attempts to find suitable annealing conditions were made by applying in-situ reactor annealing or additional rapid thermal annealing with different temperatures and ambients. However, all investigated WQWHs seem to deteriorate under all examined conditions in structural quality due to the applied annealing steps. This was attributed to an over-annealing since all structures endured already a long annealing step in the form of cladding growth.

All in all, the development of a proof of principle laser device was successful, with the first ever demonstrated room temperature laser emission of dilute nitride-based type-II WQWH.

As the presented WQWH lasers still suffer from severe losses, multiple optimizations regarding the optical and structural quality of these devices will be conducted in the very near future. At first, a

further purification of the experimental nitrogen source DTBAA will result in superior material quality. Besides that, attempts to grow these structures with UDMHy will be started. As dilute nitride-based materials profit from optimized annealing conditions, in-depth studies regarding optimized annealing will presumably improve the material quality while using quantitative scanning transmission electron microscopy to verify changes in the microscopic structure. Parameter studies examining the influence of the individual quantum well layer thicknesses and chemical compositions will additionally shift the emission to longer wavelengths while improving essential figures of merit like threshold current and differential efficiency. Supplementary improvements of the internal interfaces could significantly improve the type-II transition efficiency across these interfaces. Additionally, high reflection coatings on the device facets could reduce the total optical losses and hence reduce the threshold current.

A careful adjustment of the nitrogen content while exchanging the GaAs barriers with other materials exhibiting a higher conduction band offset like (Al,Ga)As or Ga(P,As) could lead to room temperature lasing for Ga(N,As)/Ga(As,Sb)/Ga(N,As) WQWH as well. Further high reflection coatings of the laser facets will provide a sufficient photon density in the cavity.

When it comes to dilute nitride based semiconductor lasers in general, studies regarding (Ga,In)(N,As,Sb) quantum wells could be promising because such structures already showed gain when grown with molecular beam epitaxy²⁵⁵. A realization of these quantum wells was not possible until now due to drastically reduced nitrogen incorporation in MOVPE experiments when indium and antimony are present. Due to the availability of an alternative nitrogen precursor DTBAA the growth could principally be possible.

Furthermore, fundamental research will be conducted in order to further clarify the effect behind the reduced nitrogen incorporation when indium and antimony atoms are present. For that, more detailed mass spectrometry experiments will be carried out investigating the decomposition products of UDMHy as a function of the antimony or indium supply. Combined with in-situ surface analysis with reflectance anisotropy spectroscopy (RAS) measurements, a clear picture will be obtained.

Chapter 9 Bibliography

1. Murphy, E. The semiconductor laser: Enabling optical communication. *Nat. Photonics* **4**, 287 (2010).
2. Agrawal, G. P. *Fiber-Optic Communication Systems. EC and M: Electrical Construction and Maintenance* **90**, (Wiley, 2021).
3. Thijs, P. J. A. *et al.* High quality InGaAsPnP for multiple quantum well laser diodes grown by low-pressure OMVPE. *J. Cryst. Growth* **93**, 863–869 (1988).
4. Phillips, A. F., Sweeney, S. J., Adams, A. R. & Thijs, P. J. A. The temperature dependence of 1.3- and 1.5- μ m compressively strained InGaAs(P) MQW semiconductor lasers. *IEEE J. Sel. Top. Quantum Electron.* **5**, 401–412 (1999).
5. Piprek, J., Kenton White, J. & SpringThorpe, A. J. What limits the maximum output power of long-wavelength AlGaInAs/InP laser diodes? *IEEE J. Quantum Electron.* **38**, 1253–1259 (2002).
6. Hess, K., Vojak, B. A., Holonyak, N., Chin, R. & Dapkus, P. D. Temperature dependence of threshold current for a quantum-well heterostructure laser. *Solid. State. Electron.* **23**, 585–589 (1980).
7. Bradford, T. & Li, Z. M. A Comparative Study of Temperature Sensitivity of InGaAsP and AlGaAs MQW Lasers Using Numerical Simulations. *IEEE J. Quantum Electron.* **31**, 1841–1847 (1995).
8. Meyer, J. R., Hoffman, C. A., Bartoli, F. J. & Ram-Mohan, L. R. Type-II quantum-well lasers for the mid-wavelength infrared. *Appl. Phys. Lett.* **67**, 757–759 (1995).
9. Zegrya, G. G. & Andreev, A. D. Mechanism of suppression of Auger recombination processes in type-II heterostructures. *Appl. Phys. Lett.* **67**, 2681 (1995).
10. Fuchs, C. Epitaxial growth and characterization of type-II (GaIn)As / Ga(AsSb)/(GaIn)As / GaAs “W”-quantum well heterostructures and lasers. (2017).
11. Mawst, L. J. *et al.* MOCVD-grown dilute nitride type II quantum wells. *IEEE J. Sel. Top. Quantum Electron.* **14**, 979–991 (2008).
12. Yeh, J. Y. *et al.* Characteristics of InGaAsN-GaAsSb type-II “W” quantum wells. *J. Cryst. Growth* **287**, 615–619 (2006).
13. Rath, M. K. *et al.* High antimony content GaAs_{1-z}N_z - GaAs_{1-y}Sb_y type-II “w” structure for long wavelength emission. *J. Appl. Phys.* **106**, (2009).
14. Khandekar, A. A. *et al.* Characteristics of GaAsNGaAsSb type-II quantum wells grown by metalorganic vapor phase epitaxy on GaAs substrates. *J. Appl. Phys.* **98**, 1–5 (2005).
15. Volz, K. *et al.* Annealing effects on the nanoscale indium and nitrogen distribution in Ga(NAs) and (GaIn)(NAs) quantum wells. *J. Appl. Phys.* **102**, 1–6 (2007).
16. Renk, K. F. *Basics of Laser Physics – For Students of Science and Engineering. Graduate Texts in Physics* (2012).
17. Möller, C. *et al.* Type-II vertical-external-cavity surface-emitting laser with Watt level output powers at 1.2 μ m. *Appl. Phys. Lett.* **108**, (2016).
18. Schlenker, D., Miyamoto, T., Chen, Z., Koyama, F. & Iga, K. Long wavelength GaInAs/GaAs

- quantum well lasers. *Conf. Proc. - Int. Conf. Indium Phosphide Relat. Mater.* 499–502 (1999). doi:10.1109/iciprm.1999.773742
19. Su, Y. K. *et al.* Optimization of the highly strained InGaAs/GaAs quantum well lasers grown by MOVPE. *J. Cryst. Growth* **310**, 3615–3620 (2008).
 20. Chen, W. C. *et al.* Highly Strained 1.22- μm InGaAs Lasers Grown by MOVPE. *IEEE Photonics Technol. Lett.* **20**, 264–266 (2008).
 21. Chen, W. C., Su, Y. K., Chuang, R. W. & Tsai, M. C. Highly strained InGaAs lasers grown by MOVPE with low threshold current density. *Nov. In-pl. Semicond. Lasers VI* **6485**, 648518 (2007).
 22. Sundgren, P., Berggren, J., Goldman, P. & Hammar, M. Highly strained InGaAsGaAs multiple quantum-wells for laser applications in the 1200-1300 nm wavelength regime. *Appl. Phys. Lett.* **87**, 10–13 (2005).
 23. Tansu, N., Yeh, J. Y. & Mawst, L. J. Extremely low threshold-current-density InGaAs quantum-well lasers with emission wavelength of 1215-1233 nm. *Appl. Phys. Lett.* **82**, 4038–4040 (2003).
 24. Sato, S. & Satoh, S. 1.21 μm continuous-wave operation of highly strained GaInAs quantum well lasers on GaAs substrates. *Japanese J. Appl. Physics, Part 2 Lett.* **38**, 1–4 (1999).
 25. Schlenker, D., Miyamoto, T., Chen, Z., Koyama, F. & Iga, K. 1.17- μm Highly Strained GaInAs – GaAs Quantum-Well Laser. **11**, 946–948 (1999).
 26. Choi, W. J., Dapkus, P. D. & Jewell, J. J. 1.2- μm GaAsP/InGaAs strain compensated single-quantum-well diode laser on GaAs using metal-organic chemical vapor deposition. *IEEE Photonics Technol. Lett.* **11**, 1572–1574 (1999).
 27. Yu, S.-Q., Jin, X., Johnson, S. R. & Zhang, Y.-H. Gain saturation and carrier distribution effects in molecular beam epitaxy grown GaAsSb/GaAs quantum well lasers. *J. Vac. Sci. Technol. B Microelectron. Nanom. Struct.* **24**, 1617 (2006).
 28. Noh, M. S., Dupuis, R. D., Bour, D. P., Walter, G. & Holonyak, N. Long-wavelength strain-compensated GaAsSb quantum-well heterostructures laser grown by metalorganic chemical vapor deposition. *Appl. Phys. Lett.* **83**, 2530–2532 (2003).
 29. Liu, P. W., Lee, M. H., Lin, H. H. & Chen, J. R. Low-threshold current GaAsSb/GaAs quantum well lasers grown by solid source molecular beam epitaxy. *Electron. Lett.* **38**, 1354–1355 (2002).
 30. Hossain, N. *et al.* Improved performance of GaAsSb/GaAs SQW lasers. *Nov. In-pl. Semicond. Lasers IX* **7616**, 761608 (2010).
 31. Ryu, S.-W. & Dapkus, P. D. Low threshold current density GaAsSb quantum well (QW) lasers grown by metal organic chemical vapour deposition on GaAs substrates. *Electron. Lett.* **36**, 1387 (2000).
 32. Yu, S.-Q. *et al.* High performance GaAsSb/GaAs quantum well lasers. *J. Vac. Sci. Technol. B Microelectron. Nanom. Struct.* **25**, 1658 (2007).
 33. Wang, J. B. *et al.* Band edge alignment of pseudomorphic GaAs $1-y$ Sb y on GaAs. *Phys. Rev. B - Condens. Matter Mater. Phys.* **70**, 1–8 (2004).
 34. Yamada, M. *et al.* Low-threshold lasing at 1.3 μm from GaAsSb quantum wells directly grown on GaAs substrates. *Conf. Proc. - Lasers Electro-Optics Soc. Annu. Meet.* **1**, 149–150 (1998).
 35. Huang, C. T. *et al.* Optical characterization of a GaAsSb/GaAs/GaAsP strain-compensated

- quantum well structure grown by metal-organic vapor phase epitaxy. *J. Cryst. Growth* **370**, 182–185 (2013).
36. Anan, T. *et al.* GaAsSb: A novel material for 1.3 μm VCSELs. *Electron. Lett.* **34**, 2127–2129 (1998).
 37. Blum, O. & Klem, J. F. Characteristics of GaAsSb single-quantum-well-lasers emitting near 1.3 μm . *IEEE Photonics Technol. Lett.* **12**, 771–773 (2000).
 38. Noh, M. S., Ryou, J. H., Dupuis, R. D., Chang, Y. L. & Weissman, R. H. Band lineup of pseudomorphic GaAs 1-xSb x quantum-well structures with GaAs, GaAsP, and InGaP barriers grown by metal organic chemical vapor deposition. *J. Appl. Phys.* **100**, (2006).
 39. Hossain, N. *et al.* The influence of growth conditions on carrier recombination mechanisms in 1.3 μm GaAsSb/GaAs quantum well lasers. *Appl. Phys. Lett.* **102**, (2013).
 40. Maros, A., Faleev, N. N., Bertoni, M. I., Honsberg, C. B. & King, R. R. Carrier localization effects in GaAs1-xSbx/GaAs heterostructures. *J. Appl. Phys.* **120**, 1–8 (2016).
 41. Kurakake, H., Soda, H., Uchida, T. & Yamazaki, S. 1.3 μm InGaAs/GaAs strained quantum well lasers with InGaP cladding layer. *Electron. Lett.* **30**, 563–565 (1994).
 42. Bogusevski, S., Broderick, C. A. & O'Reilly, E. P. Theory and Optimization of 1.3- μm Metamorphic Quantum Well Lasers. *IEEE J. Quantum Electron.* **52**, 1–11 (2016).
 43. Arai, M., Kobayashi, W. & Kohtoku, M. 1.3- μm Range Metamorphic InGaAs Laser With High Characteristic Temperature for Low Power Consumption Operation. *IEEE J. Sel. Top. Quantum Electron.* **19**, (2013).
 44. Broderick, C. A., Usman, M., Sweeney, S. J. & O'Reilly, E. P. Band engineering in dilute nitride and bismide semiconductor lasers. *Semicond. Sci. Technol.* **27**, (2012).
 45. Kim, H., Guan, Y., Babcock, S. E., Kuech, T. F. & Mawst, L. J. Characteristics of OMVPE grown GaAsBi QW lasers and impact of post-growth thermal annealing. *J. Appl. Phys.* **123**, 1–7 (2018).
 46. Ludewig, P. *et al.* Electrical injection Ga(AsBi)/(AlGa)As single quantum well laser. *Appl. Phys. Lett.* **102**, 1–4 (2013).
 47. Fuyuki, T., Yoshida, K., Yoshioka, R. & Yoshimoto, M. Electrically pumped room-temperature operation of GaAs 1- x Bi x laser diodes with low-temperature dependence of oscillation wavelength. *Appl. Phys. Express* **7**, 082101 (2014).
 48. Marko, I. P. *et al.* Optical gain in GaAsBi/GaAs quantum well diode lasers. *Sci. Rep.* **6**, 1–10 (2016).
 49. Biefeld, R. M. The metal-organic chemical vapor deposition and properties of III-V antimony-based semiconductor materials. *Mater. Sci. Eng. R Reports* **36**, 105–142 (2002).
 50. Ungaro, G., Le Roux, G., Teissier, R. & Harmand, J. C. GaAsSbN: a new low-bandgap material for GaAs substrates. *Electron. Lett.* **35**, 1246 (1999).
 51. Harmand, J. C. *et al.* GaNAsSb: How does it compare with other dilute III-V-nitride alloys? *Semicond. Sci. Technol.* **17**, 778–784 (2002).
 52. Peake, G. M., Waldrip, K. E., Hargett, T. W., Modine, N. A. & Serkland, D. K. OMVPE of GaAsSbN for long wavelength emission on GaAs. *J. Cryst. Growth* **261**, 398–403 (2004).
 53. Kondow, M. *et al.* GaInNAs: A novel material for long-wavelength semiconductor lasers. *IEEE J. Sel. Top. Quantum Electron.* **3**, 719–729 (1997).

54. Höhnsdorf, F. *et al.* Reduced threshold current densities of (GaIn)(NAs)/GaAs single quantum well lasers for emission wavelengths in the range 1.28 – 1.38 μm . *Electron. Lett.* **35**, 571 (1999).
55. Gokhale, M. R., Studenkov, P. V., Wei, J. & Forrest, S. R. Low-threshold current, high-efficiency 1.3- μm wavelength aluminum-free InGaAsN-based quantum-well lasers. *IEEE Photonics Technol. Lett.* **12**, 131–133 (2000).
56. Sato, S. I., Osawa, Y. & Saitoh, T. Room-temperature operation of GaInNAs/GaInP double-heterostructure laser diodes grown by metalorganic chemical vapor deposition. *Japanese J. Appl. Physics, Part 1 Regul. Pap. Short Notes Rev. Pap.* **36**, 2671–2675 (1997).
57. Tansu, N., Kirsch, N. J. & Mawst, L. J. Low-threshold-current-density 1300-nm dilute-nitride quantum well lasers. *Appl. Phys. Lett.* **81**, 2523–2525 (2002).
58. Andreev, A. D. & O'Reilly, E. P. Theoretical study of Auger recombination in a GaInNAs 1.3 μm quantum well laser structure. *Appl. Phys. Lett.* **84**, 1826–1828 (2004).
59. Harris, J. S. GaInNAs long-wavelength lasers: progress and challenges. *Semicond. Sci. Technol.* **17**, 880–891 (2002).
60. Korpijärvi, V.-M., Viheriälä, J., Koskinen, M., Aho, A. T. & Guina, M. High-power temperature-stable GaInNAs distributed Bragg reflector laser emitting at 1180 nm. *Opt. Lett.* **41**, 657 (2016).
61. Tansu, N., Yeh, J. Y. & Mawst, L. J. Physics and characteristics of high performance 1200 nm InGaAs and 1300–1400 nm InGaAsN quantum well lasers obtained by metal-organic chemical vapour deposition. *J. Phys. Condens. Matter* **16**, (2004).
62. Hader, J., Koch, S. W. & Moloney, J. V. Microscopic theory of gain and spontaneous emission in GaInNAs laser material. *Solid. State. Electron.* **47**, 513–521 (2003).
63. Choquette, K. D. *et al.* Room temperature continuous wave InGaAsN quantum well vertical-cavity lasers emitting at 1.3 μm . *Electron. Lett.* **36**, 1388–1390 (2000).
64. Qu, Y., Liu, C. Y. & Yuan, S. High-power 1.3- μm InGaAsN strain-compensated lasers fabricated with pulsed anodic oxidation. *Appl. Phys. Lett.* **85**, 5149–5151 (2004).
65. Sato, S. & Satoh, S. Room-temperature continuous-wave operation of 1.24- μm GaInNAs lasers grown by metal-organic chemical vapor deposition. *IEEE J. Sel. Top. Quantum Electron.* **5**, 707–710 (1999).
66. Palmer, D. J. *et al.* Effect of nitrogen on gain and efficiency in InGaAsN quantum-well lasers. *Appl. Phys. Lett.* **86**, 1–3 (2005).
67. Kondow, M., Nakatsuka, S., Kitatani, T., Yazawa, Y. & Okai, M. Room-temperature pulsed operation of GaInNAs laser diodes with excellent high-temperature performance. *Japanese J. Appl. Physics, Part 1 Regul. Pap. Short Notes Rev. Pap.* **35**, 5711–5713 (1996).
68. Spruytte, S. G. *et al.* Nitrogen incorporation in group III-nitride-arsenide materials grown by elemental source molecular beam epitaxy. *J. Cryst. Growth* **227–228**, 506–515 (2001).
69. Li, L. H. *et al.* Investigations on GaInNAsSb quinary alloy for 1.5 μm laser emission on GaAs. *Appl. Phys. Lett.* **83**, 1298–1300 (2003).
70. Wonill Ha *et al.* A 1.5 μm GaInNAs(Sb) laser grown on GaAs by MBE. in *International Conference on Molecular Beam Epitaxy* **38**, 61–62 (IEEE, 2002).
71. Bank, S. R. *et al.* Low-threshold CW GaInNAsSb/GaAs laser at 1.49 μm . *Electron. Lett.* **39**, 1445 (2003).

72. Yang, X., Héroux, J. B., Mei, L. F. & Wang, W. I. InGaAsNSb/GaAs quantum wells for 1.55 μm lasers grown by molecular-beam epitaxy. *Appl. Phys. Lett.* **78**, 4068–4070 (2001).
73. Shimizu, H. *et al.* 1.3 μm -band low threshold GaInNASb quantum well lasers. *Conf. Proc. - Lasers Electro-Optics Soc. Annu. Meet.* **1**, 161–162 (2002).
74. Ledentsov, N. N. Long-wavelength quantum-dot lasers on GaAs substrates: From media to device concepts. *IEEE J. Sel. Top. Quantum Electron.* **8**, 1015–1024 (2002).
75. Ledentsov, N. N. *et al.* QD lasers: physics and applications. *Semicond. Org. Optoelectron. Mater. Devices* **5624**, 335 (2005).
76. Kovsh, A. R. *et al.* InAs/InGaAs/GaAs quantum dot lasers of 1.3 μm range with enhanced optical gain. *J. Cryst. Growth* **251**, 729–736 (2003).
77. Zhang, Z. Y. *et al.* 1.55 μm InAs/GaAs quantum dots and high repetition rate quantum dot SESAM mode-locked laser. *Sci. Rep.* **2**, 1–5 (2012).
78. Mi, Z., Bhattacharya, P. & Yang, J. Growth and characteristics of ultralow threshold 1.45 μm metamorphic InAs tunnel injection quantum dot lasers on GaAs. *Appl. Phys. Lett.* **89**, 2004–2007 (2006).
79. Ledentsov, N. N. *et al.* High performance quantum dot lasers on GaAs substrates operating in 1.5 μm range. *Electron. Lett.* **39**, 1126–1128 (2003).
80. Kittel, C. *Einführung in die Festkörperphysik*. (Oldenbourg Wissenschaftsverlag GmbH, 2013).
81. Ashcroft, N. W. & Mermin, D. N. *Festkörperphysik*. (Oldenbourg Wissenschaftsverlag GmbH, 2013).
82. Grundmann, M. *The Physics of Semiconductors*. (Springer International Publishing, 2021). doi:10.1007/978-3-030-51569-0
83. Varshni, Y. P. Temperature dependence of the energy gap in semiconductors. *Physica* **34**, 149–154 (1967).
84. Sze, S. M. Semiconductor devices. *Springer Ser. Mater. Sci.* **207**, 195–233 (2014).
85. Blakemore, J. S. Semiconducting and other major properties of gallium arsenide. *J. Appl. Phys.* **53**, (1982).
86. Vurgaftman, I., Meyer, J. R. & Ram-Mohan, L. R. Band parameters for III–V compound semiconductors and their alloys. *J. Appl. Phys.* **89**, 5815–5875 (2001).
87. Vurgaftman, I. & Meyer, J. R. Band parameters for nitrogen-containing semiconductors. *J. Appl. Phys.* **94**, 3675–3696 (2003).
88. Vegard, L. Die Konstitution der Mischkristalle und die Raumfüllung der Atome. *Zeitschrift für Phys.* **5**, 17–26 (1921).
89. Leshko, A. Y. *et al.* High power single-mode ($\lambda = 1.3\text{--}1.6\ \mu\text{m}$) laser diodes based on quantum well InGaAsP/InP heterostructures. *Semiconductors* **36**, 1308–1314 (2002).
90. Volz, K. *et al.* Specific structural and compositional properties of (GaIn)(NAs) and their influence on optoelectronic device performance. *J. Cryst. Growth* **272**, 739–747 (2004).
91. Karpov, S. Y. Advances in the modeling of MOVPE processes. *J. Cryst. Growth* **248**, 1–7 (2003).
92. Jensen, K. F., Fotiadis, D. I. & Mountziaris, T. J. Detailed models of the MOVPE process. *J. Cryst. Growth* **107**, 1–11 (1991).

93. Mihopoulos, T. G., Gupta, V. & Jensen, K. F. A reaction-transport model for AlGa_N MOVPE growth. **195**, 733–739 (1998).
94. Dauelsberg, M. & Talalaev, R. Progress in Modeling of III-Nitride MOVPE. *Prog. Cryst. Growth Charact. Mater.* **66**, 100486 (2020).
95. Stringfellow, G. B. *Organometallic Vapor-Phase Epitaxy*. (1999).
96. Sweeney, S. J., Eales, T. D. & Adams, A. R. The impact of strained layers on current and emerging semiconductor laser systems. *J. Appl. Phys.* **125**, 1–11 (2019).
97. Beyer, A., Stolz, W. & Volz, K. Metastable cubic zinc-blende III/V semiconductors: Growth and structural characteristics. *Prog. Cryst. Growth Charact. Mater.* **61**, 46–62 (2015).
98. Liu, X., Pistol, M. E., Samuelson, L., Schwetlick, S. & Seifert, W. Nitrogen pair luminescence in GaAs. *Appl. Phys. Lett.* **56**, 1451–1453 (1990).
99. Anderson, R. L. Germanium-Gallium Arsenide Heterojunctions. *IBM J. Res. Dev.* **4**, 283–287 (1960).
100. Tersoff, J. Theory of semiconductor heterojunctions: The role of quantum dipoles. *Phys. Rev. B* **30**, 4874–4877 (1984).
101. Weseloh, M. J., Oelerich, J. O. & Koch, S. W. Half-occupation approach for the ab initio calculation of strained Ga(AsSb)/GaAs valence band offsets. *AIP Adv.* **10**, (2020).
102. Van De Walle, C. G. Universal alignment of hydrogen levels in semiconductors and insulators. *Phys. B Condens. Matter* **376–377**, 1–6 (2006).
103. Zhu, Y. *et al.* Band offset determination of mixed As/Sb type-II staggered gap heterostructure for n-channel tunnel field effect transistor application. *J. Appl. Phys.* **113**, 1–6 (2013).
104. Coldren, L. A., Corzine, S. W., Publication, A. W.-I. & Wiley, J. *Diode Lasers and Photonic Integrated Circuits*. (1995).
105. O'Reilly, E. P. Valence band engineering in strained-layer structures. *Semicond. Sci. Technol.* **4**, 121–137 (1989).
106. Jones, G. & O'Reilly, E. P. Improved Performance of Long-Wavelength Strained Bulk-like Semiconductor Lasers. *IEEE J. Quantum Electron.* **29**, 1344–1354 (1993).
107. Kuo, C. P., Vong, S. K., Cohen, R. M. & Stringfellow, G. B. Effect of mismatch strain on band gap in III-V semiconductors. *J. Appl. Phys.* **57**, 5428–5432 (1985).
108. Adams, A. R. Strained-layer quantum-well lasers. *IEEE J. Sel. Top. Quantum Electron.* **17**, 1364–1373 (2011).
109. Wei, S. H. & Zunger, A. Giant and composition-dependent optical bowing coefficient in GaAsN alloys. *Phys. Rev. Lett.* **76**, 664–667 (1996).
110. Weyers, M., Sato, M. & Ando, H. Red shift of photoluminescence and absorption in dilute gaasn alloy layers. *Jpn. J. Appl. Phys.* **31**, L853–L855 (1992).
111. O'Reilly, E. P. & Lindsay, A. k · P model of ordered Ga_NAs_{1-x}. *Phys. Status Solidi Basic Res.* **216**, 131–134 (1999).
112. Harris, C., Lindsay, A. & O'Reilly, E. P. Evolution of N defect states and optical transitions in ordered and disordered GaP_{1-x}N_x alloys. *J. Phys. Condens. Matter* **20**, (2008).
113. O'Reilly, E. P., Lindsay, A., Klar, P. J., Polimeni, A. & Capizzi, M. Trends in the electronic structure of dilute nitride alloys. *Semicond. Sci. Technol.* **24**, (2009).

114. Sakai, S., Ueta, Y. & Terauchi, Y. Band Gap Energy and Band Lineup of III-V Alloy Semiconductors Incorporating Nitrogen and Boron. *Jpn. J. Appl. Phys.* **32**, 4413–4417 (1993).
115. Veal, T. D., Mahboob, I. & McConville, C. F. Negative band gaps in dilute $\text{In}_x\text{Sb}_{1-x}$ alloys. *Phys. Rev. Lett.* **92**, 92–95 (2004).
116. Shan, W. *et al.* Band anticrossing in gainnas alloys. *Phys. Rev. Lett.* **82**, 1221–1224 (1999).
117. Klar, P. J. *et al.* From N isoelectronic impurities to N-induced bands in the $\text{Ga}_x\text{N}_{1-x}\text{As}_1$ alloy. *Appl. Phys. Lett.* **76**, 3439–3441 (2000).
118. Broderick, C. A., Usman, M., Sweeney, S. J. & O'Reilly, E. P. Band engineering in dilute nitride and bismide semiconductor lasers. *Semicond. Sci. Technol.* **27**, (2012).
119. Kitatani, T. *et al.* Analysis of Band Offset in GaNAs/GaAs by X-Ray Photoelectron Spectroscopy. *Jpn. J. Appl. Phys.* **38**, 5003–5006 (1999).
120. Sun, B. Q. *et al.* Interband luminescence and absorption of GaNAs/GaAs single-quantum-well structures. *Appl. Phys. Lett.* **76**, 2862–2864 (2000).
121. Buyanova, I. A. *et al.* Type I band alignment in the $\text{Ga}_x\text{N}_{1-x}\text{As}_1/\text{GaAs}$ quantum wells. *Phys. Rev. B - Condens. Matter Mater. Phys.* **63**, 333031–333034 (2001).
122. Egorov, A. Y., Odnoblyudov, V. A., Krizhanovskaya, N. V., Mamutin, V. V. & Ustinov, V. M. Band-edge line-up in $\text{GaAs}/\text{GaAsN}/\text{InGaAs}$ heterostructures. *Semiconductors* **36**, 1355–1359 (2002).
123. Klar, P. J. *et al.* Interband transitions of quantum wells and device structures containing $\text{Ga}(\text{N}, \text{As})$ and $(\text{Ga}, \text{In})(\text{N}, \text{As})$. *Semicond. Sci. Technol.* **17**, 830–842 (2002).
124. Lindsay, A. & O'Reilly, E. P. Theory of enhanced bandgap non-parabolicity in $\text{Ga}_x\text{N}_{1-x}\text{As}_1$ and related alloys. *Solid State Commun.* **112**, 443–447 (1999).
125. Skierbiszewski, C. *et al.* Effect of nitrogen-induced modification of the conduction band structure on electron transport in GaAsN alloys. *Phys. Status Solidi Basic Res.* **216**, 135–139 (1999).
126. Hai, P. N., Chen, W. M., Buyanova, I. A., Xin, H. P. & Tu, C. W. Direct determination of electron effective mass in GaNAs/GaAs quantum wells. *Appl. Phys. Lett.* **77**, 1843–1845 (2000).
127. Bellaiche, L. & Zunger, A. Effects of atomic short-range order on the electronic and optical properties of GaAsN , GaInN , and GaInAs alloys. *Phys. Rev. B - Condens. Matter Mater. Phys.* **57**, 4425–4431 (1998).
128. Kent, P. R. C. & Zunger, A. Evolution of electron states with composition in GaAsN alloys. *Phys. Status Solidi Basic Res.* **228**, 253–257 (2001).
129. Kent, P. R. C. & Zunger, A. Theory of electronic structure evolution in GaAsN and GaPN alloys. *Phys. Rev. B - Condens. Matter Mater. Phys.* **64**, 16–20 (2001).
130. Volz, K., Koch, J., Kunert, B., Nemeth, I. & Stolz, W. Influence of annealing on the optical and structural properties of dilute N-containing III/V semiconductor heterostructures. *J. Cryst. Growth* **298**, 126–130 (2007).
131. Kurtz, S. R. *et al.* InGaAsN solar cells with 1.0 eV band gap, lattice matched to GaAs . *Appl. Phys. Lett.* **74**, 729–731 (1999).
132. Baldassarri Höger Von Högersthal, G. *et al.* Magnetophotoluminescence studies of $(\text{InGa})(\text{AsN})/\text{GaAs}$ heterostructures. *Phys. Rev. B - Condens. Matter Mater. Phys.* **67**, 1–4 (2003).

133. Masia, F. *et al.* Interaction between conduction band edge and nitrogen states probed by carrier effective-mass measurements in GaAs_{1-x}N_x. *Phys. Rev. B - Condens. Matter Mater. Phys.* **73**, 2–5 (2006).
134. Masia, F. *et al.* Early manifestation of localization effects in diluted Ga(AsN). *Appl. Phys. Lett.* **82**, 4474–4476 (2003).
135. Zhang, Y., Mascarenhas, A., Xin, H. & Tu, C. Formation of an impurity band and its quantum confinement in heavily doped GaAs:N. *Phys. Rev. B - Condens. Matter Mater. Phys.* **61**, 7479–7482 (2000).
136. Liebich, S. *et al.* Laser operation of Ga(NAsP) lattice-matched to (001) silicon substrate. *Appl. Phys. Lett.* **99**, (2011).
137. Sterzer, E. (Ga, In)(N, As, Sb) Solar Cells : N Incorporation using Novel Precursor in MOVPE Growth and Solar Cell Characteristics. (2018).
138. Sterzer, E. *et al.* (GaIn)(NAs) growth using di-tertiary-butyl-arsano-amine (DTBAA). *J. Cryst. Growth* **467**, 132–136 (2017).
139. Sentosa, D., Tang, X., Yin, Z. & Chua, S. J. Thermal annealing effect on GaNAs epilayers with different nitrogen compositions grown by MOCVD. *J. Cryst. Growth* **307**, 229–234 (2007).
140. Kitatani, T., Nakahara, K., Kondow, M., Uomi, K. & Tanaka, T. Mechanism analysis of improved GaInNAs optical properties through thermal annealing. *J. Cryst. Growth* **209**, 345–349 (2000).
141. Klar, P. J. *et al.* (Ga, In)(N, As)-fine structure of the band gap due to nearest-neighbor configurations of the isovalent nitrogen. *Phys. Rev. B - Condens. Matter Mater. Phys.* **64**, 1–4 (2001).
142. Rubel, O. *et al.* Columnar [001]-oriented nitrogen order in Ga(NAs) and (GaIn)(NAs) alloys. *Appl. Phys. Lett.* **85**, 5908–5910 (2004).
143. Kim, K. & Zunger, A. Spatial correlations in GaInAsN alloys and their effects on band-gap enhancement and electron localization. *Phys. Rev. Lett.* **86**, 2609–2612 (2001).
144. Albrecht, M. *et al.* Effect of annealing on the In and N distribution in InGaAsN quantum wells. *Appl. Phys. Lett.* **81**, 2719–2721 (2002).
145. Oye, M. M., Govindaraju, S., Sidhu, R., Reifsnider, J. M. & Holmes, A. L. Diffusion mechanisms of indium and nitrogen during the annealing of InGaAs quantum wells with GaNAs barriers and GaAs spacer layers. *Appl. Phys. Lett.* **86**, 1–3 (2005).
146. Hugues, M., Damilano, B., Chauveau, J. M., Duboz, J. Y. & Massies, J. Blue-shift mechanisms in annealed (Ga,In)(N,As) GaAs quantum wells. *Phys. Rev. B - Condens. Matter Mater. Phys.* **75**, 1–6 (2007).
147. Litvinov, D. *et al.* Determination of the nitrogen distribution in InGaAs/GaAs quantum wells by transmission electron microscopy. *Appl. Phys. Lett.* **85**, 3743–3745 (2004).
148. Sun, Y. *et al.* Redshift and blueshift of GaNAs/GaAs multiple quantum wells induced by rapid thermal annealing. *J. Cryst. Growth* **483**, 190–194 (2018).
149. Li, L. H. *et al.* Effects of rapid thermal annealing and SiO₂ encapsulation on GaNAs/gaAs single quantum wells grown by plasma-assisted molecular-beam epitaxy. *Appl. Phys. Lett.* **78**, 2488–2490 (2001).
150. Janotti, A., Wei, S. H., Zhang, S. B., Kurtz, S. & Van de Walle, C. G. Interactions between nitrogen, hydrogen, and gallium vacancies in GaAsN alloys. *Phys. Rev. B - Condens. Matter Mater. Phys.* **67**, 2–5 (2003).

151. Ciatto, G. *et al.* Nitrogen-hydrogen complex in Ga As_xN_{1-x} revealed by x-ray absorption spectroscopy. *Phys. Rev. B - Condens. Matter Mater. Phys.* **71**, 1–4 (2005).
152. Janotti, A., Zhang, S. B., Wei, S. H. & Van de Walle, C. G. Effects of hydrogen on the electronic properties of dilute GaAsN alloys. *Phys. Rev. Lett.* **89**, 086403/1-086403/4 (2002).
153. Cheah, W. K. *et al.* Analysis and optimization of the annealing mechanisms in (In)GaAsN on GaAs. *Semicond. Sci. Technol.* **21**, 808–812 (2006).
154. Ikeda, M. & Uchida, S. Blue-violet laser diodes suitable for blu-ray disk. *Phys. Status Solidi Appl. Res.* **194**, 407–413 (2002).
155. Azadgoli, B. & Baker, R. Y. Laser applications in surgery. *Ann. Transl. Med.* **4**, 1–7 (2016).
156. Cieslak, M. J. & Fuerschbach, P. W. On the weldability, composition, and hardness of pulsed and continuous Nd:YAG laser welds in aluminum alloys 6061, 5456, and 5086. *Metall. Trans. B* **19**, 319–329 (1988).
157. Hecht, J. Lidar for Self-Driving Cars. *Opt. Photonics News* **29**, 26–33 (2018).
158. Dupuis, R. D., Dapkus, P. D., Holonyak, N., Rezek, E. A. & Chin, R. Room-temperature laser operation of quantum-well Ga(1-x)Al_xAs-GaAs laser diodes grown by metalorganic chemical vapor deposition. *Appl. Phys. Lett.* **32**, 295–297 (1978).
159. Kroemer, H. A proposed class of hetero-junction injection lasers. *Proc. IEEE* **51**, 1782–1783 (1963).
160. Kapon, E. Quantum wire lasers. *Proc. IEEE* **80**, 398–410 (1992).
161. Ledentsov, N. N. Quantum dot laser. *Semicond. Sci. Technol.* **26**, (2011).
162. Messmer, C. & Bilello, J. C. The surface energy of Si, GaAs, and GaP. *J. Appl. Phys.* **52**, 4623–4629 (1981).
163. Hecht, E. *Optik*. (De Gruyter, 2018). doi:10.1515/9783110526653
164. Saleh, B. E. A. & Teich, M. C. *Fundamentals of Photonics*. (John Wiley & Sons, Inc., 1991). doi:10.1002/0471213748
165. Bai, Y., Darvish, S. R., Bandyopadhyay, N., Slivken, S. & Razeghi, M. Optimizing facet coating of quantum cascade lasers for low power consumption. *J. Appl. Phys.* **109**, (2011).
166. Ettenberg, M. A new dielectric facet reflector for semiconductor lasers. *Appl. Phys. Lett.* **32**, 724–725 (1978).
167. Salin, F. & Squier, J. Gain guiding in solid-state lasers. *Opt. Lett.* **17**, 1352 (1992).
168. van Druten, N. J. *et al.* Observation of transverse modes in a microchip laser with combined gain and index guiding. *J. Opt. Soc. Am. B* **18**, 1793 (2001).
169. Shockley, W. & Read, W. T. Statistics of the recombinations of holes and electrons. *Phys. Rev.* **87**, 835–842 (1952).
170. Hall, R. N. Electron-Hole Recombination in Germanium. *Phys. Rev.* **87**, 387–387 (1952).
171. Sze, S. M. & Irvin, J. C. Resistivity, mobility and impurity levels in GaAs, Ge, and Si at 300°K. *Solid State Electron.* **11**, 599–602 (1968).
172. Sprengel, S. *et al.* InP-based type-II quantum-well lasers and LEDs. *IEEE J. Sel. Top. Quantum Electron.* **19**, (2013).
173. Wang, C., Pan, W., Kolokolov, K. & Wang, S. Band Structure and Optical Gain of InGaAs/GaAsBi

- Type-II Quantum Wells Modeled by the $k \cdot p$ Model. *Chinese Phys. Lett.* **35**, 1–4 (2018).
174. Arif, R. A., Zhao, H. & Tansu, N. Type-II InGa_N-Ga_NAs quantum wells for lasers applications. *Appl. Phys. Lett.* **92**, 95–98 (2008).
 175. Sprengel, S. *et al.* Type-II InP-based lasers emitting at 2.55 μm . *Appl. Phys. Lett.* **100**, 2–5 (2012).
 176. Gies, S., Holz, B., Fuchs, C., Stolz, W. & Heimbrodt, W. Recombination dynamics of type-II excitons in (Ga,In)As/GaAs/Ga(As,Sb) heterostructures. *Nanotechnology* **28**, (2017).
 177. Rost, L. *et al.* Correlation of optical properties and interface morphology in type-II semiconductor heterostructures. *J. Phys. Condens. Matter* **31**, 014001 (2019).
 178. Rost, L. *et al.* The influence of growth interruption on the luminescence properties of Ga(As,Sb)-based type II heterostructures. *J. Lumin.* **231**, 117817 (2021).
 179. Berger, C. *et al.* Novel type-II material system for laser applications in the near-infrared regime. *AIP Adv.* **5**, (2015).
 180. Fuchs, C. *et al.* Electrical injection type-II (GaIn)As/Ga (AsSb)/(GaIn)As single 'W'-quantum well laser at 1.2 μm . *Electron. Lett.* **52**, 1875–1877 (2016).
 181. Möller, C. *et al.* Fundamental transverse mode operation of a type-II vertical-external-cavity surface-emitting laser at 1.2 μm . *Electron. Lett.* **53**, 93–94 (2017).
 182. Stein, M., Fuchs, C., Stolz, W., Mittleman, D. M. & Koch, M. Direct Probe of Room-Temperature Quantum-Tunneling Processes in Type-II Heterostructures Using Terahertz Emission Spectroscopy. *Phys. Rev. Appl.* **13**, 1 (2020).
 183. Kükelhan, P. *et al.* Segregation at interfaces in (GaIn)As/Ga(AsSb)/(GaIn)As- quantum well heterostructures explored by atomic resolution STEM. *J. Cryst. Growth* **524**, 125180 (2019).
 184. Tansu, N. & Mawst, L. J. Design analysis of 1550-nm GaAsSb-(In)GaAsN type-II quantum-well laser active regions. *IEEE J. Quantum Electron.* **39**, 1205–1210 (2003).
 185. Vurgaftman, I., Meyer, J. R., Tansu, N. & Mawst, L. J. (In)GaAsN-based type-II "W" quantum-well lasers for emission at $\lambda = 1.55 \mu\text{m}$. *Appl. Phys. Lett.* **83**, 2742–2744 (2003).
 186. Gonzalo, A. *et al.* Type-II GaAsSb/GaAsN superlattice solar cells. in *Physics, Simulation, and Photonic Engineering of Photovoltaic Devices VII* (eds. Freundlich, A., Sugiyama, M. & Lombez, L.) 13 (SPIE, 2018). doi:10.1117/12.2290079
 187. Reyes, D. F. *et al.* Modelling of the Sb and N distribution in type II GaAsSb/GaAsN superlattices for solar cell applications. *Appl. Surf. Sci.* **442**, 664–672 (2018).
 188. Braza, V. *et al.* Compositional inhomogeneities in type-I and type-II superlattices for GaAsSbN-based solar cells: Effect of thermal annealing. *Appl. Surf. Sci.* **459**, 1–8 (2018).
 189. Ruiz, N. *et al.* Control of nitrogen inhomogeneities in Type-I and Type-II GaAsSbN superlattices for solar cell devices. *Nanomaterials* **9**, (2019).
 190. Hantke, K. *et al.* Time-resolved photoluminescence of type-I and type-II (GaIn)As Ga(NAs) heterostructures. *Phys. Rev. B - Condens. Matter Mater. Phys.* **71**, 1–9 (2005).
 191. Schlichenmaier, C. *et al.* Type I-type II transition in InGaAs-GaNAs heterostructures. *Appl. Phys. Lett.* **86**, 1–3 (2005).
 192. Springer, P. *et al.* Charge transfer luminescence in (GaIn)As/GaAs/Ga(NAs) double quantum wells. *J. Lumin.* **175**, 255–259 (2016).

193. Hepp, T. *et al.* Room-temperature laser operation of a (Ga,In)As/Ga(As,Bi)/(Ga,In)As W-type laser diode. *Electron. Lett.* **1–3** (2021). doi:10.1049/ell2.12353
194. Hepp, T. *et al.* Dilute Bismuth Containing W - Type Heterostructures for Long- Wavelength Emission on GaAs Substrates. (2021). doi:10.1021/acs.cgd.1c00754
195. Peter, M. *et al.* Realization and modeling of a pseudomorphic (GaAs $1-x$ Sb x –In y Ga $1-y$ As)/GaAs bilayer-quantum well. *Appl. Phys. Lett.* **67**, 2639–2641 (1995).
196. Meyer, J. R. *et al.* Auger coefficients in type-II InAs/Ga $_{1-x}$ In x Sb quantum wells. *Appl. Phys. Lett.* **73**, 2857–2859 (1998).
197. Chow, W. W. & Schneider, H. C. Charge-separation effects in 1.3 μ m GaAsSb type-II quantum-well laser gain. *Appl. Phys. Lett.* **78**, 4100–4102 (2001).
198. Chow, W. W., Spahn, O. B., Schneider, H. C. & Klem, J. F. Contributions to the large blue emission shift in a GaAsSb type-II laser. *IEEE J. Quantum Electron.* **37**, 1178–1182 (2001).
199. Wang, M. W., Collins, D. A., McGill, T. C., Grant, R. W. & Feenstra, R. M. Effect of interface composition and growth order on the mixed anion InAs/GaSb valence band offset. *Appl. Phys. Lett.* **66**, 2981 (1995).
200. Georgiev, N. & Mozume, T. Photoluminescence study of InGaAs/AlAsSb heterostructure. *J. Appl. Phys.* **89**, 1064–1069 (2001).
201. Shenai-Khatkhate, D. V. Ultrapure Metal-Organic Precursors for MOVPE. in *Metalorganic Vapor Phase Epitaxy (MOVPE)* 467–506 (Wiley, 2019). doi:10.1002/9781119313021.ch13
202. Irvine, S. J. C. & Capper, P. Introduction to Metalorganic Vapor Phase Epitaxy. in *Metalorganic Vapor Phase Epitaxy (MOVPE)* 1–18 (Wiley, 2019). doi:10.1002/9781119313021.ch1
203. Kuech, T. F., Veuhoff, E., Kuan, T. S., Deline, V. & Potemski, R. The influence of growth chemistry on the MOVPE growth of GaAs and Al $_x$ Ga $_{1-x}$ As layers and heterostructures. *J. Cryst. Growth* **77**, 257–271 (1986).
204. Kuech, T. F. & Veuhoff, E. Mechanism of carbon incorporation in MOCVD GaAs. *J. Cryst. Growth* **68**, 148–156 (1984).
205. Dimroth, F., Agert, C. & Bett, A. W. Growth of Sb-based materials by MOVPE. *J. Cryst. Growth* **248**, 265–273 (2003).
206. Chen, C. H., Larsen, C. A. & Stringfellow, G. B. Use of tertiarybutylarsine for GaAs growth. *Appl. Phys. Lett.* **50**, 218–220 (1987).
207. Larsen, C. A., Buchan, N. I., Li, S. H. & Stringfellow, G. B. Decomposition mechanisms of tertiarybutylarsine. *J. Cryst. Growth* **94**, 663–672 (1989).
208. Stolz, W. Alternative N-, P- and As-precursors for III/V-epitaxy. *J. Cryst. Growth* **209**, 272–278 (2000).
209. Maßmeyer, O. *et al.* Decomposition Mechanisms of Di- tert-butylaminoarsane (DTBAA). *Organometallics* **38**, 3181–3186 (2019).
210. Fewster, P. F. *X-ray Scattering from Semiconductors*. (2003).
211. Bragg, P. W. H. & Bragg, W. L. The reflection of X-rays by crystals. *Proc. R. Soc. London. Ser. A, Contain. Pap. a Math. Phys. Character* **88**, 428–438 (1913).
212. Tapfer, L. High resolution x-ray diffraction in multilayered semiconductor structures and superlattices. *Phys. Scr.* **1989**, 45–50 (1989).

213. Tapfer, L. & Ploog, K. X-ray interference in ultrathin epitaxial layers: A versatile method for the structural analysis of single quantum wells and heterointerfaces. *Phys. Rev. B* **40**, 9802–9810 (1989).
214. Deslattes, R. D. *et al.* X-ray transition energies: New approach to a comprehensive evaluation. *Rev. Mod. Phys.* **75**, 35–99 (2003).
215. Heitzinger, J. M., Jackson, M. S. & Ekerdt, J. G. Comparison of triethylaluminum, triethylgallium, triethylindium, and triethylantimony on GaAs(100). *Appl. Phys. Lett.* **352**, 352 (1995).
216. Maßmeyer, O., Sterzer, E., Nattermann, L., Stolz, W. & Volz, K. Influence of UDMHy on GaAs (0 0 1) surface reconstruction before and during growth of Ga(NAs) by MOVPE. *Appl. Surf. Sci.* **458**, 512–516 (2018).
217. Drozdov, Y. N. *et al.* Segregation of indium in InGaAs/GaAs quantum wells grown by vapor-phase epitaxy. *Semiconductors* **37**, 194–199 (2003).
218. Muraki, K., Fukatsu, S., Shiraki, Y. & Ito, R. Surface segregation of In atoms and its influence on the quantized levels in InGaAs/GaAs quantum wells. *J. Cryst. Growth* **127**, 546–549 (1993).
219. Höhnsdorf, F. Herstellung und Untersuchung von (GaIn)(NAs)/GaAs-Halbleiterstrukturen. (Philipps Universität Marburg, 2000).
220. Ruiz, J. E., Lackner, D., Souza, P. L., Dimroth, F. & Ohlmann, J. Nitrogen and carbon incorporation in GaN_xAs_{1-x} grown in a showerhead MOVPE reactor. *J. Cryst. Growth* **557**, 125998 (2021).
221. Ougazzaden, A. *et al.* Metal organic vapor phase epitaxy growth of GaAsN on GaAs using dimethylhydrazine and tertiarybutylarsine. *Appl. Phys. Lett.* **70**, 2861–2863 (1997).
222. Moto, A. *et al.* Metalorganic vapor phase epitaxial growth of GaNAs using tertiarybutylarsine (TBA) and dimethylhydrazine (DMHy). *Japanese J. Appl. Physics, Part 1 Regul. Pap. Short Notes Rev. Pap.* **38**, 1015–1018 (1999).
223. Volz, K., Koch, J., Höhnsdorf, F., Kunert, B. & Stolz, W. MOVPE growth of dilute nitride III/V semiconductors using all liquid metalorganic precursors. *J. Cryst. Growth* **311**, 2418–2426 (2009).
224. Zhang, S. B. & Zunger, A. Surface-reconstruction-enhanced solubility of N, P, As, and Sb in III-V semiconductors. *Appl. Phys. Lett.* **71**, 677–679 (1997).
225. Sterzer, E. *et al.* Efficient nitrogen incorporation in GaAs using novel metal organic As-N precursor di-tertiary-butyl-arsano-amine (DTBAA). *J. Cryst. Growth* **439**, 19–27 (2016).
226. Maßmeyer, O. Investigation of the Surface Reconstruction and Gas Phase Composition during Growth by MOVPE. (2020).
227. Pristovsek, M., Zorn, M., Zeimer, U. & Weyers, M. Growth of strained GaAsSb layers on GaAs (0 0 1) by MOVPE. *J. Cryst. Growth* **276**, 347–353 (2005).
228. Weeke, S. *et al.* Segregation and desorption of antimony in InP (0 0 1) in MOVPE. *J. Cryst. Growth* **298**, 159–162 (2007).
229. Pitts, O. J., Watkins, S. P., Wang, C. X., Fink, V. & Kavanagh, K. L. Antimony segregation in GaAs-based multiple quantum well structures. *J. Cryst. Growth* **254**, 28–34 (2003).
230. Kaspi, R. & Evans, K. R. Sb-surface segregation and the control of compositional abruptness at the GaAsSb/GaAs interface. *J. Cryst. Growth* **175–176**, 838–843 (1997).

231. Cherng, M. J., Cohen, R. M. & Stringfellow, G. B. GaAs_{1-x}Sb_x growth by OMVPE. *J. Electron. Mater.* **13**, 799–813 (1984).
232. Stringfellow, G. B. Thermodynamic aspects of organometallic vapor phase epitaxy. *J. Cryst. Growth* **62**, 225–229 (1983).
233. Kaspi, R. Compositional abruptness at the InAs-on-GaSb interface: Optimizing growth by using the Sb desorption signature. *J. Cryst. Growth* **201**, 864–867 (1999).
234. Hawkins, B. E., Khandekar, A. A., Yeh, J. Y., Mawst, L. J. & Kuech, T. F. Effects of Gas switching sequences on GaAs/GaAs_{1-y}Sb_y super-lattices. *J. Cryst. Growth* **272**, 686–693 (2004).
235. Friedman, D. J., Geisz, J. F., Kurtz, S. R., Olson, J. M. & Reedy, R. Nonlinear dependence of N incorporation on in content in GaInNAs. *J. Cryst. Growth* **195**, 438–443 (1998).
236. Harmand, J. C., Ungaro, G., Largeau, L. & Le Roux, G. Comparison of nitrogen incorporation in molecular-beam epitaxy of GaAsN, GaInAsN, and GaAsSbN. *Appl. Phys. Lett.* **77**, 2482–2484 (2000).
237. Dimroth, F., Howard, A., Shurtleff, J. K. & Stringfellow, G. B. Influence of Sb, Bi, Tl, and B on the incorporation of N in GaAs. *J. Appl. Phys.* **91**, 3687–3692 (2002).
238. Biefeld, R. M. *et al.* The growth of infrared antimonide-based semiconductor lasers by metal-organic chemical vapor deposition. *J. Mater. Sci. Mater. Electron.* **13**, 649–657 (2002).
239. Garrod, T. J. *et al.* Narrow band gap GaInNAsSb material grown by metal organic vapor phase epitaxy (MOVPE) for solar cell applications. *J. Cryst. Growth* **315**, 68–73 (2011).
240. Kim, T. W. *et al.* Properties of “bulk” GaAsSbN/GaAs for multi-junction solar cell application: Reduction of carbon background concentration. *J. Cryst. Growth* **393**, 70–74 (2014).
241. Kim, T. *et al.* Impact of Sb Incorporation on MOVPE-Grown Bulk InGaAs(Sb)N Films for Solar Cell Application. *IEEE J. Photovoltaics* **6**, 1673–1677 (2016).
242. Nattermann, L. *et al.* An experimental approach for real time mass spectrometric CVD gas phase investigations. *Sci. Rep.* **8**, 1–7 (2018).
243. Langmuir, I. THE ADSORPTION OF GASES ON PLANE SURFACES OF GLASS, MICA AND PLATINUM. *J. Am. Chem. Soc.* **40**, 1361–1403 (1918).
244. Howard, A. D., Chapman, D. C. & Stringfellow, G. B. Effects of surfactants Sb and Bi on the incorporation of zinc and carbo in III/V materials grown by organometallic vapor-phase epitaxy. *J. Appl. Phys.* **100**, (2006).
245. Tan, K. H. *et al.* Molecular beam epitaxy grown GaNAsSb 1 eV photovoltaic cell. *J. Cryst. Growth* **335**, 66–69 (2011).
246. Islam, M. M. *et al.* Effect of antimony on the deep-level traps in GaInNAsSb thin films. *Appl. Phys. Lett.* **105**, (2014).
247. Kollonitsch, Z., Möller, K., Willig, F. & Hannappel, T. Reconstructions of MOVPE-prepared group-V-rich GaAsSb(100) surfaces. *J. Cryst. Growth* **272**, 694–699 (2004).
248. Lehr, J. *et al.* Effect of growth interruption on Ga(N, As)/Ga(As, Sb)/Ga(N, As) type-II-“W” quantum well heterostructures. *J. Cryst. Growth* **582**, 126501 (2022).
249. Bernatz, G., Nau, S., Rettig, R., Jänsch, H. & Stolz, W. Experimental investigation of structures of interior interfaces in GaAs. *J. Appl. Phys.* **86**, 6752–6757 (1999).
250. Xie, Q., Van Nostrand, J. E., Brown, J. L. & Stutz, C. E. Arsenic for antimony exchange on GaSb,

- its impacts on surface morphology, and interface structure. *J. Appl. Phys.* **86**, 329–337 (1999).
251. Grieb, T. *et al.* Determination of the chemical composition of GaNAs using STEM HAADF imaging and STEM strain state analysis. *Ultramicroscopy* **117**, 15–23 (2012).
252. Hunziker, G., Knop, W. & Harder, C. Gain measurements on one, two, and three strained GaInP quantum well laser diodes. *IEEE J. Quantum Electron.* **30**, 2235–2238 (1994).
253. Lehr, J. *et al.* Room temperature laser emission of (Ga,In)(N,As)/Ga(As,Sb)/(Ga,In)(N,As) type-II ‘W’ quantum well heterostructures. *Electron. Lett.* 20–22 (2022). doi:10.1049/ell2.12427
254. Gao, X. *et al.* Optical characteristics of GaAsSb alloy after rapid thermal annealing. *Semicond. Sci. Technol.* **32**, (2017).
255. Harris, J. S., Bank, S. R., Wistey, M. A. & Yuen, H. B. GaInNAs(Sb) long wavelength communications lasers. *IEE Proc. Optoelectron.* **151**, 407–416 (2004).

Appendix I Sample Index

To ensure reproducibility of all experiments and analysis, all sample numbers for all discussed sample series are listed in this chapter. More details regarding specific samples can be found by searching the sample database for the respective sample number.

Sample series	Sample numbers
Type-I quantum well structures	
GaInAs QW	28248, 28250, 28252, 28253, 28268, 28269
GaAsSb QW	28514, 28516, 28522, 28525, 28403, 28404, 120337, 120338, 120349, 28056, 28058, 120339, 120340, 120342, 28800, 120343, 120341, 28053, 28054, 28060, 27891, 27892, 27893, 27894, 27981, 27982, 27984, 28057, 28059, 27980
EFSTEM GaNAs QW	28139
(Ga,In)(N,As) QW test structures UDMH _y	28731, 28733, 28736
(Ga,In)(N,As) QW test structure DTBAA	28750
GaNAs:Sb series	28513, 28515, 28510 (reference), 28517, 28527, 28531, 28537
GaNAs:Sb compensation series	28524, 28526, 28517
GaNAs:Sb DTBAA	28755, 28756, 28757, 28758
Ga(N,As)/Ga(As,Sb)/Ga(N,As) WQWH	
UDMH _y type-II QWH	28519, 28520
DTBAA type-II QWH	28742, 28749
Type-II QWH As/III (Ga(N,As))	120351, 120354, 120356
Type-II QWH V/III (Ga(As,Sb))	120346, 120348, 120350, 120351, 120352, 120353
Selective etching GaAsSb	27680, 27676, 27664, 27672, 27668
Selective etching GaAs	27697, 27675, 27663, 27671, 27667
Growth interruption series	28154, 28164, 28162, 28155, 28156, 28157
STEM sample growth interruption series	27789
UDMH _y Pp Optimization series	28765, 28766, 28767, 28769, 28782

Type-II QWH laser	28181
Nitrogen dependency WQWH laser	27706, 28787, 27911, 27914
Number of WQWH laser	28793, 28287, 28794
DTBAA vs UDMHy laser	28787, 28789
Ga(N,As)/(Ga,In)As/Ga(N,As) WQWH	
(Ga,In)As/Ga(N,As) DQW	28375, 28376
Ga(N,As)/(Ga,In)As DQWs for wavelength determination	28262, 28263, 28254, 28255, 28256, 28259, 28258, 28257
(Ga,In)As/Ga(N,As) preparation of internal interface	28255, 28260, 28264, 28266
(Ga,In)As/Ga(N,As) laser devices	28401, 28402
(Ga,In)(N,As)/Ga(As,Sb)/(Ga,In)(N,As)	
(Ga,In)(N,As)/Ga(As,Sb) laser devices	28791, 28792

Danksagung

Ohne eine Vielzahl von Personen wäre diese Arbeit in dieser Form nicht möglich gewesen. Besonders danke ich Prof. Dr. Wolfgang Stolz für die sehr gute Betreuung und die Möglichkeit diese Arbeit in seiner Gruppe anfertigen zu können. Vielen Dank an alle Mitglieder des STRL für die freundliche Aufnahme in der Gruppe und die gute Atmosphäre.

Außerdem danke ich ...

... Prof. Dr. Wolfram Heimbrodts für die Übernahme des Zweitgutachtens.

... der DFG für die Finanzierung meines Projektes im Rahmen des SFB 1083 „Structure and Dynamics of Internal Interfaces“.

... den Korrekturlesern Robin Güntel, Thilo Hepp, Stefanie Lehr und Hanna Bohnensteffen, die sich fleißig durch alle Kapitel dieser Arbeit gekämpft haben und so sehr zur Lesbarkeit der Arbeit beigetragen haben.

... den Technikern Stefan Reinhard, Thomas Ochs, Celina Becker und Michael Hellwig für die schnelle und kompetente Hilfe in den Fällen, in denen die Epitaxieanlagen und andere Laborausstattung spontan keine Lust mehr auf Experimente hatten.

... Saleh Firoozabadi, Varun Shankar Chejarla, Dr. Pirmin Kükelhan und Yurii Radiev für die STEM Messungen an meinen Proben.

... Dr. Ada Bäumner für die Bereitstellung von Simulationen meiner Laserstrukturen.

... allen Epitaxiekollegen von der Uni und von NAsP_{III/IV} für die sehr gute Arbeitsatmosphäre und gute Diskussionen.

... meinen Kollegen des 1. Zuges, mit denen ich unzählige schlaflose Nächte überstanden habe.

... meinen Freunden für die Ablenkung von meiner Arbeit.

Zum Schluss danke ich meiner Familie – insbesondere meinen Eltern – und Hanna für die dauerhafte Unterstützung, ohne die mein Studium und diese Arbeit so nicht möglich gewesen wären.

Wissenschaftlicher Werdegang